Graphène ponté pour supercondensateurs : du développement des matériaux à la caractérisation électrochimique

Omar Hassan

THÈSE

Pour obtenir le grade de

DOCTEUR DE L'UNIVERSITÉ GRENOBLE ALPES

École doctorale : CSV- Chimie et Sciences du Vivant
Spécialité : Chimie Physique Moléculaire et Structurale
Unité de recherche : Systèmes Moléculaires et Nano Matériaux pour l'Énergie et la Santé

Graphène Ponté pour Supercondensateurs: du Développement des Matériaux à la Caractérisation Électrochimique

Pillared-Graphene Materials for Supercapacitors: from Material Development to Electrochemical Characterization

Présentée par :

Omar HASSAN

Direction de thèse :

Lionel DUBOIS DIRECTEUR DE RECHERCHE, CEA	Directeur de thèse
Florence DUCLAIROIR DIRECTRICE DE RECHERCHE, CEA	Directrice de thèse

Rapporteurs :

Camelia GHIMBEU
DIRECTRICE DE RECHERCHE, CNRS délégation Alsace
Charles COUGNON
CHARGE DE RECHERCHE HDR, CNRS délégation Bretagne et Pays de la Loire

Thèse soutenue publiquement le **19 janvier 2024**, devant le jury composé de :

Camelia GHIMBEU DIRECTRICE DE RECHERCHE, CNRS délégation Alsace	Rapporteure
Charles COUGNON CHARGE DE RECHERCHE HDR, CNRS délégation Bretagne et Pays de la Loire	Rapporteur
Patrice SIMON PROFESSEUR DES UNIVERSITES, Université Toulouse 3 – Paul Sabatier	Examinateur
Saïd SADKI PROFESSEUR DES UNIVERSITES, Université Grenoble Alpes	**Président**
Lionel DUBOIS DIRECTEUR DE RECHERCHE, CEA centre de Grenoble	Directeur de thèse
Florence DUCLAIROIR DIRECTRICE DE RECHERCHE, CEA centre de Grenoble	Directrice de thèse

وَأَن لَّيْسَ لِلْإِنسَانِ إِلَّا مَا سَعَىٰ ﴿٣٩﴾ وَأَنَّ سَعْيَهُ سَوْفَ يُرَىٰ ﴿٤٠﴾
ثُمَّ يُجْزَاهُ الْجَزَاءَ الْأَوْفَىٰ ﴿٤١﴾

القرآن الكريم، سورة النجم، الآيات ٣٩-٤١

And that there is not for man except that [good] for which he strives ﴿39﴾ And that his effort is going to be seen ﴿40﴾ Then he will be recompensed for it with the fullest recompense ﴿41﴾

The Holy Quran, Surah An-Najm, verses 39-41

Acknowledgements

I would like to start this section by expressing my deepest appreciation to my jury members (Dr. **Camelia GHIMBEU**, Dr. **Charles COUGNON**, Prof. **Patrice SIMON** and Prof. **Saïd SADKI**) for their time and for agreeing to be part of my jury despite their very busy schedules, which I appreciate very much. I would also like to thank them for the fruitful and rich discussion we had during the defense. Their comments and feedback were highly insightful and open a lot of directions for my future career as a researcher.

I would also like to extend my deepest gratitude to my CSI members (Dr. **Philippe AZAIS**, Dr. **Anass BENAYAD**, Dr. **Eirini SARIGIANNIDOU** and Dr. **Encarnacion RAYMUNDO**) for their support, suggestions, recommendations, and constant encouragement during the CSI meetings which helped me not to veer off track and continue on the right path to success.

Such a success would not have been possible without the support and nurturing of my supervisors (Dr. **Florence DUCLAIROIR** and Dr. **Lionel DUBOIS**) aside of which I spent more than 3 years working, starting from my Master thesis. During this period, I got to know them and connect with them more both on the personal and professional levels which contributed in formulating the person and researcher I am today. I want to thank them for their mentoring and supervision throughout this period. It was a pleasure working along their sides and learning from them. I will take with me many memories from our discussions, especially the heated ones with Lionel :D To Florence, thank you for your constant encouragement and profound belief in my work and abilities.

I'm extremely grateful to our collaborators in CIRIMAT (Dr. **Pierre-Louis TABERNA**, Prof. **Patrice SIMON** and Dr. **Giovanna FRANKLIN**), College de France (Dr. **Ozlem SEL** and Dr. **Hubert PERROT**, Dr. **Arpita GHOSH** and Dr. **Nilanka KEPPETIPOLA**), STEP (Dr. **Hakima MENDIL-JAKANI** and Ms. **Emilie DUBARD**) and MEM at CEA Grenoble (Dr. **Gael DE PAEPE**, Dr. **Subhradip PAUL** and Dr. **Sabine HEDGER**) for their valued contributions in discussions during various scientific meetings and for hosting me in their laboratories for trainings and carrying out different experiments. I'd also like to acknowledge the assistance of Mr. **Yves CHENAVIER** throughout the PhD as he was instrumental in teaching me various techniques when I first arrived in the lab and even later on, he never let me down when I needed his help or had a question. I also had the great pleasure of working closely with Dr. **Stephanie POUGET**, Dr. **Vincent MAUREL** and Dr. **Pascal MALDIVI** whom I want to deeply thank for their time, availability, collaboration and valuable insights and discussions. Their contributions have been instrumental to this thesis.

I would like to extend my sincere thanks to all the CAMPERs, my 2nd family. I want to thank them all for welcoming me to the lab and making me feel at ease and comfortable. I would like also to thank them for the scientific discussions regarding my work and feedback on my presentations and talks that helped perfect my work and most importantly the wonderful times we had together from the breakfasts to the cakes and sweets at 4pm to the outings like the bowling, laser-tag games, and the hiking adventures even the one in the snow :O. I can't mention the CAMPERs without dedicating a section to the non-permanents represented by the Supreme Council of the Non-Permanents (SCNP). I want to thank them for making the stay in the lab more fun and enjoyable. I wish them all the best in their future careers and as I always sign my emails: Vive les non-permanents :D.

During my three years at CEA, I have made many lifelong friends, among whom I want to name Dr. **Yassine BEN CHERIFI**, Dr. **Ali DABOUS**, Dr. **Ons DAKHLAOUI**, Dr. **Adnane BOUZINA**, soon to be Dr. **Shadi ALARAB** and soon to be Dr. **Christian ELFEREKH** to thank them for all the help they offered me during my PhD work and for the precious memories we shared together all over these three years in and out of the lab and for the crazy amount of food we had together. To more and more precious moments and very delicious food :D

Besides friends from the Lab, I have made many more friends outside. I would like to mention their names, but this might take a page on its own so I will refer to them as the esteemed grenoblois members of the ADEEF (Association des Etudiants Egyptiens en France). I would like to thank them for giving me a fun work-free life outside the lab and making life warmer and cozier despite the very cold weather of Grenoble.

This journey wouldn't have been completed if it hadn't been for the unconditional love and unwavering support, I had been receiving from all my family members. I very much appreciate them and I am grateful for their presence in my life and forever deeply indebted to them. Father, mother, brother, sister, grandmother, uncles, aunts, cousins and all their husbands, wives and children. Love you all.

In the "making" of the PhD, there are people who contributed to the final product without appearing on the screen. Those people are my childhood, school, and university lifelong friends. I'm extremely grateful to them for always being there for me and for offering me a safe space and a nostalgic "break" out of the daily routine of a PhD student. I would like to name a few: **Sherif Hany**, **Eslam Ayman**, **Adnan Alaa** (This guy here proof-read my whole thesis in one day. Kudos to him), **Mohamed Maher**, **Omar Hamdy** and Dr. **Mohamed Khairy**.

At the end, I would like to thank my favorite football player and my role model in determinism, self-motivation, and consistency: **Mohamed Salah** who made my Saturdays and Sundays more joyful with him scoring more and more goals. You might wonder why I am thanking him although I have never met him, well, maybe someone would read this paragraph, share it online, it goes viral, reaches Salah and then I get an invitation to see Salah play and get to meet him in person, who knows ? :D (AKA do it if you have reached so far in this section haha).

Me humming:

"Mo Salah! Mo Salah! Mo Salah! Running down the wing.

"Salah la-la-la la-ahh, The Egyptian King!"

Dedication

I would like to dedicate this Thesis to my whole Family especially my mother (Dr. Manal Fekry), father (Dr. Sabry El-Basha), sister (Ms. Noura El-Basha), brother (Mr. Khaled El-Basha) and Grand-Mother (Mrs. Laila El-Kayal) who always encouraged me to become a doctor.

I would also like to dedicate this Thesis to the soul of the late Professor Ahmed Zewail, the 1999 Nobel laureate in Chemistry and the founder of Zewail City of Science and Technology, to whom I owe my passion for science and my gratitude for the opportunity given to me to study sciences and technology in such a high caliber institute as Zewail City.

Table of Contents

List of Abbreviations

A AB: Acetylene Black

AC: Activated Carbon

AFM: Atomic Force Microscopy

AN: Acetonitrile

B BDA: Butane-1,4-diamine

bGF: bulk Graphite Fluoride

C CDCs: Carbide-Derived Carbons

CE: Counter Electrode

CHDA: 1,4-Cyclohexane diamine

CL: Cross-Linking/Cross-Linked

CNTs: Carbon NanoTubes

C_{SP}: Specific/gravimetric Capacitance (units: F/g)

CV: Cyclic Voltammetry/Voltammogram

CVD: Chemical Vapor Deposition

D DH-AA: DeHydroAscorbic Acid

E EA: Elemental Analysis

EDA: Ethylene diamine

EDLC: Electrochemical Double Layer Capacitance/Capacitor

EIS: Electrochemical Impedance Spectroscopy

$EMIBF_4$/$EMIMBF_4$: 1-Ethyl-3-methylimidazolium tetrafluoroborate

EPR: Electron Paramagnetic Resonance

EQCM: Electrochemical Quartz Crystal Microbalance

F FT-IR: Fourier-Transform InfraRed spectroscopy

FWHM: Full Width at Half Maximum

G GA: Graphene Aerogel

GCD: Galvonostatic Charge-Discharge

GH/GHG: Graphene Hydrogel

GO: Graphene Oxide

H HDA: Hexane-1,6-diamine

HR: High Resolution

Hz: Hydrazine

L L-AA: L-Ascorbic Acid

M MPD: Meta-phenylenediamine

MWCNTs: Multi-Walled Carbon NanoTubes

N NMP: N-Methyl-2-pyrrolidone

O OCV: Open Circuit Voltage

ODA: 4,4'-oxydianiline

OPD: Ortho-phenylenediamine

P PC: Propylene carbonate

PD: Phenylenediamine

PDA: Para-phenylenediamine

PGM: Pillared Graphene Materials

PPD: Para-phenylenediamine

PTFE: Polytetrafluoroethylene

PVA: Poly VinylAlcohol

PVDF: Polyvinylidene fluoride

Q QENS: Quasi-Elastic Neutron scattering

R R_{CT}: Charge Transfer Resistance

RE: Reference Electrode

R_{ESR}: Equivalent Series Resistance

rGO: reduced Graphene Oxide

S SANS: Small Angle Neutron Scattering

SAXS: Small Angle X-ray Scattering

SC: SuperCapacitors

SG: Spherical Graphene

SECM: Scanning ElectroChemical Microscopy

SEM: Scanning Electron Microscopy

SS: Stainless Steel

ssNMR: solid state Nuclear Magnetic Resonance

SWCNTs: Single-Walled Carbon NanoTubes

SXI: X-ray induced secondary electron images

T TBABF$_4$: Tetrabutylammonium tetrafluoroborate

TEABF$_4$: Tetraethylammonium tetrafluoroborate

TEM: Transmission Electron Microscopy

TEMABF$_4$: Triethylmetylammmonium tetrafluorobotate

TGA: Thermal Gravimetric Analysis

THABF$_4$: Tetrahexylammonium tetrafluoroborate

TPABF$_4$: Tetrapropylammonium tetrafluoroborate

Tris: Tris(2-aminoethyl) amine

V VitC: Vitamin C

W WANS: Wide Angle Neutron Scattering

WAXS: Wide Angle X-ray Scattering

WCA: Water Contact Angle

WE: Working Electrode

X XPS: X-ray Photoelectron Spectroscopy

XRD: X-Ray Diffraction

List of Figures

Chapter 1

Chapter 2

Chapter 3

Chapter 4

Chapter 5

Abstract

Supercapacitors are increasingly sought-after energy storage devices as they serve in many applications, such as means of transportation like electric vehicles, heavy construction equipment, wind turbines, etc. They owe their popularity to their merits, which include high power density, high cyclability, long lifetime, being independent of toxic and noble materials, and wide range of operational temperature. However, they suffer from low energy density. Research has been going on to improve this property through i) developing new electrode materials to enhance their capacitance and ii) enlarging the potential window of the electrolyte employed. Activated carbon is the most commonly used electrode material for supercapacitors due to its high specific surface area, cheap price, and ease of production. Nevertheless, its capacitance is limited to 150 F/g in organic electrolytes, which constrains its domains of applicability. One of the promising materials as an alternative to activated carbon is graphene. Since its discovery in 2004 [1], it has been considered a "Wonder" material with lots of potential due to its attractive properties. Owing to such properties, graphene is theoretically expected to possess an electrochemical double layer capacitance of 550 F/g [2]. However, due to the high cost and difficulty of producing and handling single sheets of graphene, the presence of graphene in the market has been hindered. Luckily, many methods were devised to synthesize graphene-like materials that would be easier and cheaper to produce. Unfortunately, such methods end up producing reduced Graphene Oxide (rGO) with restacked graphene layers that impedes the full exploitation of graphene's surface area. Spacing-out graphene sheets using organic linkers, also known as pillaring, was proven to be one of the efficient techniques in limiting π-π interactions and partially preventing the restacking of the graphene sheets in rGO [3]. Consequently, the work at hand aims at better understanding the effect of the surface chemistry, the polarity of the pillars, and the inter-graphene sheet distance on the performance of these materials as electrode materials for supercapacitors and on their associated energy storage mechanisms. These correlations will help optimize the materials to reach higher storage performances.

Herein, three molecular pillars with different chemical nature and lengths were utilized as pillaring agents for graphene to yield pillared graphene assemblies with different structural and chemical properties, such as different d-spacing values and different pillars' chemical composition. To assess the success of the pillaring technique and to decipher the chemical composition and the structure of the samples, various characterization techniques were employed such as XRD, TGA, XPS, EA, SEM, TEM, WCA, FT-IR, Raman spectroscopy, and electrical conductivity measurements. This work aims also at investigating the ion-pore size

matching phenomena in aqueous electrolytes as well as the role played by the solvation shell. Accordingly, the performance of these pillared assemblies as electrode materials for supercapacitors was assessed against that of rGO as a reference sample. Different electrolytes were used to test the electrochemical performance in different environments (acidic and neutral with different cation and anion sizes). The pillared graphene assemblies demonstrated an enhanced capacitive performance compared to rGO in all tested electrolytes. A correlation between such enhanced performances and the different physico-chemical characteristics was established, highlighting the important role played by the pillar/surface chemistry and the d-spacing. The former was manifested in the various roles played by carbonyl groups whether in redox reactions or in formation of ion-specific adsorption sites, while the later was revealed through the restricted access of ions to pores smaller than their hydrated sizes. Insights about the charging mechanism of such samples were also demonstrated.

Despite the demonstrated efficiency of Pillared Graphene Materials (PGM), most of their preparation methods are not green as they entail the use of hydrazine hydrate (Hz) as a reducing agent. Since hydrazine is a very toxic chemical, research has been conducted to find alternatives to its use. Many reducing agents have been experimented, yet L-Ascorbic Acid (L-AA), commonly known as Vitamin-C (VitC), was found to be an efficient reducing agent, offering a mild green reduction process [4]. In literature, many diverse protocols involving L-AA have been used. Accordingly, the work at hand aims at rationalizing the correlation between important reaction parameters and rGO-VitC properties, as well as providing mechanistic insights on the reduction process.

Herein, a full study on the reduction of graphene oxide using L-AA was carried out including varying the reaction parameters such as the amount of L-AA and the reaction time. Various characterization techniques were employed to analyze the physico-chemical, structural, and morphological differences between rGO reduced with L-AA and Hz, including XPS, EA, XRD, TGA, SEM, TEM, Raman spectroscopy, and electrical conductivity measurements. L-AA demonstrated good reduction capabilities. The relationship between experimental conditions and graphene intrinsic properties were presented. Short reaction time with higher amount of L-AA yields high C/O ratio with high electrical conductivity, while the inverse leads to lower C/O ratio and lower electrical conductivity. In addition, thanks to EPR, a reaction mechanism involving the formation of ascorbyl radicals was postulated, leading to the formation of H_2O_2, a potential oxidizing agent that oxidized back rGO. The various characterization results allowed devising models to explain structural, chemical, and property (ex. electrical conductivity) differences between the different reduced samples inspected.

Furthermore, being a material of high interest for supercapacitor applications, the electrochemical storage performances of the rGO samples reduced with those two reducing agents were assessed in various electrolytes (acidic, basic, and neutral). rGO-VitC showed superior performance compared to that of rGO-Hz, while maintaining similar resistance values (ionic and ESR), in all electrolytes. The obtained results pave the road for the employment of L-AA as a mild green reduction method for not only GO but also for different GO-based materials, such as pillared graphene materials.

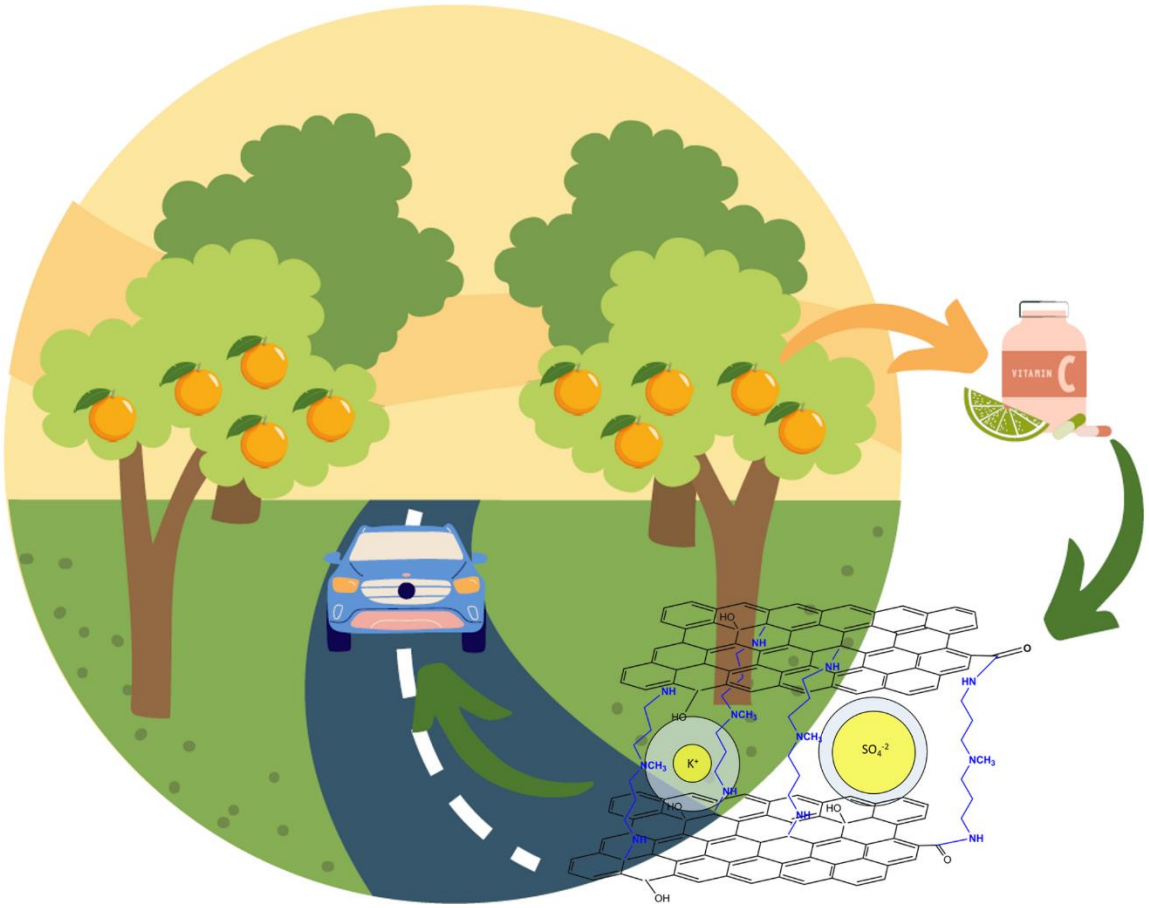

References

[1] K. S. Novoselov *et al.*, 'Electric Field Effect in Atomically Thin Carbon Films', *Science*, vol. 306, no. 5696, pp. 666–669, Oct. 2004, doi: 10.1126/science.1102896.

[2] J. Zhu, D. Yang, Z. Yin, Q. Yan, and H. Zhang, 'Graphene and Graphene-Based Materials for Energy Storage Applications', *Small*, vol. 10, no. 17, pp. 3480–3498, 2014, doi: 10.1002/smll.201303202.

[3] H. Banda *et al.*, 'Sparsely Pillared Graphene Materials for High-Performance Supercapacitors: Improving Ion Transport and Storage Capacity', *ACS Nano*, vol. 13, no. 2, pp. 1443–1453, Feb. 2019, doi: 10.1021/acsnano.8b07102.

[4] K. K. H. De Silva, H.-H. Huang, R. K. Joshi, and M. Yoshimura, 'Chemical reduction of graphene oxide using green reductants', *Carbon*, vol. 119, pp. 190–199, Aug. 2017, doi: 10.1016/j.carbon.2017.04.025.

Introduction

&

Literature Review

Chapter 1: Introduction and Literature Review

I.1 Need for Energy Storage Devices

Renewable energy resources have been proposed as environmentally friendly alternatives to the almost ending polluting fossil fuels with a forecasted run out time of around 100 years [1], [2]. A common attribute for these alternative energy sources (ex. wind power and solar power), apart from being renewable and green, is that they are intermittent in nature, and therefore need systems to store the harnessed energy to be used later and/or away from the energy harvesting locations [3], [4]. Not only are the energy storage devices important for storing green energy, but also they are crucial for storing energy in general for a myriad of vital applications in today's world. The increasing demand for energy, and hence on energy storage devices, rising from the diversity of applications and their growing complexity, requires energy storage devices. Such devices should be capable of i) storing energy with high efficiency and ii) displaying high energy densities (able to store energy in large quantities), high power densities (able to deliver large amounts of energy in short periods of time), and long life time to be used multiple times efficiently. These devices should fulfill the aforementioned requirements while iii) being light and portable, iv) supporting fast charging, v) being of low cost, and made from available materials with no toxic or noble elements.

I.1.1 Energy Storage Devices

Among the electrochemical energy storage devices, supercapacitors and batteries are the ones that meet most of these requirements, leading to their implementation in many applications. Batteries are characterized by their high energy densities, but they lack long lifetime, fast charging, and high power densities. On the other hand, supercapacitors are characterized by their high power densities, fast charging, long lifetime, and independence of toxic materials. However, they display limited energy densities and are more expensive compared to batteries when looking at their price per kWh. This latter cost drawback can be leveled out as the supercapacitors extended cycle life leads to lower price per kWh per cycle than that of batteries.

I.2 Applications of Supercapacitors (SCs)

Owing to their high power density and fast charging times, SuperCapacitors (SCs) have found their way to many crucial applications. Those applications either require high power (bursts of energy in short periods of time) - whether continuous or pulsed - or need to exploit transient opportunities to generate energy, aiming at reducing fuel consumption, boosting performance, and/or reducing CO_2 emissions. The former type of applications includes high

power demanding equipment, such as rock crushers that utilize supercapacitors in a pulse fashion to deliver power only when high power peaks are needed (Ex. Rockster R1100DE rock crusher shown in Figure (I.1(a)). It also includes construction and mining hardware like the Caterpillar 6120 H FS 1400-ton mining shovel (Figure I.1(b)) which gets ~44% of its horsepower from the use of supercapacitors in a bidirectional fashion where it discharges and charges as the machine goes on. Such a way of operation saves 25% of fuel that would have been used to deliver same power levels without the supercapacitors [5]. The later type of applications encompasses applications that reduce energy losses and capitalizes on ephemeral energy storage opportunities such as cars' start-stop technologies and regenerative braking that transforms braking energy into electrical energy stored in under a minute and then uses it for different processes up to even powering the whole vehicle for short distances. This process has been applied to multiple hybrid means of transportation, such as buses and trams (Figure I.1(c)) in France, Germany, China, and others, showing a great potential in the reduction of fuel consumption and thus CO_2 emissions [6]. Other applications include wind turbines [7], [8], supporting the operation of different devices connected to the grid, when power goes off, and before the power generator takes control [9], [10], and heavy construction equipment such as cranes [11].

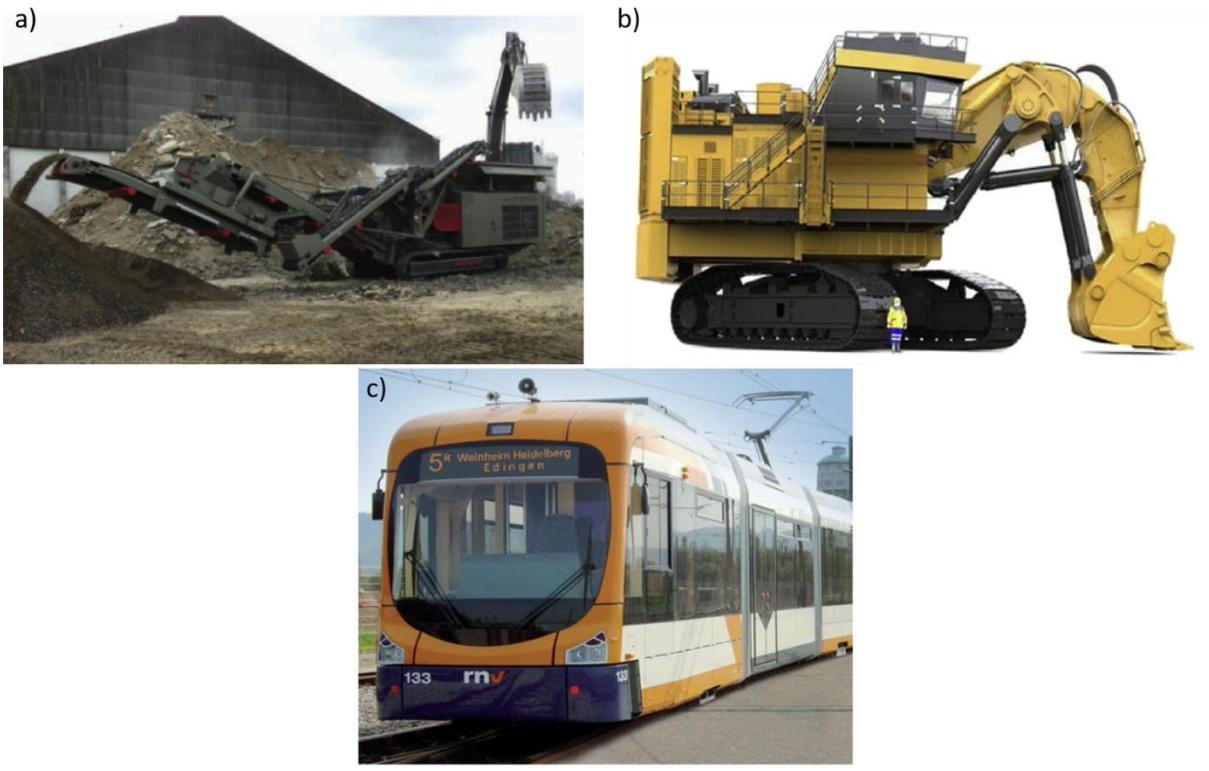

Figure I. 1 : a) Rockster R1100DE rock crusher [5], b) Caterpillar 6120 H FS 1400-ton mining shovel [5] and c) a supercapacitor-powered tram in Germany [6]

I.3 How do Supercapacitors Work: A Global Picture

The interesting properties of supercapcitors, listed before, are direct consequences of their fundamental working principle. Supercapacitors are composed of two polarizable high surface area conducting electrodes, an electrolyte, current collectors and a separator (Figure I.2). When an external potential is applied to charge the supercapacitor, electronic charges start accumulating on the electrodes, triggering the diffusion and adsorption of the electrolytic ions to compensate such charges in an electrostatic manner (Figure I.2(b)). On the discharge, the opposite occurs; electrons flow to the external circuit to power a device, and the ions diffuse back to the bulk electrolyte (Figure I.2(c)).

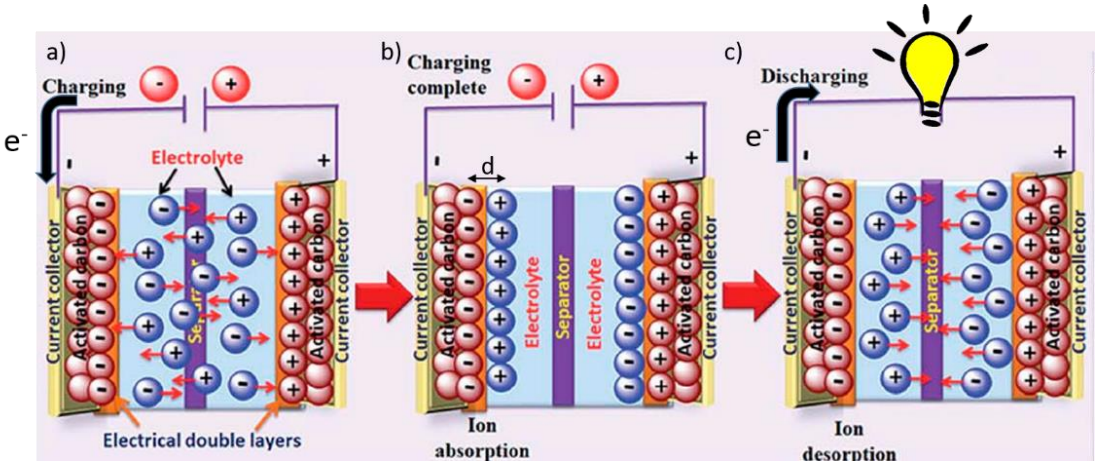

Figure I. 2 : A supercapacitor during its operational cycle (adapted from [12])

There are 2 main types of supercapacitors that can be distinguished by their energy storage mechanisms. Firstly, Electrochemical Double Layer Capacitors (EDLCs) only store energy through adsorption and desorption of electrolytic ions at the surface of highly porous carbonaceous electrode materials, with no charge transfer occurring across the electrode-electrolyte interface (non-faradaic process) (Figure I.3(a)) [13]. The second type, named pseudocapacitors, rely on highly reversible surface or near surface faradaic processes taking place between the electrode (not anymore a full carbonaceous material but for example transition metal oxides, hydroxides (ex. RuO2) or conducting polymers (ex. polyaniline and polypyrrole)) and the electrolyte, in addition to the electrochemical double layer charge storage mechanism (ion adsorption and desorption) (Figure I.3(b)) [14]. The aforementioned faradaic processes can include either redox reactions or intercalation/de-intercalation processes. Some reports do treat the pseudocapacitive intercalation/de-intercalation as a 3rd type of supercapcitor (Figure I.3(c)). Figure (I.3) summarizes the different charge storage mechanisms of supercapactiors.

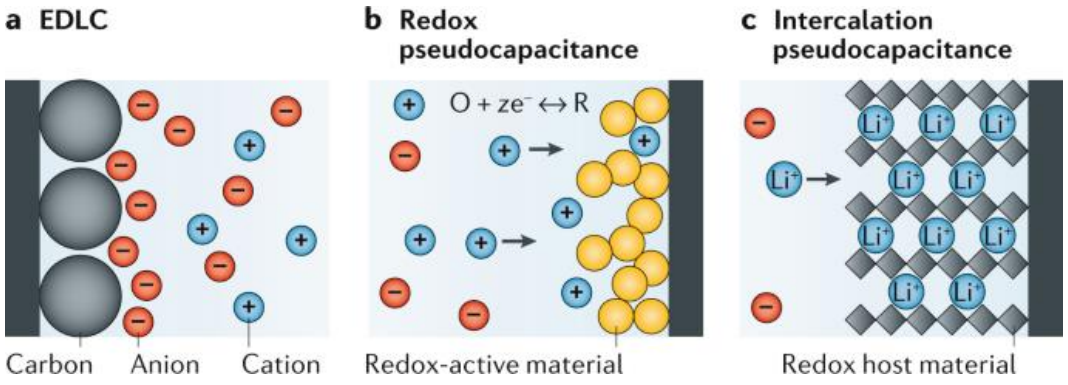

Figure I. 3 : a) Electrochemical Double Layer Capacitance (EDLC), (b) Redox Pseudocapacitance and (c) Intercalation Pseudocapacitance [15]

I.4 How Do Supercapacitors Work: Charge Storage Mechanisms

In order to dig deep in the fundamentals behind the mechanism of EDLC and pseudocapacitor, it is important to know how batteries operate and see how all those electrochemical systems compare. Such a discussion about batteries is also useful because a discussion regarding supercapacitors always raises the question: Will supercapacitors be able to replace batteries if their energy density shortcomings are overcome? So, in order to try and answer that question thoroughly based on the published literature on that matter, a distinction has to be made between what is a battery and what is a supercapacitor along with their mechanism of charge storage and their distinct characteristics and signatures to realize that the two energy storage devices are meant to complement each other and work together in tandem. Herein, the charge storage mechanisms of EDLC and batteries are explained and then compared to each other.

I.4.1 EDLC

In EDLC, the energy storage mechanism relies solely on electrostatic charge compensation mechanism (no redox reactions) through rapid non-diffusion limited surface adsorption, thus responding rapidly to changes in potential, leading to high power densities. The EDLC are characterized by long-term stability, as there is no chemical degradation due to the absence of chemical or phase changes. However, the amount of charges that can be stored on the surface is bound by the surface area of the material used and by the Coulombic repulsion between charges of similar sign, resulting in low energy densities, according to the following equations:.

$$C = \frac{\varepsilon_0 \varepsilon_r A}{d} \qquad (I.1)$$

$$E = \frac{1}{2} CV^2 \qquad (I.2)$$

Where C is the capacitance (F), ε_0 is the vacuum permittivity (F/m), ε_r is the relative permittivity, A is the electrochemically active surface area (m^2), d is the charge separation distance (m), E is the Energy (J) and V is the volatage (V). Based on Eq.(I.1), it is clear that much higher capacitances values (C) can be achieved through increasing the electrochemically active surface area (A) and decreasing the charge separation distance (d) which is the distance between the charged electrode and the oppositely charged species adsorbed on its surface (Figure I.2(b)). However, it has been shown recently that increasing the surface area on its own is not the key to higher capacitances [16]–[24]. Pores' shapes and size distributions as well as their relation to both the naked ion and solvated ion sizes are in fact more crucial and critical than the surface area itself. Increasing the surface area without considering such other aspects might result in very tight pores that are inaccessible to the ions (blocked pores). It might also lead to tortuous passes and channels that hinder the ion transport process and/or large pores that result in a large separation distance (d) between the oppositely charged particles and the electrode, thus decreasing the capacitance. Hence, the achievement of a hierarchical pore size distribution has to be targeted, as hierarchical pore size distribution is a key aspect for EDLC electrode materials. Furthermore, it has been shown, experimentally and theoretically, that the presence of pores of sizes approximately equal to the size of the naked ion employed, helps in boosting the capacitance, in case of organic electrolytes and ionic liquids (Figure I.4(a)) [17]–[19]. This phenomenon was explained by the electrolytic ions partially shedding their solvation shells before entering the pores of sizes approximately equal to their naked ion sizes, leading to a better exploitation of the surface area and smaller charge separation distance (d). Less or no solvent molecules screening the charge leads to an excess charge density on the electrode side (Figure I.4(b)) [20]–[23]. In ionic liquids, such an increase in capacitance in micropores was attributed to the image charges induced in the carbon walls that overcome the Coulombic repulsive interaction between ions of similar charges, allowing them to form pairs of the same ion, thus enhancing the filling of the pores [24]. Fleischmann, S. et al. discussed the nano-confinment phenomena and showed that as the desolvation degree of the nano-confined ions increase, their interaction with the electrode increases [25]. The optimum pore size was found to be around 0.7-0.8 nm for most of the used electrolytes. Such revelation shed light on the importance of tailoring the electrochemically active surface area to achieve ion-pore size matching.

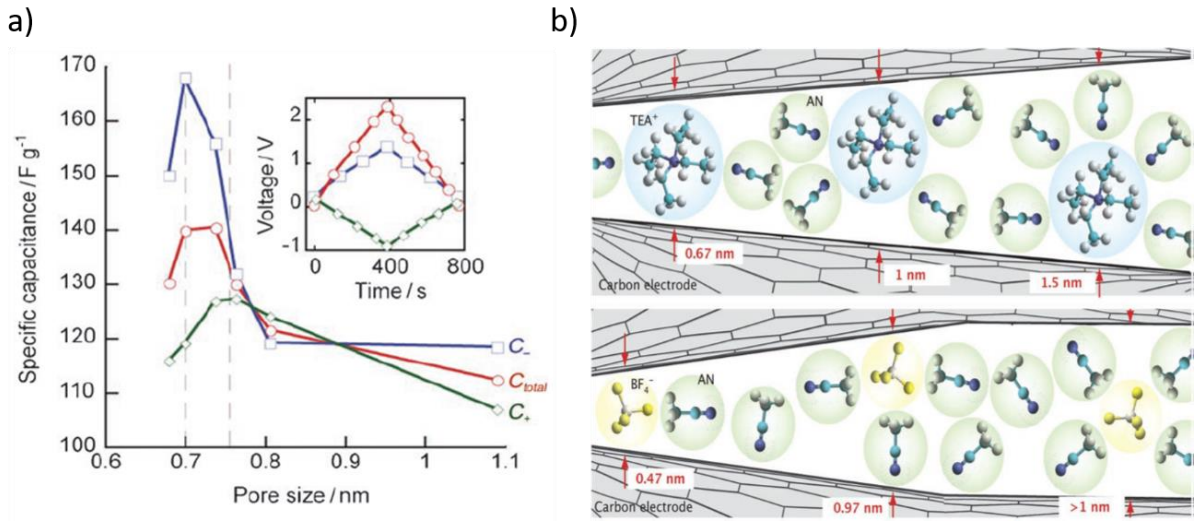

Figure I. 4: a) The capacitance at the positive electrode (C_-), at the end negative electrode (C_+), and total specific capacitance (C_{total}) values versus the average pore size for the CDC samples and b) Ion confinement in pores of different sizes where higher degrees of partial de-solvation occurs as the pore size gets narrower. Also different sizes are shown for both cations and anions. The materials used were a CDCs in 1.5m tetraethylammonium tetrafluoroborate ($TEABF_4$) in acetonitrile (AN) [19]

I.4.2 Batteries

In batteries, contrary to EDLC, the charge storage mechanism predominantly relies on the occurrence of redox reactions (Ex. Li^+ ions intercalation and de-intercalation in Li-ion batteries). Such intercalation involves phase changes and has slower kinetics compared to the electrostatic interactions occurring in supercapacitors as, typically, they entail diffusion-controlled processes. Accordingly, high power densities and long life-time are not among the assets of batteries. However, since there is no charge accumulation and the charges are consumed in faradic processes, much more charges can be stored, leading to high energy densities.

I.4.3 EDLC versus Batteries: Electrochemical Signature

The different charge storage mechanisms involved in both devices result in unique electrochemical signatures, differentiating them. Such signatures can be accessed through potentiostatic and galvanostatic techniques. Those signatures are shown in Figures (I.5(a), (b), (d) & (e)). EDLC supercapacitors yield a rectangular Cyclic Voltammogram (CV) while batteries show distinct strong oxidation and reduction peaks that are usually separated with large voltage (by more than 0.1V-0.2V) due to phase changes. The galvanostatic charge and discharge curves of supercapacitors show a time linear dependence of the potential at constant applied current leading to triangular charge and discharge profiles; while that of batteries show a non-linear behavior with a sloping part and a plateau, where a solid solution is formed and the two phases co-exist (intercalated and de-intercalated phases). These charging and discharging curves show that the charge stored (Q) in EDLC is directly proportional to the

applied potential (V), with the capacitance value (C) being the proportionality constant (Eq. I.3); while in the case of batteries the amount of charges stored follows a non-linear behavior with the potential.

$$Q = CV \qquad (I.3)$$

Classifying pseudocapacitors as supercapacitors is sometimes perplexing due to the fact that the charge storage mechanism of pseudocapacitors is faradic by nature (very fast surface or near surface redox reactions) which makes them confused with batteries. However, they are indeed a class of supercapacitors. To set them apart from batteries, the faradic charge storage of pseudocapacitors is always accompanied by highly reversible and very fast redox reactions, with the oxidation and reduction peaks having little to no voltage separation. The electrochemical signature of pseudocapacitors resembles that of the EDLC; the overall shape of the CVs of a pseudocapacitor is similar to the rectangular shape of an EDLC's CV. Additionally, a linear relation in the potential versus time of the galavanostatic charging and discharging plots are also observed for both pseudocapacitors and EDLC which allows their classification as supercapacitors (Figures I.5(c) & (f)). [26], [27]

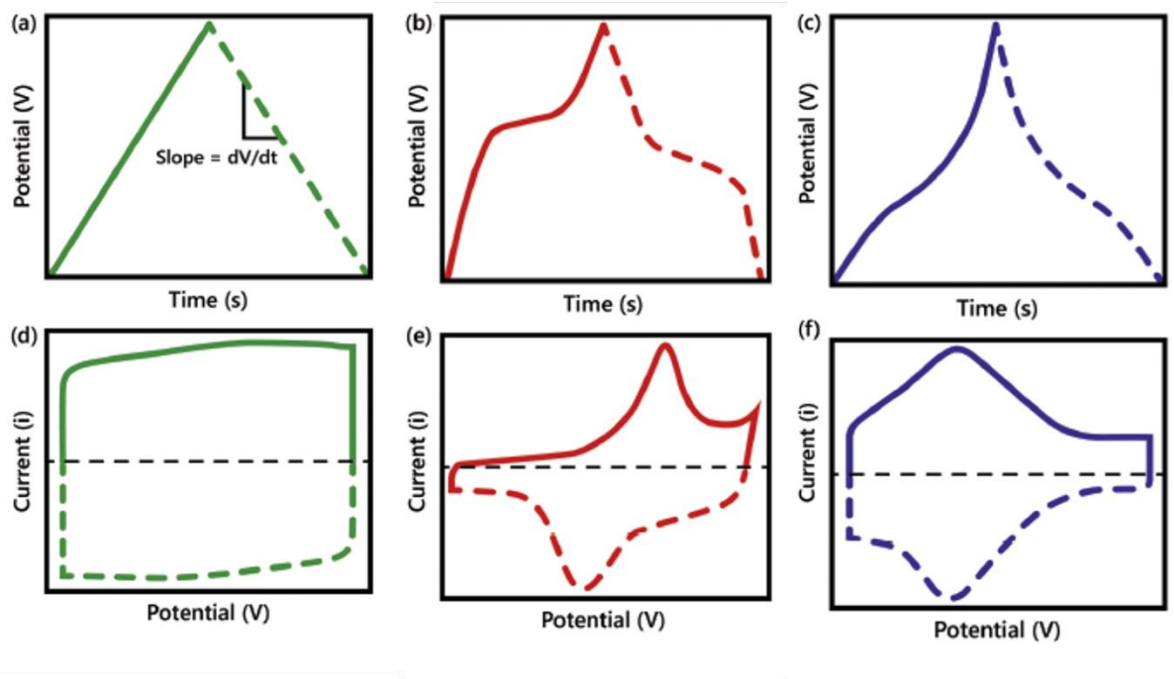

Figure I. 5 : CVs and galavanostatic charge and discharge curves of (a & d) EDLC supercapacitor, (b & e) battery and (c & f) Pseudocapacitance supercapacitor (adapted from [26])

I.4.3.1 Conway, Trassati and Dunn

Due to the rising complexity of the energy storage systems, the operating mechanisms boundaries between such systems become blurred. An example of when a distinction among batteries, EDLCs and pseudocapacitors is tricky is nano-sized battery electrode materials where more of the external surface area is exposed leading to more charge storage on the surface, faster ion and electron transport, and thus higher power density [27]. Accordingly, in order to avoid wrong classifications and hence wrong choice of performance metrics, resulting in misleading reported values and interpretations, multiple methods have been devised to differentiate the non-diffusion limited contributions* and the diffusion limited ones+. Trassati and co-workers proposed a method to decipher whether the charge storage mechanism is dominated by a diffusion limited, typical of batteries, or a non-diffusion limited behavior, typical of EDLCs and pseudocapacitors. The method relies on the assumption that a non-diffusion limited process of ion adsorption on the electrode surface follows an infinite diffusion model with no dependence whatsoever on the scan rate; while a diffusion-limited process follows a semi-infinite diffusion model with the response current being directly proportional to the square root of the scan rate.

Conway proposed an empirical method where the current response at a certain potential (usually used for peak potential, if any exists) follows a power-law relationship with the scan rate. Depending on the values of the power, a quick indication of the electrode's kinetics can be inferred, indicating whether the process can be characterized as purely non-diffusion limited process (surface-driven behavior), purely diffusion limited (battery-like kinetics) or a mix of both.

Dunn generalized Conway's method and proposed the uncoupling of the total current response at any potential value into two current responses: one arising from diffusion limited processes and another one arising from non-diffusion limited processes. This allows deciphering the electrode's kinetics at different potential values and relate such diffusion or non-diffusion contribution to processes occurring at certain potentials.

A general note regarding both methods proposed by Trassati and Dunn is that data recorded at slow scan rates should be used for such calculations to avoid errors arising from ohmic drops occurring at high scan rates. [28]

* "Surface", "Inner-Surface", "Capacitive", "Non-Kinetically limited" are other terms used interchangeably in literature to mean non-diffusion limited contributions

+ "Bulk", "Outer-Surface", "Battery-like", "Kinetically limited" are other terms used interchangeably in literature to mean diffusion limited contributions

I.5 Most Commonly Used Materials for EDLC

The differences between the operating principles of batteries, EDLC supercapacitors and Pseudocapacitors stem from the physico-chemical properties of the electrode material as well as the electrolyte used. Hence, to develop EDLC supercapacitors, the devices investigated in this PhD work, the proper electrode/electrolyte couple has to be selected. Many materials have been tested as electrode materials for EDLCs, showing different merits and inferiorities. For a material to be used as an electrode for an EDLC, it has to meet a set of requirements: i) high electrical conductivity, ii) high electrochemically active surface area, iii) hierarchical pore size distribution, iv) chemical, electrochemical and thermal stabilities, v) ease of processing, and vi) low cost. As highlighted earlier, hierarchical pore size distribution is a key factor when designing materials for supercapacitors. Having such a distribution means combining connected pores of different size domains, each serving a certain purpose. In general, pore sizes can be categorized as follows: i) macropores (more than 50 nm), ii) mesopores (from 2 to 50 nm) and iii) micropores (less than 2 nm). The latter is divided into submicropores (from 0.7 nm to 2 nm) and ultramicropores (less than 0.7 nm). Micropores have been previously shown to play an important role in enhancing the capacitance through the nano-confinement phenomena; mesopores are known to provide a facile ion diffusion pathway, enabling fast charge and discharge, and macropores are thought to serve as an ion-buffering reservoirs that decrease the diffusion distance of the electrolytic ions into the inner pores [29]. Various carbonaceous materials offer these varied physico-chemical and morphological properties.

I.5.1 Activated Carbon (AC)

Among those materials used for non-faradaic EDLCs, Activated Carbons (ACs) are the ones used commercially because they are low-cost ($15 per kilogram in 2013 [30], expected to be much lower nowadays), easy to produce, and possess large surface area (>2000 m^2/g) [31]. However, they display low electrical conductivity and non-hierarchical porosity, limiting their associated capacitance and energy density (around 100–120 F/g in organic electrolytes and 150–300 F/g in aqueous electrolytes [32]). ACs are made out of carbon-rich organic precursors that are firstly carbonized and then activated. The carbonization occurs through the thermal decomposition (pyrolysis) at high temperatures, leading to the growth of micro-crystallites of graphite along with expelling volatile materials, which include heteroatoms. The carbon precursor and its processing conditions will affect the size of crystallites, the number of stacked graphene sheets, and their relative orientation. These properties control the degree of electrical conductivity, texture, and pore size distribution. Some precursors (ex. petroleum pitch and coal pitch) can, upon carbonization, lead to pre-graphitic structure which can be further converted

to highly ordered graphite upon high-temperature treatment (>2500 °C). Some other organic precursors (ex. wood, nutshells, etc.) would lead to randomly oriented graphene in the form of rigid amorphous highly porous structure when carbonized.

Thermal or chemical activation is carried out on the carbonized carbon (char) to create new pores or unblock the already existing ones that might be blocked with 'disorganized' carbon residues (tars). Activation conditions such as temperature, time and/or reagents can be modulated to engineer these chars porosity. Thermal activation takes place at temperature between 700 and 1100°C under oxidizing gases such as steam, CO_2, air, or mixtures of these gases. On the other hand, chemical activation takes place at lower temperatures with the presence of chemicals such as phosphoric acid, zinc chloride or potassium hydroxide.[33]

I.5.2 Carbon Nano Tubes (CNTs)

Studies have been conducted on Carbon Nano Tubes (CNTs) which are one dimensional carbon cylinders consisting of curled up graphene sheet or sheets for single-walled CNT (SWCNT) and multi-walled CNT (MWCNT), respectively (Figure I.6(c)). They can be synthesized through arc discharge, metal catalyzed CVD growth or laser ablation with the first two methods being the most successful and most common [34]. CNTs are endowed with large surface area, high electrical conductivity, low mass density, and high chemical stability [35]. However, the performance of untreated CNTs as SCs electrode material turned out to be less than that of ACs (around 50–80 F/g in organic electrolytes [32]). Such values can be enhanced through treating the surface of the CNTs to increase oxygen functionalities or coupling them with other materials to form composites. However, their employment as electrode materials for supercapacitors would be hindered due to their high production cost. MWCNTs are cheaper than SWNCTs; however, theu usually tend to get entangled into bundles that are difficult to separate leading to compromised properties compared to that of individual CNTs. [32], [36]

I.5.3 Carbide-Derived Carbons (CDCs)

Carbide-Derived Carbons are carbons synthesized from the etching of different metal carbides in the presence of chlorine gas at elevated temperatures. During the process, the removal of the metal centers and their expulsion in the form of gaseous metal chlorides yield highly porous carbon networks (Figure I.6(a)). The specific surface area and the pore size can be controlled by altering the chlorination time and temperature. CDCs have been proposed as electrode materials for supercapacitors as they can be synthesized in a controllable manner allowing to target very specific average pore sizes ranging from 0.5 nm to 30 nm with 0.05 nm accuracy while maintaining a narrow pore size distribution [17]. This pore size distribution

specificity enables to trigger ion and pore size matching, allowing them to reach energy densities roughly double that of activated carbons [30]. Unfortunately, these tunable production processes are expensive and rely on the use of corrosive gases like chlorine. However, they remain very interesting for fundamental studies regarding ion-pore size matching [17]–[19], charge storage mechanism and ion-dynamics understanding [22].

I.5.4 Carbon Nano-Onions

Carbon nano-onions are 0-dimensional carbon structures, usually in the form of spheres or polyhedral carbon nanoparticles of sizes less than 10nm (Figure I.6(b)). These spheres or polyhedrals are formed of multiple concentric fullerene-like shells giving the shape of an onion, hence the name carbon nano-onions. The most used synthesis method is the graphitization of nanodiamonds under vacuum or under an inert gas at high temperatures (>1700 °C) [37]. They have been experimented with as materials for supercapacitors due to their high electrical conductivity, and external surface area with absence of internal porous network, leading to high power density and short charging time; however, they showed limited capacitance of around 25-50 F/g because of their limited specific surface area (200-600 m^2/g) and hydrophobic nature. The capacitance values were pushed till 246 F/g through functionalization with quinone based molecules [38] and to around 100 F/g in aqueous electrolytes through some thermal treatments to control the amounts of defects and functional groups [39]. Regardless of the low capacitance, this class of materials is quite useful for fundamental studies as their surface is quite accessible to the electrolytic ions as a direct consequence of not having an internal porous structure. [39]

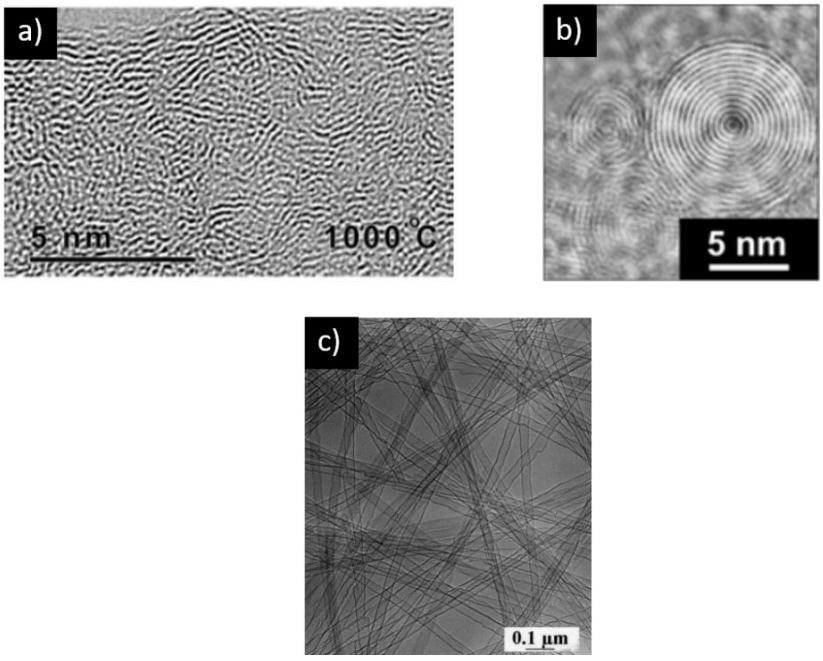

Figure I. 6 : TEM images of a) CDC [17], b) Carbon Nano-Onions [37] and c) CNTs [40]

I.6 Potential of Graphene as an Electrode Material for SCs, its Limitations and Different Approaches to Overcome them

I.6.1 Properties of Graphene

Graphene, the 2-dimensional (sheet) form of carbon, has gained great attention since its discovery and successful exfoliation in 2004 [41]. It has a one atom thick (0.34 nm) honeycomb lattice structure consisting of sp^2 σ-bonded C-atoms with free π-orbitals perpendicular to the surface, leading to electrons delocalization on both sides of the graphene sheets. Graphene's exceptional properties stem from such a cloud of π-delocalized electrons along with the strong σ-bonds. Graphene has been considered as a potential candidate for many applications including, supercapacitors, batteries, photovoltaics, fuel-cells, wearable electronics, transparent materials, water-splitting, drug delivery, bio-imaging, catalysis, sensing and many more [42], [43]. Such promises of graphene are direct consequences of its high electrical conductivity (~10^6 S/cm), high charge mobility that is 200 times higher than that in silicon (~$2x10^5$ cm^2/Vs), large specific surface area (2630 m^2/g), chemical and electrochemical inertness and resistance to gas permeation.

I.6.2 Expected Capacitance

More specifically in the field of energy storage, owing to its single sheet nature, graphene has been theoretically predicted to have high specific capacity of around 744 mAh/g and high specific capacitance of 550 F/g as well. Beside these high expected performances, graphene has high strength (130 GPa), elasticity (ultrahigh Young's modulus of ~1.1 TPa) and flexibility which would allow making more durable devices that more probable to withstand harsh mechanical conditions (ex. bending and stressing). Graphene is also compatible with metal oxides and hydroxides and polymers which would allow the formation of graphene composites combining both EDLC and pseudocapacitance. [42]

I.6.3 Overview of the Synthesis Methods of Graphene

Unfortunately, the full capabilities of graphene have not been unleashed yet. The main reason why researchers are not able to unlock such full potential of graphene is the absence of a synthesis method that would be capable of large-scale production of defect-free, high quality, crystalline, single-layer graphene sheets at reasonable or comparable costs to those of the commercial materials used in supercapacitors nowadays. So far, the synthesis of graphene follows either a "Top-down approach" or a "Bottom-up approach". The latter means starting from carbon precursors and assembling the carbon atoms into the graphene lattice and can be

achieved mainly through physical processes such as Chemical Vapor Deposition (CVD) and epitaxial growth on SiC (Figure I.7). The former method depends on extracting graphene from graphene-containing or based structures such as graphite or graphite-intercalated compounds (Figure I.7). This approach can include processes such as solid-phase, liquid-phase and electrochemical exfoliation of graphite as well as chemical oxidation of graphite into graphite oxide, its exfoliation to graphene oxide (GO) and then its chemical, thermal, and/or electrochemical reduction to (partially-) reduced graphene oxide.

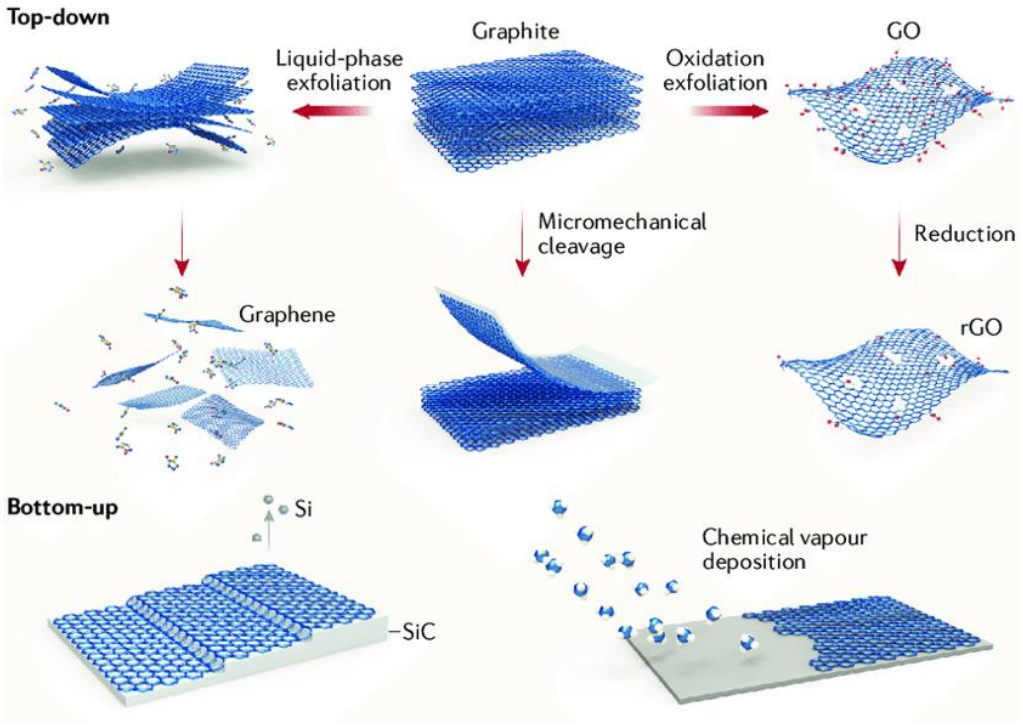

Figure I. 7 : Different common synthesis methods of graphene [44]

I.6.3.1 Up-Scalable Methods

The most widely employed graphene synthesis processes with potential of large-scale production are the liquid-phase exfoliation and the reduction of graphene oxide. The latter yields usually few-layer graphene sheets as a result of the restacking of the graphene layers, called reduced Graphene Oxide (rGO). Those few-layer graphene sheets have some impurities, structural damage and lattice defects due to the evolution of gases during the reduction, as well as the harsh chemical or thermal conditions that it is exposed to during the process. Some residual oxygen-containing functional groups will persist, making it impossible to get a defect- and impurity-free graphene sheets and thus, leading to relatively lower electrical conductivity compared to that of graphene. In addition, it involves complicated procedures, use of corrosive and toxic chemicals, and multiple purification steps. Nevertheless, such method allows functionalization to be made prior to reduction, which allows tailoring the materials for various applications.

The liquid-phase exfoliation process requires the use of high boiling point solvents that need high temperature to evaporate, thus high energy consumption. These solvents are usually toxic and raise environmental concerns. In addition, sometimes surfactants such as polymers or other organic molecules are used to stabilize the graphene dispersion and avoid restacking; however, it is difficult to get rid of them entirely due to favorable interactions taking place between them and graphene. As a consequence of these strong interactions, the electrical and electrochemical properties of graphene are modified. Such a technique has a very low production rate of 0.04 g/hr and involves sonication set-ups, which imposes difficulties for its industrial up-scaling. [43]–[47]

I.7 Graphene in SCs

Regardless of such synthetic drawbacks, graphene has been tested as an electrode material for supercapacitors and showed very good performance, yet not unleashing its full theoretical potential and not offering a better alternative at a comparable cost to the currently used activated carbon. In this section, various graphene based materials used as electrode materials for supercapacitors will be discussed.

Sonication and KOH assisted sonication were carried out on graphite to synthesize graphene and KOH-activated graphene by Li, Y. et al. [48]. The supposedly pristine graphene showed a capacitance of 101 F/g at a scan rate of 10 mV/s in 1 M Na_2SO_4. This was mainly attributed to the restacking of the graphene layers back to graphite, thus, decreasing both the accessible specific surface area and the electrical conductivity. When KOH was employed during the sonication, the specific capacitance increased to 136 F/g under the same conditions. The energy density also jumped from 14 Wh/kg to 18.9 Wh/kg. These enhancements were attributed to the edge defects and the oxygen containing groups that appeared on the graphene sheets as a result of using KOH. These physico-chemical modifications resulted in a better accessibility of the graphene sheets to the electrolyte ions and a pseudocapacitance behavior coming from the oxygen functionalities.

Thermally exfoliated functionalized graphene sheets were prepared and tested for supercapacitor applications by Du, Q. et al. [49]. A maximum capacitance of 232 F/g was achieved in a 2 M KOH electrolyte at 1 A/g and dropped to 113 at 20 A/g with 49% capacity retention. Such a capacitance was attributed to the pseudocapacitive effect of different oxygen functionalities.

Chemically Modified Graphene (CMG) was synthesized through the reduction of GO with hydrazine monohydrate by Stoller, M. et al. [50]. This yielded rGO particles consisting of an

agglomeration of graphene sheets that showed a specific capacitance of 135 F/g and 101 F/g at a current density of 0.01 A/g and a scan rate of 20 mV/s, respectively, in 5.5 M KOH. Using 1 M $TEABF_4$ in AN and 1 M $TEABF_4$ in PC resulted in capacitances of 99 F/g and 94 F/g at a current density of 0.01 A/g and 99 F/g and 82 F/g at a scan rate of 20 mV/s, respectively. A small contribution from pseudocapacitance was proposed. Also, such values show that graphene has a potential use as an electrode material for supercapacitors. In this example, only the portions of the graphene sheets that were at the surface of the graphene particles were exposed to the electrolyte, meaning that if all the surface area of graphene was made accessible to the electrolyte ions, the capacitance would be vastly improved.

rGO was again obtained through GO reduction but this time through a gas-based hydrazine reduction process by Wang, Y. et al. [51]. The obtained graphene showed a maximum gravimetric capacitance of 205 F/g at a current density of 0.1 A/g in 30 wt% KOH. This good capacitance was accompanied by an energy density of 28.5 Wh/kg at a power density of 10 kW/kg. Such value of capacitance was higher than that reported in the case of solution reduction. This was attributed to the structure of the resulting graphene, which although still aggregated, had a lower degree of agglomeration compared to that observed in case of solution reduction. This allows for a better accessibility of the graphene inner layers to the electrolytic ions, and the electrolytic ions would get access to the two sides of many more graphene sheets than they would when RGO is agglomerated into particles.

These selected examples highlight, that one of the main problems of using graphene for SCs so far is the inaccessibility of the entire specific surface area of the graphene layers to the electrolytic ions. This inability to reach the high specific area expected is a result of the partial and sometimes nearly full re-stacking of graphene sheets to form graphitic agglomerates, driven by the π-π interaction between the graphene sheets. Consequently, research has been directed to mitigate such a shortcoming through utilizing and/or devising different classes of graphene based materials.

I.7.1 3D Graphene Based Materials

3-dimensional graphene based materials are among those materials. As the name suggests, they are 3-dimensional materials that are assembled using graphene sheets as the building blocks. This family of graphene assemblies includes graphene hydrogels, aerogels, xerogels, foams and others. They were devised as a step towards utilizing the full specific surface area of graphene to realize the full capabilities of graphene as an electrode material for supercapacitors. They are expected to have macroporous networks that would ease the ion transport. Their forecasted high accessible specific surface area would increase the contact

between the electrode and the electrolytic ions. Their robust percolation network is meant to lead to high electrical conductivity and high mechanical stability, fast electron transfer, hierarchical porosity. These macrostructures also offer the possibility to be used to form binder-free and current collector free electrodes, thus reducing the resistance of the cell and decreasing the cell's overall weight, thereby increasing the final cell energy density (current collectors account for 30% of the weight of the supercapacitor cell assembly). [52], [53]

Graphene Aerogel (GA) and H_3PO_4 activated GA were synthesized by Sun, X. et al. [54]. GA was synthesized hydrothermally using Urea and the H_3PO_4 activated GA was synthesized similarly but with an extra-step of impregnating the GA with an H_3PO_4 solution (Figure I.8). The GA and H_3PO_4 activated GA showed maximum capacitances of 186 F/g and 204 F/g, respectively, at a current density of 0.2 A/g in 6 M KOH. The increased capacitance of H_3PO_4 activated GA consequently enhanced the energy density from 1.7 Wh/kg at a power density of 10 kW/kg to 4.5 Wh/kg at the same power density. The high performance of GA was related to the addition of macropores that would allow better accessibility of the surface area to the electrolytic ions. The activation using H_3PO_4 further improved the capacitance by introducing hierarchical porosity through adding mesopores, from 2 nm to 8 nm that would improve the accessibility as well as the kinetics of ions transfer by opening up some holes in the surface of graphene sheets. Such added porosity lead to a higher Specific Surface Area as well as higher pore volume compared to the non-activated GA.

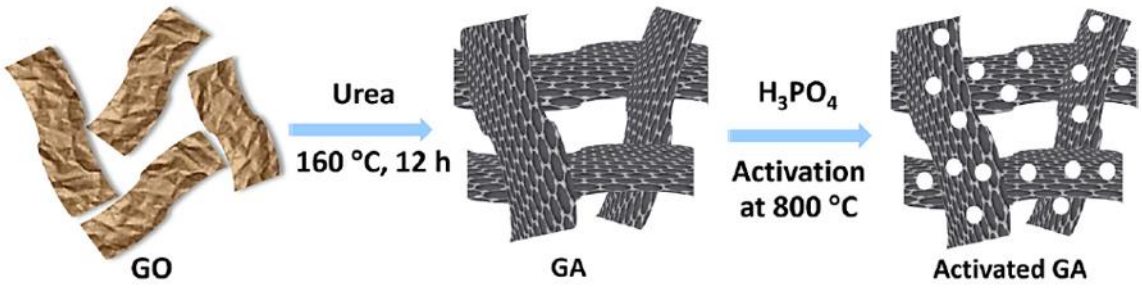

Figure I. 8 : GO transformation to GA using hydrothermal treatment with Urea and its further activation with H_3PO_4 [54]

Highly corrugated graphene sheets were synthesized through thermal reduction of GO followed by rapid cooling with liquid nitrogen by Yan, J. et al. [55]. This graphene-based material showed a high specific capacitance of 349 F/g at a scan rate of 2 mV/s in 6 M KOH solution. Such a high value of capacitance was attributed to the high electrolyte-accessible surface area, resulting from the less agglomerated and less restacked graphene sheets due to the wrinkling of those sheets. The high capacitance value was also attributed to the presence of mesopores on the graphene surface due to the formation of holes, facilitating the fast ion diffusion. A 3D

holey graphene framework was synthesized by Xu, Y. et al. through hydrothermal reduction of GO with hydrogen peroxide as a nanopore etching agent, creating holes on the graphene basal planes [56]. Such a 3D material showed high capacitance of 310 F/g, 298 F/g and 289 F/g at a current density of 1 A/g in 6 M KOH, 1 M $EMIMBF_4$ in AN and neat $EMIMBF_4$, respectively. A high energy density of 127 Wh/kg and 123 Wh/kg were achieved for the organic electrolyte and the ionic liquid, respectively. Such high values for capacitance and energy densities were attributed to highly ion accessible surface area and efficient ion and electron transport pathways. Self-assembled Graphene Hydrogel (GH) was prepared through a hydrothermal synthesis by Xu, Y. et al. [57]. Such a GH offered macroporosity and connectivity between the layer, thus offering a robust 3-dimensional macroporous conductive network (Figure I.9) that yielded a capacitance of 175 F/g in 5 M KOH at a scan rate of 10 mV/s.

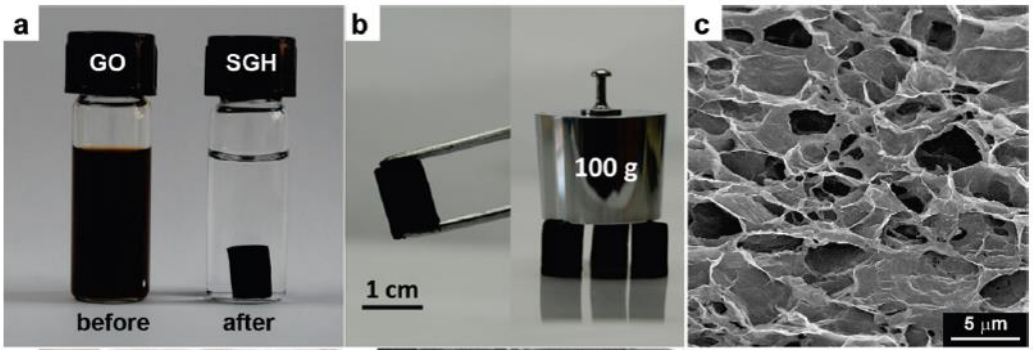

Figure I. 9 : a) GO before and after the hydrothermal treatment, b) Mechanical robustness of the formed GH, and (c) SEM of the macroporous network of the GH [57]

Another GH was synthesized by Zhang, L. and Shi, G. through hydrothermal treatment of GO, followed by its further reduction using hydrazine monohydrate [58]. The extra reduction step removed some of the residual oxygen groups, thus enhancing the electrical conductivity of the 3D network. This, along with high SSA and wettability enhancement by nitrogen doping, lead to a maximum capacitance of 222 F/g at a current density of 1 A/g in a 5 M KOH with an energy density of 5.7 Wh/kg at a power density of 30 kW/kg. The chemical (in opposition to hydrothermal) formation of GH was evidenced when using an optimized amount of hydrazine hydrate with respect to GO concentration, resulting in a highly conductive 3D GH [59]. This optimized material yielded a specific capacitance of 190 F/g at a current density of 0.5 A/g in 6 M KOH.

I.8 Pillared Graphene as a Potential Solution to Prevent Restacking

In order to (partially) avoid the restacking of the graphene sheets, the term “expanded graphite” was coined. It is a broad term that includes the materials in which graphene layers are

further apart from each other than they are in graphite as a result of partially preventing their restacking. In expanded graphite, such sheet separation is achieved by any means whether by pillaring, intercalation, surfactants, chemical functionalization, altering the surface chemistry, etc. A few examples are graphene spaced by nanoparticles [60], carbon black particles [61], ionic liquids [62] or horizontally aligned CNTs [63].

I.8.1 What are Pillared Graphene Materials (PGM) ?

Among these various expanded graphite materials, Pillared Graphene Materials (PGM) showed huge potential in limiting the restacking, in addition to offering a mean to control the spacing between graphene sheets in order to match it with the electrolytic ion size [23]. This class of materials is a recently sprung one that shows many merits. It relies on organic species covalently intercalated between graphene sheets, bridging them; hence, the name pillared graphene. These pillars are used to mechanically separate graphene sheets. Using the analogy depicted in Figure (I.(10)); these units behave the same way pillars would hold ceilings in buildings (and prevent them from collapsing onto the floors). Recent developments have shown that PGM can enhance the properties of supercapacitors, namely the values of capacitance and energy density, as well as helping with understanding the fundamentals behind the charge storage mechanism, thus paving the way for developing high performance supercapacitors.

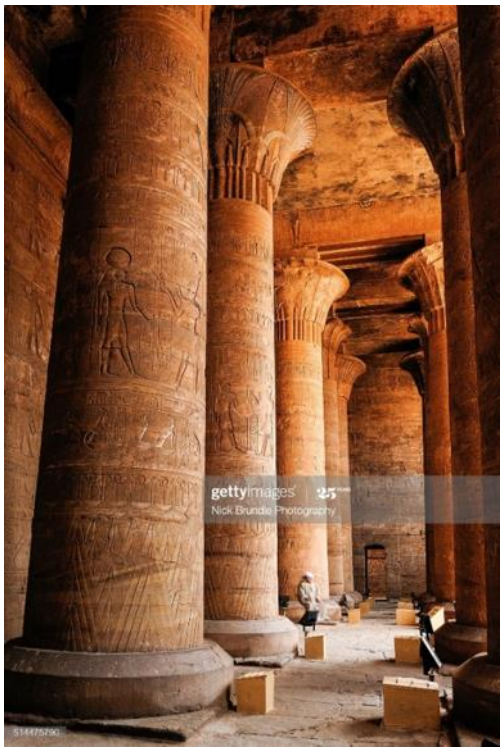

Figure I. 10 : A large scale analogy to chemical pillars. From Temple of Horus, Edfu, Egypt, by Nick Brundle Photography, 2020, https://www.gettyimages.fr/detail/photo/temple-of-horus-edfu-egypt-image-libre-de-droits/514475790?adppopup=true. Copyright 2020 by Getty Images

Such pillaring enables controlled creation of so-called graphene galleries of tunable height: microporous channels (in height < few nm) that would increase the specific surface area and open new sites for sorption that were inaccessible before. These galleries can be altered chemically and physically by changing the length of the pillars, the number of the pillars, and/or the chemical nature of the pillars. Controllability and design-ability are on top of the competitive edges of such materials due to the myriad of pillars available to be utilized. This opens the door to multifarious pillared graphene materials that can be engineered to suit specific applications. This class of materials has been applied to gas storage [64]–[68], lithium-ion batteries [69], [70], removal of heavy metals from water [71], capacitive-deionization [72], theoretical studies for different fields [73]–[90] and others as well [91]–[96]. Supercapacitors represent a very active field for the application of pillared graphene materials as they greatly benefit from controlling the spacing between graphene layers [23], [97]–[107].

I.8.2 Setting PGM apart from Expanded Graphite

To stand out from other types of expanded graphite, pillared graphene requires the presence of actual molecular pillars. PGM possess a competitive edge on other expanded graphite materials: i) PGM engineering allows for better control on the spacing between the graphene layers with high accuracy compared to intercalated graphene sheets, ii) PGM utilize identical pillars of the exact same shape and size compared to nanoparticles, for example, that usually have a size distribution and tend to aggregate, and iii) PGM offer robust assemblies due to the covalent bonding between the pillars and the graphene layers and not just physical interactions. Such assemblies can suffer from performance degradation over time due to the leaking of the spacers from in-between the graphene sheets through the repetitive charge-discharge cycles. An example is the rapid desorption of catechol molecules physically adsorbed on AC compared to stable catechol-functionalized AC grafted using diazonuim chemistry demonstrated by Pognon, G. et al. [108].

I.8.3 Setting up a Definition for “Pillaring” in Chemistry

The word “pillaring” has been used differently in the literature with different meanings and/or conceptual representations. It has been used for physical and covalent interactions, molecular and non-molecular pillars, graphene functionalization, etc. Considering such variety of denominations, a definition of pillared graphene materials has to be set-up to hopefully be used by others working in this blooming field to avoid any confusions caused by wrong classifications. A relevant definition of the word “Pillar” in Cambridge online dictionary is “a strong column made of stone, metal, or wood that supports part of a building” [109] and in Merriam-Webster online dictionary is “a firm upright support for a superstructure” (Figure I.10)

and “a usually ornamental column or shaft” [110]. To reflect such definitions onto chemistry, equivalent vocabulary must be found to define the chemical pillars. The definition can be divided into two parts, a structural part and a functional one. The structural part is related to the description of the pillar itself: a columnar structure. The chemical equivalent of such columns or posts can be molecular entities roughly having a columnar or cylindrical projected volumes. Such a definition would rule out 2D entities like sheets, spherical particles like nanoparticles, or carbon black particles, etc. as such structures do not mimic the columnar structure of a pillar. The functional part of the definition is related to the role of the pillar and that is to support. Such a role would require good strength and stability, which are the two terms used in chemistry to describe covalent sigma bonds. This leaves out physically attached pillars in which weak interactions are dominating and which might not display a long lasting supporting role. Thus, our description groups pillaring molecules covalently sandwiched between graphene sheets and emphasizes on the concept of locking two graphene sheets together. The latter implies that pillaring units possess two reactive terminal end groups to be able to achieve such locking. The distance between the two graphene sheets is also controlled by this pillaring unit. This definition excludes molecular entities that satisfy the structural condition of separating graphene sheets, but do not lock them together; as it is the case for instance with pillars connected to only one graphene sheet. In this latter case, we believe that such assemblies can be referred to as hanging-pillars-functionalized graphene. To summarize our definition, Figure (I.11) is presented below.

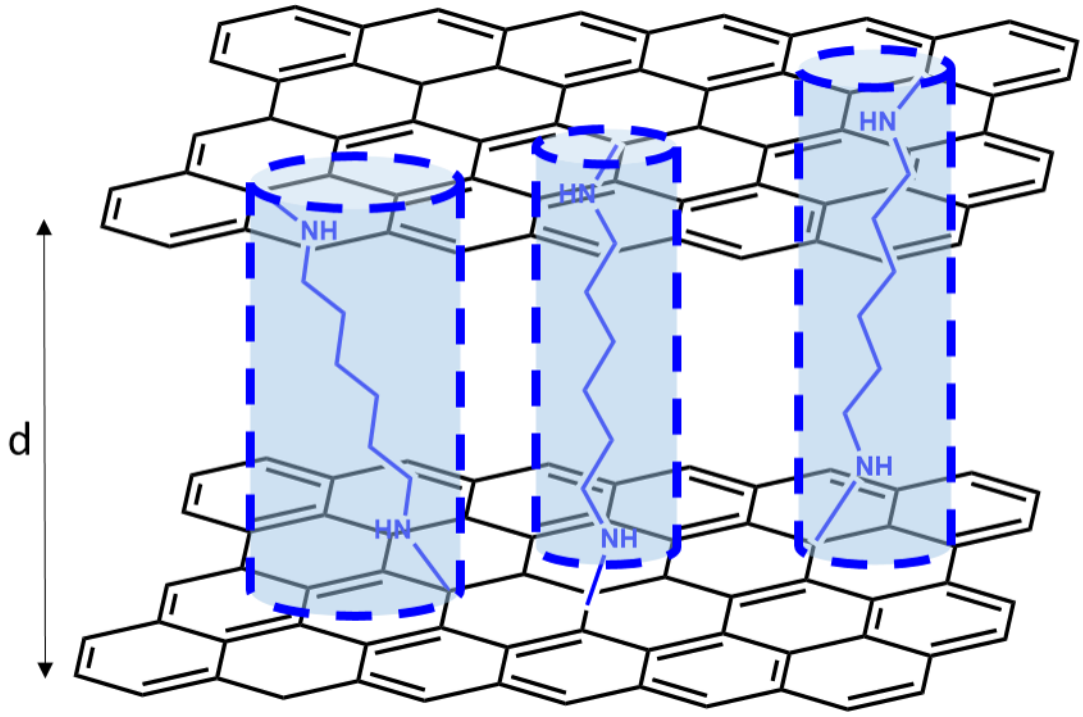

Figure I. 11 : Pillared graphene as per our definition.

I.8.4 An Important Parameter: The d-spacing

The interlayer spacing "d", distance between graphene sheets in pillared graphene materials, is an important parameter that proves that the cross-linking reaction took place between graphene and the pillar and allows a rough evaluation of their approximate orientation. This "d" spacing is a key parameter to tune depending on the targeted applications. This parameter enables choosing the proper molecules or ions that would fit the size of the created microporous galleries in applications involving sorption and/or filtration. Such an interlayer spacing can be extracted from XRD reflections, pore size distribution plots and TEM images; however, XRD remains the most accurate technique among the three as it provides a local scale information recorded on a large probed volume. In a monophasic material, one XRD peak is expected corresponding to the d-spacing. However, in a bi-phasic material, where a part of the material is pillared and the other is restacked rGO, two XRD peaks are expected: one for the rGO crystallites and one for the pillared crystallites.

I.8.5 Synthesis of Pillared Graphene Materials

Various synthetic routes have been devised in literature to synthesize PGM such as Pillaring using diazonium grafting, amine reactivity, and silylation reaction. An overview of these synthesis methods is first given followed by examples of their use to prepare PGM for supercapacitor applications.

I.8.5.1 Pillaring using Diazochemistry

The diazochemistry route relies on the de-diazotization of different diazonium salts. Diazonium salts have the following chemical formula: $R\text{-}N_2^+X^-$ with R being an alkyl or aryl group, N_2^+ is the diazonium function itself, and X^- is an organic or an inorganic anion. Aromatic diazonium are the most reactive. Such salts are known to be very reactive because the diazonium function ($\text{-}N_2^+$) is a highly electron withdrawing group. The aryl diazonium salts can be readily used to modify different substrates such as activated carbon [108], [111] , graphene [112], silica nanoparticles [113], gold electrodes [114], etc.. When conductive substrates, such as graphene, are concerned, a charge-transfer (de-localized electron) occurs from the substrate to the diazonium molecules leading to the de-diazotization of these molecules yielding an aryl radicals ($R^{\cdot}$). In turn, these radicals can react with the electron-rich network of graphene sheets creating a C-C bond between the aromatic group and a newly formed sp^3 carbon on the graphene sheets. The electron transfer step is the rate limiting step as it requires a matching in energy between an occupied electronic state of the graphene with an unoccupied electronic state of the diazonium. [115]. This chemistry has been applied to synthesize different PGM as will be illustrated in the upcoming sub-sections.

I.8.5.2 Pillaring using Silylation Reactions

In silylation reaction, the pillars are attached to the graphene sheets through the replacement of the active hydrogen of the –OH, –OOH, –NH2 groups of the functionalized graphene by the silyl based group (R_3Si) of the pillar. The molecule is thus anchored on graphene via a C(graphene)-O-SiR_3 or C(graphene)-NH-SiR_3 linkage units. Such grafting is carried out through a nucleophilic attack on the silicon from the deprotonated active hydrogen containing groups ($–O^-$, $–OO^-$ and $–N^-H$). These reactions are usually carried out in aprotic solvents [116]. Also, the pillars might be formed in-situ through polycondensating monomers of di- or tri-substituted silyls.

I.8.5.3 Pillaring using Amines Reactivity

Pillaring has also been achieved through exploiting the amine reactivity towards different functional groups with which graphene sheets can be decorated. In case of GO, the covalent bonding between the GO layers and the amine linkers can take place as a result of the chemical reaction between the amine groups in the pillars and the different oxygen moieties on the GO (epoxide, carboxylic and hydroxyl). Nucleophilic substitution reactions can take place between primary amine functional groups and the epoxide and carboxylic functions, resulting in epoxide ring opening or amide bond formation, respectively, yielding covalent bonds [103], [117]. Condensation reactions can take place between primary amines and hydroxyl groups, leading also to covalent bonding [117]. Protonated amines can also be formed depending on the pH and act as a non-covalent electrostatic binder [118]. It can also be formed through the acidity of the GO; carboxylic acid functions of GO can be deprotonated which in turn can protonate the amines, forming an ionic bond between them ($COO^- N^+H_3$-R) [117]. Hydrogen bond formation can be also expected between the amines and the various oxygen containing groups [117]. Those amine-based linkers are also mild reducing agents that help as well in the reduction of the GO.

Beside GO, bulk Graphite Fluoride (bGF) is also very reactive towards amine. C-N bonds are formed through nucleophilic substitution of the C-Fx units that are spread all over the surface of this very specific type of graphene sheets. A base is used to promote the deprotonation of the amine linkers, facilitating the nucleophilic attack [106].

Beside this difference in grafting chemistry and subsequent covalent bond nature between amine based pillars and different graphene based materials, amine chemistry has the advantage of being applied onto materials that have not yet been restacked. Both GO and bGF are more exfoliated than rGO which is the graphene building block for de-diazotization chemistry for PGM. In addition, amine reactivity has another edge as it allows the use of aliphatic and

aromatic amines, compared to mostly aromatic amines in case of diazonium grafting as aromatic diazonium salts are more stable than their aliphatic counterparts. On another note, it is worth noting that aromatic amines, when reacting with various oxygen functionalities on GO, are less, but sufficiently, reactive compared to the aliphatic amines which can be attributed to the high resonance stability leading to a lesser electron density available for nucleophilic substitution reactions on the amine nitrogens [117].

I.8.6 PGM for supercapacitor applications

PGM have been applied for supercapacitor applications in many occasions, owing to their interesting properties and tunability discussed earlier. In this section, a literature review of the performance of this class of materials in the field of supercapacitors is presented. PGM prepared using different synthesis methods as highlighted in the previous section and incorporating pillars of different nature (different lengths, aliphatic vs aromatic, different functionalities, etc.) are included. The results of electrochemical analysis techniques will be discussed in light of data from various physico-chemical and morphological characterization techniques. Finally, light will be shed on the potential of this class of materials for composites formation for supercapacitor applications.

I.8.6.1 PGM Materials Synthesized by Diazonium Chemistry

A porous graphene framework has been synthesized by Yuan, K. et al. through the functionalization of rGO by 4-iodophenyl groups, followed by aryl-aryl coupling to generate bridging pillars (Figure I.12) [97]. Such functionalization resulted from the de-diazotization reaction that occurred between rGO and 4-iodobenzene diazonium salt in aqueous conditions. A bis(cyclooctadiene)nickel-catalyzed Yamamoto coupling was then performed between the iodo-functionalized sheets to lock them together through the formation of a C-C bond between top- and bottom-layer iodo-phenyl substituents. In 6 M KOH, the pillared structure showed a gravimetric capacitance of 198 F/g compared to 75 F/g obtained for rGO at a scan rate of 200 mV/s. This nearly three-fold increase in gravimetric capacitance was attributed to the inherent and stable microporous structure, the proper pore size distribution, and the increase in the surface area that is accessible to ions. Collectively, all these structural properties improved the ion diffusion and sorption kinetics. The pore size distribution is an important characterization result as it gives information about how the pores are distributed, and whether the pores of sizes matching that of the electrolytic ions are the dominant ones or not. It gives also information about the share of the very tight pores that will not be accessible to the used ions. Here, a unimodal pore size distribution was obtained with a peak around ~1 nm which is good, not optimum, for the 0.6 nm hydrated K^+ ion size [98]. It is good because it is larger than the

hydrated size of the ion but not optimal as it is too loose leading to unused area as well as a large charge separation distance.

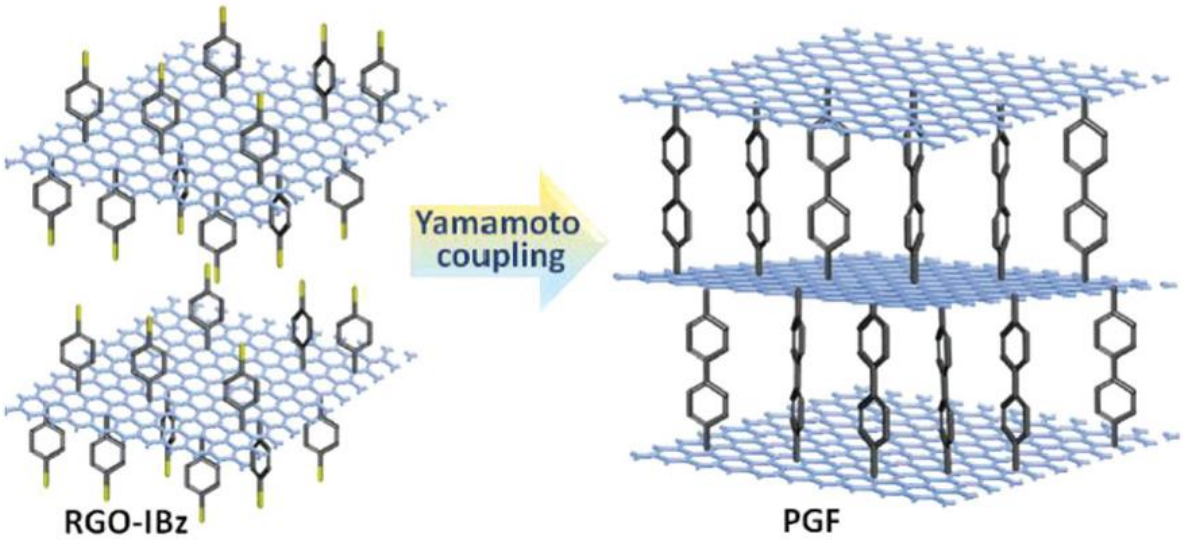

Figure I. 12 : Pillared Graphene synthesized by functionalizing rGO with 4-iodophenyl followed by aryl-aryl coupling [97]

Another work by Lee, K. et al. reported the use of aromatic diazonium salts based pillars. Three different pillared graphene materials were synthesized utilizing three pillars of different lengths, consisting of 3 different linear polyaromatic systems, giving access to three different spacings between graphene sheets [98]. In this study, an aqueous suspension of surfactant-stabilized reduced graphene oxide was used. The surfactant prevents graphene sheets from aggregating back to graphite and maintain a good dispersion in the aqueous media prior to their reaction with the diazonium salt pillars. The pillars were introduced through reacting phenyl, biphenyl and p-terphenyl bis-diazonium salts with this rGO solution, and yielded pillared materials with d-spacing values of 0.49, 0.72, and 0.96 nm, respectively. Such an interlayer spacing was obtained from TEM images showing distinctly the edges of graphene sheets, thus allowing the observation of such distances between the sheets. These d-spacing values were then confirmed through the pore size distribution determined through gas sorption (Figures I.13(a), (b) & (c)). The pillared graphene material with the intermediate 0.72 nm d-spacing showed the best performance in terms of capacitance, energy and power densities in 1 M $TEABF_4$ in PC and in 6 M KOH. In these electrolytes, the size of the naked TEA^+ cation is 0.68 nm and the size of the hydrated K^+ cation is 0.6 nm. This further highlights the importance of the pore-ion size matching in enhancing the electrochemical characteristics of the supercapacitors. Figure (I.13(d)) illustrates how the charge storage takes place in rGO and in the different pillared materials synthesized here. For rGO, the KOH sorption takes place on the

outer surface of the RGO stacks (d=0.38nm) as the distances between the layers are too tight to allow the ions to access. For the rGO-BD1, the sorption occurs through distortion of the ions' solvation shells. For rGO-BD2, the optimum inter-layer distance is achieved as it matches the size of the ions. For the rGO-BD3, there are some unused inter-layer spaces, increasing the charge separation distance between the electrode and the electrolytic ions. The pillared material with an optimized spacing of 0.72 nm (rGO-BD2) achieved a gravimetric capacitance of 250 F/g and 165.98 F/g at a current density of 0.1 A/g while the rGO achieved 27.4 F/g and 123.84 F/g at the same current density in KOH and $TEABF_4$ in PC, respectively. The higher capacitance values recorded with KOH versus $TEABF_4$ in PC was attributed to the presence of a redox peak on the CV cycles, indicative of a pseudocapacitive behavior in such basic electrolyte. The remaining oxygen containing groups in the pillared materials such as the alcohol groups can indeed take part in redox reactions in basic aqueous solutions. It might also be a result of the high viscosity of the PC solvent, leading to lower mobility of the ions. Such a better performance over the rGO was attributed to the shorter charge separation distance and to the increase of electrochemically active surface area through preventing the restacking of the rGO, thus allowing better ion transport kinetics.

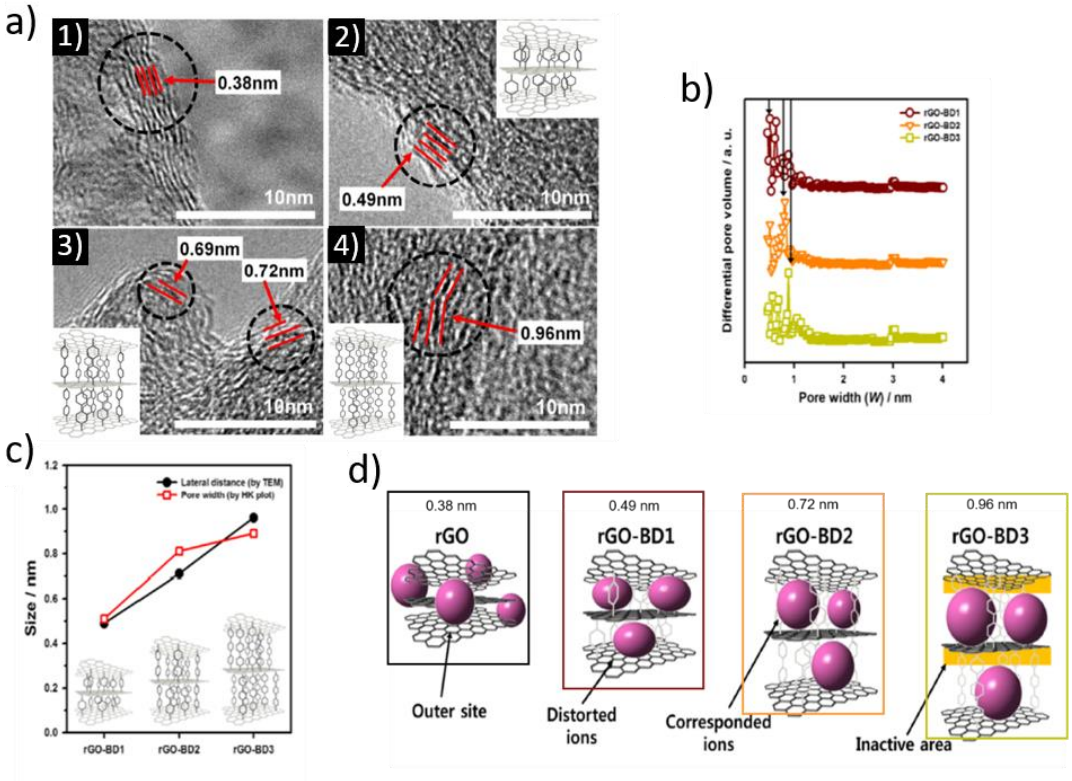

Figure I. 13 : a) TEM for 1) rGO, 2) rGO-BD1, 3) rGO-BD2 and 4) rGO-BD3 with the d-spacing values shown. Inserts are showing the structure of the three pillared graphene samples, b) Pore size distribution showing maximum pore volumes at certain pore widths, corresponding to the newly created d-spacing which is in agreement with the results obtained from TEM as shown in c) and d) The charge storage mechanism for the different materials synthesized by Lee, K. et al. [98]

Another pillared graphene material synthesized through de-diazotization was prepared through the pillaring of rGO using anthraquinone-2,6-diazonium salts, by Qin, Y. et al. [99]. This PGM was synthesized by adding rGO dispersed in DMF/H_2O to the diazonium salts at 0°C under Ar. Here again, the main aim was to prevent the restacking of rGO and increase the electrochemically active surface area. Also, additional pseudocapacitive behavior was targeted through the redox activity of the quinone moieties in the pillars. The authors also intended to harness what they described as the "nanopore effect", which is the optimization of the spacing between the graphene layer to match the ion size (0.92 nm obtained from XRD and confirmed through gas sorption). A specific capacitance of 210 F/g and 123 F/g was achieved at 1 A/g in 1 M H_2SO_4 for the pillared graphene material and rGO, respectively. The PG material retained nearly 200 F/g at a huge current density of 100 A/g, showing high rate capabilities and power density. This enhanced behavior was assigned to higher micropore volume and added pseudocapacitance. The same anthraquinone pillar was used in a recent example in which diazonium chemistry has been used to functionalize hydrazine-reduced rGO [100]. Xie et al. used a 2,6-diaminoantraquinone as a precursor of a pseudocapacitive molecular pillar. The diamine compound was transformed into a bis-diazonium salt and grafted onto rGO in a single step. A similar molecule with a single anchor group was also used in order to compare functionalization and pillaring effects. XRD characterization only showed a variability in graphitic peak shape and position with respect of the experimental conditions tested, but no additional peak was observed in the 10 to 60° 2θ range. However, the capacitive contribution of rGO and mono-amine-functionalized rGO were shown to be very close, while that of the diamine-pillared rGO seemed higher. This observation was used as an indirect proof of the molecule playing the role of a spacer letting more ions access the adsorption active surface area. So overall, a specific capacitance as high as 522 F/g was reached for this pillared material (vs 224 F/g for rGO – at 5 mV/s), owing to the improved electrolytic ions diffusion and adsorption, combined with pseudocapacitance brought about by the redox nature of the quinone based pillar.

I.8.6.2 PGM Materials Synthesized by Amine Chemistry

(a) Aliphatic Amine Pillars

Graphene hydrogel was synthesized using graphene layers pillared by ethylene diamine linkers by Luan, V. et al. [101]. Ethylene diamine acted as pillaring molecules, chemically bonding different graphene oxide sheets together through reacting with different oxygen functionalities. Such an assembly was then reduced to a graphene hydrogel using hydrazine. The material's performance as an electrode material for supercapacitors was evaluated and a specific capacitance of 232 F/g was achieved in 2 M KOH at a current density of 1 A/g. Such

a performance was attributed to the high electrical conductivity of such cross-linked network and high electrochemically active surface area, allowing for better electron and ion transport. The reduction step led to a 14-47 fold increase in the electrical conductivity depending on the GO content. A sample electrical conductivity of 1351 S/m was achieved for an initial GO content of 15 mg/ml. Such a high value of electrical conductivity is quite important for the performance of a material as supercapacitor electrode because it affects the kinetics of the charge transport of both electrons and ions.

A variety of aliphatic pillars was experimented by Bo, S. et al. [102]. Six different aliphatic linkers with different lengths, structure and backbone chemistry were tested through a hydrothermal synthesis as shown in Figure (I.14(a)). Namely, the used pillars are: ethylene diamine (EDA), butane-1,4-diamine (BDA), hexane-1,6-diamine (HDA), 1,4-cyclohexane diamine (CHDA), ether diamine (EA148), and tris(2-aminoethyl) amine (Tris). The main aim was to study the pillars with different chain sizes (EDA, BDA and HDA), chain conformations (CHDA), hydrophilicities (EA148) and degrees of functionalization (Tris). The d-spacing values of the synthesized samples were obtained through XRD and the values are shown in Figure (I.14(b)). An expected increase in d-spacing from EDA to BDA to HDA was expected. The trend was expected to continue to EA148 as it had a longer aliphatic chain, however, almost no peak was observed for EA148 and this was attributed to a disordered molecular structure with the pillars adopting their thermodynamically stable helical or coil configurations instead of being stretched out. The Tris had the largest d-spacing value of 1.2 nm as it was believed that it could form more chemical linkages with graphene than the other pillars owing to its trifunctional nature. In Figure (I.14(b)), the d-spacing values for the GO counterpart of these materials are summarized. The small decrease in the d-spacing values observed after reduction was attributed to less intermolecular interactions and less repulsion, yet the 3D structure seems to be retained. The electrochemical tests, Cyclic Voltammetry (CV) and Galvonostatic Charge-Discharge (GCD), were done in three different solvents: H_2SO_4, $TEABF_4$ in AN and $BMIMBF_4$ Ionic Liquid (IL). The CVs were mainly rectangular which is indicative of a capacitive behavior (Figure I.14(c)) and the charge and discharge cycles were linear and symmetric with not much IR drops, also indicating EDLC character (Figure I.14(d)). The highest capacitance value was obtained for the BDA pillar in both the aqueous and organic electrolytes: 216 F/g at 2 mV/s in H_2SO_4 and 134 F/g at 10 mV/s in $TEABF_4$ in AN. This was attributed to the increased electrochemically active surface, good electrical conductivity along with the proper pore-ion size matching. Regarding the BDA pillared sample, a d-spacing of ~ 0.95 nm was obtained and this is less than the sizes of the solvated $TEABF_4$ ions (1.35 nm for cations and 1.40 nm for

anions), thus, allowing for partial desolvation and hence decreased charge separation distance. In IL, the Tris pillared sample showed the highest performance owing to its larger electrochemically active surface area and pore size distribution that is matching the ions size of the IL (BMIMBF$_4$), leading to the enhancement of the accumulation of the charges at the electrolyte/electrode interface. In this media, the Tris pillared sample showed a capacitance of 119 F/g at 10 mV/s, a high energy density of 51 Wh/kg at a power density of 552 W/kg and a relatively high energy density of 30 Wh/kg at a power density of 6 kW/kg. Such high energy density was related to the wider operational voltage window of 3.5 V which was only achievable using ionic liquids as the electrolytes.

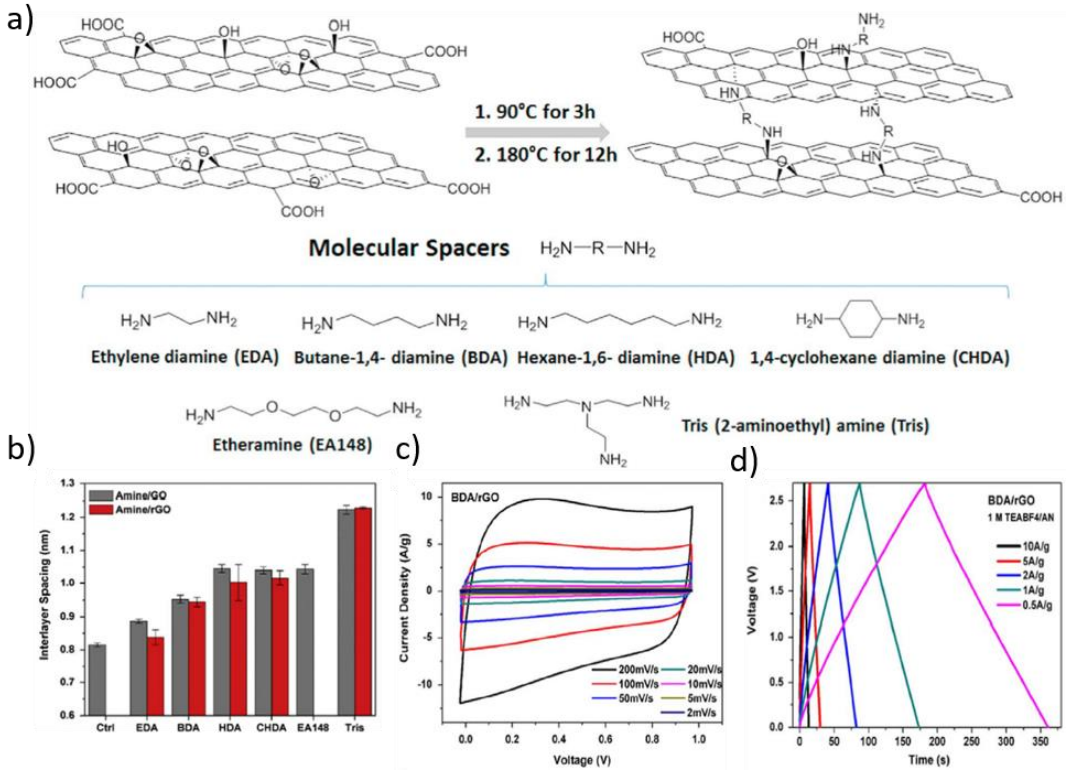

Figure I. 14 : a) A schematic for the synthesis done by Bo, S. et al., b) The d-spacing values for the different pillared rGO and pillared GO samples, c) CV curves for the rGO sample pillared with BDA in 1M TEABF$_4$ in AN at different scan rates and d) Charge-discharge cycles of the rGO sample pillared with BDA in 1M TEABF$_4$ in AN [102]

Longer aliphatic pillars such as 1,5-Diaminopentane, 1,6-Diaminohexane and 1,8-Diaminooctane were also experimented by Banda, H. et al. [23]. In this report, the chemical synthesis of the pillared graphene oxide was followed by an additional reduction step using hydrazine hydrate to overcome the weak reducing capability of the alkyl diamines (especially the longer ones). The aim of this work was to increase the separation between the produced graphene layer, thus, creating the so-called “galleries” which are micropores designed to be

accessible to the electrolytic ions. Controlling the distance between the sheets (the galleries height), identified by the d-spacing, is crucial for the ion-pore size matching. This d-sapcing modulation can be achieved by changing the length of the pillars employed, for example using a pillar with five carbons instead of four. The formation of such galleries was confirmed by the XRD diffractograms showing new peaks at lower 2θ values (denoted as Cross-Linked peaks (CL)), indicating the presence of larger d-spacing values between the rGO sheets (Figure I.15(a)) compared to the d-spacing coming from the graphitic peak at larger 2θ values. Such a CL peak is completely absent in the case of the non-pillared rGO, reduced using the same reducing agent. It confirms that this CL peak is a direct attribute coming from the bridging of the graphene sheets through the pillaring molecules. Also, the fact that the d-spacing values are roughly matching the sizes of the pillars and the fact that the spacing increases when using longer aliphatic pillars are important clues that confirm the pillaring of the rGO sheets. From the 2θ values, the d-spacing values were found to be 0.78 nm, 0.8 nm and 0.86 nm for the samples containing alkyl diamines of 5 Cs (5 RP), 6 Cs (6 RP) and 8 Cs (8 RP), respectively. Figure (I.15(b)) shows a depiction of the particles responsible for the CL peaks. Salts of different cation sizes (TEA^+, TPA^+, THA^+) have been tested with such materials of different pillar lengths as well as with reference rGO where no galleries are present. For each sample-cation pair, the shape of the CV (Figure I.15(d)) and also the evolution of the trend in specific capacitance (Figure I.15(e)) were monitored. These electrochemical studies allowed concluding that cations have limited access to pores smaller than their naked size (Figure I.15(c)). When the bare ion size is larger than the interlayer spacing, the shape of the CV becomes skewed and distorted away from the rectangular shape normally expected for supercapacitors. Such a distortion shows that cations of larger sizes do not access such pores which leads to the observed decrease in the capacitance values. In case of rGO, which lacks newly created galleries/micropores, the CVs were always rectangular and the capacitance was nearly the same independently of the cation size. Such observation indirectly confirms the creation of the microporous galleries in the pillared samples and their role in ion-sieving. The highest capacitance of 154 F/g was achieved for the sample pillared with 1,5-Diaminopentane in 1 M $TEABF_4$ in AN at a current density of 1 A/g.

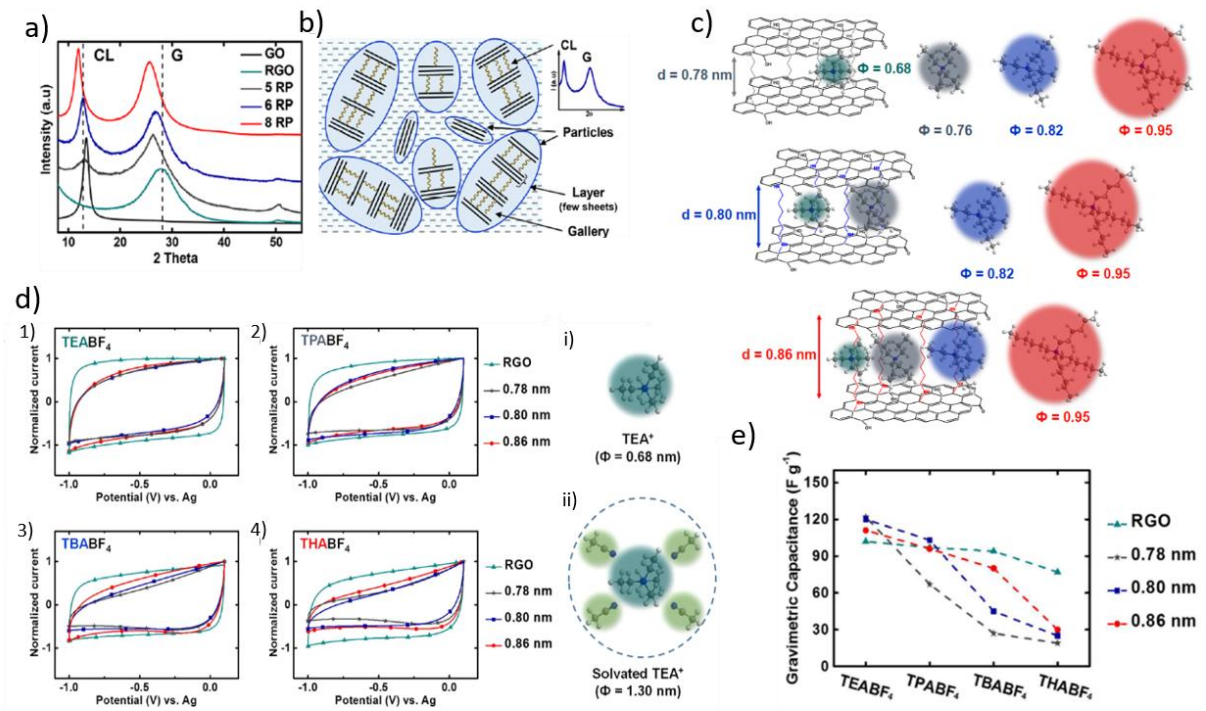

Figure I. 15 : a) XRD pattern for GO, rGO and Pillared graphene with alkyl diamines of different alkyl chain lengths (5 RP for 5 Cs, 6 RP for 6 Cs and 8 RP for 8 Cs), b) conceptual scheme of the structure of the pillared samples, c) Ions of different sizes are sieved based on the graphene galleries interlayer height (0.78 nm for 5 RP, 0.8 nm for 6 RP and 0.86 nm for 8 RP). The cations shown here are, from the smallest to the largest, tetraethylammonium (TEA+), tetrapropylammonium (TPA+), tetrabutylammonium (TBA+) and tetrahexylammonium (THA+), d) CV cycles on the negative potential for rGO, 5 RP, 6 RP and 8 RP with 4 electrolytes of different cation sizes 1) $TEABF_4$, 2) $TPABF_4$, 3) $TBABF_4$ and 4) $THABF_4$ with i) and ii) showing the size of the naked and solvated TEA+, respectively and e) The gravimetric capacitances of rGO, 5 RP, 6 RP and 8 RP using electrolytes of different cationic sizes under negative potential

In a subsqueuent work by Banda, H. et al., pillared graphene (6RP) and pillared graphene hydrogel (6GH) were obtained through the functionalization of GO using optimized quantity of 1,6-Diaminohexane followed by its hydrazine reduction in case of 6RP, while both steps were performed simultaneously in a hydrothermal process for 6GH [103]. The 6GH showed a capacitance of 230 F/g at a scan rate of 10 mV/s in 1 M $TEABF_4$ in AN, higher than the 6RP counterpart with 205 F/g after optimizing the pillar density which in turn is higher than the non-optimized 6RP with 126 F/g at 20 mV/s in the same solvent . The high values of the 6RP was a result of the pillar density optimization. Initial tests were conducted on 6RP samples with a higher density of pillars. Decreasing the pillar amount in between the sheets opened up new adsorption sites that were previously occupied by the pillars themselves. It also allowed a better accessibility of the ions to the galleries with limited obstruction from the pillars as evidenced by the lower ionic charge transfer resistance recorded (Figure I.16(a)). The higher capacitance values for the 6GH were mainly attributed to better ions accessibility to the active sites and to the less restacked macroporous 3D structure. An ambient-dried (rather than freeze-dried) sample was prepared and tested as an electrode for supercapacitor. Surprisingly, it

showed the same performance in terms of the gravimetric capacitance although its macroporous structure was lost after being ambient-dried. This shows that the micro/meso structuration is critical for such materials and that the macrostructure is not the main key to higher capacitance values. It might become crucial at higher scanning rates. The air-dried sample showed a much greater volumetric capacitance as a result of the sample density increase from 0.02 g/cm^3 for the freeze-dried sample to 1.1 g/cm^3 for the ambient-dried sample. A summary of the different pillared graphene materials synthesized by Banda, H. et al. is shown in Figure (I.16(b)).

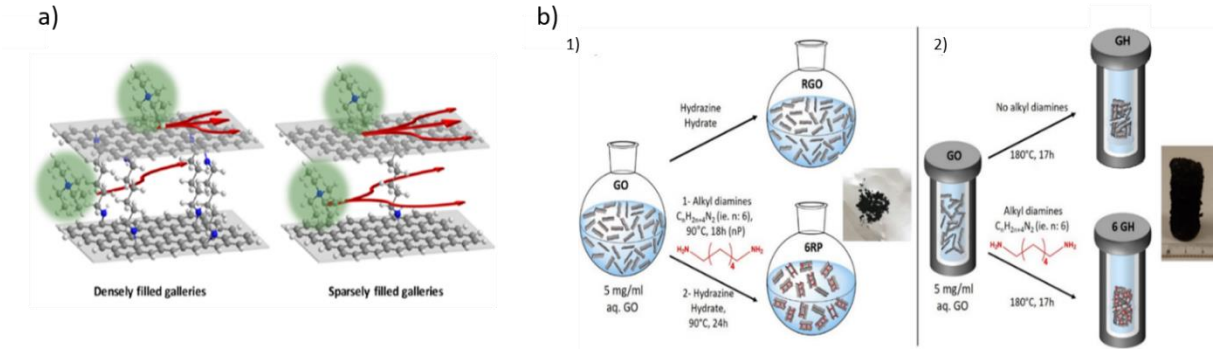

Figure I. 16 : a) Difference between densely and sparsely filled galleries, b) Different pillared graphene materials synthesized by Banda, H. et al. using 1) Open-air synthesis and 2) Hydrothermal synthesis

Instead of GO, the exotic Bulk Graphite Fluoride (bGF) was utilized as a precursor for pillared graphene materials by Zhao, F. et al. in this very interesting attempt [106]. It was chosen over GO because it almost preserves all the hexagonal structure of graphene with no defects in comparison to the very defective GO. Three different diamines have been used: two aliphatic ones and one aromatic. Specifically, ethylenediamine (EDA), p-phenylenediamine (PDA) and 4,4'-oxydianiline (ODA), have been tested as pillaring materials (Figure I.17(a)). A base ($NaNH_2$) was added to deprotonate the amine linkers and increase their nucleophilicity towards the partial positively charged Cs in the C-F_x bonds. The produced materials were characterized using XRD and HR-XPS (Figures I.17(a) & (b)). The XRD patterns of the pillared samples confirm the pillaring and the prevention of the restacking as only peaks corresponding to the new interlayer spacing were observed. This implies the structural homogeneity of the samples prepared. Such a homogeneity can be attributed to the organization and structuration of the starting material (bGF) and to its high reactivity compared to the completely random and distorted structure of rGO. The C1s HR-XPS spectra show an almost complete disappearance of the CF and CF_2 peaks with the appearance of a stronger C=C peaks in the pillared samples, indicating the reduction of the bGF into graphene and the restoration of the π delocalized network. The presence of C-N peaks show the successful functionalization of the graphene layers with the molecular pillars. On the other hand, the N1s HR-XPS spectra of the pillared

samples show two peaks corresponding to NH and NH_2, indicative of the functionalization. The highest performance was achieved with the material pillared with ODA. A gravimetric capacitance of 328.5 F/g and a volumetric capacitance of 354.8 F/cm^3 were recorded for the ODA sample at 0.5 A/g in 1 M Na_2SO_4. This is the highest value reported so far for an EDLC PGM. It showed a high rate capability as the capacitance reached 296.7 F/g and 320.4 F/cm^3 when the current density was increased to 10 A/g and 274.9 F/g when the scan rate reached 2000 mV/s. It showed a remarkable stability of around 90% capacitance retention after 20,000 cycles at a high current density of 10 A/g, which is indicative of high cyclability and long life time. Both gravimetric and volumetric energy and power densities were on the high benchmarks with energy densities of 19.6 Wh/kg, 17.7 Wh/kg, 21.6 Wh/L and 19.5Wh/L at power densities of 415 W/kg, 8266 W/kg, 457 W/L and 9093 W/L, respectively. This remarkable performance of such a material was attributed to the rigid pillars preventing the graphene from restacking, thus increasing the electrochemical active surface area and leading to hierarchical porosity, facilitating the ion diffusion and sorption. It was also attributed to the added pseudocapacitance coming from the oxygen moiety in the ODA pillar. In addition to this, the reduction of the unsubstituted C-F_x units by the pillars allowed the recovery of the π-conjugation of the graphene layer, yielding very conductive samples (1375 S/m, 1026 S/m and 1264 S/m for EDA-G, PDA-G and ODA-G, respectively).

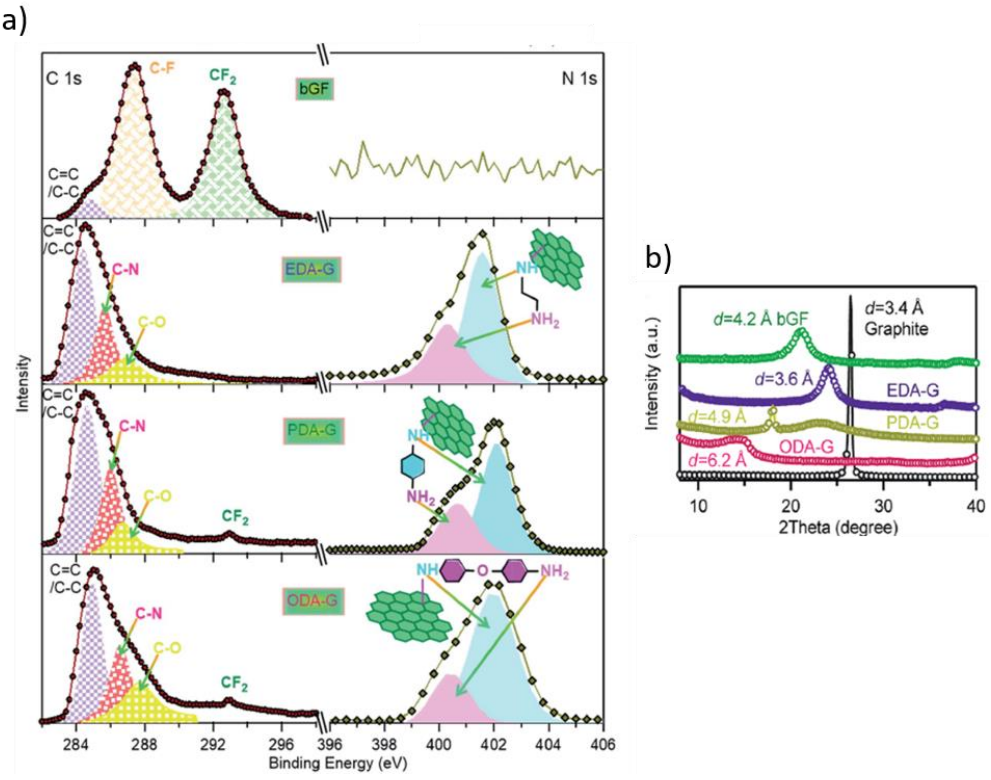

Figure I. 17 : a) C1s and N1s HR-XPS spectra for bGF, EDA-G, PDA-G and ODA-G and b) XRD diffractograms for bGF, EDA-G, PDA-G and ODA-G

(b) Aromatic Amine Pillars

As mentioned earlier, amine reactivity towards different oxygen functionalities on the graphene oxide can be utilized through both aliphatic and aromatic pillars. Song et al. employed phenylenediamines (PD) as redox pillars instead of alkyldiamines [118]. It was shown in early examples that these aromatic pillars were rather converted into their corresponding diazonium salt prior to grafting onto graphene or rGO. In this study, the diamine were reacted directly with graphene oxide in a 2-steps hydrothermal process. Differently substituted PD were tested: ortho-, para- and meta-phenylenediamine (OPD, PPD and MPD). XRD revealed graphene sheet cross-linking for (PPD and MPD) with the appearance of new peaks at 6.3° and 6.8° respectively. OPD grafting yielded less ordered structures as 2 broad peaks appeared at higher 2θ values. Electrochemical studies in a supercapacitor cell (2-electrodes – coin-cell in H_2SO_4) allowed to identify an optimum pillar density below and above which lower specific capacitance values were achieved due to lower adsorption active surface area and lower amount of redox unit, as well as to impeded ionic diffusion due to high amount of molecules, respectively. At this optimum loading value, a specific capacitance as high as 412 F/g (at 10 mV/s) for PPD/RGO sample was reached. Such value was attributed to the synergistic effect of graphene inter-layer expansion and PPD's pseudocapacitance. A lower capacitance value was achieved for OPD/RGO (281 F/g at 2 mV/s) explained by hindered charge mobility of the disorderly bonded or non-bonded pillars due to their inter-sheet aggregation.

Such PD grafting potential explains the variety of studies describing the use of PPD as molecular pillars. Different synthesis procedures have been demonstrated in various publications. A similar work was conducted by Lu et al. [119]. PPD was grafted on GO and then reduced using a chemical rather than hydrothermal process. Reference samples involving rGO functionalized with PPD post-reduction and a mixture of rGO and PPD have been comparatively studied. The highest Specific Capacitance value was obtained for the hybrid material revealing the added-value of graphene sheets restacking mitigation. The pillaring strategy enabled to promote an appropriate pore size distribution for the electrolytic ions to adsorb. Pseudo-capacity brought about by the PPD molecule is established by comparing all these values to that of rGO.

Few studies also tackled the issue of grafting density showing that intermediate amounts of PD grafted molecules display the best storage performances [120]. Different grafting substrates have been explored as well. PPD was grafted onto holey rGO under hydrothermal conditions and showed good performances not only for regular supercapacitors but also for flexible solid-state supercapacitors [121].

The use of aromatic amine-terminated pillars is not exclusive to PPD. Other aromatic linkers have been used in literature. Cui et al. used 3,3′-diaminobenzidine and 1,2,4,5-benzenetetraamine tetrahydrochloride as aromatic pillars to bridge GO sheets through the formation of benzimidazole rings, resulting from the reaction of the ortho amines with carboxylic groups [68]. This sample showed a high electrochemical performance in 2 electrode configuration as a specific capacitance of 370 F/g was achieved at 0.1 A/g with 90% capacitance retention after 5000 cycles. Such a high value was attributed to the high surface area, the pore size distribution, the electrical conductivity and the pseudocapacitance contribution coming from the imidazole rings. In another example, melamine was employed by Xing L. et al. as both a cross-linker and a reducing agent in aqueous solution in presence of ammonia [71]. Such a reaction medium, without stirring, yielded a hydrogel with a 3D structure. Owing to such a structure and to the pseudocapacitance arising from different nitrogen functionalities, a specific capacitance of 170.5 F/g was obtained in 6M KOH at 0.2 A/g based on the active material's weight.

Another exotic example is the work from Matsuo,Y. et al. A pillared graphene material with a silicon-containing pillar, namely silsesquioxane type pillars was synthesized [107]. The synthesis was done through the silylation of GO with methyltrichlorosilane to form the silsesquioxane pillars through covalently grafting the monomers (methyltrichlorosilane) and then using them as guides to grow the pillar. This was followed by a thermal reduction at 500°C under vacuum, to obtain the final pillared rGO material. The material was characterized by XRD and showed a d-spacing value of 1.3 nm. The material was tested as a supercapacitor using triethylmetylammmonium tetrafluorobotate ($TEMABF_4$) in PC. The capacitance was shown to increase when enlarging the potential window after hitting a potential plateau at the end of the first charge discharge curves. This electrochemical observation was attributed to an electrochemical activation step of the pillars. Upon cycling as positive or negative electrode, the d-spacing was shown to increase, from 1.3 nm initially, to 1.9 and 1.6 nm, respectively, as a result of the change in orientation of the pillars upon charging. $EMIBF_4$ IL was used and it was found out that zero capacitance was achieved for few cycles before the capacitance started increasing when using the materials as the negative electrode. This nearly zero capacitance values at the beginning shows the importance of the electrochemical activation step for such materials and shows its dependence on the type of electrolyte employed.

I.8.6.3 Composites Involving PGM for Supercapacitor Applications

Composites formation has always been a good method for combining the merits of two or more different components to achieve performances exceeding those of any of the

constituting samples alone and even sometimes exceeding their combined performance due to synergistic effects. PGM, same as Graphene [122], have been used in composite formation, mainly with metal oxide nanoparticles for supercapacitor applications. It has been shown that such assemblies aid in preventing the aggregation of the nanoparticles and having a final NPs uniform distribution, while offering a high electrical conductive backbone for such insulating metal-oxide. These NPs can bring pseudocapacitive signal to the final material.

Mazloum-Ardkani, M. et al. synthesized a pillared rGO and a Sm_2O_3-pillared rGO composite using an aromatic pillar (p-phenylenediamine) in a hydrothermal synthesis process [105]. The pillared samples had a d-spacing value of 0.77 nm and an increased electrochemically active surface area, thus confirming the prevention of aggregation of the rGO sheets. The pillaring also reduced the aggregation of the Sm_2O_3 nanoparticles in the composite and led to better NPs distribution and thus more accessible active materials compared to the composite without pillaring. The pillared materials without the nanoparticles showed enhanced capacitance performance compared to rGO due to the 3-dimensional structure, and to the newly created pores which offer better accessibility to the ions and facilitate their sorption and de-sorption. The Sm_2O_3 NPs introduction resulted in a boost of capacitance, from 222 F/g to 591 F/g in 6 M KOH electrolyte at a scan rate of 5 mV/s, arising from the pseudocapacitance of the metallic oxide component.

In a similar approach, Gholipour-Ranjbar, et al. hydrothermally synthesized an Fe_2O_3 nanoparticles - pillared rGO composite also using p-phenylenediamine as pillars [123]. This process yielded a porous nanocomposite with a surface area higher than that of the non-pillared version. This increase of specific surface area was ascribed to the decreased re-stacking of graphene sheets during the hydrothermal reduction. Such a reaction resulted also in N-doping of the graphene sheets and helped in decreasing the agglomeration of the Fe_2O_3 nanoparticles. Such a 3D porous N-doped Fe_2O_3/Pillared Graphene aerogel nanocomposite enhanced the electrochemical performance of the samples in 3M KOH compared to its non-pillared version as the specific capacitance went from 300 F/g to 409 F/g at 5 mV/s scan rate (based on the mass of the active material). The Fe_2O_3 nanoparticles on their own resulted in a specific capacitance of 204 F/g at 2 mV/s scan rate, owing to their pseudocapacitive nature.

The studies presented so far emphasize on the different materials engineering approaches that lead to properties alteration and tweaking to reach better performing supercapacitor electrodes. Indeed these PGM materials can be defined by the chemistry of pillaring, the nature and length of the pillars, the type of starting material, the reduction method, that all control the structure and physico-chemical properties of the resulting materials:

microstructure, level of reduction, defects, functionalities, surface chemistry, pore size, pore shape, pore size distribution and hierarchical porosity. All these physico-chemical and structural features dictate the final PGM properties such as electrical conductivity, electrochemically active surface area, wettability, charge transport kinetics, capacitance, energy and power densities, stability, cyclability, mechanical properties, and flexibility. Each study focused on the tuning of few of the above-cited parameters, and hence it is the combined effect of multiple factors that drives different performance of such pillared assemblies. For instance, the d-spacing parameter has to be combined with the proper choice of electrolytic salt to match the porosity created and achieve ion-pore sizes matching.

The electrochemical performances of PGM clearly show that the pillaring strategy applied to graphene oxide/reduced graphene oxide materials, common to all previously discussed articles, enables to achieve higher storage performances than their non-pillared counter-parts. The reported storage performances values show that significant capacitance or energy density improvement can be achieved by following the pillaring methodology that is often easy to implement.

I.9 PGM from an Ecological Point of View

Any technological or scientific advancement must consider its impact on the environment and the human beings themselves and strive to reduce such impact by looking for greener options. From the previous examples, it can be noticed that rGO is a common material in most of those studies whether as a platform for pillaring using the diazonium grafting method or a reference material for comparison. It has also been widely used for other applications. To produce such a material, GO has to be reduced to rGO and one of the easy ways of doing so is the use of a chemical reducing agent. The most efficient one is Hydrazine hydrate (Hz). Hydrazine is also employed in reducing the PGM after the functionalization step to reduce the amount of remaining oxygen functionalities and restore back the sp^2 carbon network to enhance the electrical conductivity. Unfortunately, Hz is notorious for being, potentially carcinogenic, flammable, (environmentally) corrosive, and toxic (Figure I.18) [124]. More over, the non-hydrated form of hydrazine is an explosive that is used as propellant in rocket fuels. This implies lots of precautions when dealing with Hz, high cost for its waste disposal, as well as limited applicability in large-scale production of graphene-based materials. Such downsides of such a great reducing agent must be weighed and balanced against its efficiency and performance.

Figure I. 18 : Safety pictograms of Hz according to UN Globally Harmonized System (GHS) criteria

I.9.1 Search for a Green Reducing Agent

Consequently, researchers started looking for milder, safer, cheaper, and greener reducing agents as alternatives for Hz. De Silva, K.K.H. et al. reviewed multiple greener reducing agents such as sodium citrate, sugars, microorganisms, amino acids, etc. that were tested in literature (Figure I.19), highlighting that only ascorbic acid's reducing power gets close to that of Hz [125].

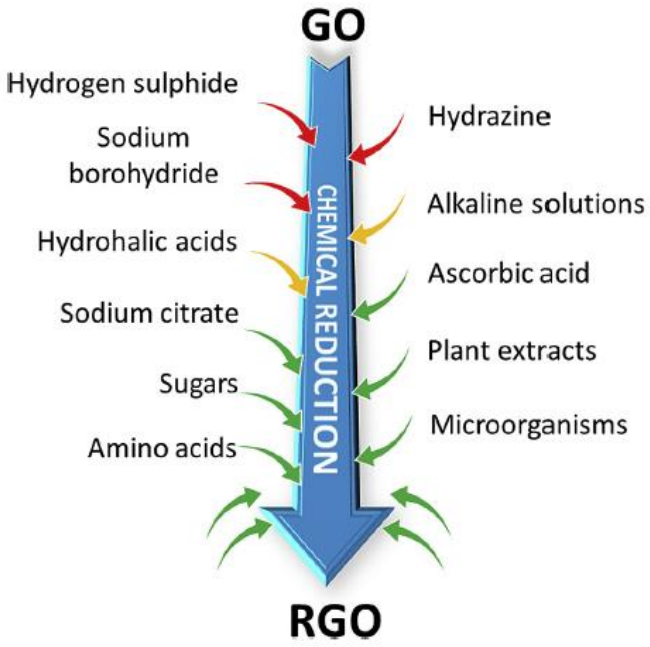

Figure I. 19 : Various GO reducing agents classified according to their environmental friendliness with red being dangerous, yellow means moderate and green means environmentally friendly

I.9.2 L-Ascorbic Acid as a Promising Green Alternative Reducing Agent

L-Ascorbic Acid (L-AA) is an organic molecule, commonly known as Vitamin C (VitC), with the molecular formula $C_6H_8O_6$, the molecular weight of 176.12 g/mole and the structure shown in Figure (I.20). It is a widely known ubiquitous chemical as it is a water soluble vitamin necessary for maintaining different metabolic functions in different plant and animal cells [126]. It is well known for being a vital anti-oxidant, anti-diabetic, anti-tumour, anti-inflammatory vitamin, as well as for being a drug for scurvy, common cold, slowing aging, hardening of arteries, and preventing clots in veins [125]. Its ease of oxidation (resulting from

its reactive functional groups) lead to its nomination as an alternative reducing agent for the production of GO instead of Hz.

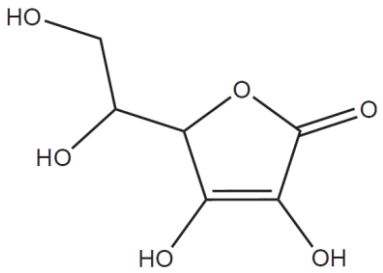

Figure I. 20 : Structure of ascorbic acid

The mechanism of the reduction is not fully understood yet, however the most accepted proposed mechanism is that proposed by Gao, J. et al. [127]. It was proposed that the reduction proceeds through 2 successive S_N2 nucleophilic attacks on the epoxide and hydroxyl groups of GO followed by a thermal elimination step as shown in Figure (I.21). In case of the epoxide group, the first S_N2 nucleophilic attack opens the epoxide ring and the second one is a back-side S_N2 that completes the reduction with the removal of water. In case of hydroxyls, the reduction proceeds through 2 successive back-side S_N2 attacks eliminating a water molecule per attack. These hydroxyl groups are acidic as they are attached to an electron withdrawing five-membered ring. The nucleophilic nature of L-AA, is resulting from such hydroxyls acidity that allows them to lose their protons, thus becoming neutrophiles.

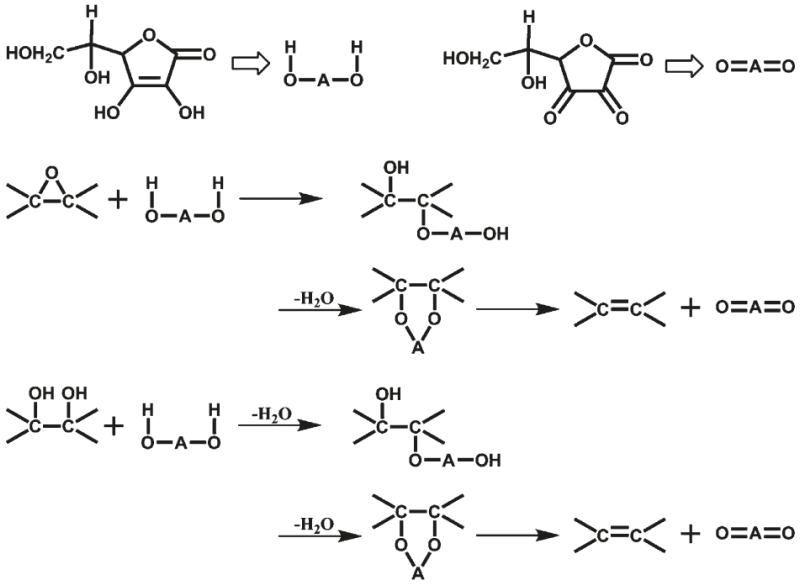

Figure I. 21 : Proposed mechanism of the reduction of GO by L-AA

During the reduction of GO, the L-AA is simultaneously oxidized. The 1st oxidative intermediate is the DeHydroAscorbic Acid (DH-AA) which can reversibly go back to L-AA or get irreversibly oxidized, especially in alkaline media, to 2,3-diketogulonic acid, which gets

immediately oxidized into oxalic acid and threonic acid (Figure I.22) [125], [128]. It is believed that some of the oxidized products might form hydrogen bonds with the remaining oxygen functionalities on the rGO such as hydroxyl, epoxy groups on the basal plane and carboxylic groups on the edges, thus stabilizing the rGO dispersion in polar solvents such as water [128], [129].

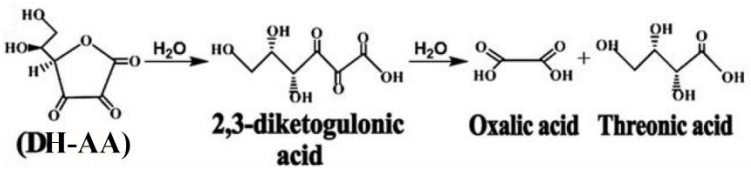

Figure I. 22 : Possible degradation products of DH-AA

In the upcoming section, an overview of the efforts that have been done in the direction of using L-AA as a reducing agent for the production of rGO from GO will be put forward. The synthesis conditions will be discussed along with the common characterization techniques utilized for the verification and the monitoring of the reduction of the GO and its extent. Also, examples from literature in which ascorbic acid reduced graphene oxide (rGO-VitC) have been employed for supercapacitor applications are to be analyzed.

Various attempts have been carried out in literature for the reduction of GO using L-AA using different synthesis methods under different reaction conditions including i) reaction time, ii) reaction temperature, iii) concentration of both GO and added L-AA, iv) pH of the reaction medium and v) special conditions such as stabilizers, post-treatment, etc. Table (I.1), adapted from [125], summarizes all those synthesis conditions along with the results obtained from various characterization techniques such as i) d-spacing from XRD, ii) I_D/I_G ratio from Raman spectroscopy, iii) C/O ratio from XPS and EA, iv) λ_{max} of rGO from UV-VIS, and v) electrical conductivity. Table (I.1) clearly shows the vast reaction conditions carried out and the wide range of characterization techniques that can be utilized to characterize the resulting rGO samples. In this section, a breakdown of the reaction parameters and the interest of using a combination of different characterization techniques for characterizing the samples are presented.

I.9.3 Reduction Conditions

Most often, a chemical reduction method is employed to reduce GO using L-AA; however, VitC reduced hydrogels are also reported in literature [130]–[133] as well as freeze-casted rGO-VitC [134], [135]. A higher amount of L-AA, even in excess, is believed to increase the efficiency and rate of reduction in a given period of time, with the unreacted L-AA remaining in the reaction medium [131], [136], [137]. A basic reaction medium (usually of a

pH around 9-10), achieved by the addition of NH_4OH, NaOH, or NH_3, is often employed in the literature as it is believed to promote the colloidal stability of GO via electrostatic repulsion among negatively charged graphene sheets obtained from the deprotonation of the carboxylic and phenolic functional groups [137], [138]. The base is also employed to neutralize the L-AA's oxidized products, thus preventing the accumulation of DH-AA and thus facilitating the reduction [128], [139]. On the other hand, an acidic pH was found to increase the reaction rate of L-AA reduced graphene hydrogels compared to neutral media [131]. Reaction temperatures ranging from Room Temperature (RT) to 95°C (up to 180°C for hydrothermal synthesis) have been investigated, as well as different reaction durations from 5 min up to 6 days. A high temperature is always desired to overcome the activation energy barrier and enhance the rate of reduction [140]. The reaction time has mainly been tracked through monitoring the maximum red-shift of the rGO absorbance peak from the UV-Vis. The optimum duration is selected when the shift reaches a stable maximum value with time, indicating that longer reaction time probably would not further affect the degree of reduction [128], [129], [137]. Functionalized GO or stabilizers can be used to obtain water stable rGO dispersions for different applications [127], [136], [141]. Pre- and post-reduction treatments such as thermally treating the sample prior to the chemical reduction to remove as many oxygen functionalities as possible [142], [143] and post washing the sample with excess of H_2O_2 to oxidize the remaining L-AA [144], [145] have also been reported.

I.9.4 Characterizing the Greener rGO-VitC

Characterizing the rGO reduced by L-AA conveys confirming the reduction, investigating the extent of reduction under different reduction conditions, and analyzing the properties of the resulting rGO. UV-Vis spectroscopy is employed to monitor the reduction reaction until its completion through monitoring the changes in the absorption spectrum of GO during its reduction to rGO. GO aqueous dispersions are known to display an absorbance peak around 230 nm and a shoulder around 300 nm, which are attributed to the π-π^* transition of the aromatic C=C bonds and n-π^* transition of the C=O bonds, respectively [146]. Upon the reduction to rGO, the peak at 230 nm red-shifts according to the reduction extent, while the peak at 300 nm disappears (Figure I.23(a)) [128], [129]. In addition, a high red-shift indicates that the reduction extent is higher; hence such red-shift is used to determine the reaction completion as indicated earlier. Moreover, the absorbance intensity increases over the whole spectrum upon reduction as a result of the color change (Figure I.23(b)) from brown to black (going from GO to rGO due to the restoration of the sp^2 carbon network), which can be a qualitative indication of the transformation of GO into rGO [129]. The reported peak shift

values are mostly around 265±3 nm as shown in Table (I.1), which is indicative of the reduction of the GO. Another important characterization technique used to confirm the reduction of the GO is X-ray Diffraction (XRD). GO shows an expanded inter-graphene layer distance of around 0.8-1 nm, due to the disrupted sp^2 carbon network and the incorporation of different oxygen functionalities on the basal plane and edges of the graphene sheets [125]. The disappearance of the 001 peak of GO and the appearance of the 002 rGO peak around 0.37-0.38 nm is indicative of the restoration of the sp^2 carbon network and thus the restoration of the π-π interactions between the graphene sheets leading to their (partial-) restacking (Figure I.23(c)) [138]. XRD data can also be used to analyze such stacking by fitting the XRD profile to get the size of crystallites and the average number of layers per crystallite. Another technique commonly used to monitor the reduction of GO into rGO is Raman Spectroscopy. Raman gives insights on the evolution of graphitic (sp^2 domains) and disordered domains (sp^3 domains and defects) through the G and D bands appearing around 1580 cm^{-1} and 1350 cm^{-1} respectively, for polycrystalline and/or nano graphite [147]. For GO and rGO, the D band appears at higher wavenumbers. Monitoring the I_D/I_G ratio gives an indication on the degree of disorder in the graphitic system. An increase in this ratio is expected when reducing GO into rGO due to the creation of small sp^2 domains in large quantities [147]. Such an increase can also be explained by higher fraction of graphene edges [138]. He, D. et al. experimented with different green reducing agents (Na2SO3, glucose, sucrose, D-fructose and L-AA). They obtained the highest I_D/I_G ratio of 2.8 with L-AA, suggesting rGO-VitC was the sample with most abundant small-sized sp^2 domains, indirectly indicating its superior reducing capabilities compared to the rest of the reducing agents tested in this study (Figure I.23(d)) [128]. Such better performance of L-AA was also confirmed with the rGO-VitC having the highest C/O ratio. The C/O ratio is basically the ratio of carbon to oxygen in the sample. It is another important parameter that allows the confirmation of the reduction as well as monitoring its progress under different conditions. Such a critical value can be extracted from X-ray Photoelectron spectroscopy (XPS) and Elemental Analysis (EA). In XPS, the ratio is calculated from atomic percentages; however, in EA, it is based on masses. During EA analysis, the whole bulk sample is burnt under different gases and the resulting gases are very accurately analyzed using gas chromatography which gives bulk representative values; while XPS provides a localized surface quasi-quantitative analysis, and is hence sensitive to bulk sample inhomogeneity. XPS offers rich information on the sample as XPS peaks can be fitted to give insights about the different bonding environments of the present elements and their atomic %. Such method allows the identification of different Os containing functionalities present on the sheets of GO along with the monitoring of their decrease in rGO. The sp^2 C1s XPS signal evolution is also a good tracker when following GO reduction (Figure

I.23(e)). Electrical conductivity measurements can be used to further confirm the restoration of the sp^2 carbon network. GO is known to be an insulator due to disruption of the conductive sp^2 carbon network resulting from the addition of oxygen functionalities, converting sp^2 Cs into sp^3 ones. When GO is reduced to rGO, the sp^2 carbon network is partially restored, allowing for enhanced electron mobility between the sp^2 domains and thus regaining the electrical conductivity. The highest XPS C/O ratio (12.5) of an rGO-VitC was achieved by Fernandez-Merino, M. J. et al., which came in agreement with the exceptional electrical conductivity reported (7700 S/m) [137].

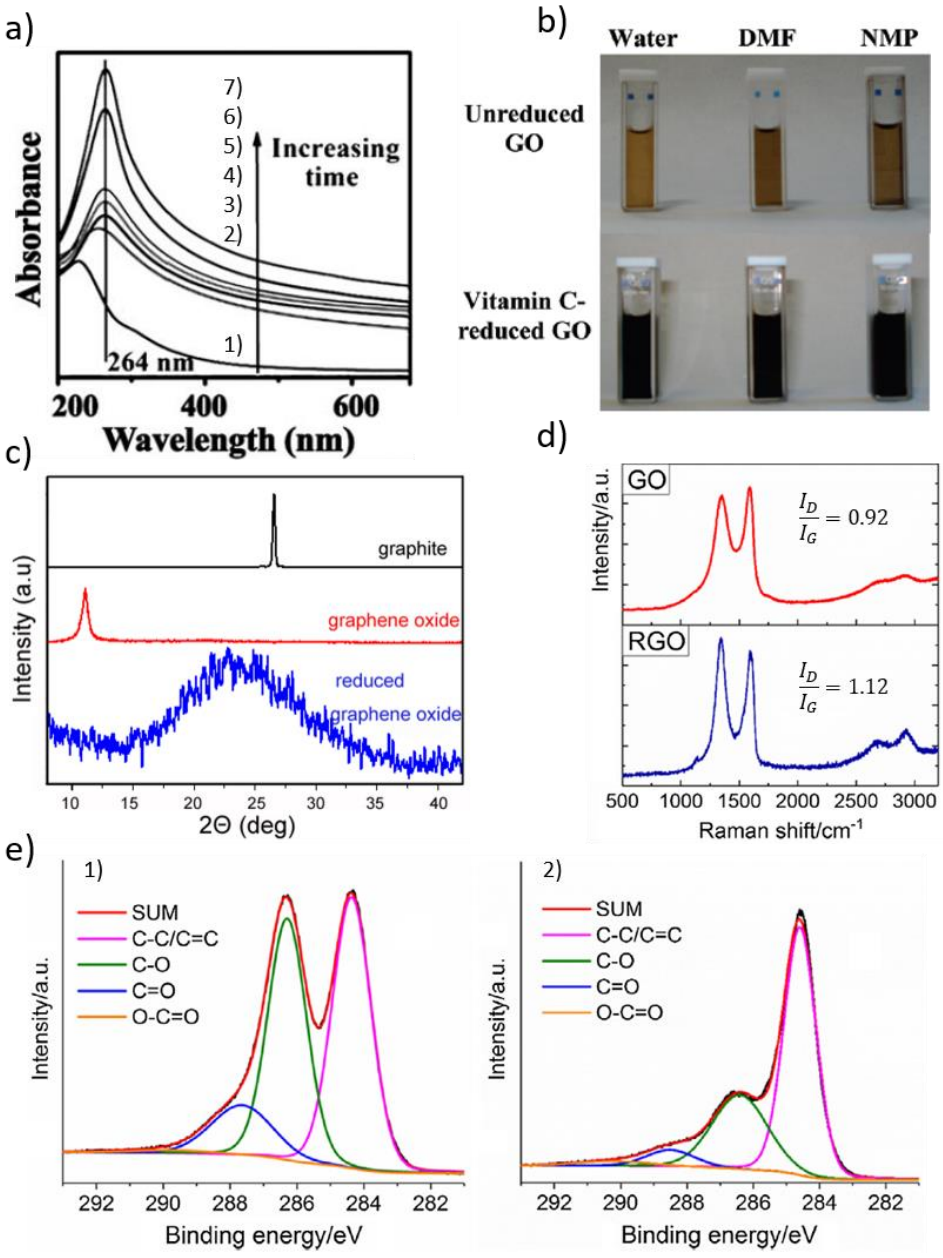

Figure I. 23 : a) UV-Vis spectra of 1) GO and 2-7) rGO-VitC at different reaction times (adapted from [128]), b) Brown color of GO suspensions in different solvents along with black rGO suspensions in the same solvents [137], c) XRD profiles of Graphite, GO and rGO-VitC [129], d) Raman spectra of GO and rGO-VitC with the corresponding I_D/I_G ratios [138] and e) XPS Profile of 1) GO and 2) rGO-VitC (adapted from [138])

I.9.5 rGO-VitC for Supercapacitor Applications

rGO-VitC has been tested as an electrode material for supercapacitors in few reports examining its performance and sometimes comparing it to that of rGO samples reduced with different reduction methods. Indujalekshmi, J. et al. reduced rGO from an aqueous suspension of GO by L-AA [148]. The reduced sample showed a higher C/O ratio (4.7) compared to that of GO (2.3), indicating the success of the reduction. The sample was cycled in 1M Na_2SO_4, showing a specific capacitance of 70F/g at a current density of 0.8 A/g as well as an energy density of 19 Wh/kg at a power density of 1120 W/kg. It also showed a capacitance retention of 93% after 1000 cycles. Despite using various characterization techniques, no correlations between the properties of such sample and its electrochemical performance were established. Lee, S. P. et al. synthesized rGO-VitC reduced aerogels from GO sheets of different oxidation levels and different sheet sizes [133]. The aerogel were synthesized using the freeze casting method in which the sample is partially reduced, frozen, thawed and then reduced again until completion. Such a method is believed to yield three-dimensional porous structures, which are templated by the formation of ice crystals [135]. The best performing sample showed a specific capacitance 182 F/g at a current density of 0.75 A/g in 5M KOH with a capacitance retention of 96% after 10000 cycles. Such performance was attributed to its highest surface area and pore volume compared to the rest of the samples in this study. Lavin-Lopez, M.P. et al. reduced GO thermally and by multi-step reduction (thermal reduction followed by L-AA reduction) and tested the effect of those reduction methods on the performance of rGO as electrode material for supercapacitor applications [143]. The multi-step reduced rGO showed a better capacitive performance compared to that of the thermally reduced rGO with a capacitance of 86.05 F/g versus 62.11 F/g at a scan rate of 200 mV/s in 1 M KCl. Such an increase in capacitance was attributed to higher surface area and more ordered structure, leading to higher accessibility of ions. In a paper by Ha, T. et al., Spherical Graphene (SGR) particles were obtained using ascorbic acid reduced rGO. These particles were obtained through spray-drying of a rGO-VitC solution under different pH conditions, and the effect of the pH on their performance as electrode materials for supercapacitors was studied [149]. Also, a comparison was made with regular non-spherical rGO-VitC which showed a lower capacitance (76 F/g compared to 143 F/g for SGR at pH 2 and 182 F/g for SGR at pH 10, in 5 M KOH in a 2-electrode system). This capacitance increase was attributed to a synergistic effect of the spherical shape and of the higher SSA of the SGR samples, allowing for more active sites and higher contact area between the electrolyte and the electrode. Basic dispersions showed better performance due to the higher specific surface area achieved as a result of the limitation of the agglomeration arising from a more stable colloidal dispersion in basic conditions as reported earlier.

Composites have been synthesized using rGO-VitC and pseudocapacitive materials, with the aim of enhancing the capacitance, while maintaining a green environmental friendly synthesis method. For example, MoO_2/rGO was synthesized by Serrapede, M. et al. using L-AA reduction in a hydrothermal synthesis [132]. First, rGO was synthesized hydrothermally with and without L-AA to choose the best material for the composite formation. The rGO-VitC showed a higher C/O ratio from XPS values. This lower oxygen content was also evident from the disappearance of redox peaks that are more clearly visible in the case of the less reduced hydrogel. The rGO-VitC showed lower capacitance than the rGO hydrogel prepared without L-AA (23 F/g versus 55 F/g in 1 M NaCl) which was attributed to lower surface area and larger pore size distribution of the former. Regardless, it was selected for the composite formation as it had better stability at different scan rates. The rGO-VitC/MoO_2 showed a higher capacitance of 210 F/g due to the pseudocapacitance brought by the redox reaction of the Mo center. rGO/MWCNTs composite was prepared by Chartarrayawadee, W. et al. [150]. GO and MWCNTs were mixed together, and then L-AA was added to reduce the GO. The composite was transferred onto a glassy carbon substrate by electrophoretic anodic deposition, and was finally tested as an electrode material for supercapacitor. The process of reduction and deposition was done without MWCNTs as a reference sample. The composite showed a superior performance compared to rGO-VitC (134.3 F/g versus 63.5 F/g in 1 M H_2SO_4). This was attributed to the remaining oxygen functionalities on both the rGO-VitC and the MWCNTs as well as the presence of the MWCNTs which served as conductive wires, thus, improving charge transfer. Various trials have been made to use the rGO-VitC for flexible all-solid-state supercapacitors. Su, H. et al. synthesized water dispersible rGO by decorating it, physically and chemically, with aminobenzenesulfonic acid followed by its reduction using L-AA [130]. The obtained stable rGO-VitC dispersion was used as an ink for direct printing on common printing paper. Such a flexible all-solid-state micro-supercapacitor yielded an aerial capacitance of 2.67 mF/cm^2 and a volumetric capacitance of 6.75 F cm^3, with 94.8% capacitance retention after 5000 cycles at a scan rate of 50 mV/s in PVA-H_2SO_4 as a solid electrolyte. Reduced GO was deposited by Stempien, Z. et al. onto different fabrics through reactive inkjet printing. The reduction by L-AA took place simultaneously with the deposition [151]. A flexible all-solid-state supercapacitor was assembled using the rGO-VitC printed on PANI as electrodes and PVA-H_3PO_4 as a solid electrolyte. This device showed an areal capacitance of 13.3 mF/cm^2 (specific capacitance of 79.9 F/g) at current density of 0.1 mA/cm^2 with nearly 100% capacitive retention after 5000 cycles. The energy density was 1.18 mWh/cm^2 at a power density of 4.6 mW/cm^2. These last 2 examples show the potential of the greener ascorbic acid reduction method to prepare rGO-based materials for flexible all-solid-state supercapacitor.

Vitamin C, a simple organic molecule, has proven its efficient applicability as a green reducing agent towards the reduction of graphene oxide, with lots of potential for different applications. This emphasizes on the feasibility of using vitamin C as a green alternative for the reduction of GO rather than the toxic and dangerous commonly used hydrazine. It also encourages further research in the green direction not only for the reduction of GO, but also for various chemical processes involving harmful and non-environmental friendly chemicals.

I.10 Aim of the PhD

It can be seen from the literature on PGM that most of the publications were performance oriented, that is to say they were mainly focused on enhancing the values of the specific and/or volumetric capacitance, energy density, power density, and stability. Only few reports dealt with the fundamentals and understanding of such materials as electrode materials for supercapacitors. Since it is a relatively new class of materials, various studies have to be carried out to understand the effect of different parameters (notably the chemistry and the structure) of such complex multi-parameter systems on their electrochemical performance and on the charge storage mechanism.

New tailored microporous galleries were created between the graphene sheets in those assemblies, supposedly opening up new inter-graphene adsorption sites for ions. Various pillars were used with different chemistry, length, rigidity, density, and redox activities to enhance the final capacitance. Such diversity (infinite number of pillars) along with the increasing complexities (various parameters) require thorough fundamental studies to investigate the key parameters influencing the performance enhancement. These correlations will enable devising a material optimization strategy relying on a guided and educated approach rather than on a trial and error one. Consequently, the thesis at hand, aims at the fundamental understanding of the effects of different structural and physico-chemical properties of this class of materials on their electrochemical performance in a way that captures the essence of this class of materials and capitalizes on their versatility and tailorable properties. The study also aims at investigating the ion-sieving effect in aqueous media and the importance of the ions' solvation shells.

Accordingly, in the 1st half of this PhD, a fundamental study shall be carried out on pillared graphene samples containing different pillars with different functionalities in an attempt to decipher the effect of their chemistry and structure on their performance as electrode materials for supercapacitors and on the associated charge storage mechanism. In order to trigger specifically these properties, the pillars will be selected as to result in different inter-layer graphene distances and different heteroatom content. The properties investigated are

chemical such as i) the surface chemistry of the graphene sheets and ii) the presence of different heteroatoms in the backbone of the pillars used, as well as structural like i) the inter-graphene sheet distance (d-spacing). The study seeks studying the effects of those parameters through a series of various experiments: i) evaluating the efficiency of this pillaring strategy in opening up new adsorption sites through comparing their performance to that of a reference non-pillared sample, ii) assessing the role of pillar and surface chemistries on the performance using acidic and neutral aqueous electrolyte, and iii) triggering the ion-pore size matching through combining samples with different d-spacing values along with cations and anions of different sizes. To carry out these studies and try to respond to such multiple questions, pillared materials, with pure aliphatic pillar, or with pillar containing oxygen hetero element or NCH_3 group, will be synthesized chemically and characterized by various characterization techniques to validate the synthesis and the pillaring and extract various valuable chemical and structural information about the samples. Moreover, electrochemical testing will be carried out on the samples to test their capabilities for supercapacitor applications in different electrolytes. Furthermore, the data from these various electrochemical techniques applied will be treated to get quantitative and comparative values. Finally, correlations between the physico-chemical properties and the electrochemical behavior will be made. Consequently, trends will be observed and put into perspective to bring valuable understanding to the fundamental electrochemical adsorption mechanism taking place in this class of materials.

A fundamental study would require good reproducible well-defined synthetic procedures to limit, as much as possible, the uncertainties regarding the conclusions which shall be drawn. Consequently, the well-studied, well-optimized and well-documented use of hydrazine as the best known reducing agent for graphene based materials makes it the best candidate when choosing a reducing agent for our fundamental study. However, the risks associated with the use of hydrazine urge researchers to look for greener alternatives, and L-ascorbic acid is the most efficient green reducing agent candidate. Unfortunately, reduction conditions involving this green reducing agent have not been quite optimized in literature. In addition, a complete characterization of the L-ascorbic acid reduced GO is lacking in the literature. Moreover, such a reduction method has never been applied to pillared graphene samples. Furthermore, the application of the ascorbic acid reduced graphene oxide as an electrode material for supercapacitors was not extensively studied in common electrolytes and the electrochemical performance was not conclusively correlated to properties and hence to reduction conditions, as highlighted in the last section. Hence the second aim of this thesis is to rationalize and optimize the synthesis conditions and test the samples' electrochemical interests

as electrode materials for supercapacitor applications in various common aqueous electrolytes. This work also endeavors to contribute to the current knowledge regarding the reactions between L-ascorbic acid and graphene based materials by providing insights on reduction mechanistic pathways. To achieve such goals, an optimization of the reduction of graphene oxide was first carried out. Such an optimization will involve testing various reaction conditions such as i) reaction duration, ii) reaction temperature and iii) quantities of ascorbic acid utilized. To select the best conditions, the study suggests a multi-disciplinary characterization protocol that involves various characterization techniques, enabling the monitoring of the reduction and its extent, the structural evolution and materials' properties like electrical conductivity. Specifically designed experiments will be used to not only to fine tune the analysis of final product, but also to further unravel the mechanism. Electrochemical tests in various electrolytes will be carried out to investigate the behavior of such samples versus that of hydrazine reduced graphene oxide, which shall be synthesized as a reference sample for the sake of comparison. The study is concerned with performance electrolytes and thus the choices of electrolytes included 3M H_2SO_4, 6M KOH and 0.5M K_2SO_4. In addition, they were selected to be able to correlate the electrochemical performance to the surface chemistry. Finally, the structural and physico-chemical properties of the samples will be the crossroads correlating the reaction conditions to the electrochemical performances.

Table I.1 : Summary of the ascorbic acid reduced graphene oxide samples mentioned in literature (to the best of my knowledge)

Reaction Conditions						Results from various Characterization Techniques										
GO Conc. (mg/ml)	L-AA Conc. (mg/ml)	Reaction Temp. (°C)	Reaction Time	pH	Special Conditions	d-spacing from XRD (nm)		I_D/I_G ratio from Raman		C/O ratio				λ_{max} of rGO from UV-VIS (nm)	Electrical conductivity (S/m)	Ref.
										XPS		EA				
						GO	rGO	GO	rGO	GO	rGO	GO	rGO			
0.1	5.0	80	24 h	Basic with NaOH	Amino Acid Stabilizer	N/A	N/A	1.56	1.75	N/A	N/A	N/A	N/A	N/A	14.1	[127]
1	9.86	95	10 min	Basic with NH_3	N/A	0.796	0.387	1.21	2.82	2	16.7	N/A	N/A	264	N/A	[128]
0.1	1.0	RT	48 h	Neutral-	N/A	0.794	0.37	N/A	N/A	N/A	N/A	N/A	N/A	264	800	[129]
0.1	1	65	1 h	Basic with NH_3	N/A	0.93	0.358	0.92	1.12	2	4.7	N/A	N/A	263	N/A	[138]
2	20	120	6 h	N/A	Functionalized GO & Hydrothermal Synthesis	N/A	N/A	0.98	1.23	2.3	5.6	N/A	N/A	270	360	[130]
1	1	RT	48 h	N/A	N/A	0.97	0.38	0.99	1.16	N/A	N/A	0.92	2.33	N/A	N/A	[142]
					Thermal Treatment		0.41		1.15				2.7			
1	1	RT	48 h	N/A	Thermal Treatment	0.98	0.41	0.94	1.15	N/A	N/A	0.93	2.7	N/A	N/A	[143]
0.1	0.3-2 mM	95	15-240 min	Basic with NH_3	N/A	N/A	N/A	N/A	N/A	2.3	12.5	N/A	N/A	268	7700	[137]
1	20	RT	10 min, 2 and 6 days	Basic with NH_4OH	N/A	N/A	N/A	N/A	N/A	N/A	N/A	N/A	N/A	268	N/A	[152]
N/A	17.6	60	30 min	Neutral	Excess H_2O_2	N/A	N/A	N/A	N/A	N/A	N/A	N/A	N/A	260	N/A	[144]
37	37	60	30 min	Neutral	Sonication+ Excess H_2O_2	N/A	N/A	N/A	N/A	N/A	N/A	N/A	N/A	N/A	N/A	[145]
N/A	10	80	1 h	N/A	Single layered GO on Si substrate	N/A	N/A	N/A	2.3	N/A	N/A	N/A	N/A	N/A	N/A	[153]

0.1	4.0	25 and 60	2 and 6 h	Basic with NaOH	Ultrasonication	N/A	N/A	N/A	N/A	N/A	N/A	N/A	N/A	268	N/A	[140]
0.1	1.0	95	2 h	Basic with NH_3	N/A	N/A	N/A	0.95	1.19	2.65	5.15	N/A	N/A	N/A	980	[139]
N/A	N/A	95	1 h	Neutral	N/A	0.925	N/A	0.95	1.33	2.4	8	N/A	N/A	N/A	N/A	[154]
1.33	0.35	90	1-2 h	Basic with NH_3	N/A	0.839	0.385	0.93	1.08	N/A	6.07	N/A	N/A	N/A	N/A	[155]
4.0	Diff. ratios	25-80	1-3 h	Neutral to Acidic	N/A	0.862	0.377	N/A	N/A	N/A	N/A	1.13	5.16	N/A	12.1	[131]
2.0	10.0	80	1 h	N/A	N/A	0.876	0.373	N/A	N/A	N/A	N/A	N/A	N/A	N/A	800	[156]
0.3	5	RT	48 h	N/A	TiO_2 composite	N/A	N/A	1.029	1.344	N/A	N/A	N/A	N/A	N/A	N/A	[157]
1	10	RT	12 h	Basic with NH_4OH	N/A	N/A	N/A	0.89	1.15	N/A	N/A	N/A	N/A	N/A	N/A	[158]
N/A	N/A	50	6 h	N/A	N/A	0.83	N/A	N/A	N/A	N/A	N/A	N/A	N/A	N/A	N/A	[159]
					Functionalized GO	0.68										
0.1	N/A	RT	24 h	N/A	Functionalized GO	0.83	0.44	N/A	N/A	N/A	N/A	N/A	N/A	240	N/A	[136]
3.0	1000	80	1 h	Neutral	Triton-X100 stabilizer	N/A	N/A	N/A	N/A	N/A	N/A	N/A	N/A	N/A	1500	[141]
N/A	N/A	95	1 h	Basic with NH_4OH	Spray dried (spherical particles)	N/A	N/A	N/A	N/A	N/A	N/A	N/A	N/A	290	N/A	[149]
2	2	180	12 h	N/A	Hydrothermal Synthesis	N/A	N/A	N/A	N/A	1.9	7.5	N/A	N/A	N/A	N/A	[132]
0.1	17.1 mM	RT	48 h	N/A	N/A	N/A	N/A	N/A	N/A	N/A	N/A	N/A	N/A	264	N/A	[150]
5	100	120	N/A	N/A	Reactive Ink Printing	N/A	N/A	0.76	1.1	N/A	N/A	N/A	N/A	N/A	N/A	[151]
4	8	80	80 min	N/A	Freeze casting followed by thermal reduction at 80°C for 8h	0.905	0.35	N/A	N/A	N/A	N/A	N/A	N/A	N/A	N/A	[133]
3	60mM	90	1 h	N/A	N/A	0.806	0.355	1.09	1.3	2.3	4.7	N/A	N/A	283	N/A	[148]

I.11 References:

[1] S. Shafiee and E. Topal, 'When will fossil fuel reserves be diminished?', *Energy Policy*, vol. 37, no. 1, pp. 181–189, Jan. 2009, doi: 10.1016/j.enpol.2008.08.016.

[2] J. Mao, J. Iocozzia, J. Huang, K. Meng, Y. Lai, and Z. Lin, 'Graphene aerogels for efficient energy storage and conversion', *Energy Environ. Sci.*, vol. 11, no. 4, pp. 772–799, 2018, doi: 10.1039/C7EE03031B.

[3] A. G. Olabi, 'Renewable energy and energy storage systems', *Energy*, vol. 136, pp. 1–6, Oct. 2017, doi: 10.1016/j.energy.2017.07.054.

[4] M. Yekini Suberu, M. Wazir Mustafa, and N. Bashir, 'Energy storage systems for renewable energy power sector integration and mitigation of intermittency', *Renewable and Sustainable Energy Reviews*, vol. 35, pp. 499–514, Jul. 2014, doi: 10.1016/j.rser.2014.04.009.

[5] J. R. Miller, 'Engineering electrochemical capacitor applications', *Journal of Power Sources*, vol. 326, pp. 726–735, Sep. 2016, doi: 10.1016/j.jpowsour.2016.04.020.

[6] P. Ball and Y. Gogotsi, 'Super-capacitors take charge in Germany', *MRS Bull.*, vol. 37, no. 9, pp. 802–803, Sep. 2012, doi: 10.1557/mrs.2012.222.

[7] C. Abbey and G. Joos, 'Supercapacitor Energy Storage for Wind Energy Applications', *IEEE Trans. on Ind. Applicat.*, vol. 43, no. 3, pp. 769–776, 2007, doi: 10.1109/TIA.2007.895768.

[8] L. Qu and W. Qiao, 'Constant Power Control of DFIG Wind Turbines With Supercapacitor Energy Storage', *IEEE Trans. on Ind. Applicat.*, vol. 47, no. 1, pp. 359–367, Jan. 2011, doi: 10.1109/TIA.2010.2090932.

[9] A. Lahyani, P. Venet, A. Guermazi, and A. Troudi, 'Battery/Supercapacitors Combination in Uninterruptible Power Supply (UPS)', *IEEE Transactions on Power Electronics*, vol. 28, no. 4, pp. 1509–1522, Apr. 2013, doi: 10.1109/TPEL.2012.2210736.

[10] X. Gao, S. Wang, and T. Wei, 'Energy management method of supercapacitors storage system for UPS applications', in *2009 International Conference on Applied Superconductivity and Electromagnetic Devices*, Sep. 2009, pp. 68–72. doi: 10.1109/ASEMD.2009.5306693.

[11] J. R. Miller and P. Simon, 'Electrochemical Capacitors for Energy Management', *Science*, vol. 321, no. 5889, pp. 651–652, Aug. 2008, doi: 10.1126/science.1158736.

[12] P. Veerakumar, A. Sangili, S. Manavalan, P. Thanasekaran, and K.-C. Lin, 'Research Progress on Porous Carbon Supported Metal/Metal Oxide Nanomaterials for Supercapacitor Electrode Applications', *Ind. Eng. Chem. Res.*, vol. 59, no. 14, pp. 6347–6374, Apr. 2020, doi: 10.1021/acs.iecr.9b06010.

[13] Z. Lin *et al.*, 'Materials for supercapacitors: When Li-ion battery power is not enough', *Materials Today*, vol. 21, no. 4, pp. 419–436, May 2018, doi: 10.1016/j.mattod.2018.01.035.

[14] S. Fleischmann *et al.*, 'Pseudocapacitance: From Fundamental Understanding to High Power Energy Storage Materials', *Chem. Rev.*, vol. 120, no. 14, pp. 6738–6782, Jul. 2020, doi: 10.1021/acs.chemrev.0c00170.

[15] C. Choi *et al.*, 'Achieving high energy density and high power density with pseudocapacitive materials', *Nature Reviews Materials*, vol. 5, no. 1, Art. no. 1, Jan. 2020, doi: 10.1038/s41578-019-0142-z.

[16] E. Raymundo-Piñero, K. Kierzek, J. Machnikowski, and F. Béguin, 'Relationship between the nanoporous texture of activated carbons and their capacitance properties in different electrolytes', *Carbon*, vol. 44, no. 12, pp. 2498–2507, Oct. 2006, doi: 10.1016/j.carbon.2006.05.022.

[17] J. Chmiola, 'Anomalous Increase in Carbon Capacitance at Pore Sizes Less Than 1 Nanometer', *Science*, vol. 313, no. 5794, pp. 1760–1763, Sep. 2006, doi: 10.1126/science.1132195.

[18] C. Largeot, C. Portet, J. Chmiola, P.-L. Taberna, Y. Gogotsi, and P. Simon, 'Relation between the Ion Size and Pore Size for an Electric Double-Layer Capacitor', *J. Am. Chem. Soc.*, vol. 130, no. 9, pp. 2730–2731, Mar. 2008, doi: 10.1021/ja7106178.

[19] J. Chmiola, C. Largeot, P.-L. Taberna, P. Simon, and Y. Gogotsi, 'Desolvation of Ions in Subnanometer Pores and Its Effect on Capacitance and Double-Layer Theory', *Angew. Chem. Int. Ed.*, vol. 47, no. 18, pp. 3392–3395, Apr. 2008, doi: 10.1002/anie.200704894.

[20] R. Lin, P. L. Taberna, J. Chmiola, D. Guay, Y. Gogotsi, and P. Simon, 'Microelectrode Study of Pore Size, Ion Size, and Solvent Effects on the Charge/Discharge Behavior of Microporous Carbons for Electrical Double-Layer Capacitors', *J. Electrochem. Soc.*, vol. 156, no. 1, p. A7, 2009, doi: 10.1149/1.3002376.

[21] C. Merlet *et al.*, 'Highly confined ions store charge more efficiently in supercapacitors', *Nat Commun*, vol. 4, no. 1, p. 2701, Dec. 2013, doi: 10.1038/ncomms3701.

[22] W.-Y. Tsai, P.-L. Taberna, and P. Simon, 'Electrochemical Quartz Crystal Microbalance (EQCM) Study of Ion Dynamics in Nanoporous Carbons', *J. Am. Chem. Soc.*, vol. 136, no. 24, pp. 8722–8728, Jun. 2014, doi: 10.1021/ja503449w.

[23] H. Banda *et al.*, 'Ion Sieving Effects in Chemically Tuned Pillared Graphene Materials for Electrochemical Capacitors', *Chem. Mater.*, vol. 30, no. 9, pp. 3040–3047, May 2018, doi: 10.1021/acs.chemmater.8b00759.

[24] R. Futamura *et al.*, 'Partial breaking of the Coulombic ordering of ionic liquids confined in carbon nanopores', *Nature Mater*, vol. 16, no. 12, pp. 1225–1232, Dec. 2017, doi: 10.1038/nmat4974.

[25] S. Fleischmann *et al.*, 'Continuous transition from double-layer to Faradaic charge storage in confined electrolytes', *Nat Energy*, vol. 7, no. 3, Art. no. 3, Mar. 2022, doi: 10.1038/s41560-022-00993-z.

[26] T. S. Mathis, N. Kurra, X. Wang, D. Pinto, P. Simon, and Y. Gogotsi, 'Energy Storage Data Reporting in Perspective—Guidelines for Interpreting the Performance of Electrochemical Energy Storage Systems', *Advanced Energy Materials*, vol. 9, no. 39, p. 1902007, 2019, doi: 10.1002/aenm.201902007.

[27] P. Simon, Y. Gogotsi, and B. Dunn, 'Where Do Batteries End and Supercapacitors Begin?', *Science*, vol. 343, no. 6176, pp. 1210–1211, Mar. 2014, doi: 10.1126/science.1249625.

[28] J. Wang, J. Polleux, J. Lim, and B. Dunn, 'Pseudocapacitive Contributions to Electrochemical Energy Storage in TiO2 (Anatase) Nanoparticles', *J. Phys. Chem. C*, vol. 111, no. 40, pp. 14925–14931, Oct. 2007, doi: 10.1021/jp074464w.

[29] D.-W. Wang, F. Li, M. Liu, G. Q. Lu, and H.-M. Cheng, '3D Aperiodic Hierarchical Porous Graphitic Carbon Material for High-Rate Electrochemical Capacitive Energy Storage', *Angewandte Chemie International Edition*, vol. 47, no. 2, pp. 373–376, 2008, doi: 10.1002/anie.200702721.

[30] L. Weinstein and R. Dash, 'Supercapacitor carbons', *Materials Today*, vol. 16, no. 10, pp. 356–357, Oct. 2013, doi: 10.1016/j.mattod.2013.09.005.

[31] Y. Wang, Y. Song, and Y. Xia, 'Electrochemical capacitors: mechanism, materials, systems, characterization and applications', *Chem. Soc. Rev.*, vol. 45, no. 21, pp. 5925–5950, Oct. 2016, doi: 10.1039/C5CS00580A.

[32] P. Simon and Y. Gogotsi, 'Materials for electrochemical capacitors', *Nature Materials*, vol. 7, no. 11, Art. no. 11, Nov. 2008, doi: 10.1038/nmat2297.

[33] A. G. Pandolfo and A. F. Hollenkamp, 'Carbon properties and their role in supercapacitors', *Journal of Power Sources*, vol. 157, no. 1, pp. 11–27, Jun. 2006, doi: 10.1016/j.jpowsour.2006.02.065.

[34] A. Szabó, C. Perri, A. Csató, G. Giordano, D. Vuono, and J. B. Nagy, 'Synthesis Methods of Carbon Nanotubes and Related Materials', *Materials*, vol. 3, no. 5, Art. no. 5, May 2010, doi: 10.3390/ma3053092.

[35] K. H. An *et al.*, 'Electrochemical Properties of High-Power Supercapacitors Using Single-Walled Carbon Nanotube Electrodes', *Advanced Functional Materials*, vol. 11, no. 5, pp. 387–392, 2001, doi: 10.1002/1616-3028(200110)11:5<387::AID-ADFM387>3.0.CO;2-G.

[36] H. Pan, J. Li, and Y. Feng, 'Carbon Nanotubes for Supercapacitor', *Nanoscale Res Lett*, vol. 5, no. 3, p. 654, Jan. 2010, doi: 10.1007/s11671-009-9508-2.

[37] M. Zeiger, N. Jäckel, V. N. Mochalin, and V. Presser, 'Review: carbon onions for electrochemical energy storage', *J. Mater. Chem. A*, vol. 4, no. 9, pp. 3172–3196, Feb. 2016, doi: 10.1039/C5TA08295A.

[38] D. M. Anjos *et al.*, 'Pseudocapacitance and performance stability of quinone-coated carbon onions', *Nano Energy*, vol. 2, no. 5, pp. 702–712, Sep. 2013, doi: 10.1016/j.nanoen.2013.08.003.

[39] G. Moussa, C. Matei Ghimbeu, P.-L. Taberna, P. Simon, and C. Vix-Guterl, 'Relationship between the carbon nano-onions (CNOs) surface chemistry/defects and their capacitance in aqueous and organic electrolytes', *Carbon*, vol. 105, pp. 628–637, Aug. 2016, doi: 10.1016/j.carbon.2016.05.010.
[40] E. Frackowiak and F. Béguin, 'Carbon materials for the electrochemical storage of energy in capacitors', *Carbon*, vol. 39, no. 6, pp. 937–950, May 2001, doi: 10.1016/S0008-6223(00)00183-4.
[41] K. S. Novoselov *et al.*, 'Electric Field Effect in Atomically Thin Carbon Films', *Science*, vol. 306, no. 5696, pp. 666–669, Oct. 2004, doi: 10.1126/science.1102896.
[42] Y. Yang *et al.*, 'Graphene-based materials with tailored nanostructures for energy conversion and storage', *Materials Science and Engineering: R: Reports*, vol. 102, pp. 1–72, Apr. 2016, doi: 10.1016/j.mser.2015.12.003.
[43] M. F. El-Kady, Y. Shao, and R. B. Kaner, 'Graphene for batteries, supercapacitors and beyond', *Nature Reviews Materials*, vol. 1, no. 7, pp. 1–14, May 2016, doi: 10.1038/natrevmats.2016.33.
[44] X.-Y. Wang, A. Narita, and K. Müllen, 'Precision synthesis versus bulk-scale fabrication of graphenes', *Nature Reviews Chemistry*, vol. 2, no. 1, Art. no. 1, Dec. 2017, doi: 10.1038/s41570-017-0100.
[45] Y. Yang *et al.*, 'Graphene-based materials with tailored nanostructures for energy conversion and storage', *Materials Science and Engineering: R: Reports*, vol. 102, pp. 1–72, Apr. 2016, doi: 10.1016/j.mser.2015.12.003.
[46] M. Pumera, 'Graphene-based nanomaterials and their electrochemistry', *Chem. Soc. Rev.*, vol. 39, no. 11, pp. 4146–4157, Oct. 2010, doi: 10.1039/C002690P.
[47] L. Bai *et al.*, 'Graphene for Energy Storage and Conversion: Synthesis and Interdisciplinary Applications', *Electrochem. Energ. Rev.*, vol. 3, no. 2, pp. 395–430, Jun. 2020, doi: 10.1007/s41918-019-00042-6.
[48] Y. Li, M. van Zijll, S. Chiang, and N. Pan, 'KOH modified graphene nanosheets for supercapacitor electrodes', *Journal of Power Sources*, vol. 196, no. 14, pp. 6003–6006, Jul. 2011, doi: 10.1016/j.jpowsour.2011.02.092.
[49] Q. Du *et al.*, 'Preparation of functionalized graphene sheets by a low-temperature thermal exfoliation approach and their electrochemical supercapacitive behaviors', *Electrochimica Acta*, vol. 55, no. 12, pp. 3897–3903, Apr. 2010, doi: 10.1016/j.electacta.2010.01.089.
[50] M. D. Stoller, S. Park, Y. Zhu, J. An, and R. S. Ruoff, 'Graphene-Based Ultracapacitors', *Nano Lett.*, vol. 8, no. 10, pp. 3498–3502, Oct. 2008, doi: 10.1021/nl802558y.
[51] Y. Wang *et al.*, 'Supercapacitor Devices Based on Graphene Materials', *J. Phys. Chem. C*, vol. 113, no. 30, pp. 13103–13107, Jul. 2009, doi: 10.1021/jp902214f.
[52] H. Banda, 'Development of graphene-based composite materials for electrochemical storage applications', phdthesis, Université Grenoble Alpes, 2018. Accessed: Jun. 18, 2020. [Online]. Available: https://tel.archives-ouvertes.fr/tel-02003297
[53] M. F. El-Kady, Y. Shao, and R. B. Kaner, 'Graphene for batteries, supercapacitors and beyond', *Nat Rev Mater*, vol. 1, no. 7, p. 16033, Jul. 2016, doi: 10.1038/natrevmats.2016.33.
[54] X. Sun *et al.*, 'Activation of graphene aerogel with phosphoric acid for enhanced electrocapacitive performance', *Carbon*, vol. 92, pp. 1–10, Oct. 2015, doi: 10.1016/j.carbon.2015.02.052.
[55] J. Yan, J. Liu, Z. Fan, T. Wei, and L. Zhang, 'High-performance supercapacitor electrodes based on highly corrugated graphene sheets', *Carbon*, vol. 50, no. 6, pp. 2179–2188, May 2012, doi: 10.1016/j.carbon.2012.01.028.
[56] Y. Xu *et al.*, 'Holey graphene frameworks for highly efficient capacitive energy storage', *Nature Communications*, vol. 5, no. 1, Art. no. 1, Aug. 2014, doi: 10.1038/ncomms5554.
[57] Y. Xu, K. Sheng, C. Li, and G. Shi, 'Self-Assembled Graphene Hydrogel via a One-Step Hydrothermal Process', *ACS Nano*, vol. 4, no. 7, pp. 4324–4330, Jul. 2010, doi: 10.1021/nn101187z.

[58] L. Zhang and G. Shi, 'Preparation of Highly Conductive Graphene Hydrogels for Fabricating Supercapacitors with High Rate Capability', *J. Phys. Chem. C*, vol. 115, no. 34, pp. 17206–17212, Sep. 2011, doi: 10.1021/jp204036a.
[59] H. Banda *et al.*, 'One-step synthesis of highly reduced graphene hydrogels for high power supercapacitor applications', *Journal of Power Sources*, vol. 360, pp. 538–547, Aug. 2017, doi: 10.1016/j.jpowsour.2017.06.033.
[60] P. E. Marina, G. A. M. Ali, L. M. See, E. Y. L. Teo, E.-P. Ng, and K. F. Chong, 'In situ growth of redox-active iron-centered nanoparticles on graphene sheets for specific capacitance enhancement', *Arabian Journal of Chemistry*, vol. 12, no. 8, pp. 3883–3889, Dec. 2019, doi: 10.1016/j.arabjc.2016.02.006.
[61] G. Wang *et al.*, 'Flexible Pillared Graphene-Paper Electrodes for High-Performance Electrochemical Supercapacitors', *Small*, vol. 8, no. 3, pp. 452–459, Feb. 2012, doi: 10.1002/smll.201101719.
[62] Z. Lin, P.-L. Taberna, and P. Simon, 'Graphene-Based Supercapacitors Using Eutectic Ionic Liquid Mixture Electrolyte', *Electrochimica Acta*, vol. 206, pp. 446–451, Jul. 2016, doi: 10.1016/j.electacta.2015.12.097.
[63] Y. Wang *et al.*, 'Preventing Graphene Sheets from Restacking for High-Capacitance Performance', *J. Phys. Chem. C*, vol. 115, no. 46, pp. 23192–23197, Nov. 2011, doi: 10.1021/jp206444e.
[64] G. Mercier *et al.*, 'Porous Graphene Oxide/Diboronic Acid Materials: Structure and Hydrogen Sorption', *J. Phys. Chem. C*, vol. 119, no. 49, pp. 27179–27191, Dec. 2015, doi: 10.1021/acs.jpcc.5b06402.
[65] R. Kumar, V. M. Suresh, T. K. Maji, and C. N. R. Rao, 'Porous graphene frameworks pillared by organic linkers with tunable surface area and gas storage properties', *Chem. Commun.*, vol. 50, no. 16, p. 2015, 2014, doi: 10.1039/c3cc46907g.
[66] Y. Matsuo, S. Ueda, K. Konishi, J. P. Marco-Lozar, D. Lozano-Castelló, and D. Cazorla-Amorós, 'Pillared carbons consisting of silsesquioxane bridged graphene layers for hydrogen storage materials', *International Journal of Hydrogen Energy*, vol. 37, no. 14, pp. 10702–10708, Jul. 2012, doi: 10.1016/j.ijhydene.2012.04.033.
[67] Z. Jin *et al.*, 'Nano-Engineered Spacing in Graphene Sheets for Hydrogen Storage', *Chem. Mater.*, vol. 23, no. 4, pp. 923–925, Feb. 2011, doi: 10.1021/cm1025188.
[68] Y. Cui, Q.-Y. Cheng, H. Wu, Z. Wei, and B.-H. Han, 'Graphene oxide-based benzimidazole-crosslinked networks for high-performance supercapacitors', *Nanoscale*, vol. 5, no. 18, pp. 8367–8374, 2013, doi: 10.1039/C3NR01480K.
[69] J. Lee, C. Kim, J. Y. Cheong, and I.-D. Kim, 'An angstrom-level d-spacing control of graphite oxide using organofillers for high-rate lithium storage', *Chem*, vol. 8, no. 9, pp. 2393–2409, Sep. 2022, doi: 10.1016/j.chempr.2022.05.002.
[70] J. Park *et al.*, 'Reduced Graphene Oxide Aerogels with Functionalization-Mediated Disordered Stacking for Sodium-Ion Batteries', *Batteries*, vol. 8, no. 2, 2022, doi: 10.3390/batteries8020012.
[71] L.-B. Xing *et al.*, 'Three dimensional nitrogen-doped graphene aerogels functionalized with melamine for multifunctional applications in supercapacitors and adsorption', *Journal of Solid State Chemistry*, vol. 230, pp. 224–232, Oct. 2015, doi: 10.1016/j.jssc.2015.07.009.
[72] S. Hu *et al.*, 'Significantly enhanced capacitance deionization performance by coupling activated carbon with triethyltetramine-functionalized graphene', *Chemical Engineering Journal*, vol. 384, p. 123317, Mar. 2020, doi: 10.1016/j.cej.2019.123317.
[73] E. Klontzas, E. Tylianakis, V. Varshney, A. K. Roy, and G. E. Froudakis, 'Organically interconnected graphene flakes: A flexible 3-D material with tunable electronic bandgap', *Sci Rep*, vol. 9, no. 1, p. 13676, Dec. 2019, doi: 10.1038/s41598-019-50037-y.
[74] G. K. Dimitrakakis, E. Tylianakis, and G. E. Froudakis, 'Pillared Graphene: A New 3-D Network Nanostructure for Enhanced Hydrogen Storage', *Nano Lett.*, vol. 8, no. 10, pp. 3166–3170, Oct. 2008, doi: 10.1021/nl801417w.
[75] R. P. Wesołowski and A. P. Terzyk, 'Pillared graphene as a gas separation membrane', *Phys. Chem. Chem. Phys.*, vol. 13, no. 38, p. 17027, 2011, doi: 10.1039/c1cp21590f.

[76] A. Pedrielli, S. Taioli, G. Garberoglio, and N. M. Pugno, 'Gas adsorption and dynamics in Pillared Graphene Frameworks', *Microporous and Mesoporous Materials*, vol. 257, pp. 222–231, Feb. 2018, doi: 10.1016/j.micromeso.2017.08.034.

[77] F. Yousefi, F. Khoeini, and A. Rajabpour, 'Thermal rectification and interfacial thermal resistance in hybrid pillared-graphene and graphene: a molecular dynamics and continuum approach', *Nanotechnology*, vol. 31, no. 28, p. 285707, Apr. 2020, doi: 10.1088/1361-6528/ab8420.

[78] R. Shahsavari and N. Sakhavand, 'Junction configuration-induced mechanisms govern elastic and inelastic deformations in hybrid carbon nanomaterials', *Carbon*, vol. 95, pp. 699–709, Dec. 2015, doi: 10.1016/j.carbon.2015.08.106.

[79] J. Park and V. Prakash, 'Thermal transport in 3D pillared SWCNT–graphene nanostructures', *J. Mater. Res.*, vol. 28, no. 7, pp. 940–951, Apr. 2013, doi: 10.1557/jmr.2012.395.

[80] A. Hassani, M. T. Hamed Mosavian, A. Ahmadpour, and N. Farhadian, 'Hybrid molecular simulation of methane storage inside pillared graphene', *The Journal of Chemical Physics*, vol. 142, no. 23, p. 234704, Jun. 2015, doi: 10.1063/1.4922541.

[81] G. Garberoglio, N. M. Pugno, and S. Taioli, 'Gas Adsorption and Separation in Realistic and Idealized Frameworks of Organic Pillared Graphene: A Comparative Study', *J. Phys. Chem. C*, vol. 119, no. 4, pp. 1980–1987, Jan. 2015, doi: 10.1021/jp511953p.

[82] S. J. Mahdizadeh, E. K. Goharshadi, and G. Akhlamadi, 'Seawater desalination using pillared graphene as a novel nano-membrane in reverse osmosis process: nonequilibrium MD simulation study', *Phys. Chem. Chem. Phys.*, vol. 20, no. 34, pp. 22241–22248, 2018, doi: 10.1039/C8CP02820F.

[83] F. Shayeganfar and R. Shahsavari, 'Oxygen- and Lithium-Doped Hybrid Boron-Nitride/Carbon Networks for Hydrogen Storage', *Langmuir*, vol. 32, no. 50, pp. 13313–13321, Dec. 2016, doi: 10.1021/acs.langmuir.6b02997.

[84] K. Duan, L. Li, Y. Hu, and X. Wang, 'Pillared graphene as an ultra-high sensitivity mass sensor', *Sci Rep*, vol. 7, no. 1, p. 14012, Dec. 2017, doi: 10.1038/s41598-017-14182-6.

[85] I. Skarmoutsos, E. N. Koukaras, C. Galiotis, G. E. Froudakis, and E. Klontzas, 'Porous carbon nanotube networks and pillared graphene materials exhibiting high SF6 adsorption uptake and separation selectivity of SF6/N2 fluid mixtures: A comparative molecular simulation study', *Microporous and Mesoporous Materials*, vol. 307, p. 110464, Nov. 2020, doi: 10.1016/j.micromeso.2020.110464.

[86] L. Bi, J. Yin, X. Huang, Y. Wang, and Z. Yang, 'Graphene pillared with hybrid fullerene and nanotube as a novel 3D framework for hydrogen storage: A DFT and GCMC study', *International Journal of Hydrogen Energy*, vol. 45, no. 35, pp. 17637–17648, Jul. 2020, doi: 10.1016/j.ijhydene.2020.04.227.

[87] H. Mert, C. U. Deniz, and C. Baykasoglu, 'Monte Carlo simulations of hydrogen adsorption in fullerene pillared graphene nanocomposites', *Molecular Simulation*, vol. 46, no. 8, pp. 650–659, May 2020, doi: 10.1080/08927022.2020.1758696.

[88] A. Sharma, R. Babarao, N. V. Medhekar, and A. Malani, 'Computational design of multilayer frameworks to achieve DOE target for on-board methane delivery', *Carbon*, vol. 152, pp. 206–217, Nov. 2019, doi: 10.1016/j.carbon.2019.05.083.

[89] H. Jiang and X.-L. Cheng, 'MD simulation of methane adsorption properties on pillared graphene bubble models', *J Mol Model*, vol. 25, no. 8, p. 236, Jul. 2019, doi: 10.1007/s00894-019-4132-2.

[90] M. M. Slepchenkov, D. S. Shmygin, G. Zhang, and O. E. Glukhova, 'Controlling the electronic properties of 2D/3D pillared graphene and glass-like carbon via metal atom doping', *Nanoscale*, vol. 11, no. 35, pp. 16414–16427, Sep. 2019, doi: 10.1039/C9NR05185F.

[91] Y. Matsuo, Y. Tachibana, and K. Konishi, 'Preparation of pillared carbon thin films and their size selective electrical response to organic vapor', *Carbon*, vol. 50, no. 14, pp. 5346–5348, Nov. 2012, doi: 10.1016/j.carbon.2012.07.013.

[92] R. Watanabe, R. Matsuzaki, H. Endo, and J. Koyanagi, 'Stretchable and insulating characteristics of chemically bonded graphene and carbon nanotube composite materials', *J Mater Sci*, vol. 53, no. 2, pp. 1148–1156, Jan. 2018, doi: 10.1007/s10853-017-1563-y.

[93] P. Bandyopadhyay, T. T. Nguyen, X. Li, N. H. Kim, and J. H. Lee, 'Enhanced hydrogen gas barrier performance of diaminoalkane functionalized stitched graphene oxide/polyurethane composites', *Composites Part B: Engineering*, vol. 117, pp. 101–110, May 2017, doi: 10.1016/j.compositesb.2017.02.035.

[94] A. Nordenström, A. Iakunkov, J. Sun, and A. V. Talyzin, 'Thermally reduced pillared GO with precisely defined slit pore size', *RSC Adv.*, vol. 10, no. 12, pp. 6831–6839, 2020, doi: 10.1039/D0RA00067A.

[95] Y. Matsuo and K. Konishi, 'Size-dependent inclusion of organic molecules into elastic pillared carbons', *Chem. Commun.*, vol. 47, no. 15, p. 4409, 2011, doi: 10.1039/c0cc05552b.

[96] N. H. Kim, T. Kuila, and J. H. Lee, 'Simultaneous reduction, functionalization and stitching of graphene oxide with ethylenediamine for composites application', *J. Mater. Chem. A*, vol. 1, no. 4, pp. 1349–1358, 2013, doi: 10.1039/C2TA00853J.

[97] K. Yuan *et al.*, 'Straightforward Generation of Pillared, Microporous Graphene Frameworks for Use in Supercapacitors', *Adv. Mater.*, vol. 27, no. 42, pp. 6714–6721, Nov. 2015, doi: 10.1002/adma.201503390.

[98] K. Lee *et al.*, 'Tunable Sub-nanopores of Graphene Flake Interlayers with Conductive Molecular Linkers for Supercapacitors', *ACS Nano*, vol. 10, no. 7, pp. 6799–6807, Jul. 2016, doi: 10.1021/acsnano.6b02415.

[99] Y. Qin *et al.*, 'Anthraquinone-functionalized graphene framework for supercapacitors and lithium batteries', *Ceramics International*, vol. 46, no. 10, pp. 15379–15384, Jul. 2020, doi: 10.1016/j.ceramint.2020.03.082.

[100] Y. Xie *et al.*, 'Graphene covalently functionalized by cross-linking reaction of bifunctional pillar organic molecule for high capacitance', *Journal of Energy Storage*, vol. 38, p. 102530, Jun. 2021, doi: 10.1016/j.est.2021.102530.

[101] V. H. Luan *et al.*, 'Synthesis of a highly conductive and large surface area graphene oxide hydrogel and its use in a supercapacitor', *J. Mater. Chem. A*, vol. 1, no. 2, pp. 208–211, 2013, doi: 10.1039/C2TA00444E.

[102] B. Song *et al.*, 'Systematic study on structural and electronic properties of diamine/triamine functionalized graphene networks for supercapacitor application', *Nano Energy*, vol. 31, pp. 183–193, Jan. 2017, doi: 10.1016/j.nanoen.2016.10.057.

[103] H. Banda *et al.*, 'Sparsely Pillared Graphene Materials for High-Performance Supercapacitors: Improving Ion Transport and Storage Capacity', *ACS Nano*, vol. 13, no. 2, pp. 1443–1453, Feb. 2019, doi: 10.1021/acsnano.8b07102.

[104] H. Banda *et al.*, 'Investigation of ion transport in chemically tuned pillared graphene materials through electrochemical impedance analysis', *Electrochimica Acta*, vol. 296, pp. 882–890, Feb. 2019, doi: 10.1016/j.electacta.2018.11.122.

[105] M. Mazloum-Ardakani, F. Sabaghian, H. Naderi, A. Ebadi, and H. Mohammadian-Sarcheshmeh, 'Electrochemical and theoretical study of novel functional porous graphene aerogel-supported Sm2O3 nanoparticles for supercapacitor applications', *J Solid State Electrochem*, vol. 24, no. 3, pp. 571–582, Mar. 2020, doi: 10.1007/s10008-019-04457-5.

[106] F.-G. Zhao *et al.*, '*In situ* tunable pillaring of compact and high-density graphite fluoride with pseudocapacitive diamines for supercapacitors with combined predominance in gravimetric and volumetric performances', *J. Mater. Chem. A*, vol. 7, no. 7, pp. 3353–3365, 2019, doi: 10.1039/C8TA09782H.

[107] Y. Matsuo, T. Kino, J. Inamoto, O. Kimizuka, M. Nishijima, and H. Kinoshita, 'Electrochemical Properties of Pillared Carbons for the Electrode of Electric Double Layer Capacitor', *Electrochemistry*, vol. 88, no. 2, pp. 53–56, Mar. 2020, doi: 10.5796/electrochemistry.19-63085.

[108] G. Pognon, C. Cougnon, D. Mayilukila, and D. Bélanger, 'Catechol-Modified Activated Carbon Prepared by the Diazonium Chemistry for Application as Active Electrode Material in Electrochemical Capacitor', *ACS Appl. Mater. Interfaces*, vol. 4, no. 8, pp. 3788–3796, Aug. 2012, doi: 10.1021/am301284n.

[109] Cambridge Online English Dictionary, 'Pillar'. Accessed: Jul. 17, 2023. [Online]. Available: https://dictionary.cambridge.org/dictionary/english/pillar

[110] Merriam-Webster Online Dictionary, 'Pillar'. Accessed: Jul. 17, 2023. [Online]. Available: https://www.merriam-webster.com/dictionary/pillar

[111] E. Lebègue, L. Madec, T. Brousse, J. Gaubicher, E. Levillain, and C. Cougnon, 'Modification of activated carbons based on diazonium ions in situ produced from aminobenzene organic acid without addition of other acid', *Journal of Materials Chemistry*, vol. 21, no. 33, pp. 12221–12223, 2011, doi: 10.1039/C1JM11538C.

[112] P. Huang, L. Jing, H. Zhu, and X. Gao, 'Diazonium Functionalized Graphene: Microstructure, Electric, and Magnetic Properties', *Acc. Chem. Res.*, vol. 46, no. 1, pp. 43–52, Jan. 2013, doi: 10.1021/ar300070a.

[113] M. Joselevich and F. J. Williams, 'Synthesis and Characterization of Diazonium Functionalized Nanoparticles for Deposition on Metal Surfaces', *Langmuir*, vol. 24, no. 20, pp. 11711–11717, Oct. 2008, doi: 10.1021/la802247k.

[114] G. Liu, J. Liu, T. P. Davis, and J. J. Gooding, 'Electrochemical impedance immunosensor based on gold nanoparticles and aryl diazonium salt functionalized gold electrodes for the detection of antibody', *Biosensors and Bioelectronics*, vol. 26, no. 8, pp. 3660–3665, Apr. 2011, doi: 10.1016/j.bios.2011.02.026.

[115] G. L. C. Paulus, Q. H. Wang, and M. S. Strano, 'Covalent Electron Transfer Chemistry of Graphene with Diazonium Salts', *Acc. Chem. Res.*, vol. 46, no. 1, pp. 160–170, Jan. 2013, doi: 10.1021/ar300119z.

[116] D. R. Parkinson, 'Analytical Derivatization Techniques☆', in *Reference Module in Chemistry, Molecular Sciences and Chemical Engineering*, Elsevier, 2014. doi: 10.1016/B978-0-12-409547-2.11454-4.

[117] W.-S. Hung *et al.*, 'Cross-Linking with Diamine Monomers To Prepare Composite Graphene Oxide-Framework Membranes with Varying d-Spacing', *Chem. Mater.*, vol. 26, no. 9, pp. 2983–2990, May 2014, doi: 10.1021/cm5007873.

[118] B. Song *et al.*, 'Molecular Level Study of Graphene Networks Functionalized with Phenylenediamine Monomers for Supercapacitor Electrodes', *Chem. Mater.*, vol. 28, no. 24, pp. 9110–9121, Dec. 2016, doi: 10.1021/acs.chemmater.6b04214.

[119] X. Lu *et al.*, 'Mechanistic investigation of the graphene functionalization using p-phenylenediamine and its application for supercapacitors', *Nano Energy*, vol. 17, pp. 160–170, Oct. 2015, doi: 10.1016/j.nanoen.2015.08.011.

[120] H. Gholipour-Ranjbar, M. R. Ganjali, P. Norouzi, and H. R. Naderi, 'Electrochemical investigation of functionalized graphene aerogel with different amount of p-phenylenediamine as an advanced electrode material for supercapacitors', *Mater. Res. Express*, vol. 3, no. 7, p. 075501, Jul. 2016, doi: 10.1088/2053-1591/3/7/075501.

[121] P. Du, Y. Dong, H. Kang, Q. Wang, and J. Niu, 'Synthesis of holey graphene networks functionalized with p-phenylene diamine monomers for superior performance flexible solid-state supercapacitors', *Electrochimica Acta*, vol. 320, p. 134610, Oct. 2019, doi: 10.1016/j.electacta.2019.134610.

[122] A. Mondal and N. R. Jana, 'Graphene-Nanoparticle Composites and Their Applications in Energy, Environmental and Biomedical Science', *Reviews in Nanoscience and Nanotechnology*, vol. 3, no. 3, pp. 177–192, Sep. 2014, doi: 10.1166/rnn.2014.1051.

[123] H. Gholipour-Ranjbar, M. R. Ganjali, P. Norouzi, and H. R. Naderi, 'Synthesis of cross-linked graphene aerogel/Fe2O3 nanocomposite with enhanced supercapacitive performance', *Ceramics International*, vol. 42, no. 10, pp. 12097–12104, Aug. 2016, doi: 10.1016/j.ceramint.2016.04.140.

[124] 'ICSC 0281 - HYDRAZINE'. Accessed: Jul. 27, 2023. [Online]. Available: https://www.ilo.org/dyn/icsc/showcard.display?p_card_id=0281&p_version=2&p_lang=en

[125] K. K. H. De Silva, H.-H. Huang, R. K. Joshi, and M. Yoshimura, 'Chemical reduction of graphene oxide using green reductants', *Carbon*, vol. 119, pp. 190–199, Aug. 2017, doi: 10.1016/j.carbon.2017.04.025.

[126] M.-L. Liao and P. A. Seib, 'Chemistry of L-ascorbic acid related to foods', *Food Chemistry*, vol. 30, no. 4, pp. 289–312, Jan. 1988, doi: 10.1016/0308-8146(88)90115-X.

[127] J. Gao, F. Liu, Y. Liu, N. Ma, Z. Wang, and X. Zhang, 'Environment-Friendly Method To Produce Graphene That Employs Vitamin C and Amino Acid', *Chem. Mater.*, vol. 22, no. 7, pp. 2213–2218, Apr. 2010, doi: 10.1021/cm902635j.

[128] D. He, L. Shen, X. Zhang, Y. Wang, N. Bao, and H. H. Kung, 'An efficient and eco-friendly solution-chemical route for preparation of ultrastable reduced graphene oxide suspensions', *AIChE Journal*, vol. 60, no. 8, pp. 2757–2764, 2014, doi: 10.1002/aic.14499.

[129] J. Zhang, H. Yang, G. Shen, P. Cheng, J. Zhang, and S. Guo, 'Reduction of graphene oxide viaL-ascorbic acid', *Chem. Commun.*, vol. 46, no. 7, pp. 1112–1114, Feb. 2010, doi: 10.1039/B917705A.

[130] H. Su *et al.*, 'Facile synthesis of water soluble reduced graphene oxide with a high concentration and its application in printable micro-supercapacitors', *Sustainable Energy Fuels*, vol. 1, no. 7, pp. 1601–1610, Aug. 2017, doi: 10.1039/C7SE00214A.

[131] Z. Sui, X. Zhang, Y. Lei, and Y. Luo, 'Easy and green synthesis of reduced graphite oxide-based hydrogels', *Carbon*, vol. 49, no. 13, pp. 4314–4321, Nov. 2011, doi: 10.1016/j.carbon.2011.06.006.

[132] M. Serrapede *et al.*, 'A Facile and Green Synthesis of a MoO2-Reduced Graphene Oxide Aerogel for Energy Storage Devices', *Materials*, vol. 13, no. 3, Art. no. 3, Jan. 2020, doi: 10.3390/ma13030594.

[133] S. P. Lee, G. A. M. Ali, H. H. Hegazy, H. N. Lim, and K. F. Chong, 'Optimizing Reduced Graphene Oxide Aerogel for a Supercapacitor', *Energy Fuels*, vol. 35, no. 5, pp. 4559–4569, Mar. 2021, doi: 10.1021/acs.energyfuels.0c04126.

[134] L. Qiu, J. Z. Liu, S. L. Y. Chang, Y. Wu, and D. Li, 'Biomimetic superelastic graphene-based cellular monoliths', *Nat Commun*, vol. 3, no. 1, Art. no. 1, Dec. 2012, doi: 10.1038/ncomms2251.

[135] H. Yang, T. Zhang, M. Jiang, Y. Duan, and J. Zhang, 'Ambient pressure dried graphene aerogels with superelasticity and multifunctionality', *J. Mater. Chem. A*, vol. 3, no. 38, pp. 19268–19272, Sep. 2015, doi: 10.1039/C5TA06452J.

[136] A. Pruna, D. Pullini, and D. Busquets, 'Influence of synthesis conditions on properties of green-reduced graphene oxide', *J Nanopart Res*, vol. 15, no. 5, p. 1605, Apr. 2013, doi: 10.1007/s11051-013-1605-6.

[137] M. J. Fernández-Merino *et al.*, 'Vitamin C Is an Ideal Substitute for Hydrazine in the Reduction of Graphene Oxide Suspensions', *J. Phys. Chem. C*, vol. 114, no. 14, pp. 6426–6432, Apr. 2010, doi: 10.1021/jp100603h.

[138] K. K. H. De Silva, H.-H. Huang, and M. Yoshimura, 'Progress of reduction of graphene oxide by ascorbic acid', *Applied Surface Science*, vol. 447, pp. 338–346, Jul. 2018, doi: 10.1016/j.apsusc.2018.03.243.

[139] C. Xu, X. Shi, A. Ji, L. Shi, C. Zhou, and Y. Cui, 'Fabrication and Characteristics of Reduced Graphene Oxide Produced with Different Green Reductants', *PLOS ONE*, vol. 10, no. 12, p. e0144842, Dec. 2015, doi: 10.1371/journal.pone.0144842.

[140] A. Abulizi, K. Okitsu, and J.-J. Zhu, 'Ultrasound assisted reduction of graphene oxide to graphene in l-ascorbic acid aqueous solutions: Kinetics and effects of various factors on the rate of graphene formation', *Ultrasonics Sonochemistry*, vol. 21, no. 3, pp. 1174–1181, May 2014, doi: 10.1016/j.ultsonch.2013.10.019.

[141] V. Dua *et al.*, 'All-Organic Vapor Sensor Using Inkjet-Printed Reduced Graphene Oxide', *Angewandte Chemie International Edition*, vol. 49, no. 12, pp. 2154–2157, 2010, doi: 10.1002/anie.200905089.

[142] M. P. Lavin-Lopez, A. Paton-Carrero, L. Sanchez-Silva, J. L. Valverde, and A. Romero, 'Influence of the reduction strategy in the synthesis of reduced graphene oxide', *Advanced Powder Technology*, vol. 28, no. 12, pp. 3195–3203, Dec. 2017, doi: 10.1016/j.apt.2017.09.032.

[143] M. P. Lavin-Lopez, J. L. Valverde, A. de Lucas-Consuegra, A. B. Calcerrada, A. Paton-Carrero, and A. Romero, 'Influence of the synthesis method on electrical storage capacity of graphene-related materials', *Materials Science and Technology*, vol. 35, no. 3, pp. 361–367, Feb. 2019, doi: 10.1080/02670836.2018.1560106.

[144] X. Zhu, Q. Liu, X. Zhu, C. Li, M. Xu, and Y. Liang, 'Reduction of Graphene Oxide Via Ascorbic Acid and Its Application for Simultaneous Detection of Dopamine And Ascorbic Acid', *International Journal of Electrochemical Science*, vol. 7, no. 6, pp. 5172–5184, Jan. 2012, doi: 10.1016/S1452-3981(23)19612-X.

[145] I. O. Faniyi *et al.*, 'The comparative analyses of reduced graphene oxide (RGO) prepared via green, mild and chemical approaches', *SN Appl. Sci.*, vol. 1, no. 10, p. 1181, Sep. 2019, doi: 10.1007/s42452-019-1188-7.

[146] J. I. Paredes, S. Villar-Rodil, A. Martínez-Alonso, and J. M. D. Tascón, 'Graphene Oxide Dispersions in Organic Solvents', *Langmuir*, vol. 24, no. 19, pp. 10560–10564, Oct. 2008, doi: 10.1021/la801744a.

[147] S. M. Tan, A. Ambrosi, C. K. Chua, and M. Pumera, 'Electron transfer properties of chemically reduced graphene materials with different oxygen contents', *J. Mater. Chem. A*, vol. 2, no. 27, pp. 10668–10675, Jun. 2014, doi: 10.1039/C4TA01034E.

[148] J. Indujalekshmi, P. Krishnan, R. V. Reji, and V. Biju, 'L-ascorbic acid-reduced graphite oxide as active material for supercapacitors', *Materials Today: Proceedings*, Feb. 2023, doi: 10.1016/j.matpr.2023.02.159.

[149] T. Ha, S. K. Kim, J.-W. Choi, H. Chang, and H. D. Jang, 'pH controlled synthesis of porous graphene sphere and application to supercapacitors', *Advanced Powder Technology*, vol. 30, no. 1, pp. 18–22, Jan. 2019, doi: 10.1016/j.apt.2018.10.002.

[150] W. Chartarrayawadee *et al.*, 'Facile synthesis of reduced graphene oxide/MWNTs nanocomposite supercapacitor materials tested as electrophoretically deposited films on glassy carbon electrodes', *J Appl Electrochem*, vol. 43, no. 9, pp. 865–877, Sep. 2013, doi: 10.1007/s10800-013-0575-9.

[151] Z. Stempien *et al.*, 'In-situ deposition of reduced graphene oxide layers on textile surfaces by the reactive inkjet printing technique and their use in supercapacitor applications', *Synthetic Metals*, vol. 256, p. 116144, Oct. 2019, doi: 10.1016/j.synthmet.2019.116144.

[152] M. A. Velasco-Soto, S. A. Pérez-García, J. Alvarez-Quintana, Y. Cao, L. Nyborg, and L. Licea-Jiménez, 'Selective band gap manipulation of graphene oxide by its reduction with mild reagents', *Carbon*, vol. 93, pp. 967–973, Nov. 2015, doi: 10.1016/j.carbon.2015.06.013.

[153] S. Eigler, S. Grimm, M. Enzelberger-Heim, P. Müller, and A. Hirsch, 'Graphene oxide: efficiency of reducing agents', *Chem. Commun.*, vol. 49, no. 67, pp. 7391–7393, Jul. 2013, doi: 10.1039/C3CC43612H.

[154] S. Abdolhosseinzadeh, H. Asgharzadeh, and H. Seop Kim, 'Fast and fully-scalable synthesis of reduced graphene oxide', *Sci Rep*, vol. 5, no. 1, Art. no. 1, May 2015, doi: 10.1038/srep10160.

[155] M. Fathy, A. Gomaa, F. A. Taher, M. M. El-Fass, and A. E.-H. B. Kashyout, 'Optimizing the preparation parameters of GO and rGO for large-scale production', *J Mater Sci*, vol. 51, no. 12, pp. 5664–5675, Jun. 2016, doi: 10.1007/s10853-016-9869-8.

[156] J. Li, J. Li, L. Li, M. Yu, H. Ma, and B. Zhang, 'Flexible graphene fibers prepared by chemical reduction-induced self-assembly', *J. Mater. Chem. A*, vol. 2, no. 18, pp. 6359–6362, Apr. 2014, doi: 10.1039/C4TA00431K.

[157] H. Ding *et al.*, 'Reduction of graphene oxide at room temperature with vitamin C for RGO–TiO2 photoanodes in dye-sensitized solar cell', *Thin Solid Films*, vol. 584, pp. 29–36, Jun. 2015, doi: 10.1016/j.tsf.2015.02.038.

[158] Y. Liu, S. Luo, S. Yan, J. Feng, and T. Yi, 'Green synthesis of reduced graphene oxide as high-performance electrode materials for supercapacitors', *Ionics*, vol. 26, no. 1, pp. 415–422, Jan. 2020, doi: 10.1007/s11581-019-03185-0.

[159] A. Pruna, D. Pullini, and D. Busquets, 'Green-Reduction of Covalently Functionalized Graphene Oxide with Varying Stoichiometry', *International Journal of Materials and Metallurgical Engineering*, vol. 7, no. 11, pp. 789–792, Oct. 2013.

A Fundamental Study on Pillared Graphene Materials for Supercapacitors

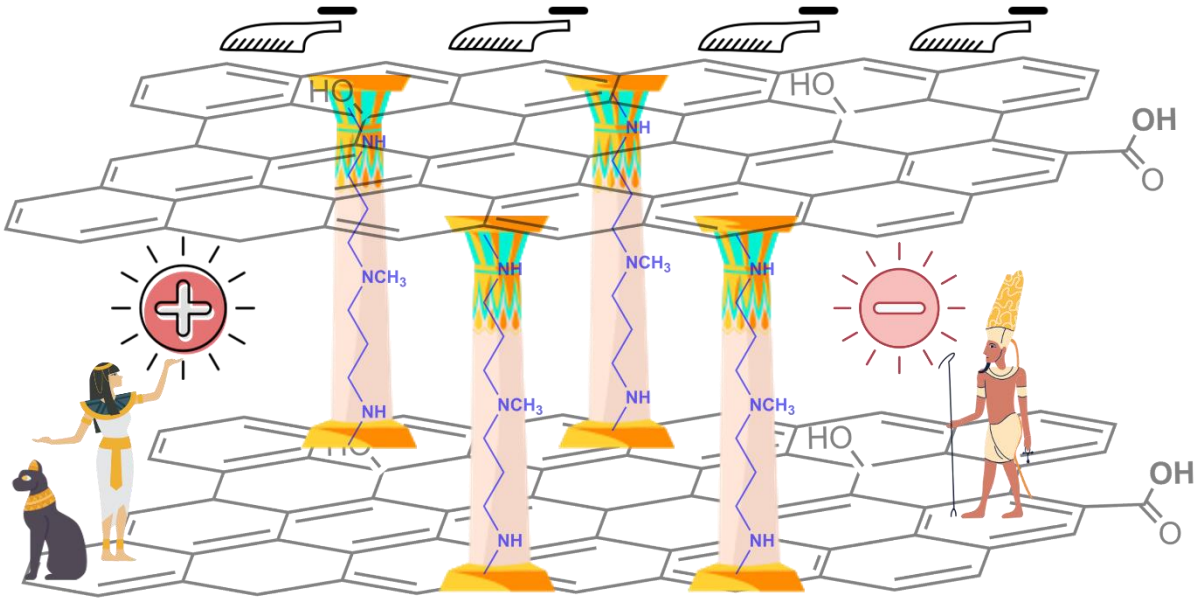

Chapter 2: A Fundamental Study on Pillared Graphene Materials for Supercapacitors

II.1 Opening

As highlighted earlier in the introduction chapter, fundamental studies on PGM are required to enable better material design and better targeting the required properties. Accordingly, herein, a fundamental study was carried out to study the effect of the chemistry and the structure of theses assemblies on their performance as electrode materials for Supercapacitors. The effect of chemistry includes the effect of the surface/pillar chemistry of the graphene sheets in these assemblies, notably the remaining oxygen functionalities on the graphene sheets and their different types. The chemistry also includes the different chemistry of the pillars arising from the presence of different heteroatoms in the carbon-based pillars, such as oxygen and nitrogen. Regarding the effect of the structure, the unique structural feature of such assemblies is the controllable creation of new microporous galleries that can be characterized by their height (the newly created inter-sheet distance). Accordingly, the effects of such structural and chemical parameters on the electrochemical performance were studied. A comparison of the performance of such PGM to that of non-pillared restacked rGO was carried out to further ascertain the viability of the pillaring technique in enhancing the performance of supercapacitors. In addition, the ion-pore size matching was triggered through combining samples with different d-spacing values along with cations and anions of different sizes to study the ion-sieving effect in aqueous media and the importance of the ions' solvation shells.

To begin with, various pillars were selected for the study, tested and then short-listed to three pillars (Figure II.1) with different chemistry and structural features. The short list was based on the success of the pillaring. For instance, short pillars with 5 or less carbon atoms between the terminal amines did not show the pillaring effect which suggests that they might be too short for bridging 2 GO sheets. The first pillar (Figure II.1(a)), 1,6-diaminohexane, is an amine linker with only 6 methylene groups between the terminal amines. The second one (Figure II.1(b)), 3,3′-Diamino-N-methyldipropylamine, is the same as the first one with an extra tertiary amine in the center of the pillar (>N-CH_3). The third one (Figure II.1(c)), 2,2'-(ethylenedioxy)bis(ethylamine), is the same as the first one but with extra two alkyl ethers (2x -O-). So these pillars possess the same number of carbon atoms (not including the carbon atom of the NCH_3 group of the 2nd pillar), but differ chemically from one another by the additional heteroatom(s) present in the 2nd and 3rd pillars.

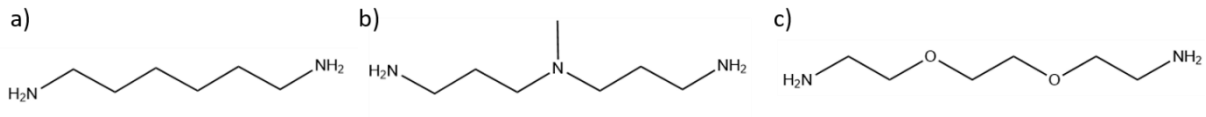

Figure II. 1 : Different Pillars identified for the study, precisely a) 1,6-diaminohexane ,b) 3,3'-Diamino-N-methyldipropylamine and c) 2,2'-(ethylenedioxy)bis(ethylamine)

The stretched lengths of those pillars are consequently different because they have different number of backbone atoms between the terminal amine anchoring functions. However, a direct correlation between their stretched lengths and the corresponding inter-sheet distance when they are employed in PGM is very difficult to draw, as they do not necessarily follow a linear proportional relationship. This is even more obvious when the pillars have heteroatoms with different bonding angles, as what will be shown in the upcoming sections. In addition, these pillars were added to graphene oxide to obtain the final PGM following a chemical synthesis method that will be presented in the upcoming section. Moreover, diverse characterization techniques were carried out including X-Ray Diffraction (XRD), Thermal Gravimetric Analysis (TGA), X-ray Photoelectron Spectroscopy (XPS), Raman spectroscopy, Fourrier-Transform InfraRed spectroscopy (FT-IR), Scanning Electron Microscopy (SEM), Transmission Electron Microscopy (TEM), Solid State NMR (ssNMR), Water Contact Angle (WCA) and 4-point probe electrical conductivity measurements. Then, electrochemical analysis was performed by Cyclic Voltammetry (CV), Galvanostatic Charging and Discharging (GCD), and Electrochemical Impedance Spectroscopy (EIS). Finally, the electrochemical data were treated in order to find correlation between chemical and structural properties, and electrochemical performances.

II.2 Synthesis

II.2.1 Synthesis of Graphene Oxide (GO)

First of all, GO was synthesized as the starting material using a modified Hummer's method [1] (Figure II.2). Sulfuric acid (H_2SO_4) and sodium nitrate ($NaNO_3$) were used as intercalating agents for graphite to space out the graphene sheets and allow a better penetration of the oxidizing agent (potassium permanganate ($KMnO_4$)). The latter was used to react with the inter-graphite intercalated acids to produce different strong oxidizing agents to oxidize graphite into graphite oxide. Hydrogen peroxide (H_2O_2) was added to quench the oxidation by converting the Mn-based oxidizing species into soluble Mn(II) ions. Hydrochloric acid (HCl) was then used to remove the remaining Na and Mn ions. The sample was then exfoliated through sonication to produce a GO water dispersion, then a final step of GO size selection was carried out by centrifugation before adjusting the concentration of the dispersion to 5 mg/ml.

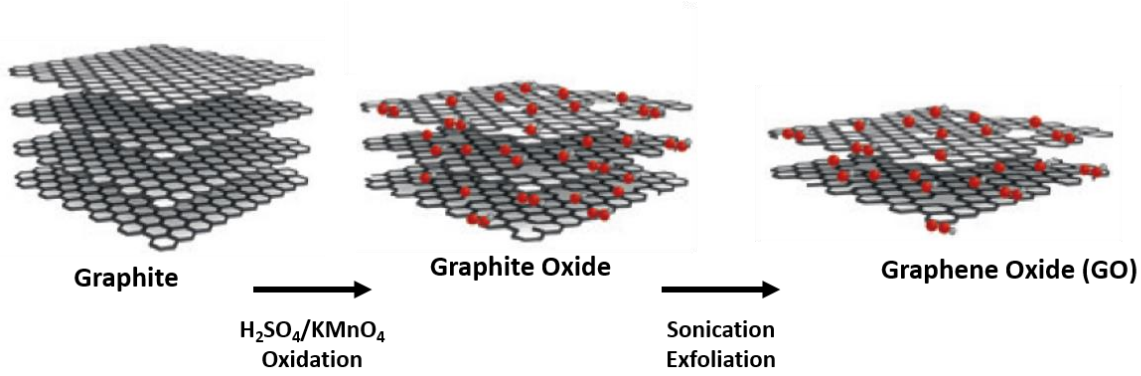

Figure II. 2: Oxidation and Exfoliation of Graphite to produce GO

II.2.2 Synthesis of reduced Graphene Oxide (rGO)

Reduced Graphene Oxide (rGO) was selected as a non-pillared reference sample. The reduction was done to remove as many as possible oxygen functionalities of GO to restore the sp^2 carbon network, thereby restoring the sample's electrical conductivity. This step was carried out through the reduction of GO using Hydrazine (Hz) in an open-air chemical synthesis at 95°C according to the reaction scheme shown in Figure (II.3).

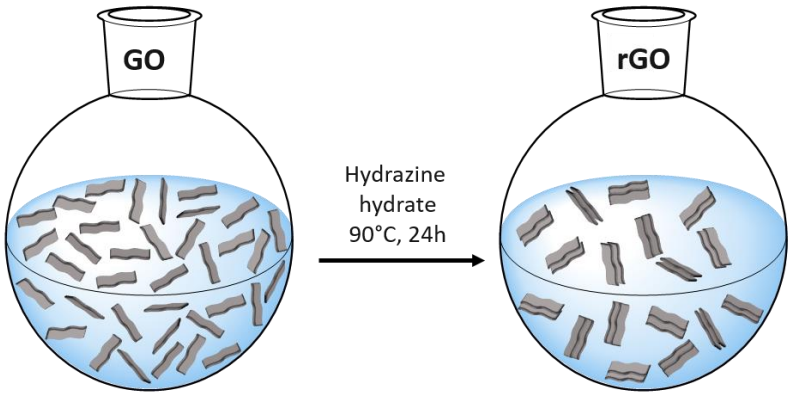

Figure II. 3 : Synthesis of reduced Graphene Oxide (rGO)

As mentioned in the previous chapter, Hz is the best-known reducing agent for GO. Despite the few mechanisms that are proposed in the literature for the reaction of Hz with the different oxygen functionalities, the reaction's pathway still remains unclear [2]. It is accepted that the reduction of GO using Hz leads to the insertion of different nitrogen groups in the rGO sheets [3] as well as some structural defects such as vacancies [4].

II.2.3 Synthesis of Pillared Samples (RPs)

The preparation method utilized herein is the chemical synthesis method relying on the chemical reaction between various oxygen functionalities on the Graphene Oxide (GO) and the amine terminated organic linkers as explained in Chapter 1. These amine-based linkers undergo nucleophilic substitution reactions with various oxygen functionalities on GO, leading to

epoxide ring opening as well as amide bond formation. Such methodology was selected for its applicability to the exfoliated non-stacked GO, its simplicity (one step reaction with no prior modifications or activations), its versatility (aliphatic and aromatic pillars can be used, if needed), and its validity in our research group as previous work was done using such technique [5]–[8]. Another advantage of such a methodology is that it requires no prior modifications on the GO because it can be used directly in its water-dispersed form with no need to dry it and re-disperse it in other solvents, risking its partial aggregation and inefficient dispersibility. The synthetic route is similar to that of rGO with an extra functionalization step prior to the reduction (Figure II.4). In such step, the amines were mixed with GO at 80°C to allow their reaction with the different oxygen functionalities on GO such as epoxide groups and phenolic groups on the basal plane and carboxylic groups on the edges of the GO sheets. The reduction was then carried out using Hz.

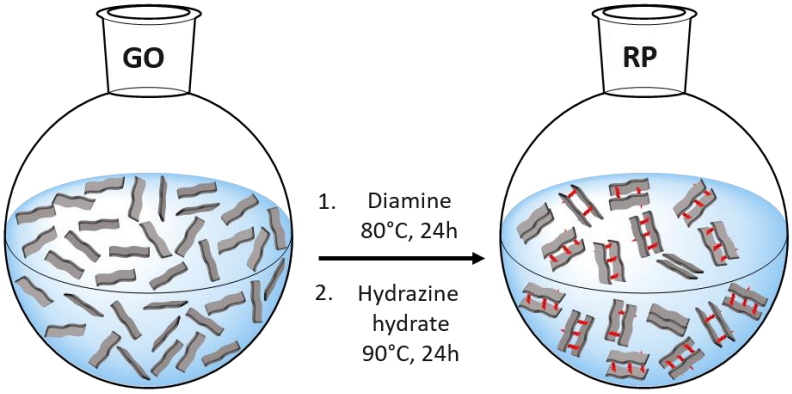

Figure II. 4: Synthesis of Pillared Graphene Materials (PGM)

The PGM were labeled as RP, where R is for reduced and P is for pillared, indicating that the samples were pillared (step 1) and reduced (step 2). To differentiate the PGM pillared using different linkers, an extra number is added at the beginning of the label to identify the number of inter-amine backbone atoms. In the case of a pillar with six methylene groups between the terminal amines, the material is referred to as 6RP. In case of hetero backbone groups (rather than the methylene groups), the groups are to be mentioned in the nomenclature, hence, the material containing the 3,3′-Diamino-N-methyldipropylamine pillar, having 6 methylene groups and 1 additional NCH_3 (Figure II.1(c)) is labelled 7RP-NCH3. Accordingly, the samples synthesized, with the three selected pillars mentioned earlier, are labeled as shown in Figure (II.5).

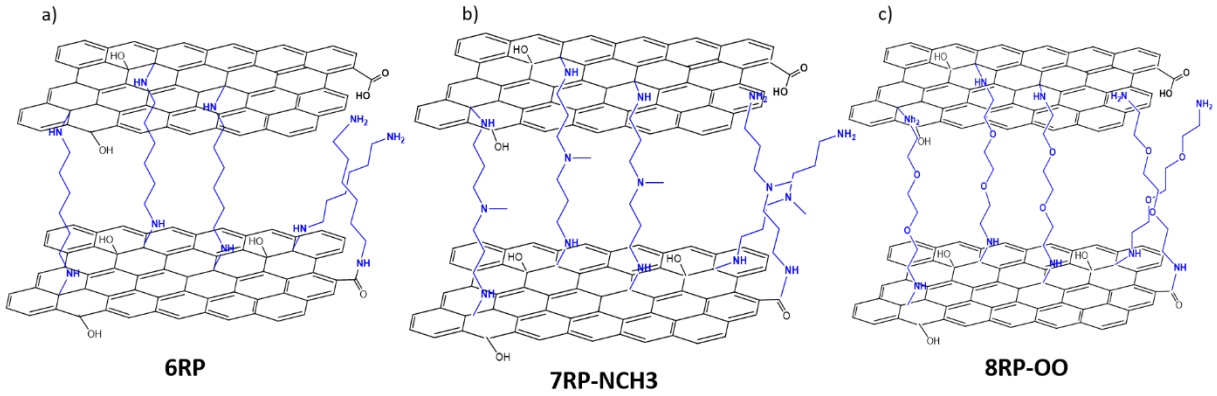

Figure II. 5: The Pillared Graphene Materials Synthesized for the study along with their respective sample codes, namely a) 6RP, b) 7RP-NCH3 and c) 8RP-OO corresponding to the pillars depicted in Figure II.1

II.3 Characterizing the synthesized samples

The samples were then characterized by a variety of characterization techniques to investigate their physico-chemical properties to be later correlated to their electrochemical performance. Precisely, the characterization is carried out on the different samples synthesized to i) verify the success of their reactions: oxidation, reduction and/or pillaring, ii) monitor the extent of their reduction, iii) check their chemical composition and bonding nature, iv) extract various structural and chemical parameters and v) assess their viability for electrochemical analysis.

II.3.1 Chemical Analysis

The samples were first analyzed chemically to verify the success of the oxidation of graphite into GO, the success of the reduction of GO into rGO and the success of grafting various grafting molecules onto GO prior to its reduction to form PGM. For carrying out such analysis, various characterization techniques were selected such as solid state NMR (ssNMR) for the nonconductive GO sample and X-Ray Photoelectron Spectroscopy (XPS), Elemental Analysis (EA), Thermal Gravimetric Analysis (TGA) and Fourier-Transform Infrared Spectroscopy (FT-IR) for all the samples.

XPS, a surface characterization technique, provides an elemental analysis of the surface composition, as well as bonding scheme information for each element. It was utilized to examine the chemical composition of the samples through identifying their different elements and investigating their bonds through the binding energies of their ejected core shell electrons. XPS was also carried out to monitor the success and the extent of the oxidation and the reduction of the various samples through calculating the C/O ratio. It is a commonly used parameter for tracking the extent of oxidation or reduction of carbonaceous based materials.

XPS showed the presence of only three elements: C, N and O as inferred from the XPS survey spectra (Figure II.6). Hydrogen can be expected but cannot be detected by XPS as it has no core electrons and a very small photoionization cross-section [9]. However, its presence can be confirmed by elemental analysis presented in the next subsection.

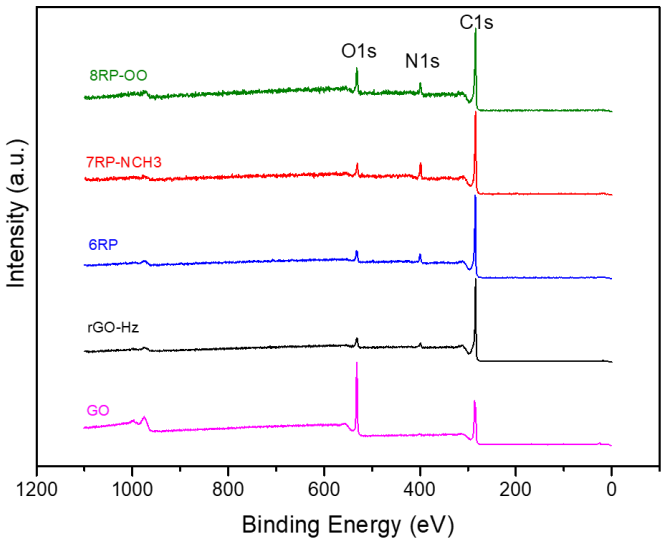

Figure II. 6 : XPS Survey spectra of GO (—), rGO (—), 6RP (—), 7RP-NCH3 (—) and 8RP-OO (—)

High Resolution XPS (HR-XPS) analysis was done on the C1s, O1s and N1s peaks to allow for more accurate semi-quantitative analysis. The integrations of the area under each of these HR-XPS peaks can be used to quantify the relative amount of each element found in the sample, in atomic percentages, using the following equation [10]:

$$Atomic\ \%\ of\ A = \frac{\frac{I_A}{S_A}}{\sum_K \frac{I_K}{S_K}} \qquad (II.1)$$

Where I_A is the measured area of the photoelectron peak of element A and S_A is the sensitivity factor of element A. The atomic percentages of the three detected elements are presented in Table (II.1).

Sample	C (at. %)	N (at. %)	O (at. %)	C/O
8RP-OO	80.52	7.66	11.82	-
7RP-NCH3	81.35	10.89	7.76	-
6RP	85.82	6.46	7.72	-
rGO-Hz	89.77	4.08	6.16	14.57
GO	67.97	0.37	31.66	2.14

Table II. 1 : C, N and O content, in atomic %, of GO, rGO, 6RP, 7RP-NCH3 and 8RP-OO along with C/O ratio for GO and rGO

GO displays a high oxygen content indicating the presence of oxygen functionalities as a result of its successful oxidation, as reflected by a quite low C/O ratio of 2.14. The C/O ratio of rGO was calculated to be 14.57 which is consistent with the observed decrease in the O content, that can be explained by the removal of the oxygen functionalities upon its successful reduction. The presence of nitrogen atoms in rGO can be explained by the N insertion in the graphene lattice during the reduction mechanism involving hydrazine hydrate, as mentioned earlier. For the PGM, a further increase in N content can be observed compared to rGO. Such a finding indicates the presence of the grafting molecules in those samples: 6RP, 7RP-NCH3 and 8RP-OO. A decrease in the O content for the PGM was also observed, showing the loss of oxygen functionalities which can be attributed to: i) the functionalization of GO with the amines and ii) the reduction using Hz.

For 7RP-NCH3, an extra increase in N content was observed compared to 6RP (10.89 at. % N versus 6.46 at. % N) which is consistent with the extra NCH_3 group present in the grafting molecules of the 7RP-NCH3 sample. On the other hand, an extra increase in O content was observed for 8RP-OO compared to 6RP (11.82 at. % O versus 7.72 at. % O) which is consistent with the presence of 2 extra O atoms in the grafting molecules of the 8RP-OO.

The HR-XPS peaks of each specific element can be fitted to get access to the different types of bonds associated with the element. Figures (II.7), (II.8) and (II.9) respectively show the peak fitting of the C1s, O1s and N1s HR-XPS spectra of all the samples.

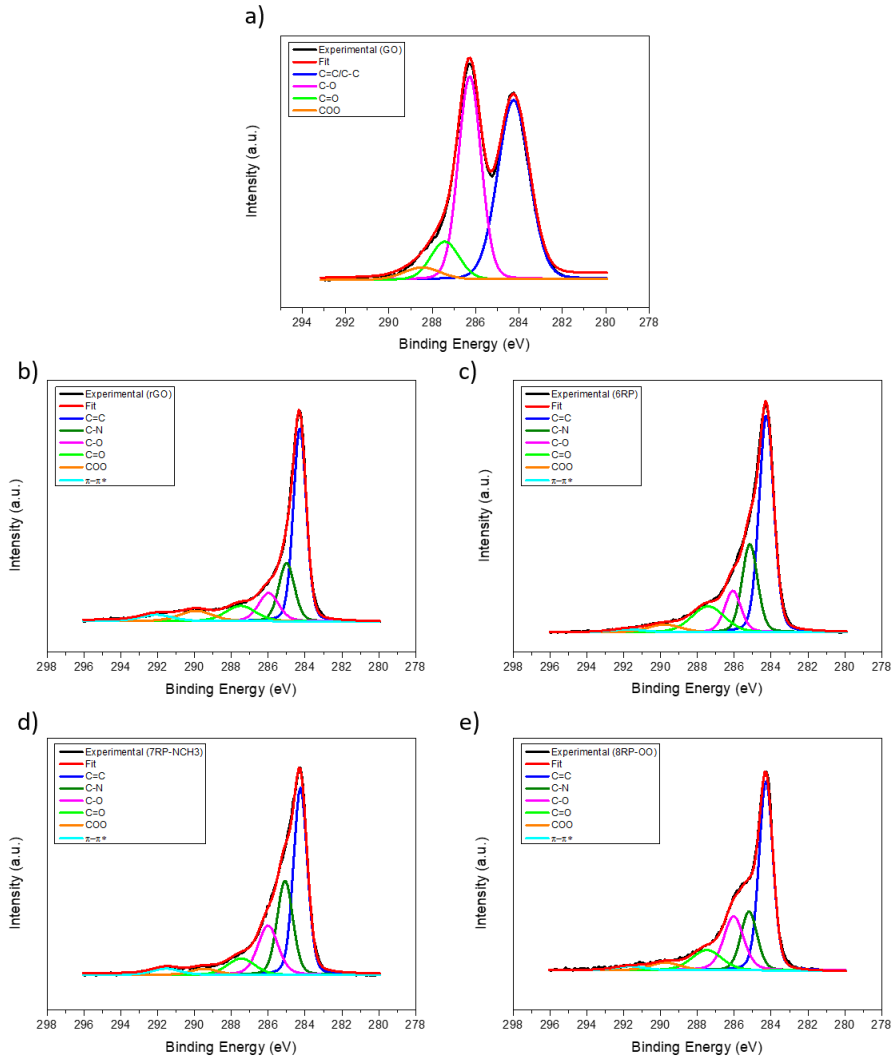

Figure II. 7 : Peak fitting of HR-XPS C1s spectra of a) GO, b) rGO, c) 6RP, d) 7RP-NCH3 and e) 8RP-OO

Table (II.2) summarizes the atomic percentage of each of the identified components of the HR-XPS C1s spectra of the samples.

Sample	sp^2/sp^3 (at. %)	C-N (at. %)	C-O (at. %)	C=O (at. %)	COO (at. %)	π-π* (at. %)
8RP-OO	46.46	16.77	19.87	10.63	4.13	2.15
7RP-NCH3	43.64	25.04	17.56	7.62	3.00	3.15
6RP	49.34	20.97	10.87	13.13	4.11	1.58
rGO-Hz	49.59	18.11	11.73	9.14	7.06	4.38
GO	48.78	-	27.84	15.57	7.81	-

Table II. 2 : Atomic percentage of each of the components of the HR-XPS C1s spectra of GO, rGO, 6RP, 7RP-NCH3 and 8RP-OO

The fitting of the C1s peak of GO (Figure II.7(a)) shows the presence of C=C/C-C, C-O, C=O and COO at 284.3, 286.3, 287.4 and 288.5 eV, respectively. The fitting of the rGO C1s XPS signal shows a decrease in the intensity of the oxygen containing carbons with the increase in the sp^2 carbon peak at 284.3 eV, confirming the success of the reduction. The FWHM value of this latter peak decreased as compared to the broader 284.3 eV peak of GO that results from the

overlap of sp^2 (C=C) and sp^3 (C-C) carbon peaks, showing an increase in the sp^2 carbon content along with a decrease in the sp^3 carbon content upon reduction. Such changes in oxygen content and sp^2 carbon content can also be observed for 6RP, 7RP-NCH3 and 8RP-OO.

Another difference compared to GO, is the presence of C-N peak at ~285.1 eV. Such peak can be attributed to the C-N bonds of the grafting molecules, to the C-N bonds between the rGO sheets and the grafting molecules as expected for a functionalized sample and/or to the C-N bonds arising from Hz reduction. The π-π* satellite peak at ~292 eV appears also for all the samples except for GO. It can be attributed to the shake-up phenomenon in which the π electrons of aromatic rings are excited by exiting photoelectrons [11]. Such a transition was not observed in the GO, which further proves the disruption of the sp^2 carbon network and its restoration after the reduction whether in rGOP or in pillared samples.

A more defined shoulder can be seen in the HR-XPS C1s spectrum of 8RP-OO around approx. ~286 eV. It can be attributed to an increase in the C-O component resulting from the extra two oxygen atoms present in the backbone of its grafting molecules. From Table (II.2), a quantitative increase in C-O component for 8RP-OO is evident as well as the increase in C-N component for 7RP-NCH3 because of the extra 2 oxygen atoms and extra NCH_3 group, respectively, further differentiating such grafting molecules from those of 6RP (pillars with only methylene groups between the terminal amines).

Two different main oxygen components can be identified from the HR-XPS O1s spectra of all the samples: C=O at ~531.4 eV and C-O at ~532.3 eV (Figure II.8). It can be seen from Figure (II.8(a)) that GO has a majority of C-O components (epoxide and hydroxyls). The rGO sample displays a slight increase in C-O compared to C=O, 6RP shows a slight increase of C=O over C-O and both 7RP-NCH3 and 8RP-OO have an appreciable increase in C-O over C=O which is expected for 8RP-OO given its two aliphatic ethers. Such observations can be ascertained numerically as shown in Table (II.3). The differences in at. % of C-O and C=O can hint to the reactivity of the different grafting molecules towards different oxygen functionalities and/or the efficiency of Hz reduction in different environments. These variations in the amounts of different types of oxygen groups is expected to influence the performance of these samples as electrode materials for supercapacitor applications. For instance, carbonyl and quinone groups will be electrochemically active in acidic aqueous electrolytes while phenolic groups will be electrochemically active in basic aqueous electrolytes [12]–[14]. The effects of the basic oxygen groups on the capacitive performance in aqueous acidic media will be tested in the electrochemical analysis section.

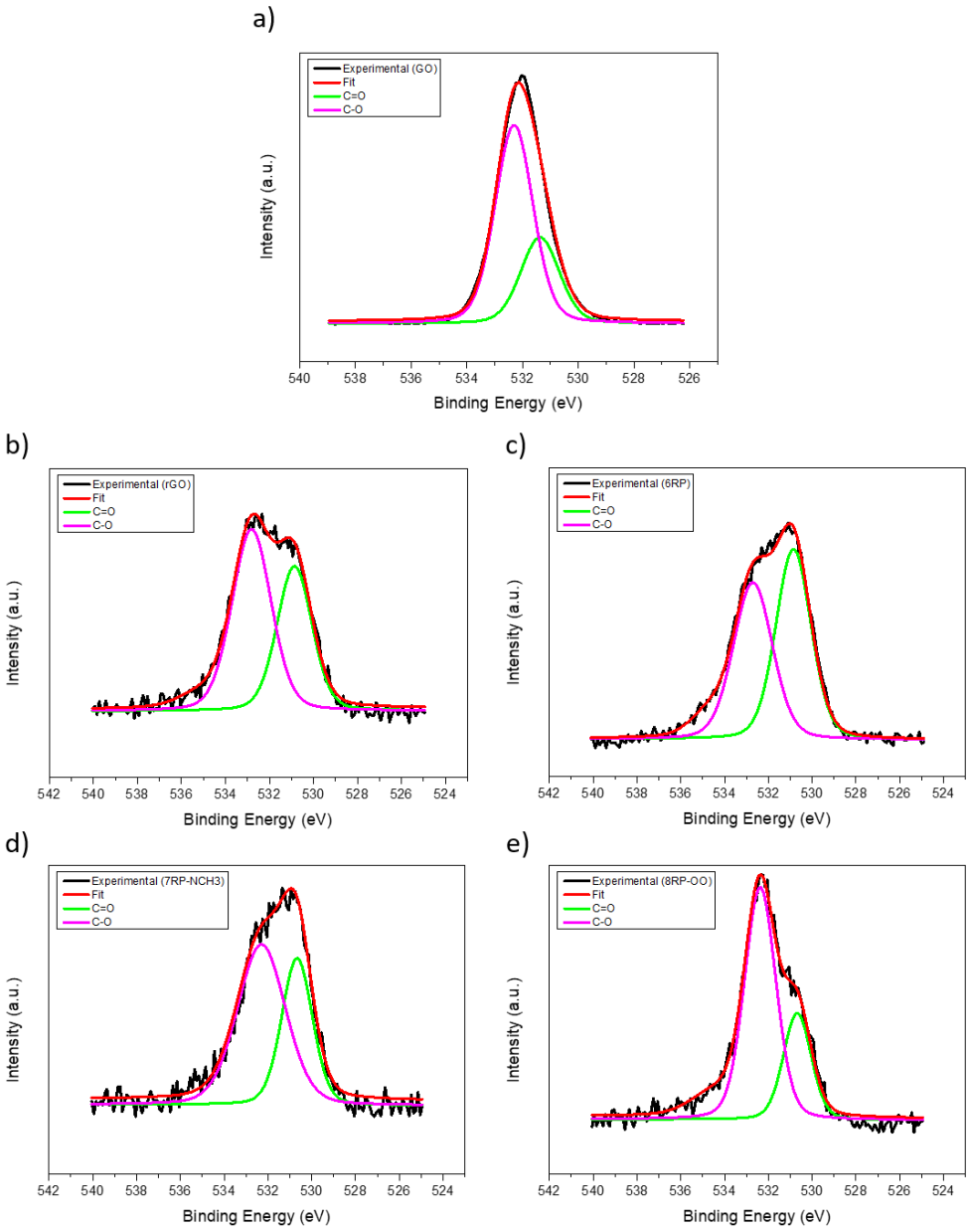

Figure II. 8 : Peak fitting of HR-XPS O1s spectra of a) GO, b) rGO, c) 6RP, d) 7RP-NCH3 and e) 8RP-OO

Sample	C=O (at. %)	C-O (at. %)	Overall C=O * (at. %)	Overall C-O * (at. %)
8RP-OO	29.01	70.99	3.43	8.39
7RP-NCH3	36.88	63.12	2.86	4.9
6RP	52.21	47.79	4.03	3.69
rGO-Hz	41.54	58.46	2.56	3.6
GO	30.72	69.28	9.72	21.93

*Overall X = (X at. % from O1s * Total O at. %) /100 X= C-O or C=O

Table II. 3 : Atomic percentage of each of the components of the HR-XPS O1s spectra of GO, rGO, 6RP, 7RP-NCH3 and 8RP-OO along with the overall contributions of those components

Nitrogen was detected for rGO, 6RP, 7RP-NCH3 and 8RP-OO. Four different components were identified, namely pyridinic N at ~398.4 eV, amine at ~399.3 eV, pyrrolic N at ~ 400.3 eV and graphitic N at ~ 402.2 eV (Figure II.9).

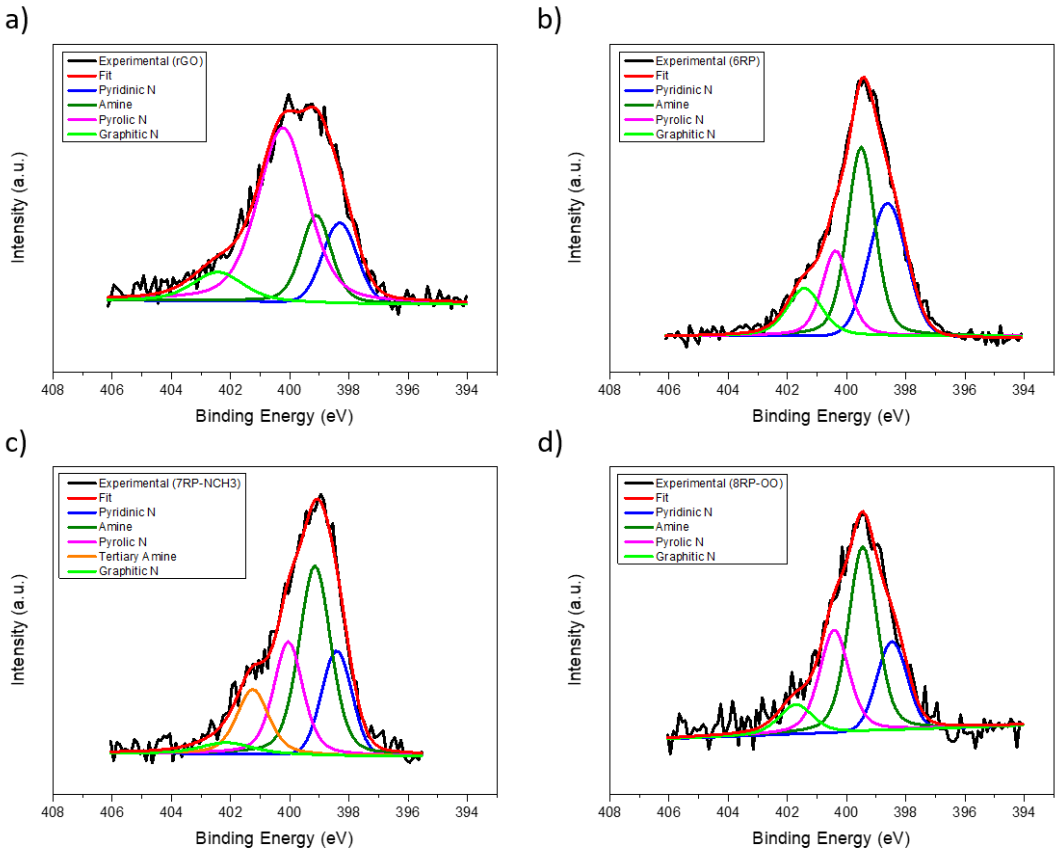

Figure II. 9 : Peak fitting of HR-XPS N1s spectra of a) rGO, b) 6RP, c) 7RP-NCH3 and d) 8RP-OO

The amine peak component seems to increase in the pillared samples compared to rGO, which is consistent with the presence of the amine-based grafting molecules in those samples. Such an increase can be verified by integrating the areas under all the peaks corresponding to different N components to calculate their atomic percentages, listed in Table (II.4).

The 7RP-NCH3 sample showed an extra shoulder (as compared to 6RP and 8RP) at higher N1s binding energies (~401 eV) than those of primary/secondary amines (~399.3 eV), which can be attributed to the extra tertiary amine, present in the middle of its grafting molecule's backbone. From Table (II.4), the ratio of primary/secondary amines to tertiary amine of 7RP-NCH3 was found to be 2.3, which is in agreement with the expected ratio of 2 primary/secondary amines per tertiary amine as inferred from the structure of the grafting molecule. Such a slight deviation from the expected ratio might be due to extra primary/secondary amines coming from the Hz reduction or from fitting errors. Such a matching shows that this shoulder peak can indeed be attributed to the tertiary amine group.

Sample	Pyridinic N (at. %)	Amine (at. %)	Pyrolic N (at. %)	Tert. Amine (at. %)	Graphitic N (at. %)	Overall pyrid N* (at. %)	Overall amine * (at. %)	Overall pyrol N* (at. %)	Overall Tert. Amine* (at. %)	Overall graph N* (at. %)
8RP-OO	19.70	45.04	26.55	-	8.71	1.53	3.5	2.1	-	0.68
7RP-NCH3	20.39	33.47	27	14.52	4.62	2.22	3.64	2.94	1.58	0.5
6RP	31.96	38.25	17.36	-	12.43	2.12	2.54	1.15	-	0.83
rGO-Hz	15.45	16.90	58.10	-	9.55	0.63	0.69	2.3	-	0.39

*Overall X = (X at. % from N1s * Total N at. %) /100 X= pyrid N, amine, pyrol N, Tert. Amine or graph N

Table II. 4 : Atomic percentage of each of the components of the HR-XPS N1s spectra of rGO, 6RP, 7RP-NCH3 and 8RP-OO along with the overall contributions of those components

To confirm the findings from XPS, get a more concrete, mass-based, C/O ratio and get a more comprehensive bulk analysis, EA experiments were done. Complementary to XPS, EA is a bulk mass-based method that gives information on the weight percentage (wt.%) of certain atoms such as carbon, hydrogen, nitrogen and sulfur. The oxygen content can be mathematically inferred from the subtraction of the percentages of the aforementioned elements from 100% in case the material being analyzed contains a mixture of only those five elements (C, H, N, S and O) which can be confirmed from XPS as shown in the previous section; only C, N and O were detected by XPS. Figure (II.10) shows the wt.% of the C, H, N and O of the samples synthesized. It can be seen that GO has a large oxygen content compared to the rest of the samples with a low C/O ratio of 1.01, showing the high extent of oxidation of GO. Almost no nitrogen was detected in GO which confirms the success of the synthesis method in producing GO with low impurities. When reduced to rGO using Hz, the C/O ratio increased to 6.46 which is an indication of the removal of the oxygen functionalities and hence of the reduction of the GO.

A 5 wt.% N content was observed for rGO, which is in-line with the nitrogen insertion reduction mechanism of Hz. Higher N contents (8.23, 11.76 and 9.29 wt.% for 6RP, 7RP-NCH3 and 8RP-OO, respectively) were observed for the PGM due to the expected functionalization of the graphene sheets by the amine-terminated pillars. A notable increase in N content for 7RP-NCH3 and O content for 8RP-OO can be related to the extra NCH_3 and two oxygen atoms in the backbones of their pillars, respectively.

The amounts of the different grafting molecules can be compared by comparing the H content of the different samples, assuming that all of them have an equal amount of H remaining from GO. Nonetheless, a correction has to be made for the extra amount of H coming from the tertiary amine in the grafting molecules of 7RP-NCH3. Considering this, it seems that there are similar amounts of H (2.27, 2.7, and 2.13 for 6RP, 7RP-NCH3 and 8RP-OO) and thus similar amounts of grafting molecules per sample.

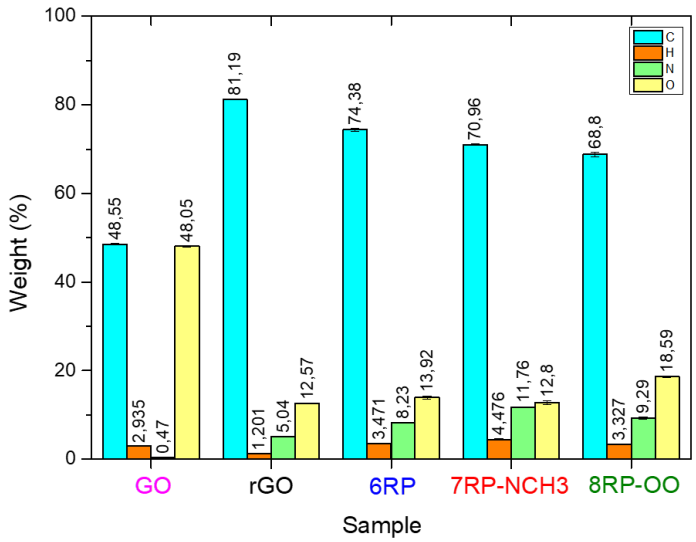

Figure II. 10 : Weight percentages of GO, rGO, 6RP, 7RP-NCH3-0.8 and 8RP-OO

After inferring the oxidation of graphite into GO from EA and XPS, an ssNMR experiment was done to further investigate the types of oxygen functional groups present in the GO. ssNMR is also a bulk technique like EA and it is the go-to technique for investigating the different environments of various elements. A ^{13}C Cross-Polarization (CP) ssNMR experiment was done at RT with a Magic Angle Spinning (MAS) of 12 KHz. The spectrum (Figure II.11(a)) shows 6 different peaks that can be ascribed to the following groups according to their chemical shifts: epoxide (C-O-C), hydroxyl (C-OH), lactol (O-C-O), sp^2 carbons (C=C), carboxylic (O=C-O) and carbonyl (C=O) at 58, 69, 97, 129, 163 and 189 ppm, respectively [15], [16]. The presence of such peaks is a direct proof of the oxidation of the GO and the presence of different oxygen functionalities on its surface. The presence of such groups is in agreement with the groups identified on the surface of the sample earlier with XPS. Figure (II.11(b)) shows, on a GO model, the different oxygen functionalities detected by ssNMR. This shows that GO can be used as platform for chemical functionalization through making use of the different possible chemical reactions involving the various oxygen functional groups present on its surface.

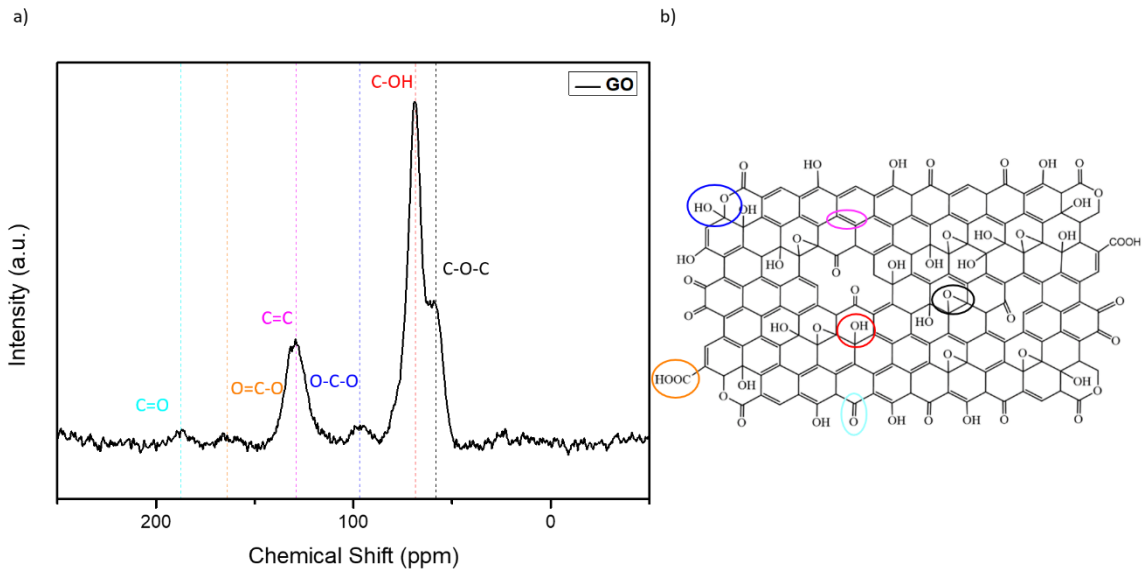

Figure II. 11 : a) ^{13}C MAS CP ssNMR GO spectrum and b) Proposed GO model (adapted from [17])

ssNMR experiments were only done on GO as the rest of the samples are conductive which might lead to spinning and heating problems due to the generation of eddy currents from the spinning of conductive samples in a magnetic field. In addition, for the nitrogen including samples, not much information is expected to be collected due to the low sensitivity of the ^{15}N arising from its low natural abundance and its low gyromagnetic ratio. Accordingly, to further investigate the different functional groups on the samples before and after pillaring and/or reduction, FT-IR experiments were carried out. Such experiments were done in ATR mode in the range 400-4000 cm^{-1}. Figure (II.12) shows the FT-IR spectra of all the samples and Table (II.5) summarizes the peak assignments to the corresponding groups and their associated vibrational modes according to references [18]–[25]. The black color of rGO means high absorbance at all visible wavelengths, thus masking some peaks, especially the weak ones. Furthermore, peaks corresponding to various vibration modes of different functionalities might be overlapping. Accordingly, interpreting FT-IR spectra, particularly for such absorbing samples, should be carefully handled and be analyzed in light of other characterization techniques.

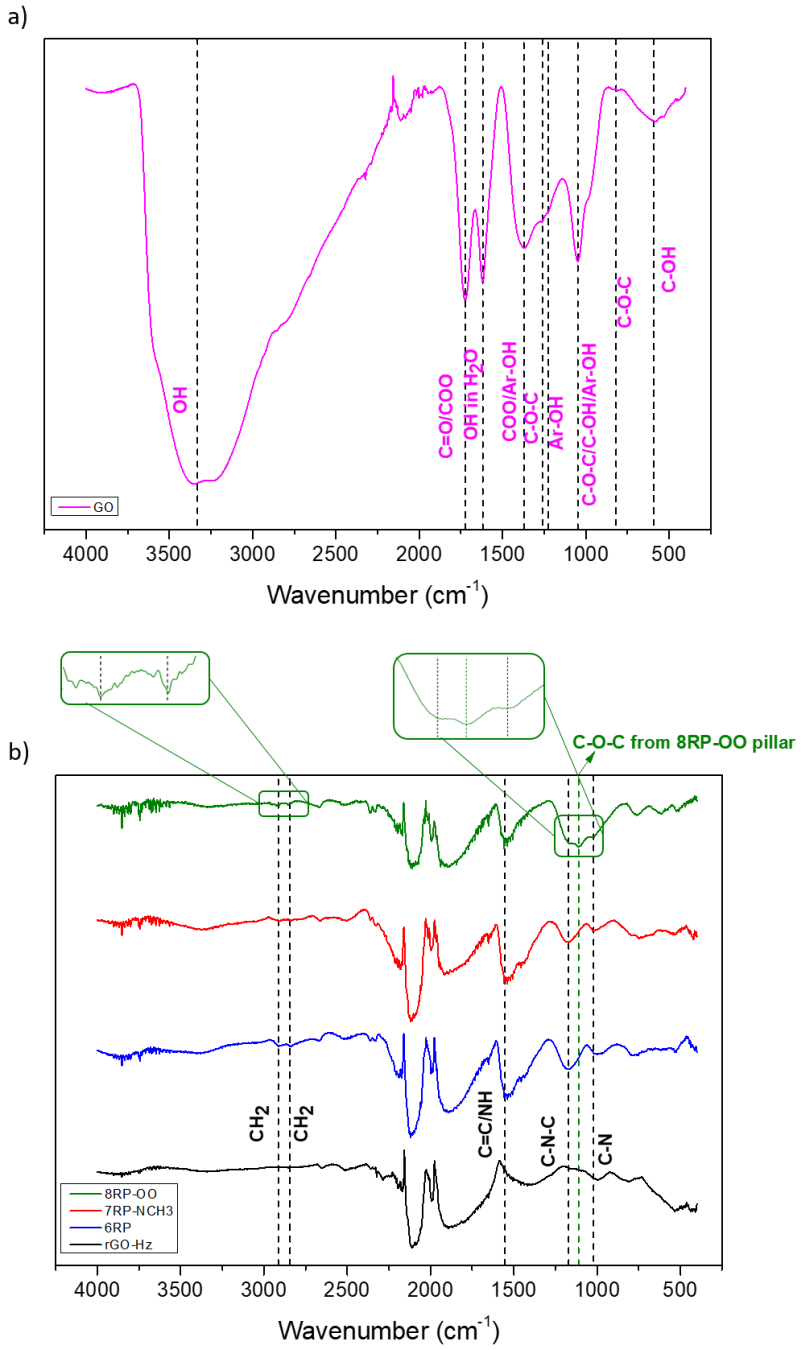

Figure II. 12: FT-IR spectra of a) GO (—) and b) rGO (—), 6RP (—), 7RP-NCH3 (—) and 8RP-OO (—)

From the IR spectra of GO, epoxy, hydroxyl, phenolic, carbonyl and carboxylic groups as well as water molecules can be identified, which is in agreement with the ssNMR and XPS (GO includes various oxygen functionalities and "structural water molecules"). When reducing the GO into rGO, the intensity of those oxygen-containing peaks diminished and a new peak appeared around 1550 cm^{-1} (C=C stretching). These observations are indicative of the GO reduction in agreement with the results from XPS and EA. For the functionalized samples, new peaks appeared such as the ones at 1034, ~1180, 1550, ~2845 and ~2920 cm^{-1}. The peak at 1034 cm^{-1} can be attributed to C-N, the peak at ~1180 cm^{-1} can be attributed to C-N-C, the peak

around 1550 cm^{-1} can be attributed to the C=C/NH while the two peaks at ~2845 and ~2920 cm^{-1} can be assigned to CH_2 groups. An extra peak appeared in the spectrum of the 8RP-OO sample at 1115 cm^{-1} that was assigned to the aliphatic C-O-C group in the backbone of the grafting molecule. All these peaks confirm the presence of the grafting molecules inside the samples and their covalent bonding with the rGO sheets as inferred from the presence of a peak corresponding to the C-N-C asymmetric vibration. The 7RP-NCH3 sample is the only sample whose grafting molecules has C-N-C bonds in their structure due to the extra tertiary amine group. Nevertheless, the peak corresponding to the C-N-C at 1550 cm^{-1} is appearing in 6RP and 8RP-OO, indicating that such a bonding scheme can be attributed to the functionalization of the rGO sheets with the grafting molecules. The asymmetry of the vibration and the absence of C-N-C symmetric vibration may hint to different C-N bonds: a C-N bond within the pillar itself and a C-N bond connecting the pillar to the rGO sheets.

Sample	Wavenumber (cm^{-1})	Functional Group	Associated Vibration
8RP-OO	2922	CH_2	C-H stretching
	2855	CH_2	C-H stretching
	1561	C=C/NH	C=C stretching/N-H in-plane stretching
	1168	C-N-C	Asymmetric C-N-C stretching
	1115	C-O-C	Aliphatic C-O-C
	1034	C-N	C-N stretching
7RP-NCH3	2913	CH2	C-H stretching
	2834	CH2	C-H stretching
	1561	C=C/NH	C=C stretching/N-H in-plane stretching
	1188	C-N-C	Asymmetric C-N-C stretching
	1034	C-N	C-N stretching
6RP	2914	CH2	C-H stretching
	2845	CH2	C-H stretching
	1561	C=C/NH	C=C stretching/N-H in-plane stretching
	1188	C-N-C	Asymmetric C-N-C stretching
	1034	C-N	C-N stretching
rGO-Hz	1550	C=C	C=C stretching
	1034	C-N	C-N stretching
GO	595	C-OH	OH out-of-plane bend
	817	COC	C-O-C stretching
	1051	C-O-C/C-OH/Ar-OH	C-O stretching
	1229	Ar-OH	OH bending in phenol
	1261	C-O-C	C-O-C stretching
	1370	COO/Ar-OH	OH deformation in COO / OH bending in Phenol
	1618	H_2O	OH stretching and bending from adsorbed H_2O
	1725	C=O/COO	C=O Stretching
	3390*	C-OH	OH Stretching

*broad band

Table II. 5 : The FT-IR peak positions of GO, rGO, 6RP, 7RP-NCH3 and 8RP-OO and their corresponding functional groups and the vibrations associated with them

In order to analyze the thermal stability of the samples and verify the existence of the grafting molecules and the extent of reduction of the samples from their thermal degradation profile, Thermal Gravimetric Analysis (TGA) was carried out under an inert gas (Figure

II.13(a)). The thermal stability can be inferred from the final weight loss at 800°C (graphite (4%) < rGO (12%) < 6RP (26%) < 8RP-OO (31%) < 7RP-NCH3 (35%) < GO (50 %)) (Figure II.13(b)).

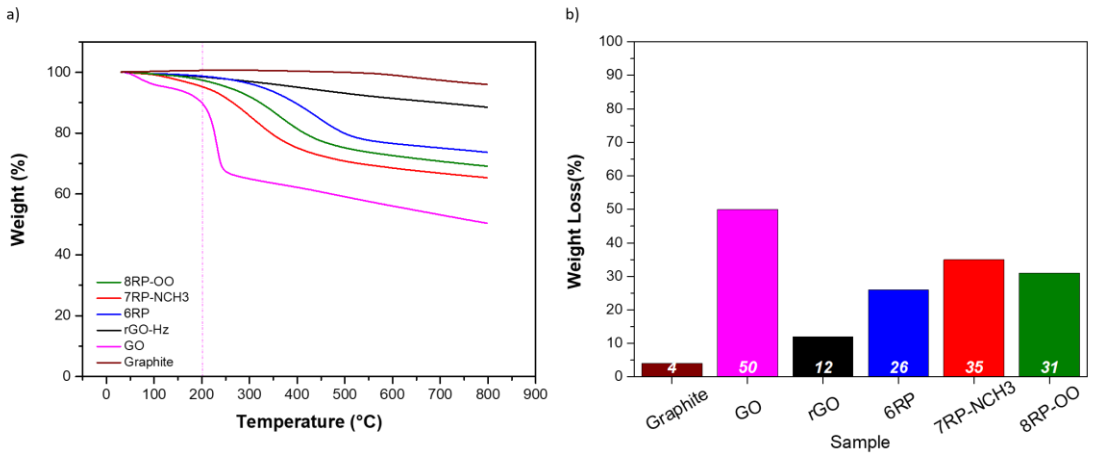

Figure II. 13 : a) TGA profile of Graphite (—), GO (—), rGO (—), 6RP (—), 7RP-NCH3 (—) and 8RP-OO (—) with a vertical line showing the onset of the abrupt weight loss of GO and b) the weight loss (%) for each sample at 800°C

The degradation profile of graphite shows only 4% weight loss at 800°C all over the temperature range, highlighting a very high thermal stability of the sample. On the other hand, the degradation profile of GO shows three weight loss steps corresponding to three degradation processes [26]: i) a weight loss of 4% up to 100°C, which can be assigned to the loss of surface adsorbed water molecules, ii) a weight loss of 29% between 100°C and 250°C with an abrupt loss (~20%) around 200°C due to the loss of labile oxygen functionalities and remaining water molecules and iii) a gradual weight loss of 17% from 250°C till 800°C attributed to the loss of strongly bonded oxygen moieties. Such a degradation profile further confirms the highly oxidized state of GO. In the rGO sample, only a slight steady degradation is observed from 250°C to 800°C with a loss of 9%, which is indicative of the removal of the labile oxygen functionalities and most of the strongly bonded ones upon reduction.

The functionalized graphene materials show degradation profiles similar to that of rGO, but with an extra gradual weight loss between 200°C and 500°C which can be attributed to the degradation of the grafting molecules and losses of some oxygen functionalities (18%, 21% and 19% for 6RP, 7RP-NCH3 and 8RP-OO, respectively). Subtracting the weight loss of rGO-Hz, in the pillars degradation temperature ranges, from those of the functionalized samples allows extracting the weight loss corresponding to the pillars. From such weight loss, the number of moles of the grafting molecules per gram of the functionalized sample can be calculated accordingly (1.1, 1.2 and 1.0 mmoles/g for 6RP, 7RP-NCH3 and 8RP-OO, respectively). The

corresponding weight losses are different but result in similar number of moles per gram because of the different molecular weights of the grafting molecules. This is indicative of the presence of the grafting molecules inside in the sample in similar quantities but does not confirm their bonding status (whether covalently bonded or physically adsorbed). However, the wide and high degradation temperature range of the grafting molecules in the functionalized sample, as opposed to a steep weight loss, hints at a strong interaction between the grafting molecules and the rGO sheets.

So far, the samples have been characterized chemically using various methods. Such chemical analysis confirms the success of the oxidation of graphite into GO, the reduction of GO into rGO via Hz and the functionalization of the GO using various pillars. The oxidation of graphite and reduction of GO were confirmed through monitoring the C/O ratio from both XPS and EA. The small C/O ratio of GO (1.01 from EA and 2.14 from XPS) confirms the oxidation and the appearance of oxygen functionalities on the surface which were then deciphered through ssNMR, FT-IR and XPS peak fitting. The increase in C/O ratio of rGO upon reduction (6.46 from EA and 14.57 from XPS) is indicative of the removal of oxygen functionalities as evidenced from less weight loss coming in the TGA degradation profile compared to GO (12 wt% for rGO and 50% for GO). The C/O ratio (from EA) was also calculated for the functionalized samples after accounting for the carbon and oxygen content coming from the grafting molecules using the amount of grafting molecules extracted from the TGA degradation profiles. In doing so, the reduction degree of the graphene support can be discussed separately. The C/O ratios obtained were ~4.8, ~4.8 and ~4 for 6RP, 7RP-NCH3, and 8RP-OO, respectively. Comparing these C/O ratios to those of GO and rGO shows that these samples are well reduced compared to GO however, they are not as reduced as rGO. The grafting molecules were detected in the functionalized samples through various observations from different techniques. For instance, an increase in the nitrogen content was observed for all the functionalized samples (by XPS and EA), especially for the one with extra tertiary amine (7RP-NCH3) which is consistent with the amount of nitrogen in these pillars. Similarly, an increase in oxygen content was detected (XPS and EA) for the sample with grafting molecules having 2 extra oxygen atoms. The covalent functionalization can be directly inferred from the FT-IR C-N-C asymmetric vibration peak observed only in the functionalized samples coupled with the presence of primary/secondary amine XPS peak in their N1s spectra and the wide and high degradation temperature range of the grafting molecules observed by TGA.

Up till now, the samples which were synthesized as pillared samples were referred to as functionalized samples instead of pillared samples as the pillaring was not confirmed yet at

such stage. The grafting of the molecules does not imply their pillaring as pillaring requires grafting from both sides and some robustness to hold the structure from falling apart. Accordingly, structural analyses were done to examine the success of the pillaring technique as well as exploring various structural parameters that can influence the samples' properties like the electrical conductivity for instance which is crucial for supercapacitor applications.

II.3.1 Structural Analysis

XRD was the first structural characterization technique to be employed as it allows a fast and accurate verification of i) the success of the pillaring procedure (bridging of graphene sheets together) and ii) the oxidation of graphite into GO and its reduction to rGO. Such verifications can be done through monitoring the "d" parameter of Bragg's law:

$$n * \lambda = 2 * d * \sin(\theta) \qquad (II.2)$$

Where n is the diffraction order, λ is the wavelength of the incident x-rays, θ is the incident angle and d is the inter-lattice plane spacing, which in case of graphene based materials, displays the inter-sheet distance. Such a spacing is a vital parameter for the work herein; as this value is sensitive to the various modifications pursued in such a study, including the oxidation of graphite, the reduction of the GO and the pillaring of the samples. The changes in the d-spacing values upon different modifications are explained when treating the XRD data. The XRD profiles of the various synthesized samples are shown in Figure (II.14) along with the XRD profile of graphite, the very first starting material used to synthesize GO.

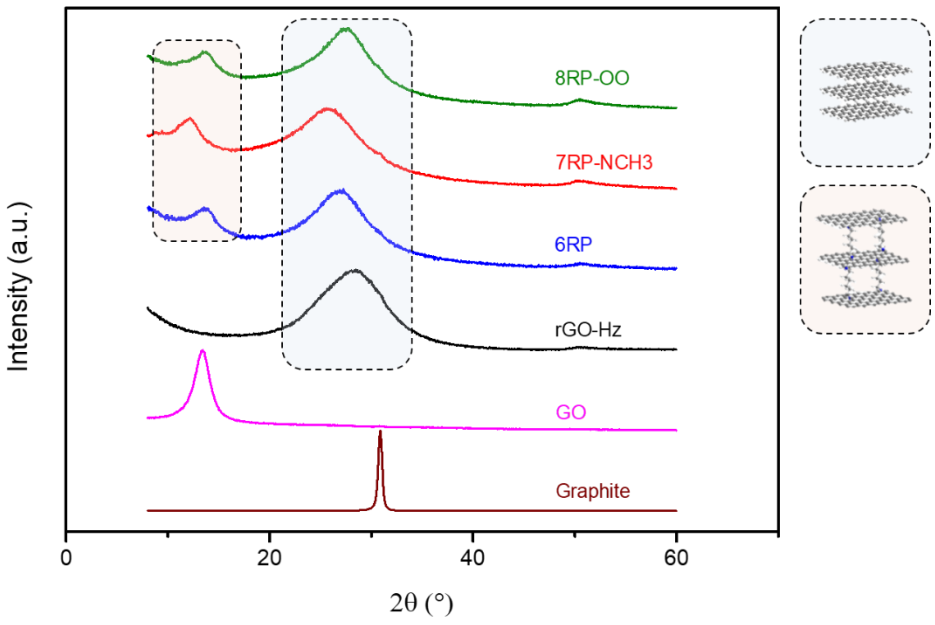

Figure II. 14 : XRD profiles of Graphite (—), GO (—), rGO (—), 6RP (—), 7RP-NCH3 (—) and 8RP-OO (—)

Graphite showed the expected narrow 002 graphitic peak with a 2θ value ~31°, corresponding to an inter-sheet distance (d-spacing) of 0.34 nm. When oxidized to GO, such a peak completely disappeared and a new broader peak, attributed to 001 reflections, appeared at a lower 2θ value (~13.5°), corresponding to an expanded d-spacing of 0.77 nm. Such an expansion confirms the disruption of the π-π interactions between the sheets of GO as a result of the disorganization of the sp^2 carbon network due to the successful chemical oxidation. This d-spacing is maintained thanks to the so-called "structural water molecules", that are present between the sheets as an integral part of the GO [27], forming hydrogen bonds with the different oxygen functionalities [28] and thus holding the structure and creating a long range order. Upon reduction of GO into rGO, a very broad 002 peak (referred to as G peak) appeared at a large 2θ value (~28°), corresponding to a d-spacing of 0.36nm. Such a d-spacing - close to that of graphite - confirms the (partial-) restoration of the π-π interactions between the sheets arising from the recovery of the sp^2 carbon network due the removal of most of the oxygen functionalities. However, the Full Width Half Maximum (FWHM) of the peak is much broader than that of graphite. This can be explained by either i) microcrystalline broadening as in rGO having small crystallites (less number of sheets per crystallite) as in few layer graphene [29] or ii) rGO having inhomogeneous crystallites with different d-spacing values. The former explanation is more consistent with other characterization techniques, as will be discussed in the TEM section. This is in addition to other factor such as strain, stacking faults and instrumental errors that might be contributing to such broadening.

When the functionalized samples were analyzed with XRD, a new peak appeared at lower 2θ values in addition to the rGO peak. This peak corresponds to a higher d-spacing value according to equation II.2. This so-called Cross-Linking peak (CL peak) was attributed to the long-range order arising from the bridging of the rGO sheets together using the molecular pillars. Such attribution was based on i) the fact that for a peak to appear in an XRD diffractogram, a long-range order has to be established and ii) such peak only appeared when pillaring was carried out before reduction and was never detected when only reduction was done as in rGO. The d-spacing values of the pillared samples corresponding to their CL peaks were found to be 0.75 nm, 0.85 nm and 0.75 nm for the 6RP, 7RP-NCH3 and 8RP-OO, respectively. Such a finding is a proof of pillaring and of the success of the synthesis procedure in producing the intended structural features; hence the samples 6RP, 7RP-NCH3 and 8RP-OO will be referred to as pillared samples from now on. As noted earlier, a direct relation between the extended length of the pillars and the corresponding d-spacing of their PGM is difficult. For instance, 8RP-OO shows a d spacing similar to that of 6RP although its pillars have a longer stretched structure;

and 7RP-NCH3 has the highest d-spacing while its pillars' stretched length is not the largest. This can be attributed to different conformations that can be adopted by the pillars as well as their different organizations inside the pillared samples (up straight or inclined with different degrees related to grafting bond orientations). A small slightly broad peak corresponding to the in-plane 100 periodicity can be seen for all the samples around 50°.

Fitting of the XRD profiles was carried out using Highscore Plus software to extract parameters such as the areas under the peaks and the FWHM in addition to the peak positions and their corresponding d-spacing values mentioned previously. Scherrer's equations (equation II.3 and II.4) were applied using the FWHM of the peaks to calculate the crystallite stack height (along c-axis) and the in-plane crystallite size (along lateral direction (a-axis)), assuming there is no peak broadening arising from mechanical strain in the samples or from instrumental effects [30]–[33]. Equation II.5 was also applied to calculate the number of sheets in the crystallite.

$$L_C\ (nm) = \frac{K_1 * \lambda}{\beta * \cos\ (\theta_1)} \qquad (II.3)$$

$$L_a(nm) = \frac{K_2 * \lambda}{\beta * \cos\ (\theta_2)} \qquad (II.4)$$

$$N_C = \frac{L_C}{d} \qquad (II.5)$$

Where the different parameters are defined as the following:

L_C : Crystallite stack height (along c-axis)

K_1 : Form factor ($K_1 = 0.9$ [31]–[33])

λ : Wavelength of the X-ray used

β : FWHM of the peak being analyzed

θ_1 : Diffraction peak position of the 001, 002 and CL peaks

L_a : In-plane crystallite size (along lateral direction (a-axis))

K_2 : Warren Form Factor constant ($K_2 = 1.84$ [30]–[33])

θ_2 : Diffraction peak position of the 100 peak

N_C : Number of graphene sheets in the crystallite

d : d-spacing of the peak analyzed

Figure (II.15) illustrates the various parameters extracted for an sp^2 graphite along with the definition of the FWHM which is the width of the peak at an intensity equal to half its maximum value. It is important to note that the in-plane crystallite size is the size of the sp^2 domains so

for a single crystal graphite, it will correspond to the lateral size of the sheets, nevertheless, for rGO samples, it will correspond to the average size of the sp^2 domains.

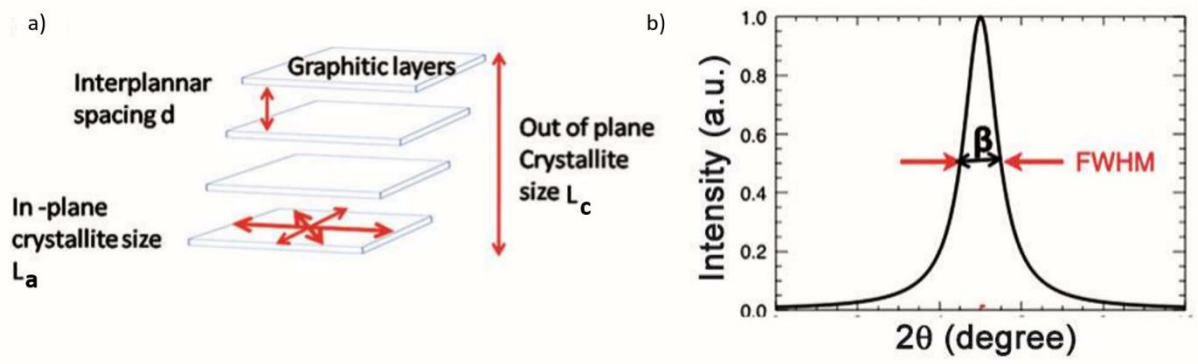

Figure II. 15 : a) Illustration of the various parameters extracted from Bragg's Law and from Scherrer's equations for a graphite sample and b) Illustration of the FWHM for a graphite sample [34]

Table (II.6) shows a summary of the data extracted from the XRD profiles of all the samples.

Sample		d-spacing (nm)	Crystallite Stack Height (nm)	Number of layers in the Crystallite	In-Plane Crystallite Size (nm)
8RP-OO	CL	0.75	3.48	5	7.8
	G	0.38	1.73	5	
7RP-NCH3	CL	0.85	4.53	5	7.5
	G	0.4	1.50	4	
6RP	CL	0.75	3.63	5	9.5
	G	0.38	1.58	4	
rGO-Hz		0.36	1.36	4	8.4
GO		0.77	5.12	8	11.3
Graphite		0.34	21.74	65	48.6

*Percentage of CL (%) = $\frac{Area\ under\ CL\ Peak}{Area\ under\ G\ Peak + Area\ under\ CL\ Peak} * 100$

Table II. 6 : Summary of the data extracted from the XRD profiles of Graphite, GO, rGO, 6RP, 7RP-NCH3 and 8RP-OO

The oxidation of graphite lead to a decrease in the in-plane crystallite size (48.61 nm for graphite compared to 11.29 nm for GO); as well as in the number of layers per crystallite (65 for graphite compared to 8 for GO) which is in agreement with the disruption of the sp^2 carbon network, and consequently the π-π interactions, respectively upon oxidation. The low number of layers in GO confirms the success of the exfoliation procedure through sonication in obtaining graphene oxide from graphite oxide, as graphene oxide is defined as a few-layer material compared to graphite oxide which is defined as a multi-layer material. In other words, graphene oxide is the exfoliated form of graphite oxide [35]. Upon reduction, the number of sheets and the in-plane crystallite size continued on decreasing. The latter can be explained by the formation of multiple small scattered sp^2 carbon regions upon reduction, leading to smaller crystallites sizes. The higher number of sheets in GO compared to the reduced samples might

be attributed to the "structural water molecules" mentioned earlier allowing for a better-sustained interaction between the sheets.

From the pieces of information gathered so far, models can be proposed for rGO and the pillared samples to explain the differences between them and show the source of the CL peak. Figure (II.16) gives a structural model that might explain such peaks. In Figure (II.16(a)), the XRD structural model of rGO shows rGO having small inter-layer spacing distance, small crystallite sizes and a low number of sheets per crystallite. On the other side, Figure (II.16(b)) shows the pillared samples as biphasic systems with rGO-like particle (responsible for the appearance of the G peak) and cross-linked crystallites (responsible for the appearance of the CL peak).

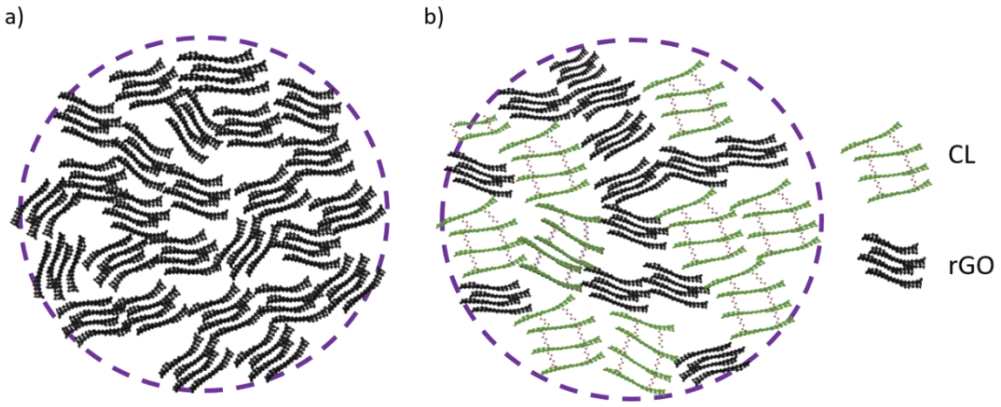

Figure II. 16 : conceptualized structural representation of a) monophasic rGO and b) bi-phasic pillared samples

Raman spectroscopy was utilized to further investigate the samples structurally to monitor their structural evolution (sp^2 and sp^3 domains) and track their density of defects (Figure II.17). The results are summarized in Table (II.7).

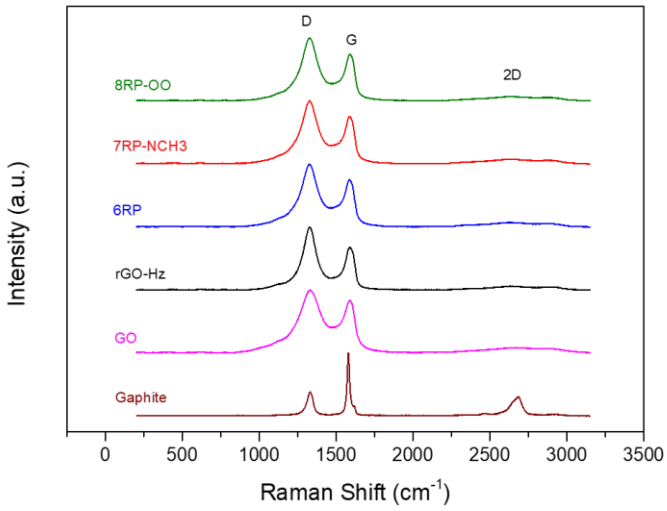

Figure II. 17 : Raman spectra of Graphite (—), GO (—), rGO (—), 6RP (—), 7RP-NCH3 (—) and 8RP-OO (—)

Sample	Raman Bands	Wavenumber (cm^{-1})	I_D/I_G	average crystallite size of the graphitic sp^2 domains (L_a)
8RP-OO	D-band G-band 2D-band	1326.2 1592.4 2629	1.35	28.5
7RP-NCH3	D-band G-band 2D-band	1326.2 1584.1 2628.1	1.34	28.7
6RP	D-band G-band 2D-band	1329.4 1586.1 2632.5	1.33	28.9
rGO-Hz	D-band G-band 2D-band	1327.2 1588.2 2636	1.47	26.2
GO	D-band G-band 2D-band	1334.8 1591.4 2670.6	1.19	32.3
Graphite	D-band G-band 2D-band	1332.6 1579.9 2688.3	0.4	96.2

Table II. 7 : Summary of the Raman data (Raman bands, their wavenumber, I_D/I_G ratio and L_a) for Graphite, GO, rGO, 6RP, 7RP-NCH3 and 8RP-OO

The Raman spectra of carbon-based materials are characterized by 2 main bands, the G and D bands, which offer valuable information about the structural state of the sample. The G-band, the Graphitic band, is related to the vibrations of the sp^2 carbon network, while the D-band, the Disorder band, is related to disorder-induced vibrational mode arising from various structural disorder or sp3-like defects on the surface of the carbon [36], [37]. The I_D/I_G ratio gives an indication on the degree of disorder in the samples. Such a ratio can also be used to estimate the average crystallite size of the graphitic sp^2 domains according to the following equation [38]:

$$L_a(nm) = (2.4 * 10^{-10}) * \lambda^4 * \left(\frac{I_D}{I_G}\right)^{-1} \qquad (II.6)$$

Where L_a is the lateral dimension of sp^2 carbon clusters in nanographite (nm), λ is the wavelenght of the excitation laser used (nm) and I_D/I_G is the ratio of the intensity of the D-band over that of the G-band. In addition, the 2D graphitic band can be used to give an indication on the extent of graphitization [39]. From the spectrum of graphite, an intense G-band can be seen at 1580 cm^{-1} as reported in literature [36]. Such a peak is accompanied by a small D-band in agreement with literature, on commercial graphite, which can be attributed to the polycrystallinity of this commercial graphite [40]. The appearance of the D-band can also be attributed to the fact that our starting graphite is a nanographite which leads to many edges that are considered defective sites. An intense 2D band is also observed, which is an indication of high degree of graphitization. When oxidized to GO, the intensity of the D-band grew,

indicating the increase of defects density, which can be explained by sp^3 carbons breaking the periodicity of the sp^2 carbon network. This increase in defects density can also be illustrated by the rise of the I_D/I_G ratio from 0.4 for graphite to 1.19 for GO. In addition, the G-band was up-shifted to higher frequencies because isolated sp^2 bonds resonate at higher frequencies [39]. All together, these observations highlight the structural disorder brought by the sp^3 carbons as a result of the oxidation. On reducing the GO, the I_D/I_G ratio, counterintuitively, kept on increasing; despite the fact that the oxygen content decreased and the sp^2 carbon network was partially restored as shown from XPS, EA and XRD. This can be explained by the formation of multiple small sp^2 islands leading to a smaller average size of sp^2 domains with more sp^2/sp^3 boundaries. The boundaries between the small sp^2 islands and the sp^3 matrix can be thought of as defective boundaries; or the presence of discontinues sp^2 carbons inside sp^3 matrices can be treated as vacancy defects in the lattice [41], thus, increasing the I_D/I_G ratio. Such an increase in I_D/I_G can also be attributed to more edges exposed upon reduction [42]. The I_D/I_G is inversely proportional to the average size of the sp^2 domains according to Eq.(II.6), thus when the average size of the sp^2 domains decrease, the I_D/I_G ratio increases accordingly. Figure (II.18) shows a graphical explanation of the growth of sp^2 carbon configurations (Figure II.18(a), (b) & (c)) and their growth into sp^2 clusters (Figure II.18(d)). Such graphical representations would be accompanied by a smaller average sp^2 carbon network size which will be manifested in a larger I_D/I_G ratio. Figure (II.18(e)) explains what would happen if the sample was reduced further: the already formed sp^2 carbon configurations and clusters would start to coalesce and percolate, leading to a larger average sp^2 carbon network size, resulting in a lower I_D/I_G ratio.

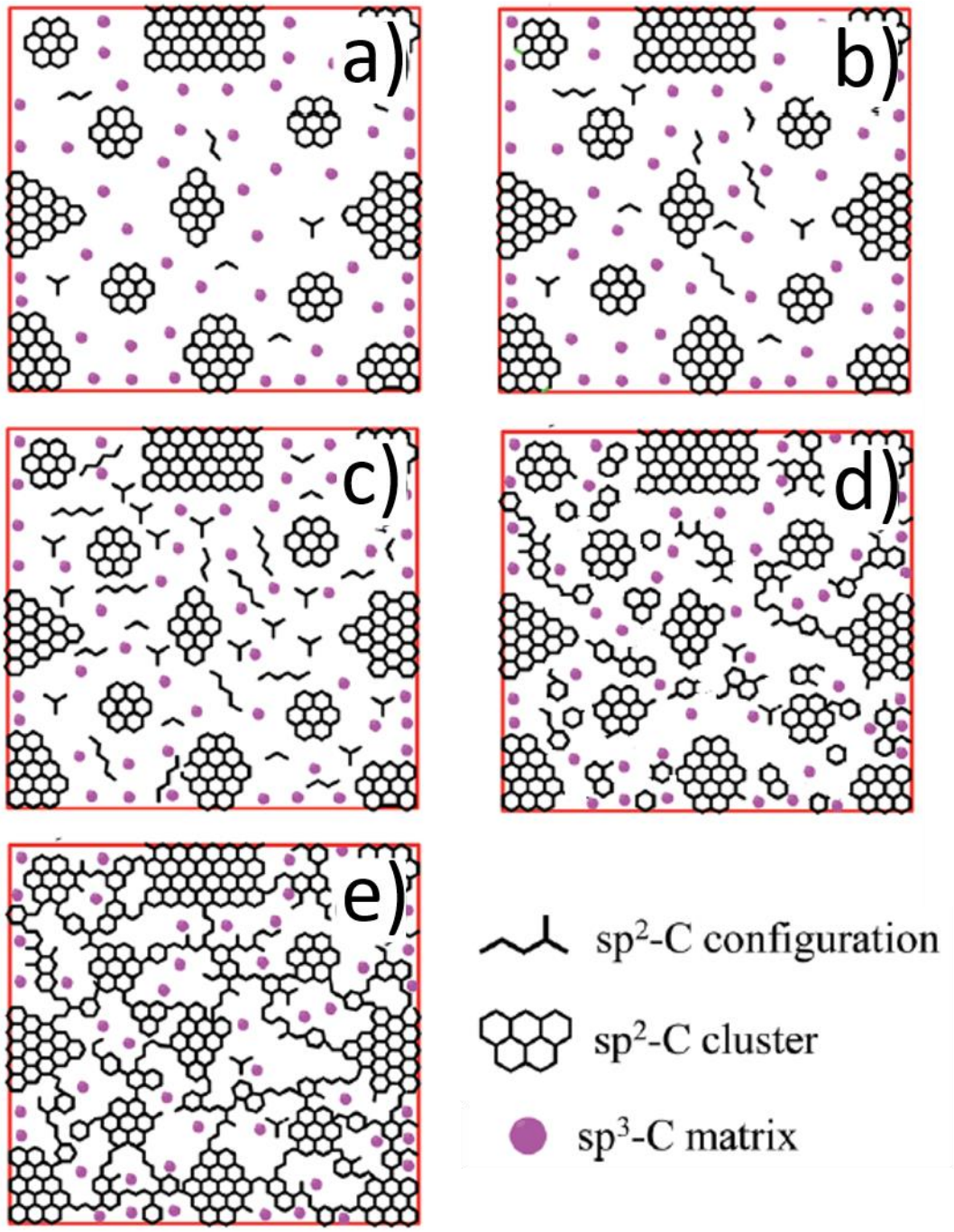

Figure II. 18 : Conceptual structural evolution of GO during its reduction into rGO (adapted from [41])

For the RPs, I_D/I_G ratios of 1.33, 1.34 and 1.35 were calculated for 6RP, 7RP-NCH3 and 8RP-OO, respectively (Figure II.19). Such values are in-between those of GO and rGO. Such observation could be explained by the lesser partial reduction of these samples compared to rGO. Hence these pillared samples do not have as many sp^3 carbons as GO. The I_D/I_G ratios can be expressed as an estimate of the average crystallite size of the graphitic sp^2 domains (L_a). The values were found to be 96.2, 32.3, 26.2, 28.9, 28.7 and 28.5 nm for graphite, GO, rGO, 6RP, 7RP-NCH3 and 8RP-OO, respectively (Figure II.19). The trend is showing a decrease in the

average size of sp^2 domains upon oxidation of graphite (96.2 nm) due to the increased sp^3 carbons in GO (32.3 nm) and a further decrease upon its reduction to rGO (26.2 nm) due to the creation of numerous small sp^2 islands. The values for the pillared samples are in-between those of GO and rGO as these samples are not as extensively reduced as rGO as they still have sp^3 carbons from the attachment of the pillars to the rGO sheets and they do not have as much sp^3 carbons as GO as they have been reduced.

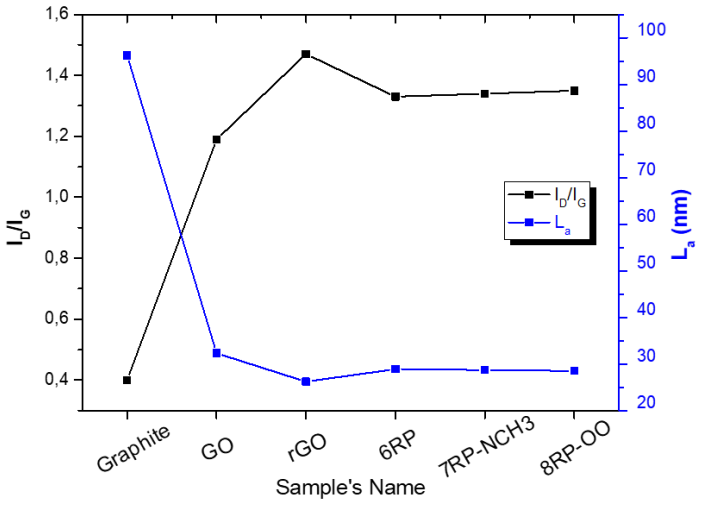

Figure II. 19: The I_D/I_G ratio and L_a obtained from Raman

The structural morphologies of the samples were analyzed by SEM which is a powerful tool that utilizes the detection of secondary electrons to form images (Figure II.20). The SEM images of GO reveal large sheets with not many wrinkles (Figure II.20(a)). The rGO images showed a highly wrinkled crumpled structure which is a result of the restacking of the graphene sheets together due to the π-π interactions arising from the restoration of the sp^2 carbon network post-reduction (Figure II.20(b)). On the other hand, the SEM observation of the pillared samples showed wrinkled sheets that are less crumpled compared to those of rGO (Figures II.20(b), (c) & (d)). This can be attributed to the partial prevention of the restacking of the rGO sheets arising from the pillaring effect as confirmed earlier by XRD.

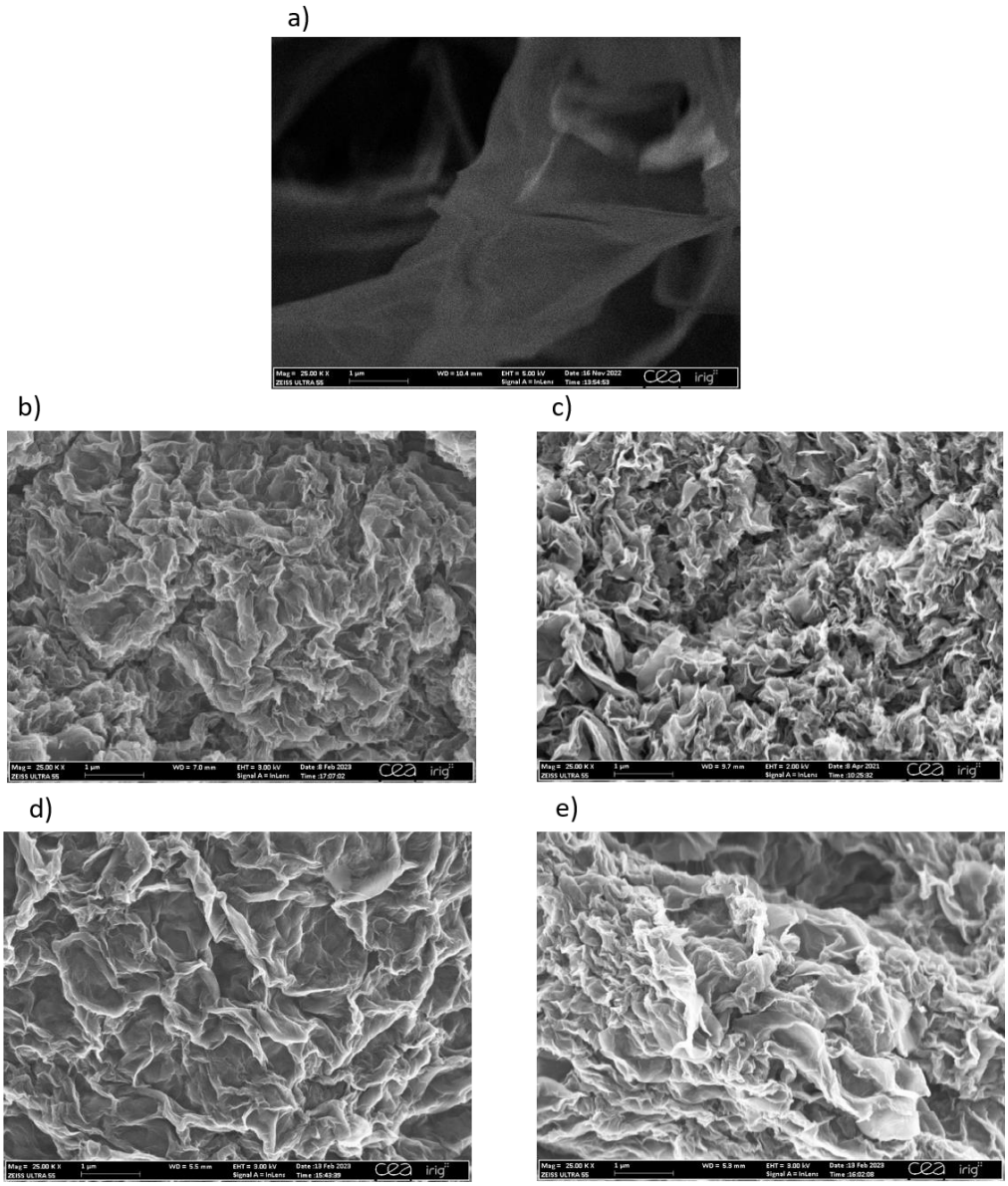

Figure II. 20 : SEM images at 25,000x of a) GO, b) rGO, c) 6RP, d) 7RP-NCH3 and e) 8RP-OO

TEM is another powerful electron microscopy technique giving 2D projections of the samples, using electrons transmitted through thin well-dispersed particles (Figure II.21). It offers high resolutions, thus, giving an insight of the surface texture and local chemical structure of the graphitic sheets in the probed samples. Figures (II.21(a), (c) & (e)) show the low-magnification TEM images of GO, rGO and 6RP, respectively. GO shows a large extended single sheet, while rGO and 6RP show wrinkled few-layer particles. Such few-layers particles can be attributed to partial restacking when restoring the sp^2 carbon network. Figure (II.21(b)) shows a high magnification zoomed-in image on a GO sheet where different surface textures can be observed. The surrounded parts might be sp^2 islands in-between an sp^3 matrix [43]. The texture of rGO seems a bit more mixed as shown in Figure (II.21(d)) owing to the presence of more sp^2 islands due to the reduction using Hz. The stacking of the sheets can also be observed

with the crystallites having between 2 and 6 layers. Same was observed for 6RP (Figure II.21(f)) with a number of layers between 4 and 6. These TEM images were made possible thanks to **Dr. Hanako Okuno.**

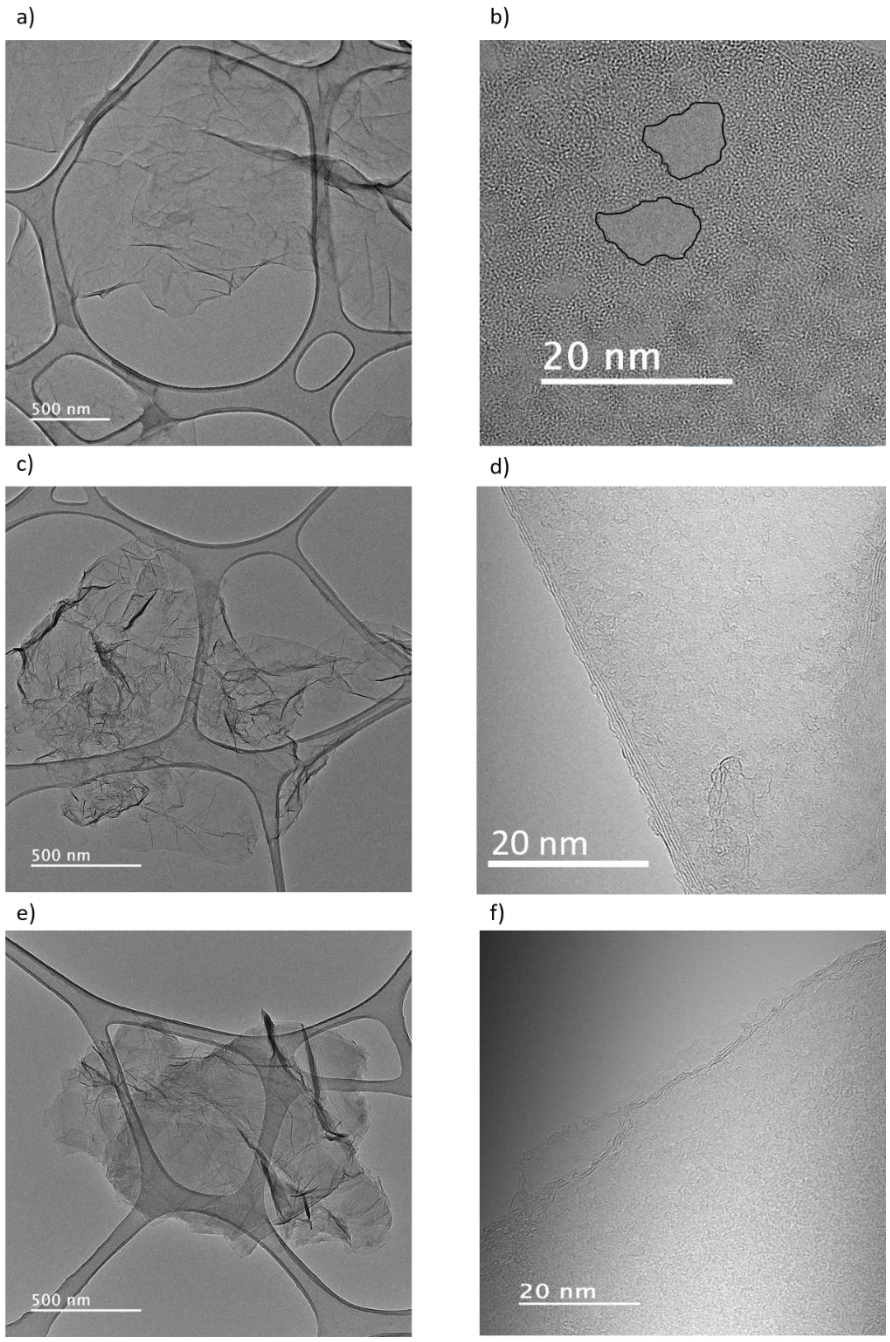

Figure II. 21 : Low magnification TEM images of a) GO, c) rGO and e) 6RP and High magnification TEM images of b) GO, d) rGO and f) 6RP

Gathering the pieces of information from various structural characterization, structural differences between the different samples can be highlighted. The starting Graphite consisted of high number of stacked sheets (65 sheet) of sp^2 carbons (I_D/I_G ratio of ~0.4) with a small interlayer spacing of 0.34 nm as evidenced from XRD and Raman. When oxidized to GO, the interlayer spacing increased to 0.77 nm, the number of stacked sheets decreased due to

successful exfoliation (8 sheets) and the defects increased due to the increase of sp^3 carbons at the expense of sp^2 carbons (I_D/I_G ratio of 1.19). The pillared samples showed the appearance of an extra XRD peak that was attributed to their bridging of the graphene sheets together. They showed more sp^3 carbons than rGO and more sp^2 than GO (I_D/I_G ratios of 1.34 ±1). They also showed a smaller number of stacked sheets (5 sheets) compared to GO and similar to that of rGO as inferred from XRD. The stacking of the sheets was also observed using TEM and it was in agreement with the number of layers calculated from XRD. The average sizes of the sp^2 carbon domains (L_a) were calculated from Raman and the trend in the values was in good agreement with the trend of in-plane crystallite size obtained from XRD (Figure II.22). The differences in the values can be a consequence of the method of calculation, knowing that Sherrer's equations require the assumption that microcrystalline broadening is the only source of peak broadening.

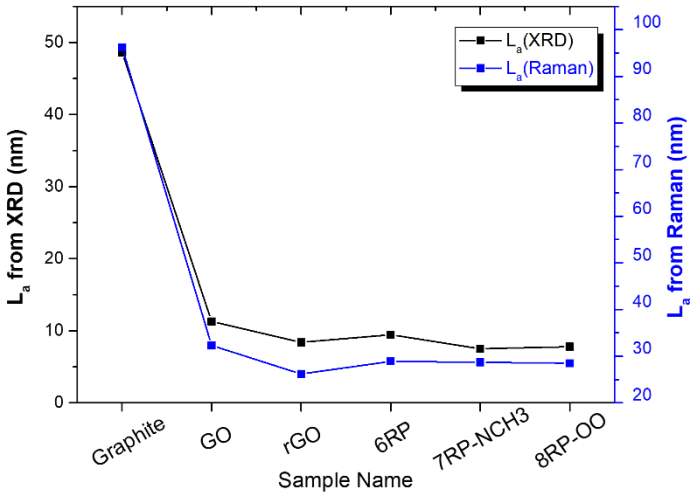

Figure II. 22 : Plot between the L_a values obtained from XRD and Raman for Graphite, GO, 6RP, 7RP-NCH3 and 8RP-OO

Prior to the electrochemical testing, two material properties crucial for the electrochemical performance of the samples as electrode materials for supercapacitors were investigated. The properties are the wettability and the electrical conductivity. The wettability is important as it gives information on the compatability of the synthesized materials and the chosen electrolytes. On the other hand, electrical conductivity is a vital parameter for any electrochemical process, including charge storage in supercapacitors, as it allows for better electron mobility and charge transfer. The wettability was assessed through Water Contact Angle (WCA) measurements and the electrical conductivity was evaluated through four-point probe electrical conductivity measurements.

WCA measurements were done to evaluate the samples' hydrophilicity by dropping water drops on their surfaces and measuring the contact angle of each drop. In this PhD work, the pillars of 7RP-NCH3 and 8RP-OO had been selected with the aim of increasing the wettability of these samples compared to that of 6RP, owing to their inclusion of heteroatoms. The WCA measurements can determine the success of our pillaring strategy in enhancing the hydrophilicity of the samples compared to 6RP. A low water contact angle is observed when the surface is hydrophilic; while, oppositely, a large water contact angle characterizes a hydrophobic surface. Figure (II.23) shows the water contact angle of the different samples synthesized.

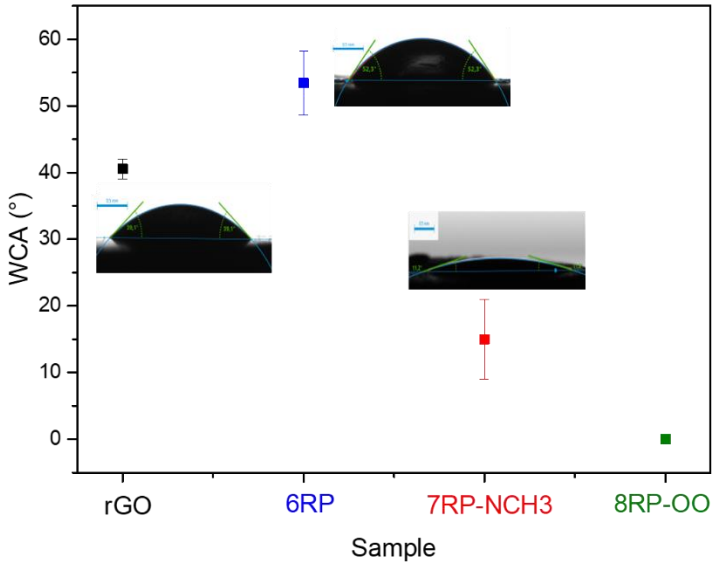

Figure II. 23 : Water Contact Angle of a) rGO, b) 6RP and c) 7RP-NCH3

It can be seen that 6RP is more hydrophobic than rGO as it has a higher WCA (53.42° ±4.75° for 6RP compared to 40.53° ±1.5° of rGO). Such hydrophobicity can be ascribed to the carbon based inter-amine backbone of the 1,6-diaminohexane pillar (6 x CH2) of such sample. On the other hand, 7RP-NCH3 and 8RP-OO turned out to be highly hydrophilic compared to rGO and 6RP. 7RP-NCH3 showed a WCA of 15° ±6°, while 8RP-OO showed ~0° as the drop was instantly absorbed upon contacting the surface of the sample. Such high hydrophilicity can be explained by the chemical nature of the pillars of 7RP-NCH3 and 8RP-OO as they possess polar groups (tertiary amine and 2 x oxygen atoms, respectively, in the middle of the pillar). Such differences in wettability are consequences of various factors, including but not limited to the degree of reduction, the degree of functionalization, the polarity of the pillars and the changes in surface roughness. For instance, increasing the surface roughness and the polarity of the pillars might enhance the wettability, while increasing the degree of reduction (less

hydrophilic oxygen groups) might decrease the wettability [44]. Nevertheless, the change in WCA of the PGM compared to rGO indirectly proves the presence of the pillars inside the samples, and the differences in WCA among the pillared samples themselves are manifestations of the chemical and structural differences between the pillars. Based on the aforementioned WCA measurements, it can be inferred that the experimental design was successful in enhancing wettability of both 7RP-NCH3 and 8RP-OO compared to the 6RP and rGO. In the following section, the effect of the enhanced wettability on the electrochemical performance of those materials as electrodes for supercapacitor applications will be investigated.

Four-point probe electrical conductivity measurements were carried out to assess the electrical conductivity of the samples, which is an important property for supercapacitor applications. No electrical conductivity value could be recorded for GO that is hence confirmed as an insulator due to the disruption of the conductive sp^2 carbon network. After the reduction, the rGO showed an electrical conductivity of 2071 ±22 S/m as it regained some of the electrical conductivity of the starting graphite material (~13350 S/m) as a result of the restoration of the sp^2 conjugated aromatic carbon structures as evidenced by various characterization techniques. The conductivities of the pillared samples are less than that of rGO by 2-3 orders of magnitude (50 ±2, 7 ±0.5 and 28 ±0.4 S/m for 6RP, 7RP-NCH3 and 8RP-OO, respectively). This can be related to the presence of sp^3 carbons due to the functionalization of the rGO sheets with the amine-based pillars.

II.3.2 A Wrap up

Herein, five different samples were synthesized. GO was synthesized as a functionalization platform owing to its various oxygen functionalities that can be involved in various grafting reactions. The synthesis of GO was confirmed through a low C/O ratio, the detection of various oxygen functionalities, the expansion in the d-spacing and the electrical insulating properties. rGO was synthesized as a reference sample against which the electrochemical performance of the PGM was compared. rGO showed an increase in the C/O ratio compared to GO, which is indicative of the partial removal of the oxygen functionalities of the GO. It also showed a higher I_D/I_G ratio and a lower d-spacing, indicating the restoration of the sp^2 carbon network which was manifested in an increase in the electrical conductivity. Various pillared samples were synthesized using different pillaring molecules to yield different parameters such as the interlayer spacing and the wettability. The syntheses were done through the various chemical reactions expected between the amine terminated pillaring molecules and the different oxygen functionalities on the surface of GO such as: i) amide bond formation and ii) epoxide ring opening. The chemical characterization techniques showed the expected

chemical differences between the three pillared samples. For instance, 7RP-NCH3 showed the highest nitrogen content and 8RP-OO showed the highest oxygen content which is in line with the extra NCH_3 group in 7RP-NCH3 and the 2 extra oxygen atoms in the 8RP-OO, respectively. The samples showed the appearance of a new peak in the XRD profile in addition to the rGO peak. Such a peak was attributed to the long-range order arising from the bridging of the rGO sheets together through the pillars. Such peaks are not to be mistaken with GO XRD peaks due to their close d-spacing values as the pillared samples are well reduced as evidenced by the C/O ratio of those samples compared to that of GO and to that of rGO, the most reduced sample, as shown in Figure (II.24).

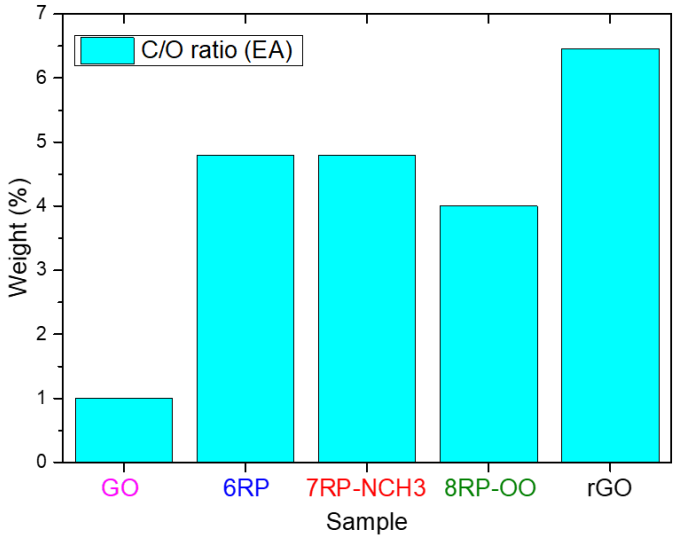

Figure II. 24 : C/O ratio calculated from EA for GO, 6RP, 7RP-NCH3, 8RP-OO and rGO

The produced samples showed the success of the pillaring through the appearance of a new interlayer spacing that is larger than that of rGO while maintaining a relatively high C/O ratio and electrical conductivity, which is necessary for supercapacitor applications. In the following section, the effect of these various chemical and structural parameters on the electrochemical performance of the pillared materials as electrode materials for supercapacitor applications will be evaluated.

II.4 Electrochemical Analysis

Electrochemical characterization was carried out to test the storage performance of the pillared samples as electrode materials of supercapacitors, to compare their performance to that of non-pillared rGO as a reference sample, to relate such performances to their chemistry and structure and to investigate their charge storage mechanisms in different electrolytes. The structure involves mainly the d-spacing parameter resulting from our pillaring methodology to

create new microporous galleries that open up new adsorption sites for the electrolytic ions. These microporous galleries are decorated with different chemistries as different pillars were used for different pillared samples, with different chemical nature and may possess different reducing capabilities, leading to samples with different contents of oxygen and nitrogen of different bonding schemes as shown in the chemical analysis section. The aim is to decipher the effects of the various factors that influence the performance of these intricate systems.

Three-electrode Teflon Swagelok® cells (Figure II.25) were used. The WE consisted of 80% active graphene-based material, 10% Acetylene Black (AB) as conductive additive, 10% PVDF as binder and NMP as dispersing media, drop casted on a Stainless Steel (SS) disc. The CE was a free standing YP50 electrode, ten times the mass of the WE so that it is not limiting. The RE was a pseudo-reference silver wire thinly coated with AgCl. Cyclic Voltammetry (CV), Galvanostatic Charging and Discharging (GCD) and Electrochemical Impedance Spectroscopy (EIS) were carried out in four different electrolytes: i) 3M H_2SO_4, ii) 0.5M Li_2SO_4 and iii) 0.5M K_2SO_4 and iv) 1M KNO_3.

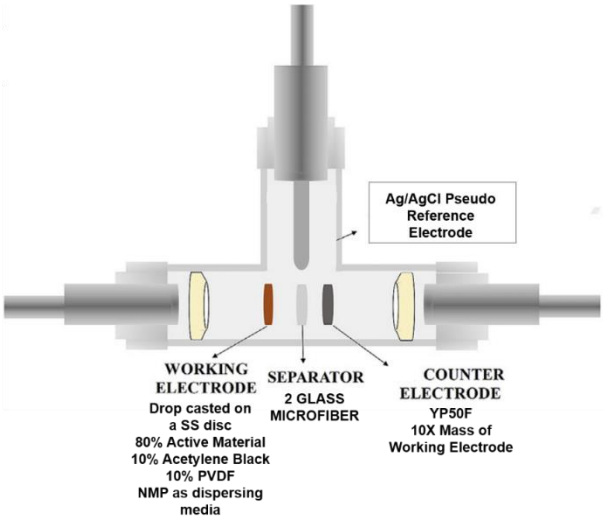

Figure II. 25: A three-electrode Swagelok® cell configuration

All the electrochemical plots are average plots of the electrochemical results produced from multiple electrodes with reproducible CVs. The error bars are always plotted except when it affects the clarity of the plots. The rationale behind this data reporting methodology is presented in chapter 5 (see page 225).

II.4.1 Performance Electrolyte (3M H_2SO_4)

The 3M H_2SO_4 electrolyte was selected as a performance electrolyte to identify the best performing samples. In addition, in this acidic media, electrochemical reactions involving redox active oxygen containing functionalities should play a role in the overall storage process

mechanism. This allows a fundamental study of the structural effect of the pillaring through comparing the performance of the pillared samples to that of non-pillared rGO. It also allows for a fundamental study on the effect of oxygen functionalities on the surface of pillared samples on the performance. The CVs at 5mV/s are presented in Figure (II.26(a)) along with the rate capability plot in Figure (II.26(b)).

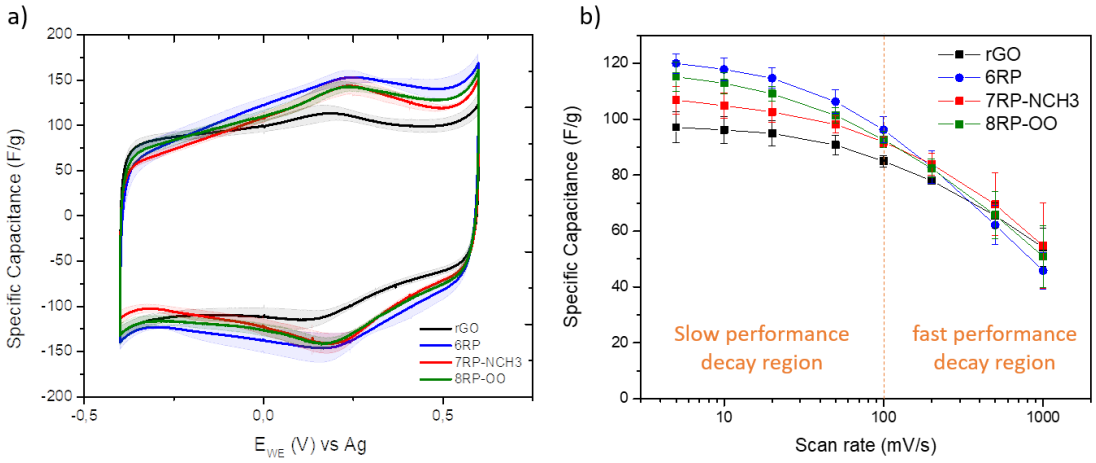

Figure II. 26 : a) Cyclic voltammograms at 5mV/s and b) rate capability of rGO (—), 6RP (—), 7RP-NCH3 (—) and 8RP-OO (—) in 3M H_2SO_4 along with their associated error bars

The CVs of the four samples (rGO, 6RP, 7RP-NCH3 and 8RP-OO) at 5mV/s are all showing quasi-rectangular shape with additional redox peaks between 0.1 and 0.3 V. This shape is indicative of EDLC behavior expected for carbonaceous materials along with redox reactions attributed to the remaining oxygen functionalities. From the rate capability plot, it seems that all the pillared samples are showing a better performance compared to that of rGO. Two regions can be identified in the rate capability plot: i) below 100 mV/s and ii) above 100 mV/s. In the 2nd region, the decrease of capacitance with the scan rate is faster. This can be attributed to higher scan rates, giving rise to limited electrolytic mass transport and hampering the electro-adsorption/desorption of ions, as the ions do not have enough time to properly respond to changes in potential. The average values of Specific Capacitance (C_{SP}) at 5mV/s are 97 ±6, 119 ±3, 106 ±5 and 115 ±5 F/g for rGO, 6RP, 7RP-NCH3 and 8RP-OO, respectively. Such an increase in capacitance with pillared samples (up to ~23% increase) can be attributed to the opening of new microporous galleries, having more oxygen functionalities, and/or making them more accessible to the ions for redox reactions to take place. To test such claims, the effects of the d-spacing and the C=O content on the average capacitance value of each sample are shown in Figure (II.27).

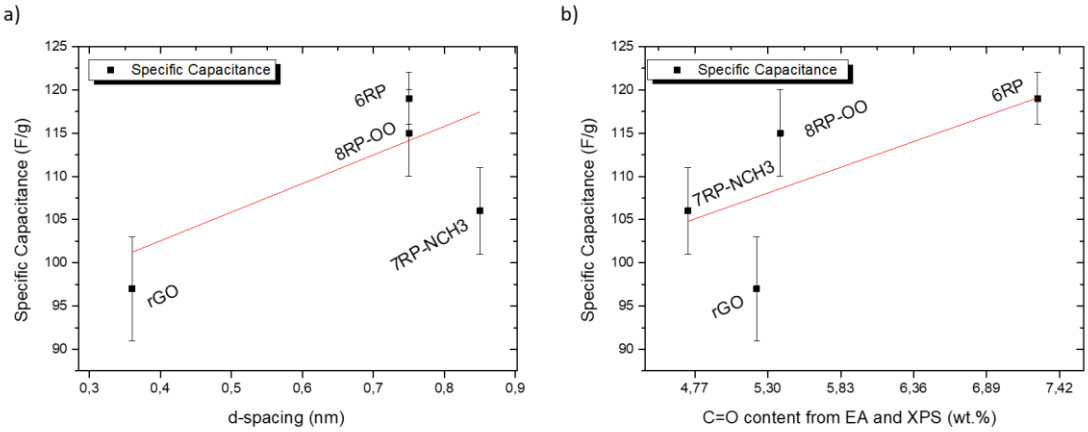

Figure II. 27 : Effect of a) d-spacing and b) C=O content on the average specific capacitance of rGO, 6RP, 7RP-NCH3 and 8RP-OO in 3M H_2SO_4 (red line is a linear fit to guide the eye)

The C=O content was chosen over the overall oxygen content to represent the active oxygen functionalities to avoid any misinterpretations, as it is well reported in literature that basic groups (such as carbonyls and quinones) undergo redox reactions in acidic media like H_2SO_4 while acidic groups (such as phenols) undergo redox reaction in basic media like KOH [13], [45]. It can be seen from Figure (II.27) that there is an increasing trend for the specific capacitance with both the d-spacing and the C=O content. All the pillared samples with larger d-spacing than rGO have higher capacitances than rGO. 7RP-NCH3 has the highest d-spacing, however, it is not the sample with highest capacitance. This may be ascribed to the fact that it is the pillared sample with the least C=O content, showing that the structure is not the only factor in play; the chemistry plays a role as well. On the other hand, 6RP and 8RP have lower d-spacing values compared to 7RP-NCH3 but higher C=O, leading to higher capacitance values. An interesting observation is that rGO has a C=O content higher than that of 7RP-NCH3 and similar to that of 8RP-OO, but its capacitance is the lowest. From that, the following can be concluded: i) the increase in d-spacing is important for opening new pores for ion-sorption and making the surface active oxygen functionalities more accessible to the electrolytic ions, and ii) when a sufficient d-spacing is established, the amount of active oxygen functional groups becomes the more capacitive influencing factor. The former has been shown with rGO having higher C=O content than 7RP-NCH3 and similar to that of 8RP-OO and yet it has the lowest average capacitance. The C=O groups of rGO seem to be less accessible than those of 7RP-NCH3 and 8RP-OO that are less dense, but seem to be more accessible thanks to their larger d-spacing (0.84 nm for 7RP-NCH3 and 0.75 nm for 8RP-OO). The latter has been shown by comparing 6RP, 7RP-NCH3 and 8RP-OO. They all have sufficient d-spacing values to make the C=O groups more accessible compared to those of rGO; however, the one with higher C=O content (6RP) is the one with the highest capacitance, confirming the electroactivity of C=O

groups as carbonyls and quinones in acidic media according to the reaction schemes in Eq. (II.6) and Eq. (II.7). Such observation further validates the dependency of the capacitance of the samples cycled in 3M H_2SO_4 on the C=O content and that such trend holds for pillared graphene materials.

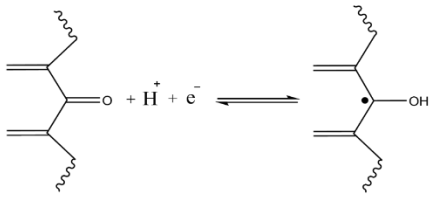

(II.7)

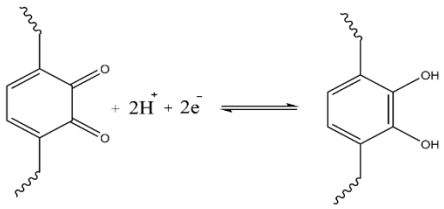

(II.8)

To verify the charge storage mechanism proposed earlier based on the shapes of the CVs (EDLC+surface fast redox reactions), the Conway's method was applied. This method allows to differentiate between capacitive non-diffusion limited (surface-driven behavior) and diffusion limited processes through examining the power dependence of the current at a certain potential on the scan rate (b-value) by fitting Eq. (II.9). Herein, the peak current of the CVs at different scan rates were used for the fitting.

$$i = av^b \qquad (II.9)$$

It can be seen that the power dependence is close to ~1 which is indicative of non-diffusion capacitive processes attributed to EDLC and surface fast redox reactions (Figure II.28).

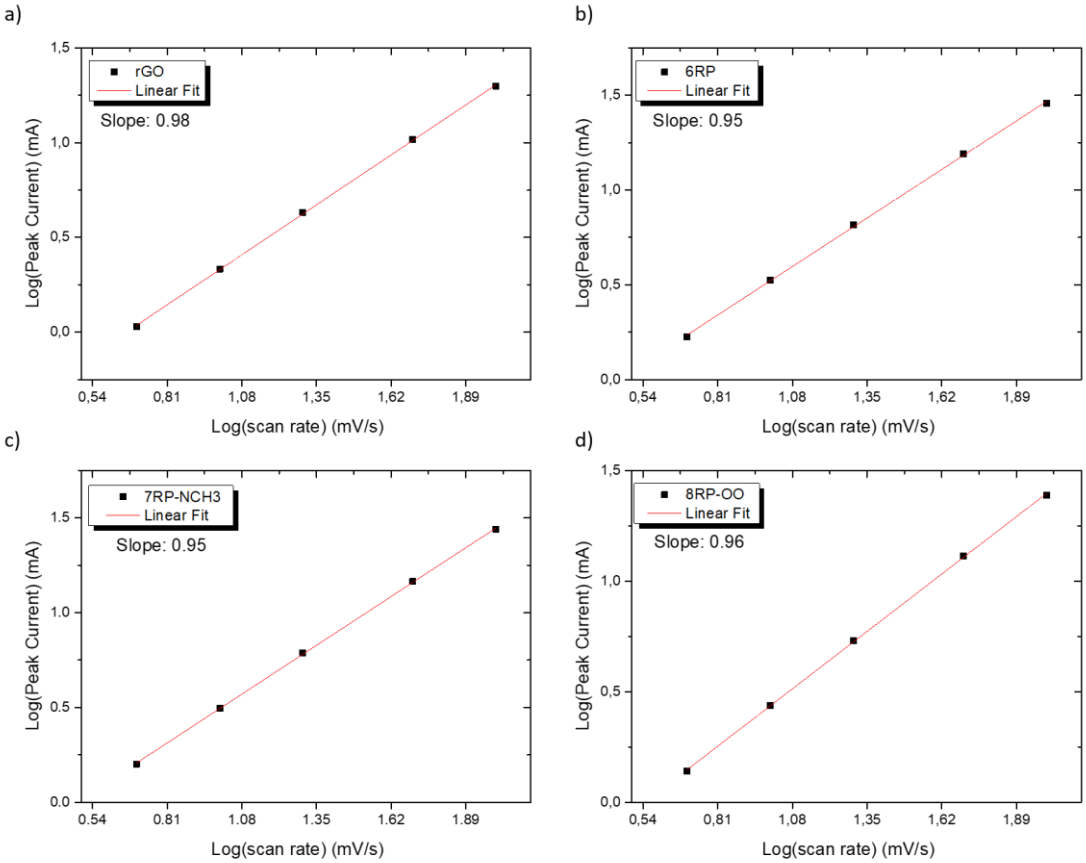

Figure II. 28 : Conway's method to find the power dependence of the current on the scan rate for a) rGO, b) 6RP, c) 7RP-NCH3 and d) 8RP-OO in 3M H_2SO_4

Galvanostatic charge/discharge experiments were performed to further assess the capacitance of the samples. Figure (II.29) shows the average charge and discharge curves of the samples at a constant current of 5mA. A linear time-dependence of the potential is observed for rGO, while a near-linear behavior is observed for 6RP, 7RP-NCH3 and 8RP-OO. Such linearity is attributed to EDLC charge storage mechanism with the absence of major redox reactions, while the small deviations from the (t-V) linear relationship of the pillared samples can be attributed to some redox reactions taking place, which is consistent with the CV shapes. The specific capacitance was plotted against the constant current values to check how the samples perform at different discharging currents (Figure II.30). It can be seen that all the pillared samples possess higher capacitance values compared to rGO (98 ±7, 126 ±6, 107 ±7, 113 ±2 F/g at 5mA (2.7 A/g) for rGO, 6RP, 7RP-NCH3 and 8RP-OO, respectively) even at high discharge current (77 ±6, 93 ±2, 95 ±2, 92 ±1 F/g at 50mA (27 A/g) for rGO, 6RP, 7RP-NCH3 and 8RP-OO, respectively). The values are in very good agreement with those obtained from CVs.

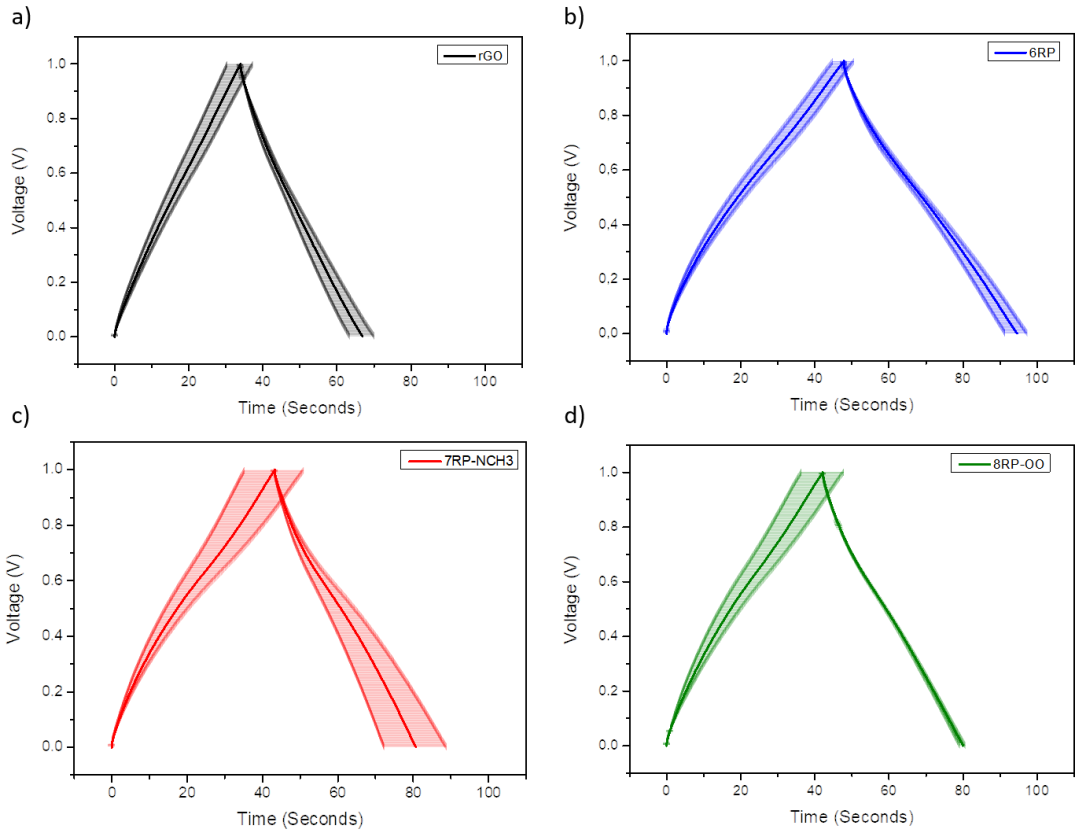

Figure II. 29 : a) Average galvanostatic charge and discharge curves at a constant current of 5mA for a) rGO (—), b) 6RP (—), c) 7RP-NCH3 (—) and d) 8RP-OO (—) along with their error bars

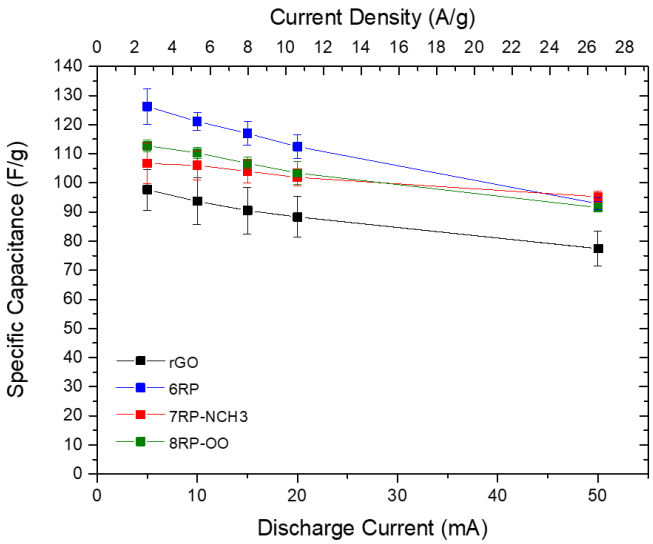

Figure II. 30 : Specific capacitance versus discharge current for rGO (—), 6RP (—), 7RP-NCH3 (—) and 8RP-OO (—) along with their associated error bars

Electrochemical Impedance Spectroscopy (EIS) was carried out to electrochemically characterize the samples in various frequency regimes. The EIS data give information on the internal resistance, ion diffusion and the capacitive nature of the system. Also, once these data are treated and plotted in various ways, the values of capacitance and the effective ionic

transport resistance inside the pores can be extracted, adding up to a broad mechanism scheme suggestion. The extracted capacitance values can be compared to those from CVs or charge-discharge curves, thus helping confirm and discuss the trends observed.

The experiments were carried out at OCV in a frequency range from 10mHz to 100KHz. Figure (II.31) shows the complex-plane plot (commonly known as Nyquist plot). Three different regions can be identified: i) a semi-circle like signature at high frequencies which can be attributed to charge transfer resistance (R_{CT}) or interfacial impedance between the electrode and the current collector, ii) a sloping line at intermediate frequencies which can be ascribed to ion diffusion, and iii) a near vertical line at low frequencies representing the differential capacitance. A deviation from the theoretical vertical line is expected for porous carbons [46].

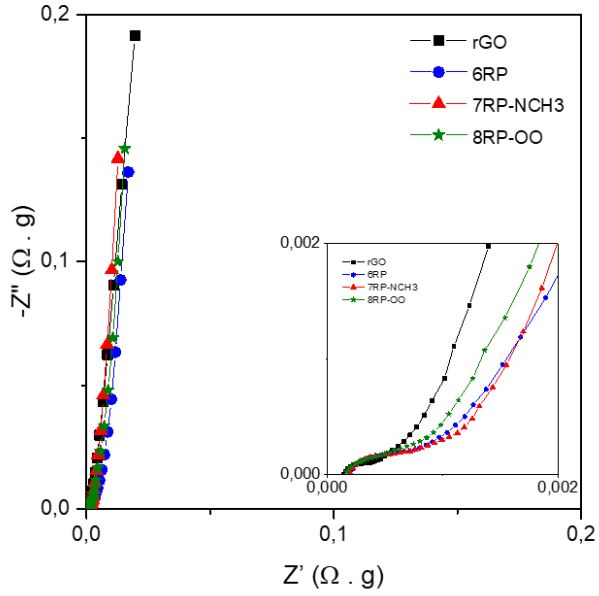

Figure II. 31 : Average Nyquist plots of rGO (—), 6RP (—), 7RP-NCH3 (—) and 8RP-OO (—). Insert: a zoom in for the high frequency region

Looking at the intercept of the plots with the real impedance axis at high frequencies, gives an insight on the Equivalent Series Resistance (R_{ESR}) that arises from the total internal resistance of the cell (electrode resistance, electrolyte resistance and contact resistance between the electrode and the current collector). It can be seen that the R_{ESR} of the samples follow the following trend: rGO (0.14 mΩ.g) < 8RP-OO (0.16 mΩ.g) < 7RP-NCH3 (0.19 mΩ.g) ≤ 6RP(0.2 mΩ.g). The rGO seems to have a lower R_{ESR} which can be attributed to the higher electrical conductivity of such sample compared to the pillared ones as shown in the previous section (2-3 orders of magnitude higher).

As stated before, the semi-circle like curve at high frequency can arise either from charge-transfer resistance or from interfacial impedance. If this semi-circle was a consequence of R_{CT}, it would change when doing EIS at different potentials [46]. Unlike R_{CT}, interfacial impedance will be constant all over the potential range. Accordingly, to try to find out the origin of this semi-circle like curve at high frequencies in the case of the pillared samples, the EIS was carried out at various DC potential inputs for 6RP as a representative sample as it is the sample with the most surface oxygen functionalities and the strongest redox peaks, so the highest probability of charge transfer resistance (R_{CT}), if any charge transfer is present. The EIS was carried at at -0.2 V, 0 V, OCV (0.247 V) and 0.4 V versus Ag (Figure II.32).

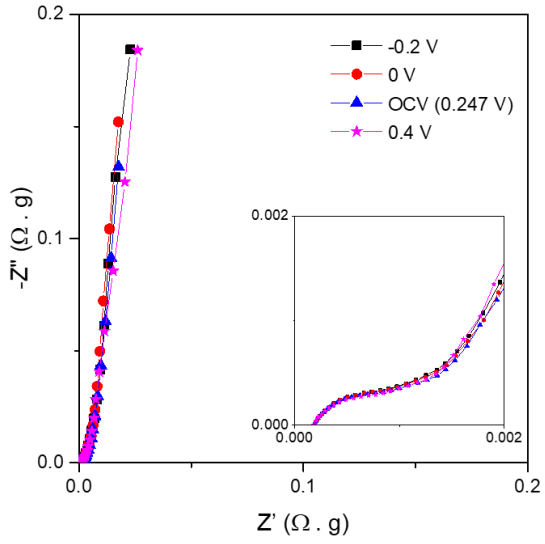

Figure II. 32 : Average Nyquist plots of 6RP at multiple potential values: -0.2V (—), 0V (—) OCV (0.247V) (—) and 0.4V (—). Insert: a zoom in for the high frequency region

It was found that the impedance at high frequency regions does not change when the EIS is recorded at multiple potentials, thus confirming that such signature at high frequency is a consequence of the interfacial impedance between the electrode and the current collector. Such a finding is consistent with what was reported by Mathis, T.S. et al. that the most likely reason for supercapacitor laboratory cells to show semi-circles is the interfacial impedance between the electrode and the current collector [46].

From the insert in Figure (II.31), rGO shows a quick transition to capacitive behavior from the high frequency region to the low frequency region as compared to the rest of the samples which can be attributed to better charge diffusion as the storage in such samples takes place on the external surfaces of the rGO sheets and in the inter-particle porosity. On the other hand, the pillared materials have microporous galleries as a result of pillaring which might impose some diffusion limitations on the ions, thus, showing a slower transition to capacitive behavior

compared to rGO. At low frequencies, a steep rise in the imaginary component of the impedance, giving near vertical lines, was observed for all the samples indicative of the capacitive nature of such materials.

Real and Imaginary capacitances were calculated based on equations (II.6) and (II.7) according to the complex model reported by Taberna, P.L. et al. [47]. This model is used to extract the values of capacitance at low frequencies and to compare them to those of CVs and charge discharge curves and also to determine the effective ion transport resistance inside the pores to inspect the effect of the pillars on such a parameter compared to the rGO.

$$C' = \frac{-Z''(\omega)}{\omega|Z(\omega)|^2} \qquad (II.6)$$

$$C'' = \frac{Z'(\omega)}{\omega|Z(\omega)|^2} \qquad (II.7)$$

Where C' and C'' are the real and imaginary parts of the capacitance, respectively, $Z'(\omega)$ and $Z''(\omega)$ are the real and imaginary parts of the impedance, respectively and ω is the angular frequency ($\omega = 2\pi f$ where f is the frequency). The real component of the capacitance (C') represents the capacitance of the electrode as a function of the frequency; thus, at low frequency, a capacitance value can be extracted, corresponding to that extracted from charge/discharge curves, for example. The imaginary component of the capacitance (C'') corresponds to energy dissipation due to irreversible processes. Accordingly, the C' was plotted versus the frequency (Figure II.33(a)) to extract the specific capacitance values. The specific capacitance values at 10 mHz were 83 ±12, 115 ±12, 112 ±8 and 108 ±7 F/g for rGO, 6RP, 7RP-NCH3 and 8RP-OO, respectively. The capacitance trend follows that of CVs and galvanostatic charge and discharge, showing that pillared samples are out-performing the rGO, especially at low scan rates or low constant currents (corresponding here to low frequencies) as shown in Table (II.8) at the end of this sub-section. In addition, the C'' was plotted against the real component of the impedance (Figure II.33(b)) in order to relate the energy losses to the impedance at different frequencies, thereby allowing to evaluate the effective ionic transport resistance inside the pores in a facile way [8]. The effective ionic transport resistance inside the pores shows the following trend rGO (1.2 mΩ.g) < 7RP-NCH3 (1.8 mΩ.g) < 8RP-OO (2 mΩ.g) < 6RP (4.1 mΩ.g). This can be attributed to the external surface adsorption in case of rGO, while for pillared samples, electrolytic ion diffusion can be impeded by the pillars. Moreover, the lower ionic resistance observed for 7RP-NCH3 and 8RP-OO compared to 6RP could be due to their higher wettability attributed to the high electronegative polar groups in the backbone of

their pillars and also due to the larger d-spacing of 7RP-NCH3. Both chemical and structural parameters might facilitate the ions diffusion in the pores of those samples compared to the 6RP. Despite higher ionic transport resistance inside the pores of the pillared samples compared to rGO, they possess higher average capacitance values than those of rGO as confirmed by various electrochemical methods.

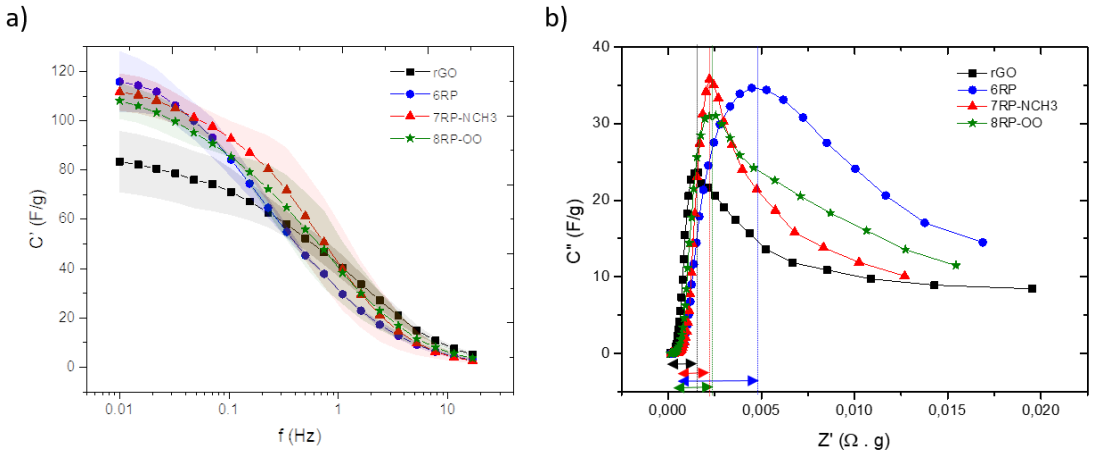

Figure II. 33 : a) Real Capacitance versus the frequency and b) Imaginary Capacitance versus the real impedance of rGO (—), 6RP (—), 7RP-NCH3 (—) and 8RP-OO (—)

The 6RP sample is having the highest R_{ESR} and the highest effective ionic transport resistance and yet, it is the sample with the highest specific capacitance, owing to its high C=O content that allows redox reactions to take place. Also, the high concentration and ionic conductivity of the 3M H_2SO_4 help mitigate the ionic resistance problem in 6RP. It can be considered that 6RP is having the highest effective ionic transport resistance among the samples tested; however, this ionic resistance value is low in absolute terms. As a comparison, it has an ionic transport resistance value in 1M $TEABF_4$ in ACN five times that in 3M H_2SO_4 [8]. This shows the important contribution of surface chemistry to pillared samples' specific capacitance values in such electrolyte, given reasonable hydrophilicity, ionic conductivity and in-pore ionic resistance are present in the sample.

Table (II.8) summarizes the results discussed so far for the different samples cycled in 3M H_2SO_4. It shows that pillared samples outperform rGO in 3M H_2SO_4, and that this was attributed to opening up new adsorption sites through pillaring, making electrochemically active surface oxygen functionalities more accessible to the electrolytic ions to counter the charges resulting from redox reactions. It also shows an increase in capacitance values as the C=O content increases, in addition to showing a b-value close to 1, indicating non-diffusion limited charge storage mechanism, that is EDLC and surface fast redox reactions.

Sample	d-spacing	C=O (wt.%)	Avg. Specific Capacitance at 5mV/s (F/g)	Increase in capacitance vs rGO at 5mV/s (%)	Avg. Specific Capacitance at 5mA (F/g)	Avg. Specific Capacitance at 10 mHz (F/g)	b-value
8RP-OO	0.75	5.39	115 ±5	19	113 ±6	108 ±7	0.96
7RP-NCH3	0.85	4.72	106 ±5	9	107 ±5	112 ±8	0.95
6RP	0.75	7.26	119 ±3	23	126 ±6	115 ±12	0.95
rGO-Hz	0.36	5.22	97 ±6	-	97 ±5	83 ±12	0.98

Table II. 8 : Summary of the electrochemical analysis of rGO, 6RP, 7RP-NCH3 and 8RP-OO in 3M H_2SO_4

II.4.2 Effect of Cation and Anion sizes on the Performance

The above work showed not only that the structure, manifested in the d-spacing parameter, has an effect on the capacitance, but also that the chemistry, particularly electrochemically active oxygen species, plays a role as well in enhancing the capacitance. Accordingly, a study was done using two sulfate-based electrolytes of different cation sizes to further test the effect of the structure and chemistry of the pillared samples, as well as studying the effect of the hydrated cation and anion sizes on the performance and charge storage mechanisms of these samples. The selected electrolytes were 0.5M Li_2SO_4 and 0.5M K_2SO_4. Lithium and potassium sulfates were selected as neutral electrolytes of different (hydrated) cation sizes in which redox reactions involving the remaining oxygen functionalities are expected to be minimized [43]. Hence, the effect of the cation size can be screened from any other factors that can affect the performance and mechanism to be able to relate performance to the different (hydrated) cation sizes of the electrolytes. Despite the small size of the protons in 3M H_2SO_4, the d-spacing seemed to have an effect on the performance; however, in this new study, the solvated ion size is in the range of the d-spacing so it may have an even more profound impact on the performance. To test the effect of the anion size, 1M KNO_3 was selected and compared to 0.5M K_2SO_4 as they both possess the same cation but anions of different sizes. The sizes of naked and solvated ions of the electrolytes involved in such a study are summarized in Figure (II.34).

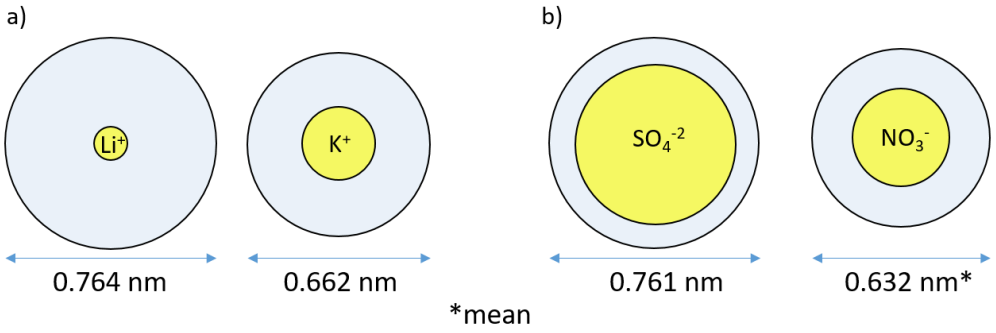

Figure II. 34 : Size of naked and water-solvated a) Cations and b) anions used in this study. Values of such spherical models were extracted from [48]

It can be seen that although naked Li^+ is smaller than naked K^+, its hydrated ion size is larger than that of K^+ owing to its higher charge density, resulting in a stronger tendency to polarize the water molecules in its vicinity.

II.4.2.1 0.5M Li_2SO_4

Figure (II.35) shows the CVs of the different samples in 0.5M Li_2SO_4. The CV of rGO looks rectangular with no redox peaks, indicative of only EDLC mechanism. 6RP and 8RP are showing quasi-rectangular CVs. 7RP is showing a rectangular CV with obvious and pronounced peaks. The presence of such peaks in neutral electrolytes was not expected as mentioned earlier. 6RP and 8RP-OO are showing asymmetric CVs as compared to the symmetric CV shape of rGO and 7RP-NCH3.

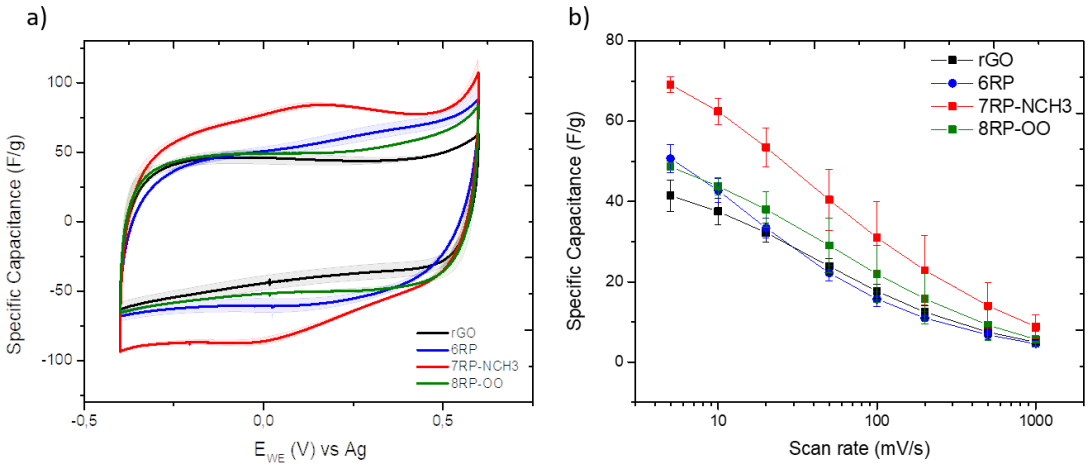

Figure II. 35 : a) Cyclic voltammograms at 5mV/s and b) rate capability of rGO (—), 6RP (—), 7RP-NCH3 (—) and 8RP-OO (—) in 0.5M Li_2SO_4 along with their associated error bars

The rate capability shows that 7RP-NCH3 and 8RP-OO are having higher average capacitance values than rGO at all scan rates, with the 7RP-NCH3 outperforming all of the tested samples (68% increase in capacitance compared to rGO at 5mV/s). 6RP seemed to have a higher average capacitance value than that of rGO, only up to 10mV/s. Above 20 mV/s 6RP's performance drops and becomes similar to that of rGO. The average capacitance values at 5mV/s are 41 ±4, 51 ±3, 69 ±2 and 49 ±1 F/g for rGO, 6RP, 7RP-NCH3 and 8RP-OO, respectively.

This rate capability study raises many questions. To investigate i) such an increase in capacitance for pillared samples compared to rGO, ii) the superiority of 7RP-NCH3 against the others, iii) the appearance of the prominent peaks for the 7RP-NCH3 sample, and iv) the slightly higher performance of 8RP-OO compared to 6RP, the average specific capacitance values obtained for the different samples have been plotted with respect to various parameters such as d-spacing, C-O content, C=O content and nitrogen content (Figure II.36).

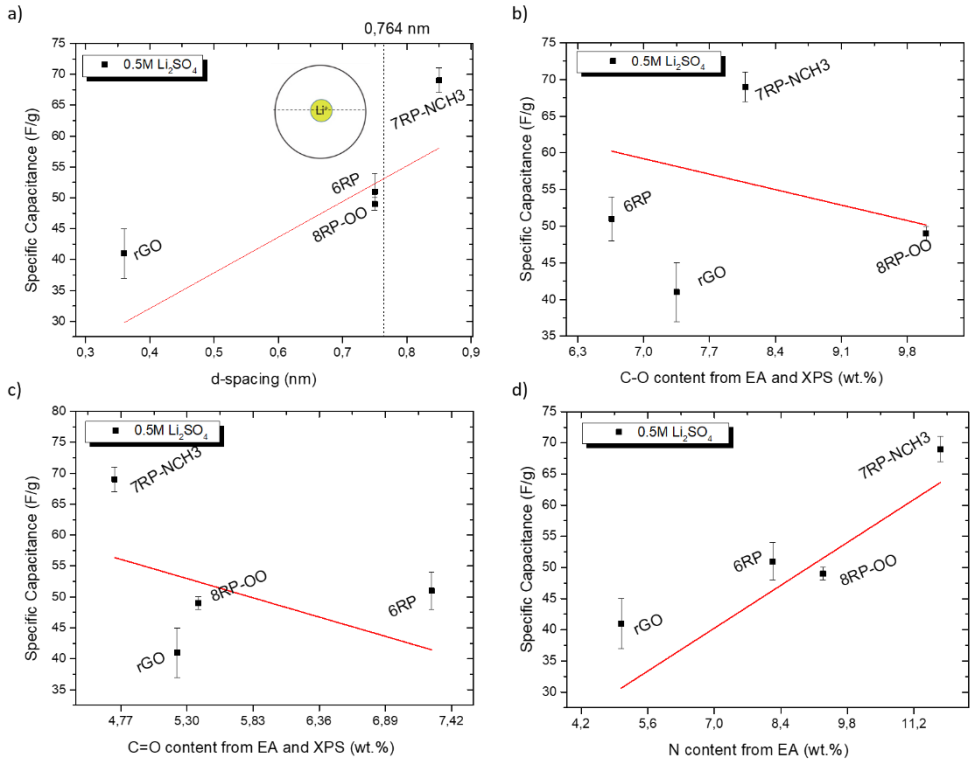

Figure II. 36 : Effect of a) d-spacing, b) C-O content, c) C=O content and d) nitrogen content on the average specific capacitance of rGO, 6RP, 7RP-NCH3 and 8RP-OO in 0.5M Li_2SO_4 (red line is a linear fit to guide the eye)

The C-O and C=O calculated from XPS and elemental analysis were selected to try to identify whether the nature of oxygen groups could explain the observed capacitance increase. When calculating the C-O content for the 8RP-OO sample, a correction was done using the number of moles of pillars extracted from the TGA plots to account for the extra C-O coming from the backbone of its pillars. In other words, the C-O content of 8RP-OO, presented above and in the upcoming figures, only represents the C-O related to the rGO sheets and no longer includes the C-O coming from the pillar.

From tracing the trend between d-spacing and C_{SP}, it can be seen that the capacitance increases with the increase in d-spacing, with 7RP-NCH3 being the sample with the largest d-spacing and the best performance. However, it has to be noted that the d-spacing values of 6RP and 8RP-OO (0.75 nm) are very close to the diameter of the hydrated lithium ion size (0.764 nm), which might be impeding the performance of these samples. Regardless, 8RP-OO seems to have a slightly better performance at different scan rates compared to 6RP despite having the same d-spacing value (Figure II.35(b)). Such an observation could be explained by the presence of the two extra oxygen atoms in the backbone of the pillars of 8RP-OO, enhancing the wettability as confirmed by WCA measurements, thus driving more ions near the surface to be adsorbed. On the other hand, 7RP-NCH3 is having a higher rate capability compared to the rest

of the samples, which might be attributed to its larger d-spacing compared to the size of the hydrated cation.

The contents of C-O and C=O do not seem to have a direct impact on the capacitance (Figures II.36(b) & (c)) despite probable ion-dipole interactions between alkali metal cations and carbonyl groups being reported in literature [49], [50]. On the other hand, the capacitance seems to follow an increasing trend with the nitrogen content with 7RP-NCH3 having the highest amount of nitrogen and the highest value of capacitance (Figure II.36(d)). However, care must be taken before concluding on the effect of the nitrogen and C=O contents because such trends might just be an outcome of the hydrated cation (Li^+) size (0.764 nm) being slightly greater than 6RP and 8RP-OO d-spacing values (0.75 nm), leading to a more restricted adsorption active surface area. Hence, relating their performances to their nitrogen and oxygen contents would not be very straightforward.

II.4.2.2 Eliminating the cation size constraint (0.5M K_2SO_4)

Consequently, another electrolyte, 0.5M K_2SO_4, was selected as it has a smaller hydrated cation (K^+) size of 0.662 nm, which would lift the cation size constraint from the 6RP and 8RP-OO samples, and enable more reliable conclusions regarding the effects of nitrogen and oxygen contents on the specific capacitance. The d-spacing value of 6RP and 8RP-OO is around 13% larger than the size of hydrated potassium ion, alleviating the hydrated cation size related concerns. The CV shapes in 0.5M K_2SO_4 are similar to those observed in 0.5M Li_2SO_4 with the peaks being more prominent, especially for 7RP-NCH3 (Figure II.37).

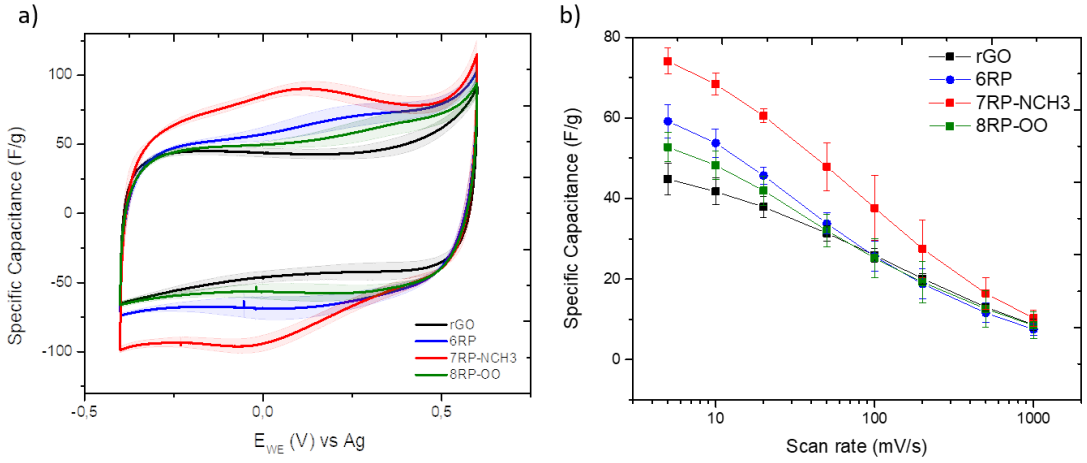

Figure II. 37 : a) Cyclic voltammograms at 5mV/s and b) rate capability of rGO (—), 6RP (—), 7RP-NCH3 (—) and 8RP-OO (—) in 0.5M K_2SO_4 along with their associated error bars

In K_2SO_4, the rGO sample is showing a quasi-rectangular CV shape, while the others are showing a quasi-rectangular CV coupled with broad bumps on positive potential for 8RP-OO

and 6RP, and with distinct peaks for 7RP-NCH3. 6RP and 8RP-OO are still possessing asymmetric CV shapes compared to symmetric CV shapes of rGO and 7RP-NCH3. The capacitance values at 5mV/s are 45 ±4, 59 ±4, 74 ±3 and 53 ±3 F/g for rGO, 6RP, 7RP-NCH3 and 8RP-OO, respectively. There is a slight increase in the capacitance of all the samples at all scan rates compared to the values obtained with 0.5M Li_2SO_4 that could be a consequence of the smaller cation size which might lead to slightly increased amount of adsorbed ions in the pores, combined with the higher ionic conductivity of the 0.5M K_2SO_4 (71 mS/cm for 0.5M K_2SO_4 and 42 mS/cm for 0.5M Li_2SO_4).

The rate capability study shows that 6RP and 8RP-OO are having higher capacitance values compared to rGO up to 100 mV/s; above this scan rate, their average capacitance values become similar to that of rGO. The deterioration of performance can be explained by electrolytic ions diffusion kinetics: at higher scan rates, ions do not have enough time to diffuse into the microporous galleries of such samples, so only external surface adsorption takes place, thus leading to C_{SP} values similar to that of rGO where only external surface adsorption is expected. Contrary to what is observed in 0.5M Li_2SO_4, 6RP displayed a slightly better rate capability compared to 8RP-OO, once the cation size constraint was removed and the ionic conductivity was enhanced (71 mS/cm for K_2SO_4 and 42 mS/cm for 0.5M Li_2SO_4). Distinctly, 7RP-NCH3 sample shows a higher capacitance compared to the rest of the samples even at very high scan rates, indicating that such sample is the best performing in this electrolyte at various scan rates. Figure (II.38) shows the effect of d-spacing, C-O content, C=O content and nitrogen content on the specific capacitance values of the samples in 0.5M K_2SO_4.

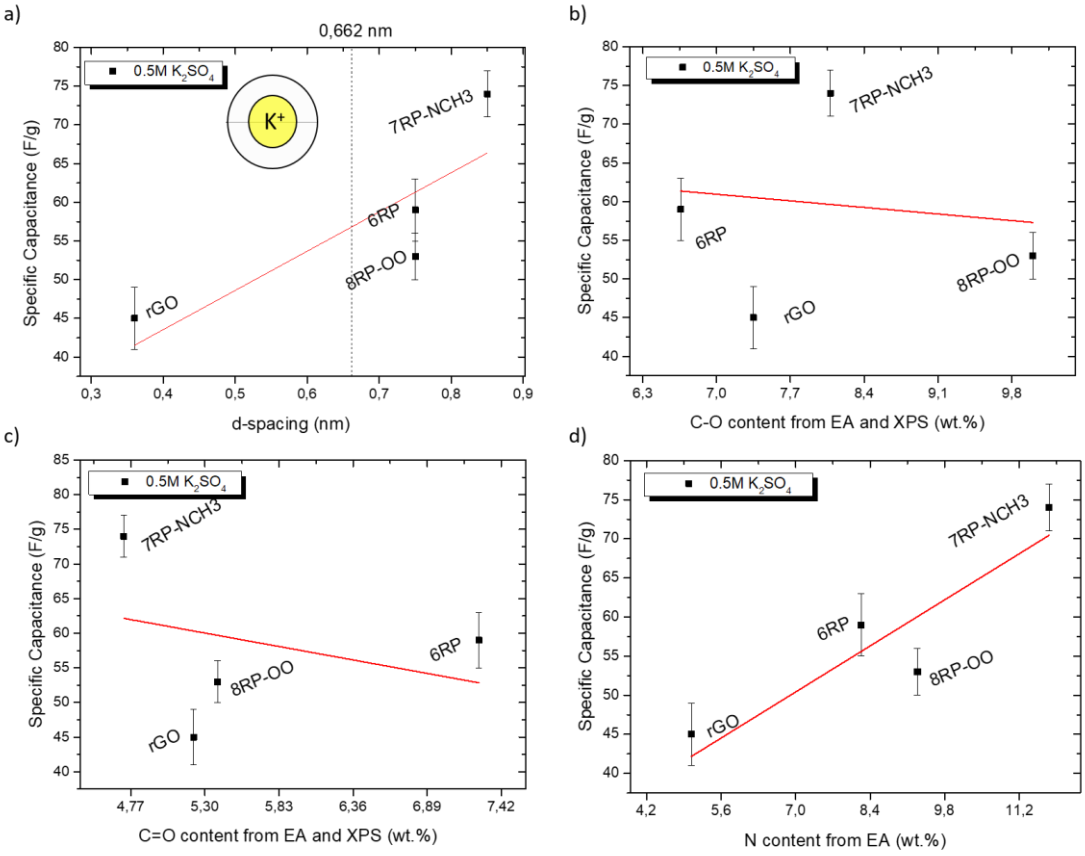

Figure II. 38 : Effect of a) d-spacing, b) C-O content, c) C=O content and d) nitrogen content on the average specific capacitance of rGO, 6RP, 7RP-NCH3 and 8RP-OO in 0.5M K_2SO_4 (red line is a linear fit to guide the eye)

The same trends spotted for 0.5M Li_2SO_4 are observed for 0.5M K_2SO_4 although cation size constraint was removed for 6RP and 8RP-OO: the capacitance increases with the increase in d-spacing and nitrogen content, while the different oxygen functionalities do not seem to have a direct impact on capacitance. The best performing sample was found to be the one with the lowest C=O content, contrary to what was expected to take place once the cation was changed to one with a hydrated size smaller than that of the d-spacing (hydrated K^+ matches this requirement), allowing them to enter inside the pores and interact with the C=O groups. This can either rule out the role of the C=O bond in increasing the capacitance in such electrolyte or hint at an restricted accessibility of the pores to the ions. Accordingly, it seems that the effect of nitrogen content could be the C_{SP} controlling parameter after cation size constraint removal. However, such a conclusion would not show the whole picture.

II.4.2.3 7RP-NCH3 under Scrutiny

The electrochemical behavior of the 7RP-NCH3 has not been fully discussed yet, especially that this sample is showing unique peaks that are not visible in the rest of the samples in 0.5M Li_2SO_4 and 0.5M K_2SO_4. On its first CV cycle in Li_2SO_4 and K_2SO_4, a strong anodic current coupled with an irreversible oxidation peak is observed (Figure II.39). Therefore, the

analysis of the appearance of such peaks could help in understanding the effect of various elements on the capacitance enhancement in such electrolytes.

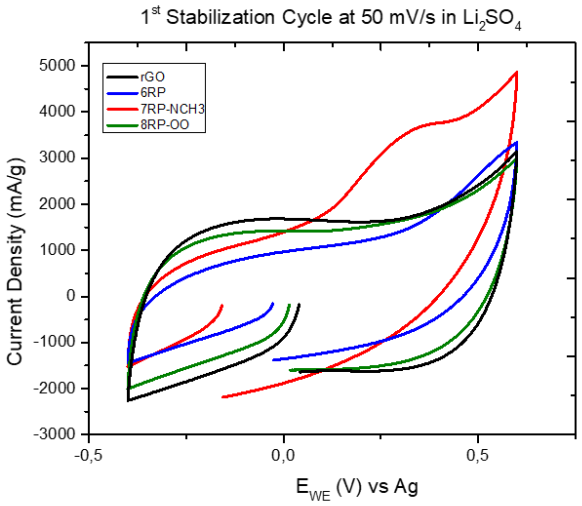

Figure II. 39 : 1st Stabilization CV cycle at 50 mV/s of rGO (—), 6RP (—), 7RP-NCH3 (—) and 8RP-OO (—) in 0.5M Li_2SO_4

In the following sub-sections, possible interpretations for the appearance of such anodic current with an irreversible peak will be presented and then a specific experiment designed to confront these hypotheses will be discussed.

II.4.2.4 Attempting to solve the Enigma

Such an increase in capacitance and appearance of peaks when cycling the 7RP-NCH3 sample in neutral electrolytes can be indirectly attributed to having more nitrogen content in the form of the extra tertiary amine group (>NCH_3) in the backbone of the pillar. The premise of higher nitrogen content coming from higher functionalization can be ruled out, since TGA analysis allowed to identify that the number of moles of pillars per gram of pillared sample was similar for the 3 grafted samples. Some explanations are proposed below as to why the pillared sample with an extra tertiary amine is showing the best performance in both 0.5M Li_2SO_4 and 0.5M K_2SO_4. First, tertiary amines are the easiest type of amines to be oxidized in their free solution form; so the tertiary amines inside the pillars might have been also easily oxidized after functionalizing the GO sheets with those pillars. Based on literature [51]–[53], the oxidation of such tertiary amine might either i) break the pillars into two halves, one terminated with a secondary amine and the other terminated with an aldehyde (Figure II.40(a)), forming specific adsorption sites/pockets for Li^+ and K^+, or ii) form a secondary amine instead of the tertiary amine by releasing the CH_3 group as a formaldehyde molecule (Figure II.40(b)). In both pathways, the secondary amines or the initial tertiary amines can be protonated by the produced protons to form stable quaternary ammonium ions. In the former case where the pillar is broken

into 2 halves, the presence of carbonyl groups from the aldehyde terminated half of the pillar and/or secondary amine groups from the other half can lead to ion-dipole interactions with the alkali metal ions such as K^+ and Li^+ leading to interactions between the ions and pillar (ion-specific adsorption of K^+ and Li^+). This interaction can lead to local changes in the electronic charge density around the carbonyl and/or amine groups, leading to an extra boost to the EDLC [50]. Such possible interactions with carbonyl groups and/or various secondary amines in such a nano-confined environment might lead to the appearance of the observed peaks. The breaking of the pillar can also give more rotational freedom to the sp^3 bonds of the pillars, which might facilitate ion diffusion or interactions

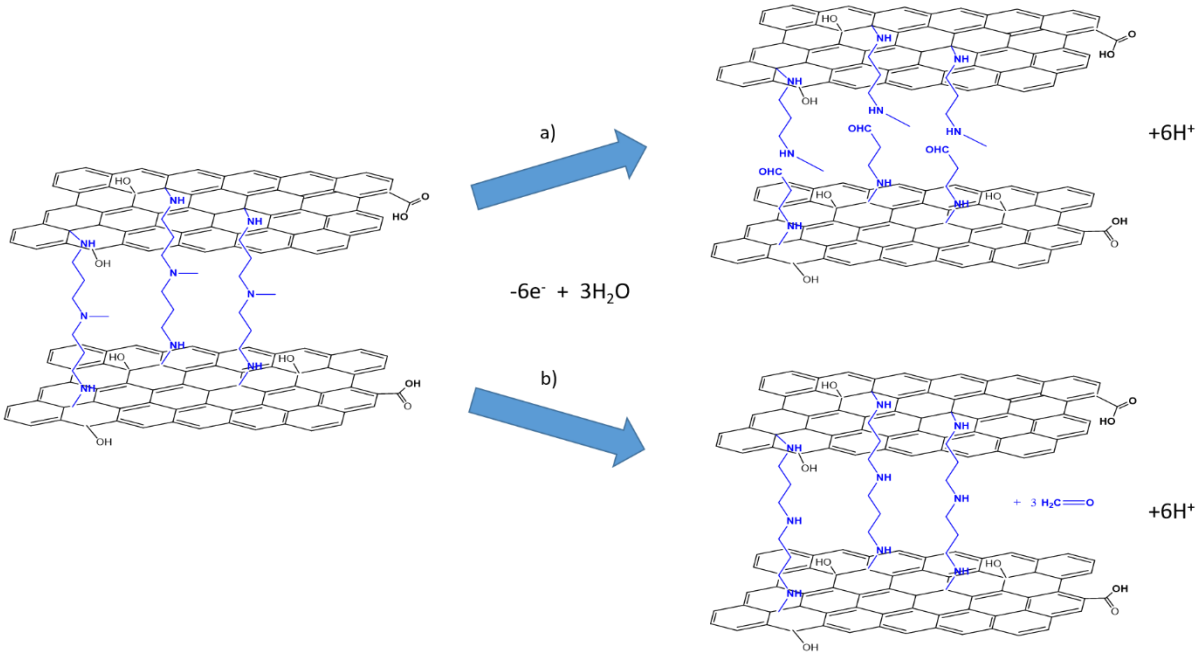

Figure II. 40 : Proposed oxidation mechanism for the tertiary amine of the pillars of 7RP-NCH3 through a) formation of a secondary amine and an aldehyde and b) formation of a secondary amine and the release of formaldehyde

Another proposed explanation for the enhanced performance of the 7RP-NCH3 samples is that the presence of such an extra group might have an effect on the electronic structure of the pillared sample, making its rGO sheets easier to get oxidized, thus forming oxygen functional groups on the rGO sheets, particularly C=O groups, that would interact with the Li^+ or K^+ cations as highlighted earlier.

II.4.2.5 Did we crack the code?

Preliminary, it was concluded that there were no existing trends between the oxygen content or nature and the average specific capacitance. However, an increase in the amount of oxygen in the 7RP-NCH3 sample after cycling, according to the aforementioned proposed mechanism of oxidation of the pillar or the rGO sheets might change the trend in capacitance.

Herein, the possible oxidation of the tertiary amine through the pathway depicted in Figure (II.40(a)) and the possible oxidation of the rGO sheets during cycling should result in an increase in the oxygen content, particularly C=O. However, the oxidation of the amine through the pathway shown in Figure (II.40(b)) should not result in any changes in oxygen content but rather to a slight decrease in carbon content. Accordingly, postmortem XPS experiments were conducted to get more insights on the chemical composition and type of bonds present after cycling and comparing that to those of the electrodes before cycling. XPS was done on a thin additive-free pellet cycled in 0.5M K_2SO_4 in order to avoid any contributions from AB or PVDF. The oxygen increased 50% and an increase in the C=O/C-O ratio was also observed. Interestingly, a 23% decrease in nitrogen content was also observed, which can be attributed to the release of various nitrogen containing molecules upon the oxidation, further strengthening the hypothesis of the pillar's oxidation.

The XPS of the sample after cycling showed an increase in the oxygen content, including C=O, which is in line with the oxidation of the pillar shown in Figure (II.40(a)) and the oxidation of the rGO sheets but not the oxidation of the pillar shown in Figure (II.40 (b)), thus, this oxidation is less likely to take place. The two claimed mechanism that are still holding (oxidation of pillar shown in Figure (II.40(a)) and oxidation of rGO) are consistent with the strong anodic current observed in the 1st CV cycle of the 7RP-NCH3 shown in Figure (II.39). Such a behavior in the 1st cycle of 7RP-NCH3 was never noted in case of 3M H_2SO_4. This may be ascribed to the protonation of the tertiary amine, forming a more oxidation resistant quaternary ammonium ion. In addition, the presence of an irreversible oxidation peak might hint on a higher probability of the oxidation of the amines. Both observations are more in line with the first proposed explanation (oxidation of the tertiary amine) coupled with the loss of nitrogen content which can be a consequence of further oxidation of the pillars. Further oxidation of the formed secondary amine might result in an extra carbonyl and the loss of the nitrogen in the form of methylamine, which would be in agreement with the observed relative loss of nitrogen and increase in oxygen (Figure II.41).

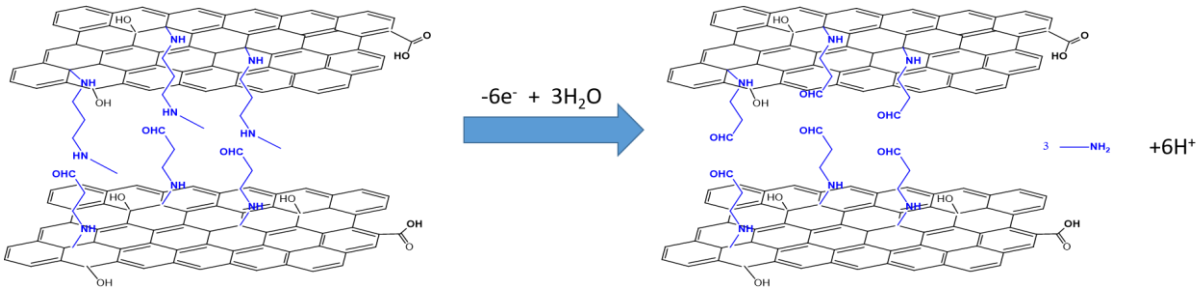

Figure II. 41 : Proposed further oxidation mechanism for the one presented in Figure II.40(a) through formation of a primary amine and an aldehyde

Therefore, based on the gathered information, such mechanism presented in Figure (II.41) seems to be the most probable one. It has to be mentioned that such conclusion is an attempt of interpretation based on the specifically designed XPS experiment, and that it does not rule out any completely different oxidation mechanisms.

II.4.2.6 Re-visiting the Effect of C=O Content on Specific Capacitance

Since there is a change in C=O content upon cycling in 0.5M Li_2SO_4 and 0.5M K_2SO_4, it would be better to try relating the C_{SP} to the C=O content after cycling rather the C=O of the pristine material C=O. The 50% increase in oxygen content in at.% should also be reflected as a 50% increase in oxygen content from EA values (used to calculate the C=O content in the samples). This leads to an increase in the C=O content (calculated from EA and XPS) of 7RP-NCH3 sample plotted earlier against C_{SP} in Figure (II.36(c)) and Figure (II.38(c)) from 4.72 to ~8.9. The same was done for the 23% decrease in N. The aforementioned figures have been replotted (Figure II.42) to try to give a more realistic representation of the effect of C=O and nitrogen contents on the capacitive performance of the samples in 0.5M Li_2SO_4 and 0.5M K_2SO_4.

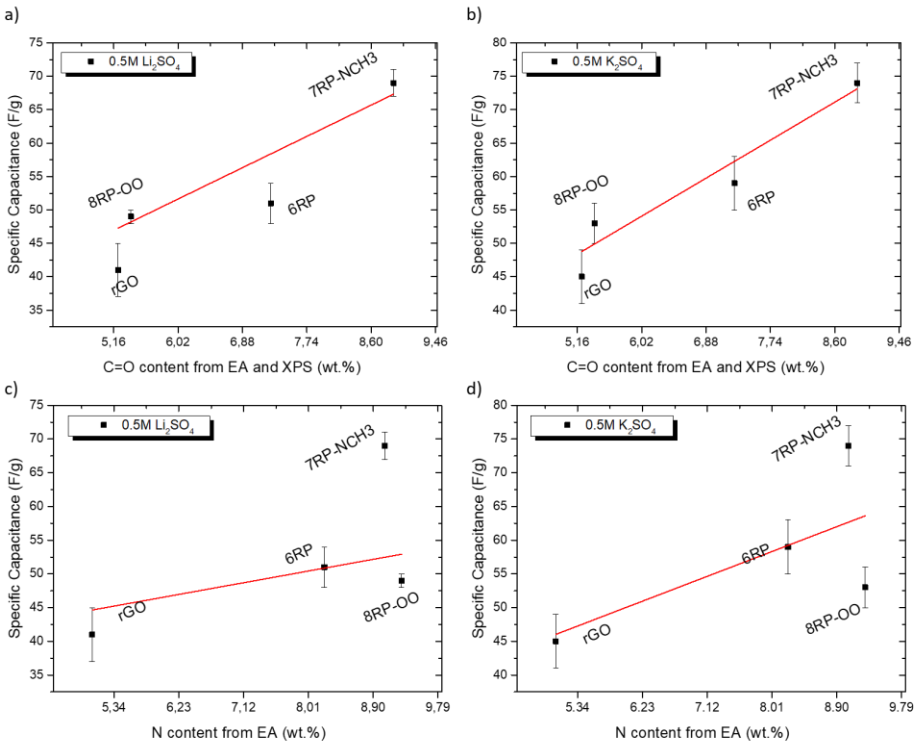

Figure II. 42 : Effect of C=O content and nitrogen content, after correction, on the average specific capacitance of rGO, 6RP, 7RP-NCH3 and 8RP-OO in (a,c) Li_2SO_4 and (b,d) 0.5M K_2SO_4 (red line is a linear fit to guide the eye)

Looking at the replotted figures, an increasing trend in capacitance with the increase of C=O and nitrogen contents can be seen in 0.5M K_2SO_4, however such trend is not so clear in 0.5M

Li_2SO_4. Such an observation can possibly be explained by the low accessibility of the C=O and nitrogen groups to the Li^+ as the size of the hydrated Li^+ is slightly larger than the size of the pores of 6RP and 8RP-OO. However, in 0.5M K_2SO_4, the cation size constraint was lifted, which is supposed to allow for better accessibility of the pores to the cations and thus, allowing more interactions with C=O and nitrogen groups. Therefore, the sample with higher C=O and nitrogen contents shows higher capacitance. Such an updated plot allows for better explaining the slightly better performance of 8RP-OO in 0.5M Li_2SO_4 compared to 6RP and the opposite trend in 0.5M K_2SO_4. In 0.5M Li_2SO_4, Li^+ ions might have limited access to the microporous galleries of both samples due to its hydrated size, thus external adsorption is the prevailing adsorption. 8RP-OO sample shows a slightly better performance owing to its more hydrophilic surface as evidenced from WCA measurements (~0° for 8RP and 53.42° ±4.75° for 6RP) allowing for slightly higher accessibility of the microporous galleries to the ions. When the restriction on the size of the cation was lifted using 0.5M K_2SO_4, the access of the ions to the microporous galleries was improved, allowing more C=O and nitrogen groups to be accessible, and thus the 6RP sample with more C=O shows a slightly better C_{SP} than 8RP-OO as they have close nitrogen content.

II.4.2.7 The story does not end up here – Anion Effect (1M KNO_3)

Although an increasing trend of capacitance with C=O content is observed which is in line with literature, the variations in capacitance when going from 8RP-OO to 6RP is not in par with the variation when going from 6RP to 7RP-NCH3 despite the differences between them in C=O contents being similar. It seems that there might be another factor playing a role in either the enhancement of the capacitance of 7RP-NCH3 or the poorer performances of 6RP and 8RP-OO. A factor that might be related to enhancing the capacitance is the nitrogen content, however the nitrogen content value of the pillared samples are close to each other. A factor that might be hindering the performance is the anion hydrated size. As far as 6RP and 8RP-OO samples are concerned, the hydrated size of the sulfate anion (0.758-0.764 nm) is slightly larger than their similar d-spacing (0.75 nm). Thus, a study was done to examine the effect of the hydrated anion size on the overall capacitance and decipher whether such differences in capacitance vs. C=O is directly related to the hydrated size of the anion or indirectly related to it through a change in the kinetics of the cations adsorption caused by the new hydrated anion size. Consequently, 1M KNO_3 was selected as the hydrated anion (NO_3^-) size is smaller than that of SO_4^{2-} (0.632 nm vs 0.758-0.764 nm) and the cation hydrated size (K^+) has already been shown to be suitable to all the pillared samples examined herein, as it has a hydrated cation size smaller than the d-spacing of all the pillared samples. KNO_3 was used in 1M concentration

rather than 0.5M as in Li_2SO_4 and K_2SO_4 as to maintain a constant number of positive and negative charges between the two electrolytes as well as a constant concentration of cations as suggested in literature for a similar study on carbon black pigments [54].

Figure (II.43) shows the CV shapes of rGO, 6RP, 7RP-NCH3 and 8RP-OO as well as their rate capability in 1M KNO_3. The shape of the CVs of 6RP and 8RP-OO look different than those in 0.5M Li_2SO_4 and 0.5M K_2SO_4 as their CVs in 1M KNO_3 look more symmetric. The CV shapes of rGO and 7RP-NCH3 in 1M KNO_3 are symmetric as when cycled in 0.5M Li_2SO_4 and 0.5 K_2SO_4.

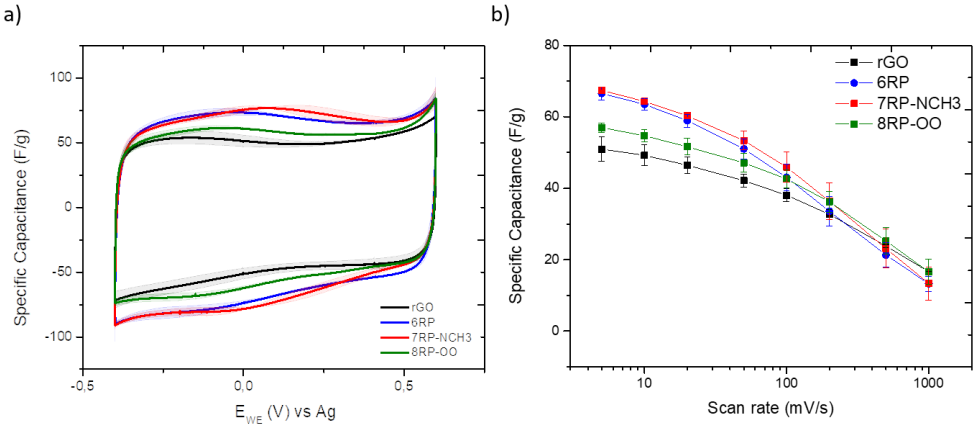

Figure II. 43 : a) Cyclic voltammograms at 5mV/s and b) rate capability of rGO (—), 6RP (—), 7RP-NCH3 (—) and 8RP-OO (—) in 1M KNO_3 along with their associated error bars

The capacitance values at 5 mV/s were 51 ±3, 68 ±2, 68 ±1 and 57 ±1 F/g for rGO, 6RP, 7RP-NCH3 and 8RP-OO respectively. Compared to cycling in K_2SO_4, the capacitance values increased for all the samples, except for 7RP-NCH3 where on the contrary, it slightly decreased. The rate capability plot (Figure II.43(b)) shows a nearly identical behavior for 6RP and 7RP-NCH3 revealing that they are the best performing samples, followed by 8RP-OO and then rGO-Hz up till 100 mV/s. At higher scan rates, the performances of all samples examined become similar as external surface adsorption dominates.

II.4.2.8 Digesting all together (0.5M Li_2SO_4, 0.5M K_2SO_4 and 1M KNO_3)

Figure (II.44) shows the CVs at 5mV/s of rGO, 6RP, 7RP-NCH3 and 8RP-OO in all neutral electrolytes tested to further investigate the changes in the CV shapes. In rGO, the CVs have a symmetric shape (Figure II.44(a)) in all neutral electrolytes regardless of the size of the cations or the anions. Its rate capability (Figure II.44(b)), however, is more sensitive to the choice of electrolyte. The average specific capacitance of rGO is improved going from 0.5M Li_2SO_4 to 0.5M K_2SO_4 to 1M KNO_3. This trend can be understood in light of the external surface

adsorption charge compensation mechanism of rGO. Since external surface and inter-particle porosity are accessible surfaces for all ions, more ions can be adsorbed on the same surface when the ions sizes are smaller. Thus, more of the smaller cations and anions of 1M KNO_3 can be stored on rGO's external surface compared to the bigger cations and anions of 0.5M Li_2SO_4, thus leading to higher capacitance values for 1M KNO_3. Another sample showing symmetric CVs in the various neutral electrolytes tested is the 7RP-NCH3 sample (Figure II.44(g)). The CVs are symmetric with prominent redox peaks, which is probably resulting from interactions of the alkali metal cations of the electrolytes with carbonyl groups as proposed earlier. The rate capability plot of the 7RP-NCH3 (Figure II.44(h)), contrary to rGO, is less sensitive to changing the sizes of the ions. This can be attributed to accessibility of the microporous galleries created upon pillaring to all the ions examined herein, as those galleries are of a size that is larger than that of all the hydrated ion sizes. On the other hand, when the size of the microporous galleries created upon pillaring is smaller than the size of the cation and/or anion, asymmetric CVs are observed as it is the case with 6RP (Figure II.44(d)) and 8RP-OO (Figure II.44(j)) in 0.5M Li_2SO_4 and 0.5M K_2SO_4. When the hydrated sizes of the ions are smaller than the d-spacing, the CV shape becomes symmetric as in 1M KNO_3. Such a transition in the symmetry of the CVs going from 0.5M Li_2SO_4 and 0.5M K_2SO_4 to 1M KNO_3, is also accompanied by an increase in capacitance at all scan rates (Figures II.44(e) and II.44(k)). In 0.5M Li_2SO_4, the hydrated sizes of both ions are greater than the d-spacing of the samples while in 0.5M K_2SO_4, only the hydrated sizes of the anions is bigger than the d-spacing of the samples, while the hydrated size of the cation is smaller. It should be noted that the smaller area enclosed by the CV is on the side of the cation adsorption even in 0.5M K_2SO_4 where the size of the cation is smaller than the d-spacing. When using 1M KNO_3, the hydrated sizes of the anions and cations are smaller than the d-spacing and a symmetric CV is observed, meaning an increased enclosed area by the CV on the cation adsorption side when an anion of a smaller hydrated size is used. Once again, such a change in CV shape is accompanied by an increase in the capacitance.

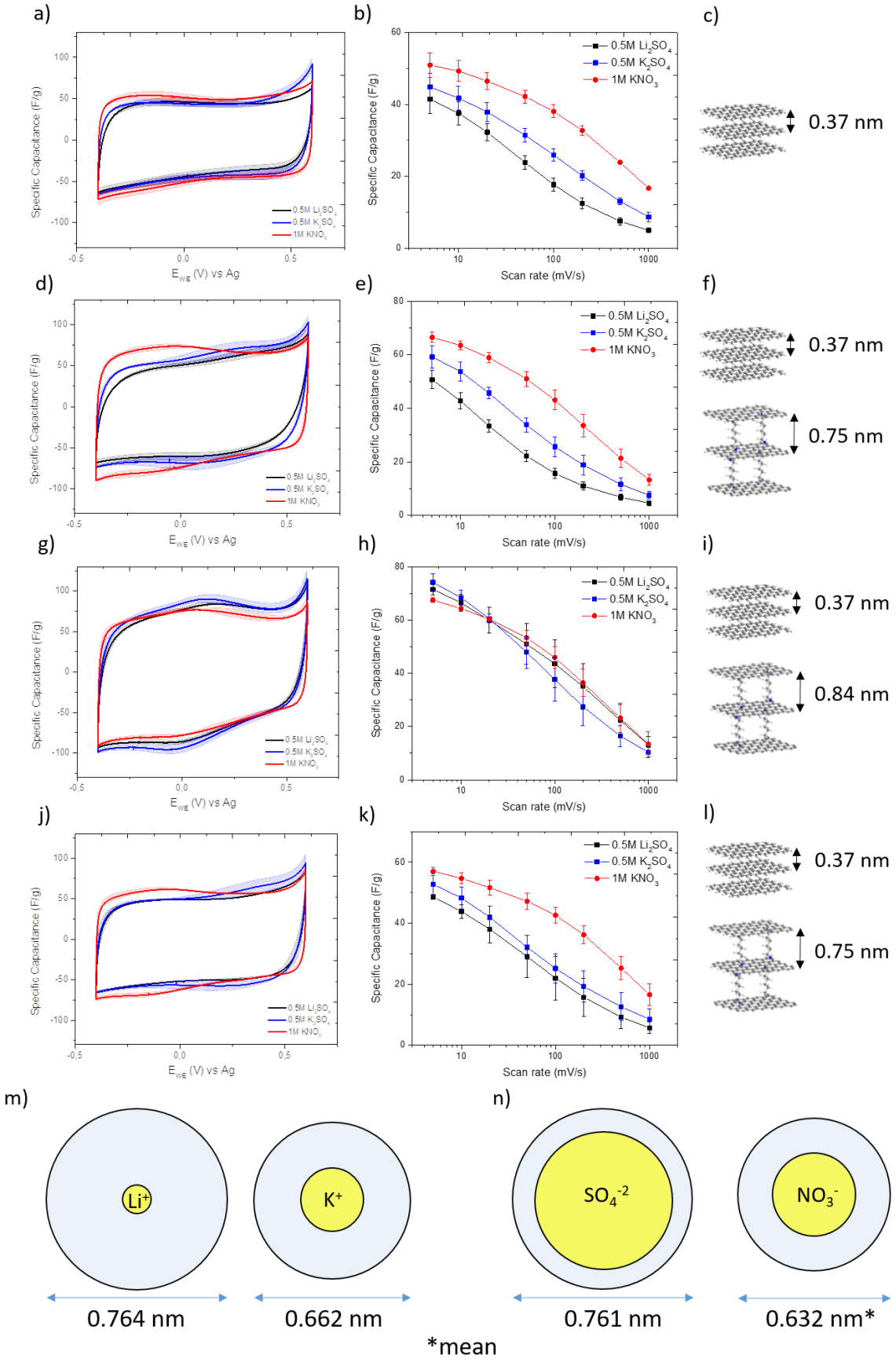

Figure II. 44 : CVs at 5 mV/s, rate capability and structural scheme of rGO (a, b and c), 6RP (d, e and f), 7RP-NCH3 (g, h and i) and 8RO-OO (j, k and l) in 0.5M Li_2SO_4 (—), 0.5M K_2SO_4 (—) and 1M KNO_3 (—) along with to-scale sizes of naked and hydrated cations (m) and anions (n)

To sum up, for PGM, distorted CV on cation-side adsorption is observed when anion is too big while cation size is appropriate. A symmetric CV is only observed when both anion and cation size are smaller than d-spacing. This hints on a role played by anions during the adsorption of cations. The SO_4^{2-} ions can impede the adsorption of the cations through clogging the pores as their hydrated sizes is comparable to the d-spacing of the 6RP and 8RP-OO. In addition, these anions can hinder any charging mechanism that involves the transport of the anions, such as the ion exchange mechanism and the co-ion desorption mechanism (Figure II.45) [55]. In the ion exchange mechanism, when a negative potential is applied, it is proposed that anions leave the pores they were occupying at 0 V applied potential and cations enter the pores to balance the charge. On the other hand, in a co-ion desorption mechanism, two anions per extra added charge are expected to exit the pores when a negative potential is applied in order to have a surplus of cations to balance the charge. In 1M KNO_3, the anion size restriction is removed, allowing anions to take part in charge storage mechanism more easily and not to clog the pores, thus, an enhancement in the adsorption of K^+ ions under negative potential can be expected as the NO_3^- ions have hydrated sizes smaller than the d-spacing, allowing for their ease of transportation in and out of the pores.

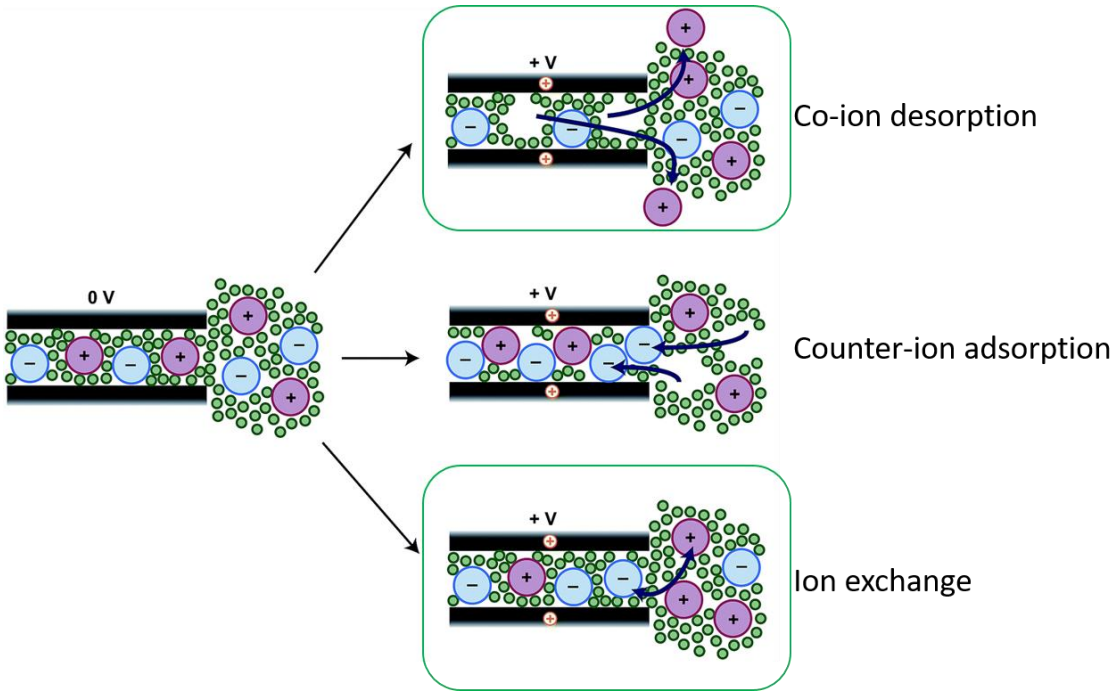

Figure II. 45 : Various charging mechanisms proposed by Forse, A. C. et al. [55]. In green boxes are the charging mechanism referred to in the text (co-ion desorption and ion exchange)

To further validate the findings and examine the behaviors of different samples in different neutral electrolytes of different hydrated ion sizes, EIS experiments were carried out at OCV in a frequency range from 10 mHz to 100 KHz. Figure (II.46) shows the average Nyquist plots of

the rGO (Figure II.46(a)), 6RP (Figure II.46(b)), 7RP-NCH3 (Figure II.46(c)) and 8RP-OO (Figure II.46(d)) in 0.5M Li_2SO_4, 0.5M K_2SO_4 and 1M KNO_3. Near vertical lines were observed for all the samples at low frequency region, indicative of capacitive behavior for porous carbon materials. From the inserts of the Nyquist plots of all the samples, a faster transition from the high frequency region to the low frequency region is observed for 1M KNO_3 compared to 0.5M K_2SO_4 and 0.5M Li_2SO_4, which can be attributed to better ion diffusion in 1M KNO_3 than in 0.5M K_2SO_4 and 0.5M Li_2SO_4. Such conclusion is consistent with the ionic conductivity values of these electrolytes (42, 71 and 80 mS/cm for 0.5M Li_2SO_4, 0.5M K_2SO_4 and 1M KNO_3) as well as with the relation between the hydrated ion size and the pore sizes of the pillared samples (Figure II.44).

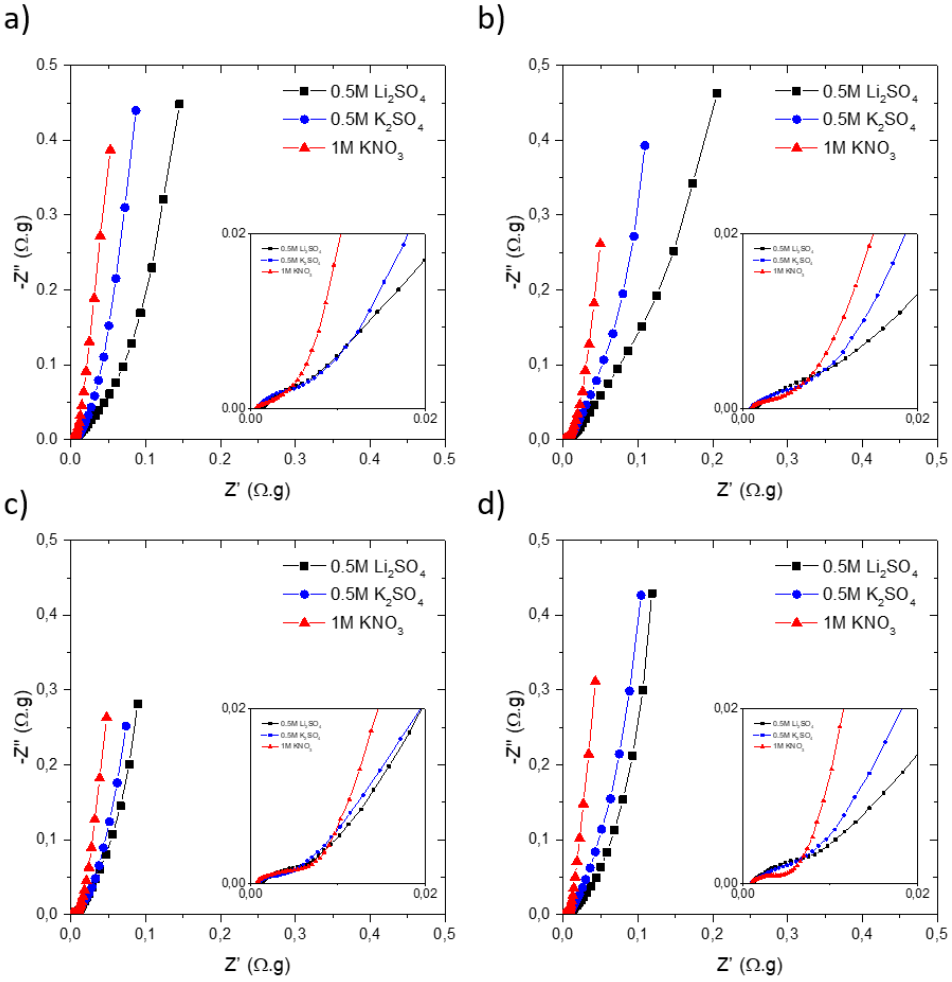

Figure II. 46 : Average Nyquist plots of a) rGO, b) 6RP, c) 7RP-NCH3 and d) 8RP-OO in 0.5M Li_2SO_4 (—), 0.5M K_2SO_4 (—) and 1M KNO_3 (—). Inserts: a zoom in for the high frequency regions

The diffusion of ions in the rGO sample is probably mainly affected by the ionic conductivity, as the adsorption is thought to take place only on the external surface and in the inter-particle porosity rather than in-between the graphene sheets. On the other hand, the ionic diffusion in 6RP and 8RP-OO are expected to be affected by ionic conductivity as well as by the hydrated

ion sizes to d-spacing relation (Figures II.44(m) & (n)). In 7RP-NCH3, ionic diffusion should be mainly affected by the ionic conductivity as the d-spacing of such sample is larger than the hydrated ion sizes of the all the tested electrolytes

The real component of capacitance was plotted versus frequency for the samples examined in different neutral electrolytes (Figure II.47) to check for trends in the values of the real capacitance component at low frequencies in different electrolytes and compare such trends to those obtained from CVs at slow scan rates. The trends in real capacitance as function of frequency is in a very good agreement with the rate capability curves displayed in Figure (II.44). rGO, 6RP and 8RP-OO are showing an increase in real capacitance going from 0.5M Li_2SO_4 to 1M KNO_3 while 7RP-NCH3 is showing similar values in all electrolytes, confirming the results obtained from the CVs, and giving strength to the proposed role played by the anions in the charging mechanism of the cations adsorption. Also the trends in real capacitance of the different samples in the same electrolytes are similar to those obtained from the CVs as shown in Tables (II.9), (II.10) and (II.11) at the end of the conclusion section.

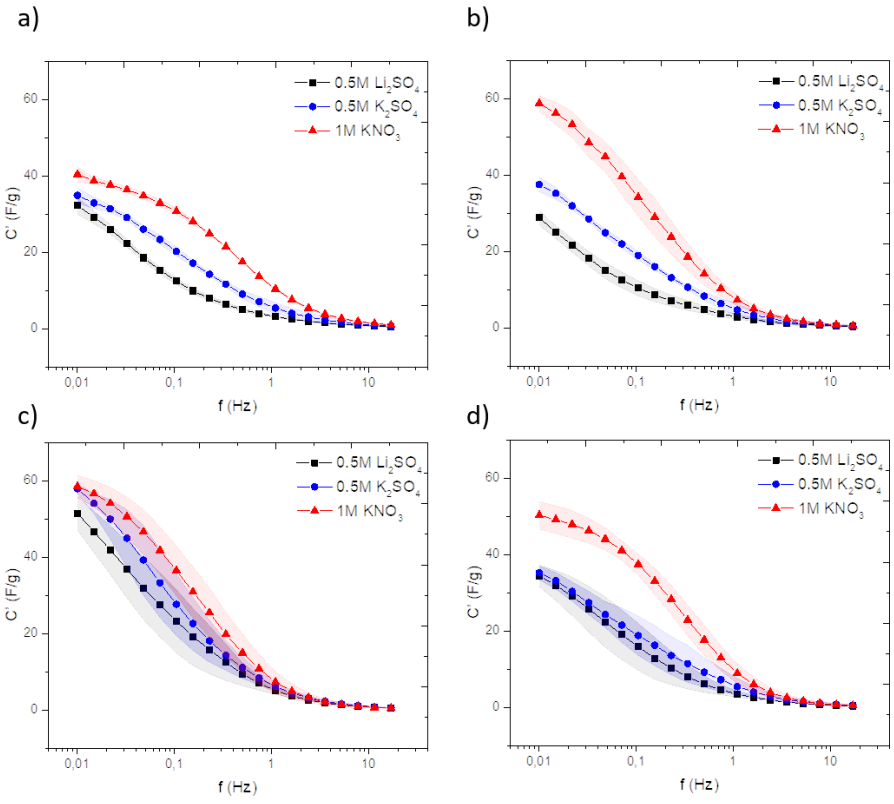

Figure II. 47 : Real Capacitance versus the frequency of a) rGO, b) 6RP, c) 7RP-NCH3 and d) 8RP-OO in 0.5M Li_2SO_4 (—), 0.5M K_2SO_4 (—) and 1M KNO_3 (—)

To further validate the findings and confirm the effect of the ionic conductivity and the hydrated ion-pore size effect on the performance, the imaginary component of the capacitance was

plotted against the real component of the impedance (Figure II.48) for all the tested samples in all the tested neutral electrolytes. This graphical representation allows extracting the effective ionic transport resistance inside the pores of the electrode.

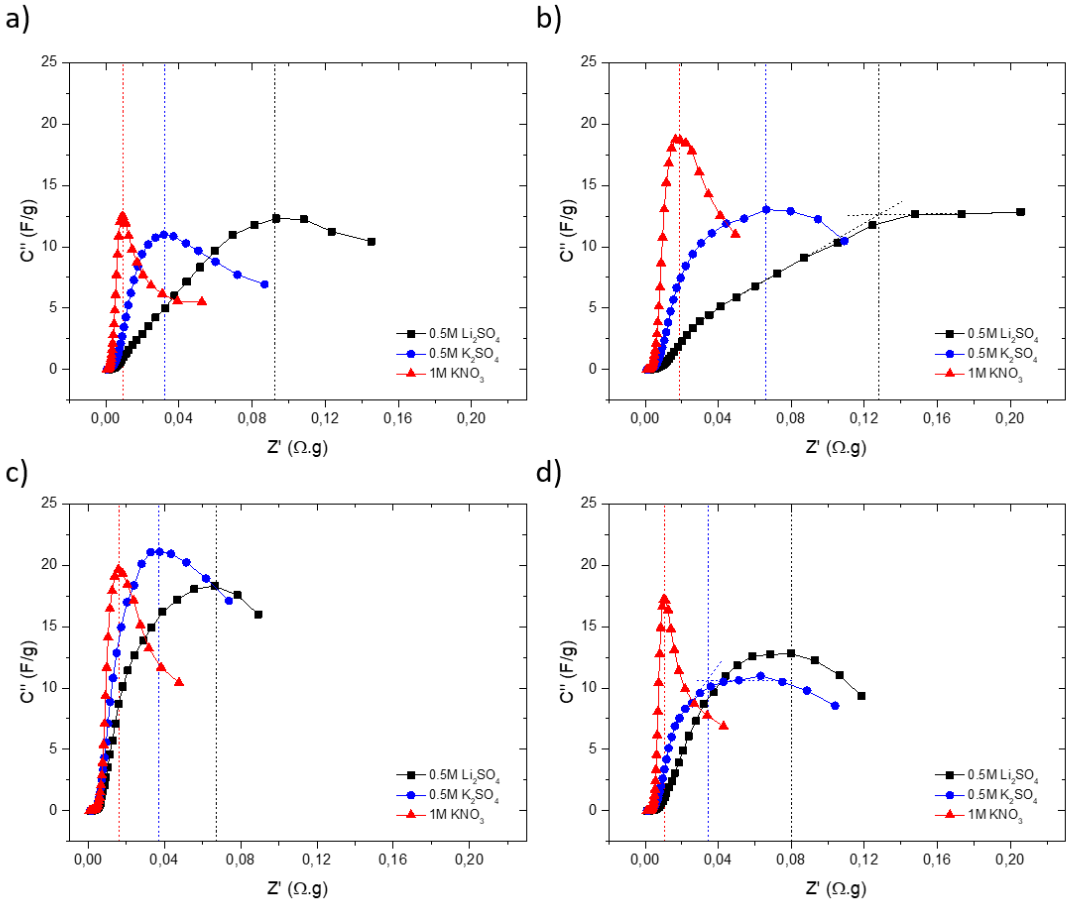

Figure II. 48 : Imaginary Capacitance versus the real impedance of a) rGO, b) 6RP, c) 7RP-NCH3 and 8RP-OO in 0.5M Li_2SO_4 (—), 0.5M K_2SO_4 (—) and 1M KNO_3 (—)

At first glance, it is clear from Figure (II.48) that for all the samples the ionic transport resistance within the pores decreases when going from 0.5M Li_2SO_4 to 0.5M K_2SO_4 to 1M KNO_3 with different resistance values for each sample. Numerical values for the ionic transport resistance in the pores was extracted from the plots in Figure (II.48) for the various samples in the different electrolytes and represented in Figure (II.49). Looking at Figure (II.49) from top to bottom, the resistance values for each sample can be seen as a function of the electrolyte. The ionic transport resistance decreases from 0.5M Li_2SO_4 to 0.5M K_2SO_4 to 1M KNO_3 as what was already observed qualitatively from Figure (II.48), showing a profound effect of the type of the electrolyte on the diffusion kinetics inside the pores. This is consistent with the ionic conductivity of these electrolytes and the hydrated ion-pore size relationship. The higher the ionic conductivity, the lesser the ionic transport resistance becomes. The ionic conductivity values are 42, 71 and 80 mS/cm for 0.5M Li_2SO_4, 0.5M K_2SO_4 and 1M KNO_3, respectively.

Also, ionic charge transport is facilitated by larger pores sizes. The low ionic transport resistance inside the pores when cycling in 1M KNO_3 compared to cycling 0.5M Li_2SO_4 or 0.5M K_2SO_4 can help explain the higher rate capability of all the samples in 1M KNO_3 as demonstrated by less steeper decay in specific capacitance with scan rate, whereas the drop in performance of the samples cycled in 0.5M Li_2SO_4, 0.5M K_2SO_4 is fast (Figure II.44).

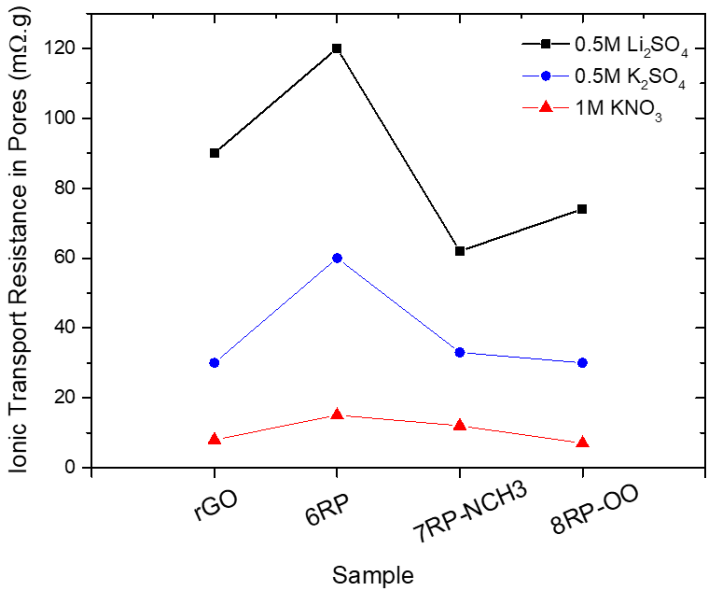

Figure II. 49 : The ionic transport resistance in the pores of rGO, 6RP, 7RP-NCH3 and 8RP-OO in 0.5M Li_2SO_4 (—), 0.5M K_2SO_4 (—) and 1M KNO_3 (—)

In addition, the ionic transport resistance in a certain electrolyte can be examined in different samples by inspecting the plots in Figure (II.49) from left to right. It is clear that 6RP is the sample with the highest ionic transport resistance in all electrolytes. This can be mainly attributed to its low wettability rather than to its d-spacing value, because the 8RP-OO has the same d-spacing and yet a lower ionic transport resistance in all electrolytes (~40-50% less). 7RP-NCH3 and 8RP-OO have ionic transport values that are comparable to that of rGO where external surface adsorption is dominated. They even have a lower ionic transport resistance in 0.5M Li_2SO_4. This is probably due their high wettability resulting from their extra polar groups which can compensate the shortcoming of the low ionic conductivity of 0.5M Li_2SO_4. 8RP-OO is having a higher ionic transport resistance in 0.5M Li_2SO_4 compared to 7RP-NCH3 although they have similar resistance values in 0.5M K_2SO_4 and 1M KNO_3. This can be attributed to the d-spacing of 8RP-OO being of a size comparable to both the sizes of the hydrated cations and the anions of Li_2SO_4, thus, impeding the ion transport. This shows that the pillaring strategy not only enhances the capacitance but also does not negatively alter the ionic transport

resistance inside the pores compared to the non-pillared rGO when polar groups are included within the pillar.

II.4.2.9 Bouncing Back to the Effects of Various Components on C_{SP}

After investigating the origins behind the different CV shapes in different electrolytes and understanding the role of the anions in the adsorption of the cations as well as investigating the ion diffusion kinetics inside the pores, the effects of d-spacing, C-O, C=O and nitrogen contents on the average specific capacitance in 1M KNO_3 were investigated (Figure II.50) to validate the results obtained with 0.5M Li_2SO_4 and 0.5M K_2SO_4.

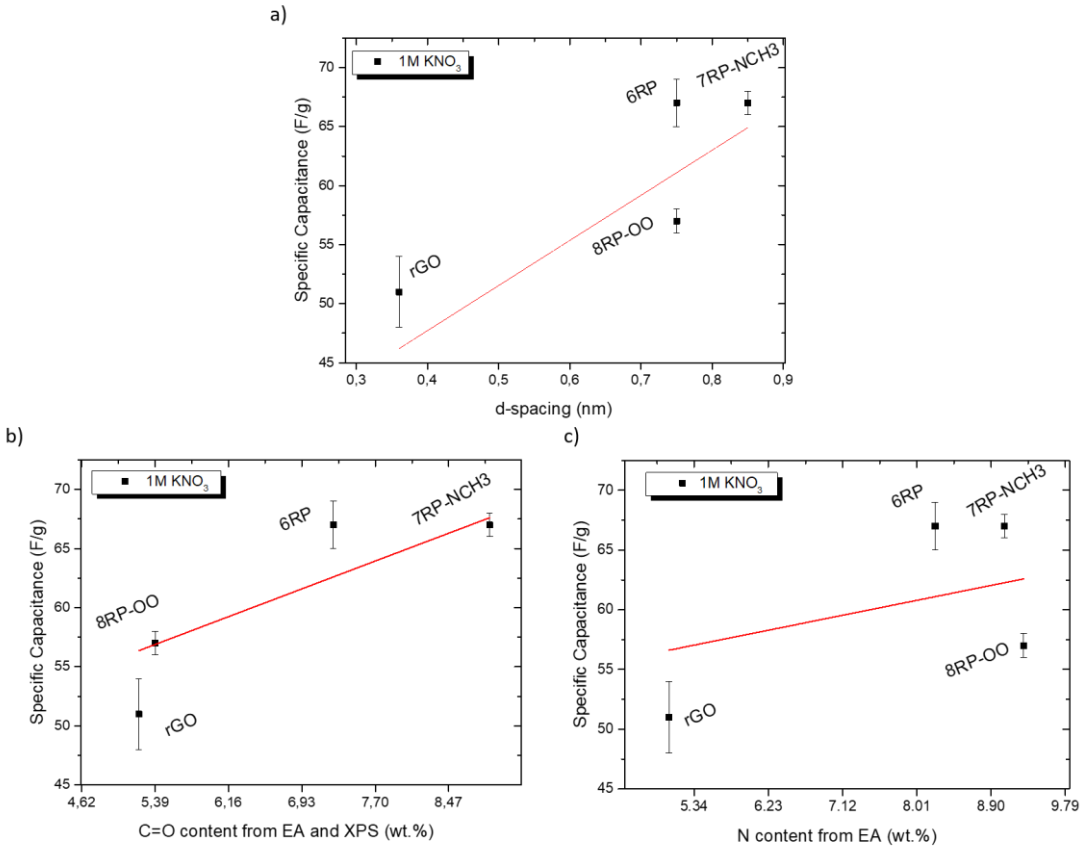

Figure II. 50 : Effect of a) d-spacing, b) C=O content and c) nitrogen content on the average specific capacitance of rGO, 6RP, 7RP-NCH3 and 8RP-OO in 1M KNO_3 (red line is a linear fit to guide the eye)

The capacitance increases with increasing C=O content while not so much with nitrogen content, implying the greater effect of the C=O on the specific capacitance; thus, emphasizing on the important role played by the surface/pillar chemistry in determining the performance of the samples as electrode materials for supercapacitor applications. The 6RP and 7RP-NCH3 samples seem to possess similar capacitance while 7RP-NCH3 is showing a higher C=O content. Such an observation could be explained by a higher number of carbonyl Os being involved in specifically adsorbing the Li^+ or K^+ ions. Such an explanation is conceptually depicted in Figure (II.51).

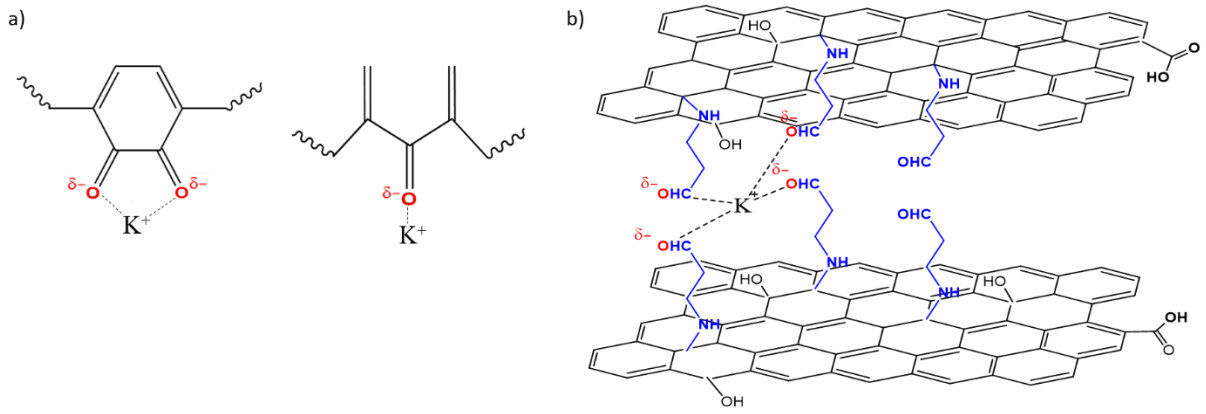

Figure II. 51 : Ion-dipole interaction between a) graphitic carbonyl and K+ ion and b) between pillar carbonyl of 7RP-NCH3 and K+ ions. Solvation shells, if any, are omitted for clarity

In all pillared samples, the ion-dipole interactions between the cation and the various graphitic carbonyls or quinone moieties is possible (Figure II.51(a)). For 7RP-NCH3, the carbonyls resulting from the oxidation of the pillar can also partake in such ion-dipole interactions (Figure II.51(b)). However, the number of C=O involved per ion is higher in case of C=O from pillars compared to graphitic C=O. These interactions are expected to take place mostly with carbonyls as the carbonyl oxygen has large dipole moment and thus would be expected to act a strong donor [56].

II.4.2.10 Verifying the Charge Storage Mechanism

Finally to elucidate the charge storage mechanism of the pillared samples in 1M KNO_3 after all the size restrictions, in relation to the d-spacing values, were lifted. The charge storage mechanism was investigated through applying the Dunn's method which gives insights on the contributions coming from diffusion and non-diffusion limited processes at every single potential point through fitting Eq. (II.10), leading to plots as in Figure (II.52).

$$i = k_1 v^{\frac{1}{2}} + k_2 v \qquad (8)$$

Where $k_1 v^{\frac{1}{2}}$ is the diffusion limited contribution of the current response and $k_2 v$ is the non-diffusion limited contribution of the current response with i being the current response, v being the scan rate and $k_1$and k_2 being constants

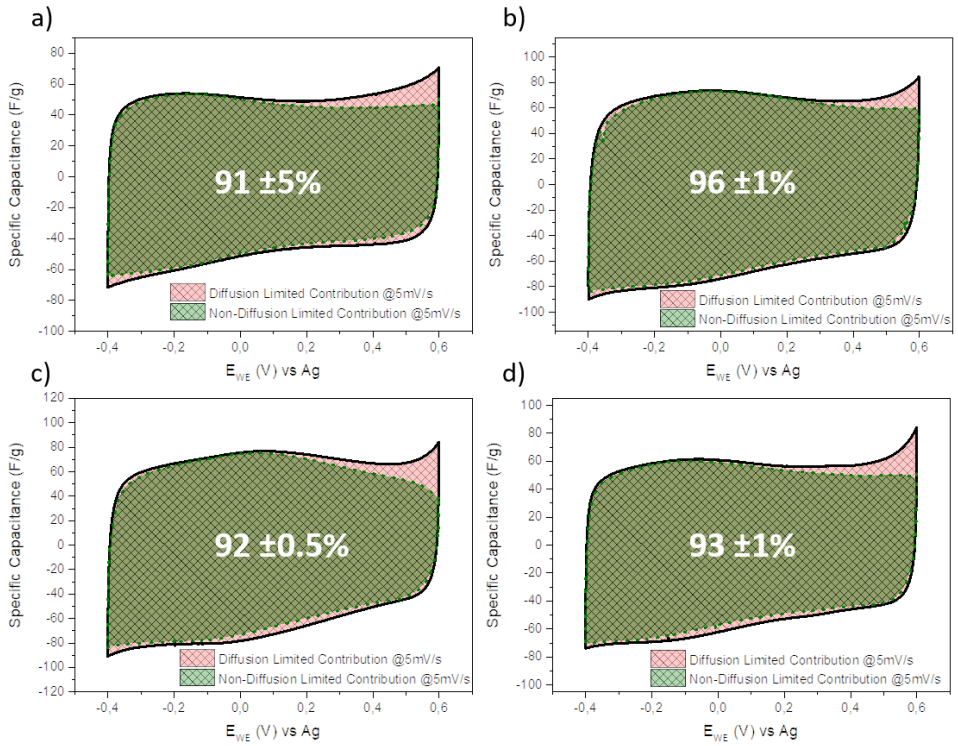

Figure II. 52 : The diffusion and non-diffusion limited contribution of a) rGO, b) 6RP, c) 7RP-NCH3 and d) 8RP-OO at a scan rate of 5 mV/s in 1M KNO_3 obtained through applying Dunn's method

It can be seen that all the pillared samples are having >90% non-diffusion limited contributions as well as rGO where only external surface adsorption is taking place. Also, these plots show that the diffusion limited contribution part is mainly seen near the borders of the CVs at positive potentials where a small anodic current is observed, which can be attributed to side redox reactions, thus, leading to diffusion limited contributions. This indicates that the true charge storage mechanism, excluding probable side reactions, is controlled by non-diffusion limited processes such as EDLC, and fast surface or near-surface redox interactions, if any, for all the samples. This shows that the pillaring strategy does not impose any diffusion limitations on the charge storage mechanism, which once again proves the validity of this strategy for such energy storage applications.

II.4.3 Stability Tests

In the previous sections, the performance of pillared samples was shown to be superior to that of non-pillared rGO in all the four tested electrolytes: i) 3M H_2SO_4, ii) 0.5M Li_2SO_4, iii) 0.5M K_2SO_4 and iv) 1M KNO_3. However, an enhancement in the capacitance is not enough for a material to be used as an electrode for supercapacitor applications. A proper supercapacitor electrode has to be stable when cycled multiple times as supercapacitors are well-known for their high cycle life time. 7RP-NCH3 was cycled for 15000 cycles at a scan rate of 200 mV/s to test its stability and compare it to that of rGO in 0.5M Li_2SO_4 (Figure II.53). The comparison

was only done between rGO and 7RP-NCH3 as they are the samples with very different average capacitance values at the tested scan rate (35 F/g for 7RP-NCH3 and 14 F/g for rGO at 200 mV/s for the electrodes cycled for stability testing). Moreover, from the previous results, 6RP and 8RP-OO showed poor performances at this scan rate due to the limited inaccessibility of the pores to the ions (due to their hydrated size that are larger than the d-spacing of those samples). 7RP-NCH3 demonstrated a very decent capacitive retention of ~98.5% after 15000 cycles compared to ~100% of rGO. This shows a very good sample cycling stability and that the presence of the pillars and the low concentration and low ionic conductivity of the electrolyte (42 mS/cm for 0.5M Li_2SO_4) did not negatively affect the sample's long-term performance. Such a long-term stability proves the robustness of such assemblies and their potential as electrode materials for supercapacitors.

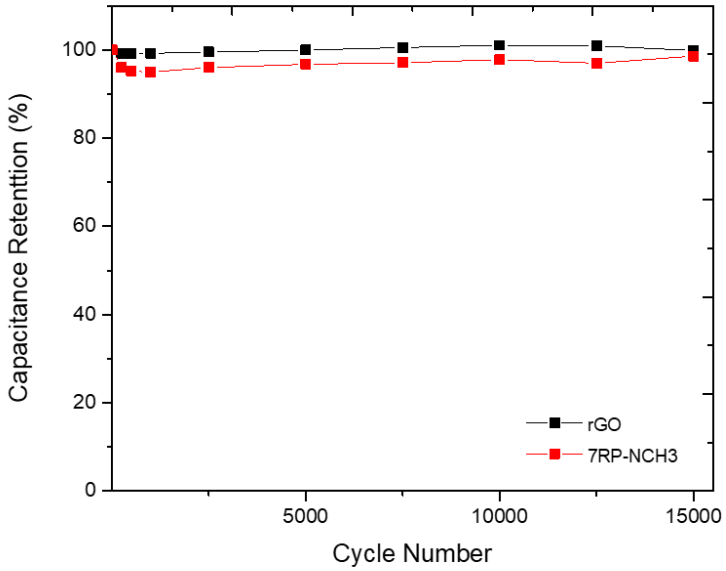

Figure II. 53 : Stability Test for rGO (–▪–) and 7RP-NCH3 (–▪–) at 200 mV/s for 15000 cycles in 0.5M Li_2SO_4

II.5 Conclusions

Graphite was oxidized into graphene oxide through a modified Hummer's Method. Its oxidation was confirmed with various characterization techniques but notably with ssNMR, elucidating the presence of various oxygen functionalities as well as their types. Starting from graphene oxide, reduced graphene oxide as a reference material, and three pillared graphene samples with different pillars were successfully synthesized. The pillaring was verified from the presence of a cross-linking XRD peak that is absent in the non-pillared rGO. The d-spacing values were obtained from the positions of these XRD peaks. The samples' modification with the pillars and their covalent bonding was also confirmed using TGA, XPS, EA and FT-IR. Using these same techniques, the extent of reduction of the samples was monitored. The structure of the samples was studied with Raman spectroscopy while the morphology and surface texture were studied by SEM and TEM, respectively. The wettability and the electrical conductivity of these samples were evaluated as important parameters for electrochemical applications in aqueous electrolytes. The samples were tested as electrode materials for supercapacitors in different electrolytes: i) acidic (3M H_2SO_4) and ii) neutral (0.5M Li_2SO_4, 0.5M K_2SO_4 and 1M KNO_3).

To begin with, the pillared graphene assemblies demonstrated an enhanced capacitive performance compared to rGO and the correlation between such an enhanced performance and the different physico-chemical characteristics was discussed. Such an enhancement was attributed to opening up new adsorption sites inside the microporous galleries created as a consequence of the pillaring which simultaneously allows the surface functionalities to be more accessible to the electrolyte for redox reactions to occur, if any are to occur. Also, the relationship between the size of the microporous galleries, presented as d-spacing, and the hydrated ion size should be highly considered before selecting the electrolytes. It was demonstrated that when the hydrated size of the ions is comparable to the d-spacing, the performance dropped compared to cases when the hydrated ion sizes was smaller than the d-spacing. The hydrated anion size was shown to have an effect on the adsorption of the cation through either clogging the pores or hindering anion-dependent charging mechanisms such as ion exchange and co-ion desorption. It was also shown that the chemistry of the surface/pillars has a greater impact on the specific capacitance once the structure is sufficiently adjusted to accommodate the ions of the electrolytes. The presence of oxygen functionalities enhanced the capacitance either through i) redox reactions involving electrochemically active oxygen species such as carbonyls and quinones in H_2SO_4 or ii) ion-dipole interactions with cations in neutral

electrolytes such as the interaction between carbonyl groups and Li^+ or K^+ ions. Such an interaction can lead to local changes in the electronic charge density.

In addition, the demonstrated results asserted on the synergetic effect of carefully matching the samples' chemical and structural features to the electrolytes. Samples with higher basic or acidic oxygen functionalities (such as 6RP and 8RP-OO) can have better performances in acidic or basic electrolytes, respectively due to redox reactions, whereas samples with larger d-spacing values and hetero groups (such as 7RP-NCH3) can be more suited to neutral electrolytes with larger cation and anion sizes such as Li_2SO_4 and K_2SO_4. besides, no ion sieving was observed in aqueous electrolytes, contrary to what is observed in literature for organic electrolytes [6]; however, modulating the d-spacing in relation to the ions is redeemed important. Similar to organic electrolytes, the pillaring strategy increased the C_{SP} in aqueous electrolytes. Table (II.9), Table (II.10) and Table (II.11) below summarize all the results obtained from the electrochemical analysis in 0.5M Li_2SO_4, 0.5M K_2SO_4 and 1M KNO_3, respectively.

Moreover, the presence of polar groups can enhance the wettability of the samples as proved by water contact angle measurements for 7RP-NNCH3 and 8RP-OO, thus reducing the effective ionic resistance. Differences in ionic diffusion resistances in different electrolytes were corborated also to electrolyte ionic conductivity and d-spacing restriction. The presence of the extra tertiary amine specifically in the 7RP-NCH3 sample could lead to specific electro-sorption sites for cations such as Li^+ and K^+ due to the formation of carbonyls upon its proposed oxidation in neutral aqueous electrolytes, as evidenced by a strong anodic current with an irreversible oxidation peak in the first electrochemical stabilization cycle. Such a result shows the importance of pillar engineering and pillar design in enhancing the capacitance.

Furthermore, the charge storage mechanism was proven to be dominated by electrochemical double layer capacitance coupled with surface or near surface fast redox reactions for all the samples in acidic electrolytes.

Finally, stability tests were done to show the high stability the pillared samples possess, which proves their high potential as electrode materials for supercapacitor applications. Such results and conclusions open the doors to better designing pillared graphene materials where the d-spacing can be well controlled to adapt to the size of the electrolytic ions and the surface/pillar chemistry can be tuned to target specific interactions.

Sample	d-spacing (nm)	C=O (wt.%)	N (wt.%)	Avg. Specific Capacitance at 5mV/s (F/g)	Increase in capacitance vs rGO at 5mV/s (%)	Avg. Specific Capacitance at 10 mHz (F/g)
8RP-OO	0.75	5.39	9.29	49 ±1	20	34 ±3
7RP-NCH3	0.85	8.9*	9.06+	69 ±2	68	51 ±4
6RP	0.75	7.26	8.23	51 ±3	24	29 ±2
rGO-Hz	0.36	5.22	5.04	41 ±4	-	32 ±2

**C=O content after cycling and + N content after cycling*

Table II. 9 : Summary of the electrochemical analysis of rGO, 6RP, 7RP-NCH3 and 8RP-OO in 0.5M Li_2SO_4

Sample	d-spacing (nm)	C=O (wt.%)	N (wt.%)	Avg. Specific Capacitance at 5mV/s (F/g)	Increase in capacitance vs rGO at 5mV/s (%)	Avg. Specific Capacitance at 10 mHz (F/g)
8RP-OO	0.75	5.39	9.29	53 ±3	18	35 ±2
7RP-NCH3	0.85	8.9*	9.06+	74 ±3	64	58 ±1
6RP	0.75	7.26	8.23	59 ±4	31	38 ±1
rGO-Hz	0.36	5.22	5.04	45 ±4	-	35 ±2

**C=O content after cycling and + N content after cycling*

Table II. 10 : Summary of the electrochemical analysis of rGO, 6RP, 7RP-NCH3 and 8RP-OO in 0.5M K_2SO_4

Sample	d-spacing (nm)	C=O (wt.%)	N (wt.%)	Avg. Specific Capacitance at 5mV/s (F/g)	Increase in capacitance vs rGO at 5mV/s (%)	Avg. Specific Capacitance at 10 mHz (F/g)	Non-Diffusion Limited Contribution at 5mV/s (%)
8RP-OO	0.75	5.39	9.29	57 ±1	12	50 ±4	93 ±1
7RP-NCH3	0.85	8.9*	9.06+	67 ±1	31	59 ±3	92 ±0.5
6RP	0.75	7.26	8.23	67 ±2	31	59 ±2	96 ±1
rGO-Hz	0.36	5.22	5.04	51 ±3	-	40 ±2	91 ±5

**C=O content after cycling and + N content after cycling*

Table II. 11 : Summary of the electrochemical analysis of rGO, 6RP, 7RP-NCH3 and 8RP-OO in 1M KNO_3

II.6 References

[1] W. S. Jr. Hummers and R. E. Offeman, 'Preparation of Graphitic Oxide', *J. Am. Chem. Soc.*, vol. 80, no. 6, pp. 1339–1339, Mar. 1958, doi: 10.1021/ja01539a017.

[2] C. K. Chua and M. Pumera, 'Chemical reduction of graphene oxide: a synthetic chemistry viewpoint', *Chem. Soc. Rev.*, vol. 43, no. 1, pp. 291–312, Dec. 2013, doi: 10.1039/C3CS60303B.

[3] S. Park *et al.*, 'Chemical structures of hydrazine-treated graphene oxide and generation of aromatic nitrogen doping', *Nat Commun*, vol. 3, no. 1, Art. no. 1, Jan. 2012, doi: 10.1038/ncomms1643.

[4] B. Lesiak *et al.*, 'Chemical and structural properties of reduced graphene oxide—dependence on the reducing agent', *J Mater Sci*, vol. 56, no. 5, pp. 3738–3754, Feb. 2021, doi: 10.1007/s10853-020-05461-1.

[5] H. Banda *et al.*, 'One-step synthesis of highly reduced graphene hydrogels for high power supercapacitor applications', *Journal of Power Sources*, vol. 360, pp. 538–547, Aug. 2017, doi: 10.1016/j.jpowsour.2017.06.033.

[6] H. Banda *et al.*, 'Ion Sieving Effects in Chemically Tuned Pillared Graphene Materials for Electrochemical Capacitors', *Chem. Mater.*, vol. 30, no. 9, pp. 3040–3047, May 2018, doi: 10.1021/acs.chemmater.8b00759.

[7] H. Banda *et al.*, 'Sparsely Pillared Graphene Materials for High-Performance Supercapacitors: Improving Ion Transport and Storage Capacity', *ACS Nano*, vol. 13, no. 2, pp. 1443–1453, Feb. 2019, doi: 10.1021/acsnano.8b07102.

[8] H. Banda *et al.*, 'Investigation of ion transport in chemically tuned pillared graphene materials through electrochemical impedance analysis', *Electrochimica Acta*, vol. 296, pp. 882–890, Feb. 2019, doi: 10.1016/j.electacta.2018.11.122.

[9] N. Stojilovic, 'Why Can't We See Hydrogen in X-ray Photoelectron Spectroscopy?', *J. Chem. Educ.*, vol. 89, no. 10, pp. 1331–1332, Sep. 2012, doi: 10.1021/ed300057j.

[10] G. Pognon, C. Cougnon, D. Mayilukila, and D. Bélanger, 'Catechol-Modified Activated Carbon Prepared by the Diazonium Chemistry for Application as Active Electrode Material in Electrochemical Capacitor', *ACS Appl. Mater. Interfaces*, vol. 4, no. 8, pp. 3788–3796, Aug. 2012, doi: 10.1021/am301284n.

[11] J. Onoe, A. Nakao, and K. Takeuchi, 'XPS study of a photopolymerized C 60 film', *Phys. Rev. B*, vol. 55, no. 15, pp. 10051–10056, Apr. 1997, doi: 10.1103/PhysRevB.55.10051.

[12] E. Frackowiak and F. Béguin, 'Carbon materials for the electrochemical storage of energy in capacitors', *Carbon*, vol. 39, no. 6, pp. 937–950, May 2001, doi: 10.1016/S0008-6223(00)00183-4.

[13] Y. J. Oh *et al.*, 'Oxygen functional groups and electrochemical capacitive behavior of incompletely reduced graphene oxides as a thin-film electrode of supercapacitor', *Electrochimica Acta*, vol. 116, pp. 118–128, Jan. 2014, doi: 10.1016/j.electacta.2013.11.040.

[14] M. Jerigová, M. Odziomek, and N. López-Salas, '"We Are Here!" Oxygen Functional Groups in Carbons for Electrochemical Applications', *ACS Omega*, vol. 7, no. 14, pp. 11544–11554, Apr. 2022, doi: 10.1021/acsomega.2c00639.

[15] W. Cai *et al.*, 'Synthesis and Solid-State NMR Structural Characterization of 13C-Labeled Graphite Oxide', *Science*, vol. 321, no. 5897, pp. 1815–1817, Sep. 2008, doi: 10.1126/science.1162369.

[16] W. Gao, L. B. Alemany, L. Ci, and P. M. Ajayan, 'New insights into the structure and reduction of graphite oxide', *Nature Chem*, vol. 1, no. 5, Art. no. 5, Aug. 2009, doi: 10.1038/nchem.281.

[17] E. Aliyev, V. Filiz, M. M. Khan, Y. J. Lee, C. Abetz, and V. Abetz, 'Structural Characterization of Graphene Oxide: Surface Functional Groups and Fractionated Oxidative Debris', *Nanomaterials*, vol. 9, no. 8, Art. no. 8, Aug. 2019, doi: 10.3390/nano9081180.

[18] S. Eigler, C. Dotzer, and A. Hirsch, 'Visualization of defect densities in reduced graphene oxide', *Carbon*, vol. 50, no. 10, pp. 3666–3673, Aug. 2012, doi: 10.1016/j.carbon.2012.03.039.

[19] T.-F. Hou, A. Shanmugasundaram, B. Q. H. Nguyen, and D.-W. Lee, 'Fabrication of surface-functionalized PUA composites to achieve superhydrophobicity', *Micro and Nano Systems Letters*, vol. 7, no. 1, p. 12, Aug. 2019, doi: 10.1186/s40486-019-0090-9.

[20] S. Rani, M. Kumar, R. Garg, S. Sharma, and D. Kumar, 'Amide Functionalized Graphene Oxide Thin Films for Hydrogen Sulfide Gas Sensing Applications', *IEEE Sensors Journal*, vol. 16, no. 9, pp. 2929–2934, May 2016, doi: 10.1109/JSEN.2016.2524204.

[21] I. O. Faniyi *et al.*, 'The comparative analyses of reduced graphene oxide (RGO) prepared via green, mild and chemical approaches', *SN Appl. Sci.*, vol. 1, no. 10, p. 1181, Sep. 2019, doi: 10.1007/s42452-019-1188-7.

[22] D. Khalili, 'Graphene oxide: a promising carbocatalyst for the regioselective thiocyanation of aromatic amines, phenols, anisols and enolizable ketones by hydrogen peroxide/KSCN in water', *New J. Chem.*, vol. 40, no. 3, pp. 2547–2553, Mar. 2016, doi: 10.1039/C5NJ02314A.

[23] F.-G. Zhao *et al.*, '*In situ* tunable pillaring of compact and high-density graphite fluoride with pseudocapacitive diamines for supercapacitors with combined predominance in gravimetric and volumetric performances', *J. Mater. Chem. A*, vol. 7, no. 7, pp. 3353–3365, 2019, doi: 10.1039/C8TA09782H.

[24] Z. Mo, H. Liu, R. Hu, H. Gou, Z. Li, and R. Guo, 'Amino-functionalized graphene/chitosan composite as an enhanced sensing platform for highly selective detection of Cu2+', *Ionics*, vol. 24, no. 5, pp. 1505–1513, May 2018, doi: 10.1007/s11581-017-2309-1.

[25] B. L. Frey and R. M. Corn, 'Covalent Attachment and Derivatization of Poly(l-lysine) Monolayers on Gold Surfaces As Characterized by Polarization−Modulation FT-IR Spectroscopy', *Anal. Chem.*, vol. 68, no. 18, pp. 3187–3193, Jan. 1996, doi: 10.1021/ac9605861.

[26] Y. Wang *et al.*, 'Magnetic graphene oxide nanocomposites: nanoparticles growth mechanism and property analysis', *J. Mater. Chem. C*, vol. 2, no. 44, pp. 9478–9488, Oct. 2014, doi: 10.1039/C4TC01351D.

[27] A. Lerf, H. He, M. Forster, and J. Klinowski, 'Structure of Graphite Oxide Revisited', *J. Phys. Chem. B*, vol. 102, no. 23, pp. 4477–4482, Jun. 1998, doi: 10.1021/jp9731821.

[28] H. Chi, Y. J. Liu, F. Wang, and C. He, 'Highly Sensitive and Fast Response Colorimetric Humidity Sensors Based on Graphene Oxides Film', *ACS Appl. Mater. Interfaces*, vol. 7, no. 36, pp. 19882–19886, Sep. 2015, doi: 10.1021/acsami.5b06883.

[29] A. Roy, S. Kar, R. Ghosal, K. Naskar, and A. K. Bhowmick, 'Facile Synthesis and Characterization of Few-Layer Multifunctional Graphene from Sustainable Precursors by Controlled Pyrolysis, Understanding of the Graphitization Pathway, and Its Potential Application in Polymer Nanocomposites', *ACS Omega*, vol. 6, no. 3, pp. 1809–1822, Jan. 2021, doi: 10.1021/acsomega.0c03550.

[30] B. E. Warren, 'X-Ray Diffraction in Random Layer Lattices', *Phys. Rev.*, vol. 59, no. 9, pp. 693–698, May 1941, doi: 10.1103/PhysRev.59.693.

[31] L. Stobinski *et al.*, 'Graphene oxide and reduced graphene oxide studied by the XRD, TEM and electron spectroscopy methods', *Journal of Electron Spectroscopy and Related Phenomena*, vol. 195, pp. 145–154, Aug. 2014, doi: 10.1016/j.elspec.2014.07.003.

[32] I. Bychko, A. Abakumov, O. Didenko, M. Chen, J. Tang, and P. Strizhak, 'Differences in the structure and functionalities of graphene oxide and reduced graphene oxide obtained from graphite with various degrees of graphitization', *Journal of Physics and Chemistry of Solids*, vol. 164, p. 110614, May 2022, doi: 10.1016/j.jpcs.2022.110614.

[33] M. P. Lavin-Lopez, A. Paton-Carrero, L. Sanchez-Silva, J. L. Valverde, and A. Romero, 'Influence of the reduction strategy in the synthesis of reduced graphene oxide', *Advanced Powder Technology*, vol. 28, no. 12, pp. 3195–3203, Dec. 2017, doi: 10.1016/j.apt.2017.09.032.

[34] R. Sharma, N. Chadha, and P. Saini, 'Determination of defect density, crystallite size and number of graphene layers in graphene analogues using X-ray diffraction and Raman spectroscopy', *Indian Journal of Pure & Applied Physics*, Jun. 2017, Accessed: Oct. 02, 2023. [Online]. Available: https://www.semanticscholar.org/paper/Determination-of-defect-density%2C-crystallite-size-Sharma-Chadha/b8b965ab26179e10c97d9d0c7e12a14a71da4998

[35] P. Wick *et al.*, 'Classification Framework for Graphene-Based Materials', *Angewandte Chemie International Edition*, vol. 53, no. 30, pp. 7714–7718, 2014, doi: 10.1002/anie.201403335.

[36] A. Ferrari, J. Robertson, S. Reich, and C. Thomsen, 'Raman spectroscopy of graphite', *Philosophical Transactions of the Royal Society of London. Series A: Mathematical, Physical and Engineering Sciences*, vol. 362, no. 1824, pp. 2271–2288, Sep. 2004, doi: 10.1098/rsta.2004.1454.
[37] S. M. Tan, A. Ambrosi, C. K. Chua, and M. Pumera, 'Electron transfer properties of chemically reduced graphene materials with different oxygen contents', *J. Mater. Chem. A*, vol. 2, no. 27, pp. 10668–10675, Jun. 2014, doi: 10.1039/C4TA01034E.
[38] L. G. Cançado *et al.*, 'General equation for the determination of the crystallite size La of nanographite by Raman spectroscopy', *Applied Physics Letters*, vol. 88, no. 16, p. 163106, Apr. 2006, doi: 10.1063/1.2196057.
[39] I. K. Moon, J. Lee, R. S. Ruoff, and H. Lee, 'Reduced graphene oxide by chemical graphitization', *Nat Commun*, vol. 1, no. 1, Art. no. 1, Sep. 2010, doi: 10.1038/ncomms1067.
[40] F. Tuinstra and J. L. Koenig, 'Raman Spectrum of Graphite', *Journal of Chemical Physics*, vol. 53, pp. 1126–1130, Aug. 1970, doi: 10.1063/1.1674108.
[41] S. Wang *et al.*, 'The role of sp2/sp3 hybrid carbon regulation in the nonlinear optical properties of graphene oxide materials', *RSC Adv.*, vol. 7, no. 84, pp. 53643–53652, Nov. 2017, doi: 10.1039/C7RA10505C.
[42] K. K. H. De Silva, H.-H. Huang, and M. Yoshimura, 'Progress of reduction of graphene oxide by ascorbic acid', *Applied Surface Science*, vol. 447, pp. 338–346, Jul. 2018, doi: 10.1016/j.apsusc.2018.03.243.
[43] K. Erickson, R. Erni, Z. Lee, N. Alem, W. Gannett, and A. Zettl, 'Determination of the Local Chemical Structure of Graphene Oxide and Reduced Graphene Oxide', *Advanced Materials*, vol. 22, no. 40, pp. 4467–4472, 2010, doi: 10.1002/adma.201000732.
[44] L. Muñoz-Rugeles, B. A. Arenas-Blanco, J. M. del Campo, and E. Mejía-Ospino, 'Wettability of graphene oxide functionalized with N-alkylamines: a molecular dynamics study', *Phys. Chem. Chem. Phys.*, vol. 24, no. 18, pp. 11412–11419, May 2022, doi: 10.1039/D2CP00292B.
[45] C.-M. Chen *et al.*, 'Hierarchically aminated graphene honeycombs for electrochemical capacitive energy storage', *J. Mater. Chem.*, vol. 22, no. 28, pp. 14076–14084, Jun. 2012, doi: 10.1039/C2JM31426F.
[46] T. S. Mathis, N. Kurra, X. Wang, D. Pinto, P. Simon, and Y. Gogotsi, 'Energy Storage Data Reporting in Perspective—Guidelines for Interpreting the Performance of Electrochemical Energy Storage Systems', *Advanced Energy Materials*, vol. 9, no. 39, p. 1902007, 2019, doi: 10.1002/aenm.201902007.
[47] P. L. Taberna, P. Simon, and J. F. Fauvarque, 'Electrochemical Characteristics and Impedance Spectroscopy Studies of Carbon-Carbon Supercapacitors', *J. Electrochem. Soc.*, vol. 150, no. 3, p. A292, Jan. 2003, doi: 10.1149/1.1543948.
[48] C. Zhong, Y. Deng, W. Hu, J. Qiao, L. Zhang, and J. Zhang, 'A review of electrolyte materials and compositions for electrochemical supercapacitors', *Chem. Soc. Rev.*, vol. 44, no. 21, pp. 7484–7539, Oct. 2015, doi: 10.1039/C5CS00303B.
[49] K. Kinoshita, *Carbon: Electrochemical and Physicochemical Properties*. 1988.
[50] C.-T. Hsieh, S.-M. Hsu, J.-Y. Lin, and H. Teng, 'Electrochemical Capacitors Based on Graphene Oxide Sheets Using Different Aqueous Electrolytes', *J. Phys. Chem. C*, vol. 115, no. 25, pp. 12367–12374, Jun. 2011, doi: 10.1021/jp2032687.
[51] J. R. L. Smith and D. Masheder, 'Amine oxidation. Part IX. The electrochemical oxidation of some tertiary amines: the effect of structure on reactivity', *J. Chem. Soc., Perkin Trans. 2*, no. 1, pp. 47–51, Jan. 1976, doi: 10.1039/P29760000047.
[52] A. Adenier, M. M. Chehimi, I. Gallardo, J. Pinson, and N. Vilà, 'Electrochemical Oxidation of Aliphatic Amines and Their Attachment to Carbon and Metal Surfaces', *Langmuir*, vol. 20, no. 19, pp. 8243–8253, Sep. 2004, doi: 10.1021/la049194c.
[53] A. K. V. Mruthunjaya and A. A. J. Torriero, 'Mechanistic Aspects of the Electrochemical Oxidation of Aliphatic Amines and Aniline Derivatives', *Molecules*, vol. 28, no. 2, Art. no. 2, Jan. 2023, doi: 10.3390/molecules28020471.

[54] J. H. Chae and G. Z. Chen, 'Influences of ions and temperature on performance of carbon nano-particulates in supercapacitors with neutral aqueous electrolytes', *Particuology*, vol. 15, pp. 9–17, Aug. 2014, doi: 10.1016/j.partic.2013.02.008.

[55] A. C. Forse, C. Merlet, J. M. Griffin, and C. P. Grey, 'New Perspectives on the Charging Mechanisms of Supercapacitors', *J. Am. Chem. Soc.*, vol. 138, no. 18, pp. 5731–5744, May 2016, doi: 10.1021/jacs.6b02115.

[56] J. A. Mattson, H. B. Mark, M. D. Malbin, W. J. Weber, and J. C. Crittenden, 'Surface chemistry of active carbon: Specific adsorption of phenols', *Journal of Colloid and Interface Science*, vol. 31, no. 1, pp. 116–130, Sep. 1969, doi: 10.1016/0021-9797(69)90089-7.

On the Lookout for a Green Mild Reducing Agent for Graphene Oxide

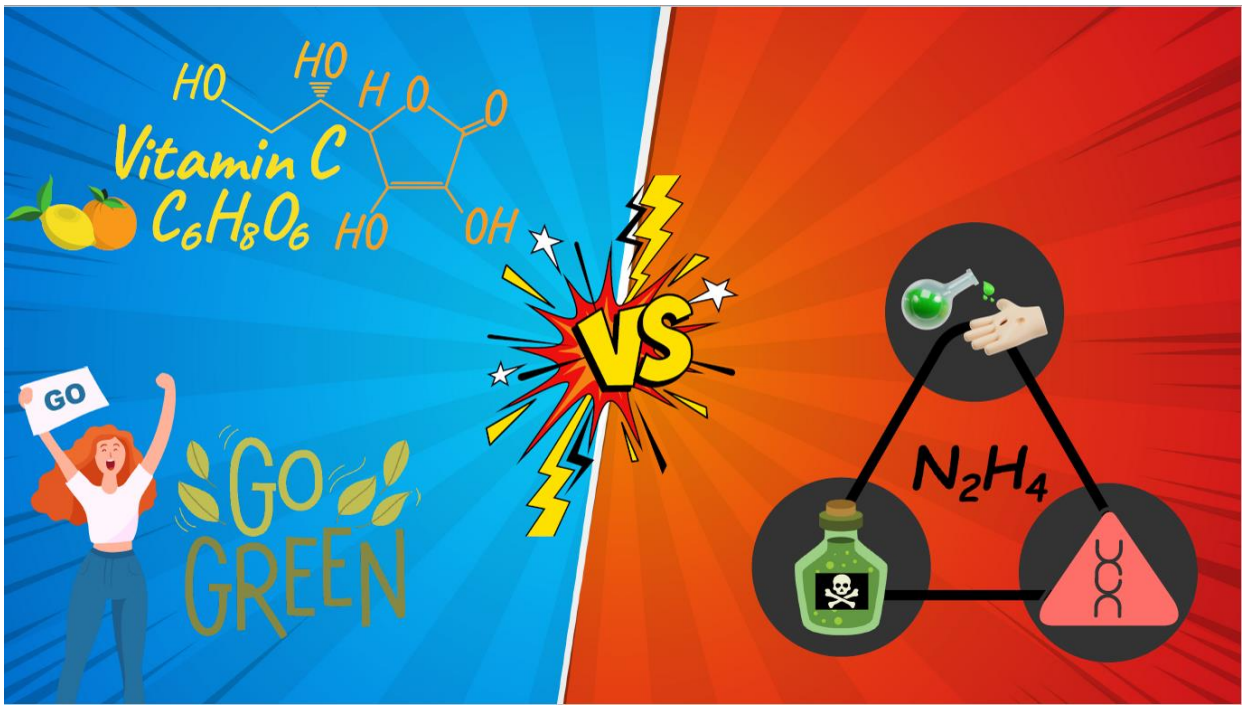

Chapter 3: On the Lookout for a Green Mild Reducing Agent for Graphene Oxide

III.1 Opening

As presented in Chapter 1, the use of the dangerous, toxic and non-environmental friendly Hydrazine (Hz) precludes the large-scale production of reduced Graphene Oxide (rGO) and other graphene-based assemblies where an efficient reducing agent is required. Various greener alternatives were proposed; however, their efficiency is too far from that of Hz, except for L-Ascorbic Acid (L-AA), commonly known as Vitamin C (VitC), which is the green reducing agent with the closest efficiency to that of Hz. VitC has shown efficient reducing capabilities for Graphene Oxide (GO) [1]. However, VitC reduction conditions are not fully optimized. Different publications utilize different reaction conditions including reaction time, reaction temperature, pH of the reaction medium, and concentration of L-AA as summarized in Table (I.1) in chapter 1 (see pages 53-54). In addition, the use of L-AA to reduce Pillared Graphene Materials (PGM) was - to the best of my knowledge - never reported. Moreover, full chemical and structural characterizations of the reduced samples are critical to relate the various reaction conditions to the resulting chemistry and structure, which would in turn allow the choice of the reaction conditions that would yield chemical and structural properties well suited to the application of interest. For energy storage devices, particularly Supercapacitors, an electrochemical analysis in common electrolytes is as essential as the structural and chemical characterizations. Consequently, a thorough study was done on the reduction of GO using L-AA. The study built on what is well-established in literature and included parameters such as the reaction time and concentration of L-AA. A complete characterization scheme was devised for such a study. Such a scheme started with chemical characterization to investigate the success of reduction and its extent to compare such parameters to those of rGO reduced by Hz. To carry out such chemical investigations, various characterization techniques were utilized such as X-ray Photoelectron Spectroscopy (XPS), Elemental Analysis (EA) and Thermal Gravimetric Analysis (TGA). Structural and morphological characterizations were conducted to analyze the structure of the samples and relate the differences in structural properties to the different degrees of reduction and thus to different reduction conditions. X-ray Diffraction (XRD), Raman Spectroscopy, Scanning Electron Microscopy (SEM), and Transmission Electron Microscopy (TEM) were used to probe the structure of the samples. Subsequently, electrical conductivity measurements were carried out to examine the effect of the various reaction conditions on such a property that is crucial for supercapacitor applications. Afterwards, electrochemical testing was performed to test the performance of the greener rGO samples (reduced with L-AA) as

electrode materials for supercapacitors and to compare their performances to that of rGO reduced by Hz. The supercapacitor testing was done in various common representative electrolytes such as 3M H_2SO_4 as an acidic electrolyte, 6M KOH as a basic electrolyte and 0.5M K_2SO_4 as a neutral electrolyte. Upon gathering such pieces of information, the optimum conditions were selected and applied, for the 1st time, to reduce PGM, and their chemical, structural and electrochemical properties were compared to those of Hz reduced PGM as demonstrated in the perspectives section in Chapter 4 (see page 201).

III.2 Synthesis

III.2.1 Synthesis of Graphene Oxide (GO)

GO was synthesized using a modified Hummer's method (Figure III.1) as summarized in Chapter 2 (see page 67) and detailed in the Materials and Methods chapter.

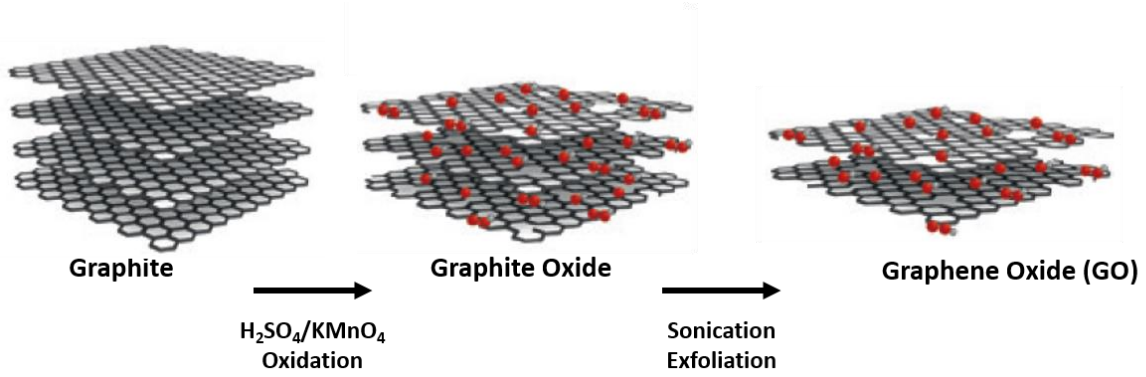

Figure III. 1 : Oxidation and Exfoliation of Graphite to produce GO

III.2.2 Synthesis of Reduced Samples

The aim of the reduction is to remove as many as possible oxygen functionalities from the surface of GO, in order to re-establish the sp^2 carbon network to restore the electrical conductivity of the samples and enhance their inertness to side reactions.

III.2.2.1 Synthesis of rGO-Hz

Reduction of GO using Hz-hydrate (referred to as rGO-Hz) was carried out to get a reference sample to which the other samples will be compared in terms of chemical, structural, and electrochemical properties. The choice of rGO-Hz was based on the fact that Hz is the best-known and most efficient known reducing agent for GO so far. The reduction using Hz was performed in excess of Hz-hydrate at 95°C according to the reaction scheme shown in Figure (III.2), yielding rGO-Hz powder that was then washed to remove excess Hz before being dried overnight in an oven.

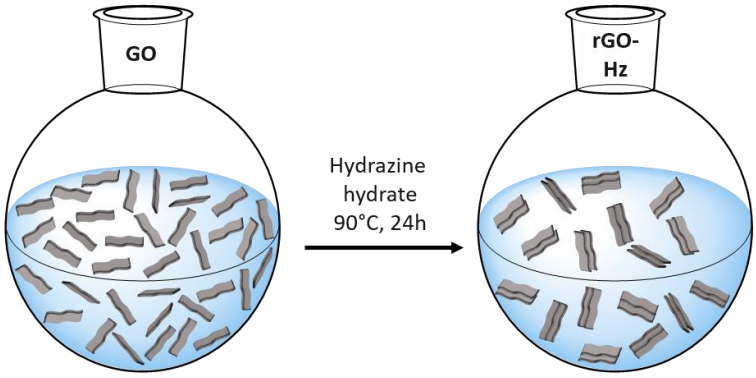

Figure III. 2 : Synthesis of Hydrazine reduced Graphene Oxide (rGO-Hz)

III.2.2.2 Synthesis of GHG

Hydrothermal reduced GO was also synthesized in order to get another common reference sample, Graphene HydroGel (GHG), to compare to VitC-reduced GO in order to ascertain the efficiency of the VitC reduction against common efficient reduction techniques. Hydrothermal synthesis is sometime regarded as a green technique; however, the use of high temperature and pressure makes it difficult to put it in the same category as VitC. Also, safety wise, it is not a safe technique as there is always the risk of explosions because of the high pressure.

Graphene hydrogel was synthesized hydrothermally in an autoclave at 180°C as shown in Figure (III.3). Following the synthesis, the resulting hydrogel was washed to remove unreacted GO and then freeze-dried to preserve its structural integrity as a self-standing monolith. Hydrothermal reduction does not involve the addition of reducing agents as the reduction takes place under the effect of high temperature and high pressure. Under such conditions, supercritical water is formed and it can play the role of the reducing agent, leading to heterolytic bond cleavage reaction and acid-catalyzed reactions of organic compounds due to sufficient concentration of H^+ under such conditions compared to normal liquid water [2].

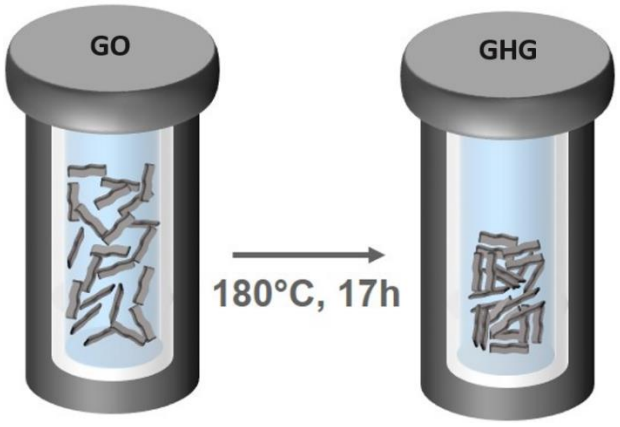

Figure III. 3 : Hydrothermal Synthesis of Graphene HydroGel (GHG)

III.2.2.3 Synthesis of rGO-VitC

The reduction of GO using L-AA was carried out at 95°C based on what was established in literature [3] and on fundamental chemistry that states that increasing the reaction temperature would increase the rate of the reaction and offer enough energy to overcome the activation energy barrier for the reaction, thus leading to the reaction taking place and increasing its rate, given that the reactants do not degrade at the temperature selected (VitC was experimentally found to start degrading at ~205°C as what will be shown in the chemical analysis section). Higher temperatures were not possible as the reaction medium is water, limiting the maximum temperature to its boiling point (100°C). The pH of the reaction medium was adjusted to ~9-10 because at such basic pH, the acidic groups of GO (carboxylic and phenolic groups) are expected to be deprotonated, leading to negatively charged surface, resulting in colloidal stability through electrostatic repulsion between the sheets [3], [4]. This high pH is also believed to facilitate the removal of the oxidized products of L-AA, namely DH-AA, and prevent its accumulation in the reaction medium [5], [6]. The reaction time was varied between short (30 minutes) and long periods (24 hr) while the concentration was varied among 2.6mM, 26 mM and 63mM. Such concentration will be referred to as 0.04, 0.4 and 1 molar equivalents to GO. The "so-called" number of moles of GO was calculated using the weighed molar mass of its components. Such a number and the equivalence are just to give an indication of how much L-AA is added in relation to GO. These values correspond to 0.55, 5.4 and 13.6 mg of L-AA per mg of GO. After the reaction, the samples were washed using a Soxhlet set-up. Such an extra step was never mentioned in literature. This method was selected to make sure that neither L-AA nor its oxidized products are still present in or on the samples after the reduction to avoid any misleading C/O ratios. L-ascorbic acid or its oxidized products are expected to be present after the reduction due to the restoration of the sp^2 carbon network that might act as an adsorbing surface for such cyclic compounds, in addition to the hydrogen bonds that can form between the oxidized products of L-AA and the remaining oxygen functionalities on the surface of the rGO [5], [7]. In literature, washing with copious amounts of water and/or using H_2O_2 to wash the side products and oxidize the remaining L-AA, respectively, were employed [8]. In order not to use additional chemicals and make the reaction as simple as possible, the Soxhlet setup was favored. Moreover, it uses boiling water that might help break the H-bonds between the side products and the rGO, leading to more efficient washing. Also, Soxhlet washing is a sustainable technique that reuses the same volume of water initially added to perform multiple cycles of washing. The reduction scheme using L-AA along with the Soxhlet washing step are presented in Figure (III.4).

The samples reduced by L-AA under various conditions are referred to as rGO-VitC-XX-YY where XX refers to the reaction time and YY refers to the number of equivalents of L-AA to GO. The rGO-VitC samples' codes are summarized in Table (III.1) along with the reaction conditions. Four different reaction conditions were selected to represent various important reaction condition-related findings. Moving from a sample to the next, all the reaction conditions are kept constant except either the reaction time or the concentration to be able to draw unbiased conclusions.

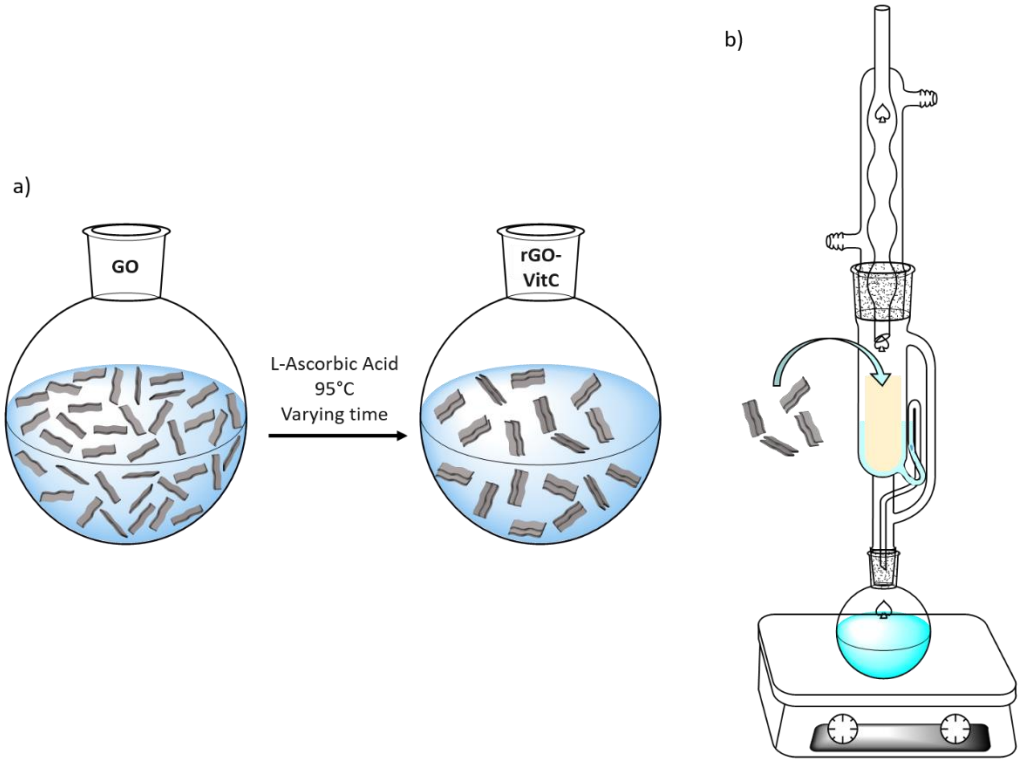

Figure III. 4 : a) Synthesis of L-ascorbic acid reduced Graphene Oxide (rGO-VitC) and b) Then Soxhlet set-up used in the washing step

Sample	Reaction Temp	pH	Reaction Time	Equivalent of L-AA	Conc of L-AA (mM)
rGO-VitC-24hr-0.04eq	95	9-10	24 hour	0.04	2.6
rGO-VitC-24hr-1eq	95	9-10	24 hour	1	63
rGO-VitC-30min-1eq	95	9-10	30 min	1	63
rGO-VitC-30min-0.4eq	95	9-10	30 min	0.4	26

Table III. 1 : The rGO-VitC samples' codes along with their corresponding reaction parameters

After the synthesis of the samples was completed, chemical and structural analysis were carried out to examine the validity of the reduction method and to compare its efficiency to that of Hz and hydrothermal reduction.

III.3 Chemical Analysis

Investigating the success of the reduction and examining the reduction extent were the main goals for carrying out the chemical analysis. As highlighted in Chapter 1, the C/O ratio is

a direct indication of both the reduction and its extent. The higher the C/O ratio is, the more reduced the sample is.

III.3.1 An Intriguing Discovery

XPS was done to explore surface elemental chemical composition, as well as to extract bonding scheme information of the present elements. XPS surveys (Figure III.5) show the presence of C, N and O with varying atomic concentrations - depending on the reduction technique - as summarized in Table (III.2).

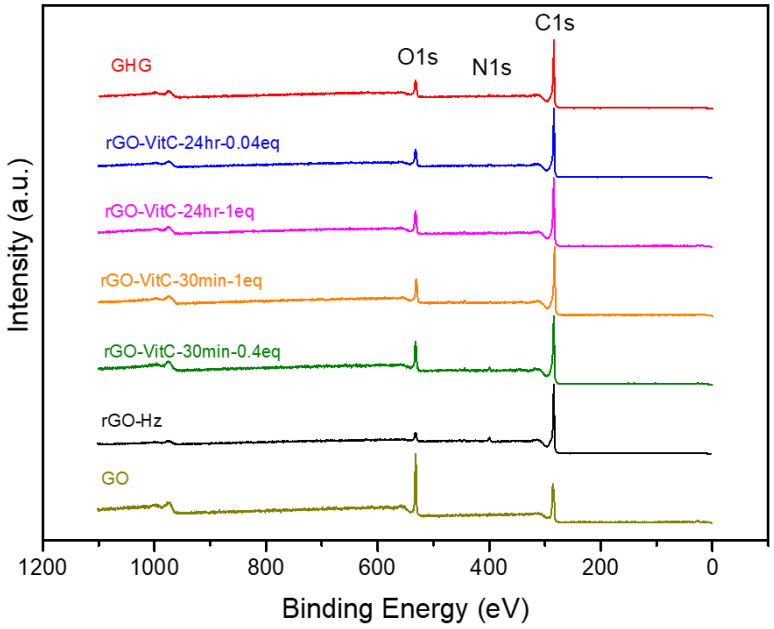

Figure III. 5 : XPS Survey spectra of GO (—), rGO-Hz (—), rGO-VitC-30min-0.4eq (—), rGO-VitC-30min-1eq (—), rGO-VitC-24hr-1eq (—), rGO-VitC-24hr-0.04eq (—) and GHG (—)

Sample	C (at. %)	N (at. %)	O (at. %)	C/O
GHG	87.66	0.65	11.69	7.5
rGO-VitC-24hr-0.04eq	87.26	1.33	11.41	7.65
rGO-VitC-24hr-1eq	84.99	0.84	14.17	6
rGO-VitC-30min-1eq	88.53	1.31	10.16	8.71
rGO-VitC-30min-0.4eq	88.53	1.10	10.37	8.54
rGO-Hz	90.51	3.04	6.45	14.03
GO	70.06	0.1	29.84	2.35

Table III. 2 : C, N and O content, in atomic % of GO, rGO-Hz, rGO-VitC-30min-0.4eq, rGO-VitC-30min-1eq, rGO-VitC-24hr-1eq, rGO-VitC-24hr-0.04eq and GHG along with their C/O ratios

The rGO-Hz sample has an appreciable amount of N content (3 at.%) while the rest of the samples have trace amount of nitrogen (~1 at.%). Such an increase in N content in the Hz-reduced sample is attributed to the nitrogen insertion reduction mechanisms of Hz reported in literature that inserts various N groups in the graphene sheets [9]. The lowest amount of N was found for the GHG sample which can be arising from N content originally present in the starting

GO. The slight increase in N content for the various rGO-VitC samples compared to GO and GHG can be attributed to the NH_4OH drops that were added before the reaction to adjust the pH level of the reaction medium to 9-10.

The C/O ratio of GO, the starting material, was the lowest (2.35) as expected because it has high oxygen content as a result of the successful oxidation. Upon reducing the GO with different methods (chemically with Hz or L-AA or hydrothermally), the C/O ratio increased. Such an increase in C/O ratio directly indicates the partial removal of the oxygen functionalities of GO and indirectly indicates the partial restoration of the sp^2 carbon network. The rGO-Hz showed the highest C/O ratio (14.03) which is in line with the Hz being the most efficient reducing agent of GO. The GHG sample showed a C/O ratio of 7.5, showing the success of such a technique in reducing the GO. The rGO-VitC samples showed C/O ratios varying from 6 to 8.71. Such high C/O ratios compared to that of GO (2.35) prove the successful reduction of GO using L-AA. The C/O ratios of GHG and all the rGO-VitC samples are lower than that of rGO-Hz (42-62% less). Such results are quite expected and such difference in C/O ratio has to be weighed against the dangers, toxicity, and cost of Hz waste removal. In addition, the samples will be further evaluated with other characterization techniques to be able to judge their properties, such as their electrical conductivity and to judge their applicability as electrode materials for supercapacitor applications.

The rGO-VitC-30min-0.4eq sample showed a high C/O ratio of 8.54 in just 30 minutes. To test the effect of the concentration of the added L-AA, more than double the L-AA quantity was added to make rGO-VitC-30min-1eq which showed nearly the same C/O ratio (8.71) to that of the one with lower concentration. This indicates that for 30 minutes of reduction time, more L-AA will not enhance the reduction. Maybe such an excess of L-AA did not have enough time to react or the reaction had already reached completion. In order to test these hypotheses, the reaction time was increased from 30 minutes to 24 hours. If the reaction was yet to proceed with the extra added L-AA, the C/O would increase. On the other hand, if the reaction had already reached completion after 30 minutes, no change should be observed in the C/O ratio. Counterintuitively, the C/O ratio decreased from 8.71 to 6! Such an unexpected finding was repeated multiple times with different batches of GO, different reaction times (30 minutes, 2 hours and 24 hours) and even with different concentrations (0.4 and 4 molar equivalents) as shown in Figure (III.6).

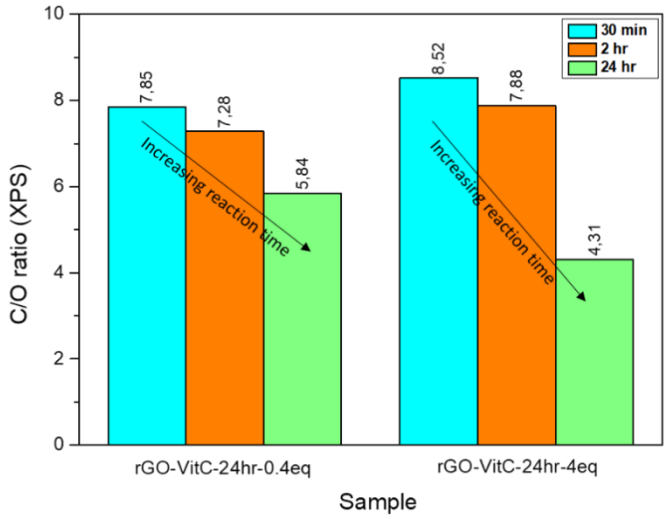

Figure III. 6 : The C/O ratio of rGO-VItC-24hr-0.4eq and rGO-VItC-24hr-4eq at different reduction times

It can be seen that the C/O ambiguously decreased with increasing the reaction time even for 2 hours in the case of the 0.4eq and 4eq samples. The decrease in C/O ratio was observed to be more drastic for the sample with the higher molar equivalents of L-AA to GO as the C/O ratio dropped by ~50% for the 4eq sample and ~26% for the 0.4eq sample reduced in 24 h. To ascertain such a finding, a much lesser amount of L-AA (0.04 equivalent) was used to reduce the samples in 24hr. To our surprise, the sample yielded a much higher C/O (7.65) compared to that of the samples reduced in the same reaction time (24 h) but with higher amount of L-AA as a reducing agent (6, 5.84 and 4.31 for samples reduced with 1, 0.4 and 4 molar equivalents of L-AA to GO).

III.3.2 Verification of the Unexpected Finding

Before going further into contemplating about the reason of such an abnormal decrease of C/O ratio when the reaction time is increased with higher amounts of reducing agent (L-AA), such decrease was further verified using EA and TGA. In this and upcoming sub-sections, the validation of this abnormal result will be presented and the fundamental understanding of such behavior will be deeply inspected. The aim, herein, is not only to select the best conditions for reducing GO using L-AA, but also, to comprehend the effects of various reaction conditions on the resulting rGO-VitC samples and their properties, as well as investigating the mechanics behind such effects, allowing for a more complete picture of how the reduction proceeds and how various conditions can yield different properties.

EA provides a bulk chemical composition analysis of the samples complementary to the surface chemical composition analysis provided by XPS. EA also allows verifying the reduction and

its extent through the C/O ratio. The C, H, N and O contents (weight percentages) of the samples are displayed in Figure (III.7). The C/O ratio of GO was the lowest (1.06 ±0.007) due to the presence of various oxygen functionalities resulting from the oxidation process. The C/O ratio for all the reduced samples were higher than that of GO, indicating the success of the reduction process using different reduction methods. The C/O ratios were 9.17 ±0.352, 3.86 ±0.007, 3.72 ±0.022, 2.92 ±0.026, 3.21 ±0.09 and 3.87 ±0.4 for rGO-Hz, rGO-VitC-30min-0.4eq, rGO-VitC-30min-1eq, rGO-VitC-24hr-1eq, rGO-VitC-24hr-0.04eq and GHG, respectively.

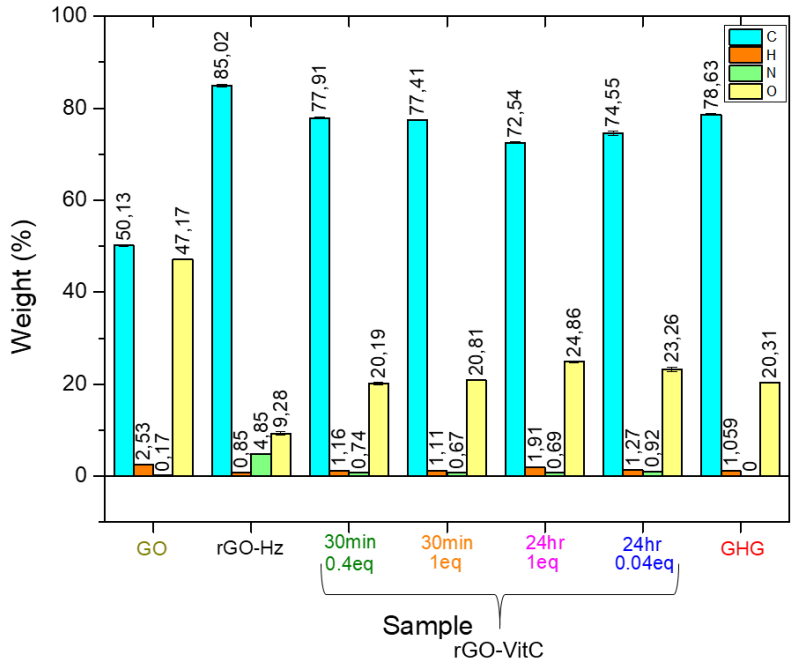

Figure III. 7 : Weight percentages of GO, rGO-Hz, rGO-VitC-30min-0.4eq, rGO-VitC-30min-1eq, rGO-VitC-24hr-1eq, rGO-VitC-24hr-0.04eq and GHG calculated from EA

The C/O ratios confirm the results and trends spotted earlier in XPS, such as i) rGO-Hz is the sample with the highest C/O ratio which is in agreement with Hz being the most efficient reducing agent of GO, ii) Hydrothermal synthesis and L-AA can successfully reduce GO, and most importantly iii) The C/O ratio anomalously decreased when the reduction time was increased from 30 minutes to 24 hours, using 1 molar equivalent of L-AA to GO (3.72 ±0.022 in 30 min compared to 2.92 ±0.026 in 24 hr). When lower amount of L-AA (0.04 eq) was used for a reduction time of 24 hours, the C/O was higher than that in the case of higher amounts of L-AA (3.21 ±0.09 with 0.04eq compared to 2.92 ±0.026 with 1eq).

TGA was carried out under an inert atmosphere to further confirm such trends in C/O as the final weight loss under such conditions is expected to have an inverse proportionality relationship with the C/O ratio. The higher the C/O ratio of the sample analyzed is, the less

oxygen functionalities are remaining in the sample, thus, less weight lost during TGA analysis because the weight loss comes from the degradation of various oxygen functionalities. Accordingly, the sample with the highest C/O ratio will have the least weight loss at the end of the analysis. The TGA profiles shown in Figure (III.8(a)) demonstrate the degradation profiles of the various samples under Ar gas from 30°C to 800°C. Figure (III.8(b)) shows the weight loss of the samples at 800°C. The values are 4, 54, 14, 16, 16, 27, 18 and 18 for Graphite, GO, rGO-Hz, rGO-VitC-30min-0.4eq, rGO-VitC-30min-1eq, rGO-VitC-24hr-1eq, rGO-VitC-24hr-0.04eq and GHG. The degradation profile of graphite shows only 4% weight loss at 800°C, highlighting the very high thermal stability of the sample. On the other hand, the degradation profile of GO shows three weight loss steps corresponding to three degradation processes [10]: i) a weight loss of 6% up to 100°C, which can be assigned to the loss of surface adsorbed water molecules, ii) a weight loss of 29% between 100°C and 250°C with an abrupt loss (~27%) around 200°C due to the loss of labile oxygen functionalities and remaining water molecules, and iii) a gradual weight loss of 19% from 250°C till 800°C attributed to the loss of strongly bonded oxygen moieties.

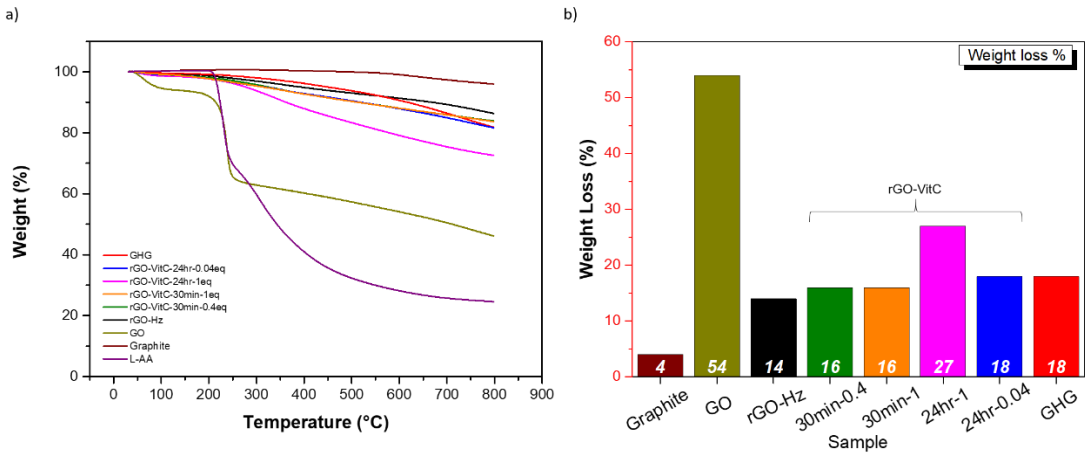

Figure III. 8 : a) TGA profile of L-AA (—), Graphite (—), GO (—), rGO-Hz (—), rGO-VitC-30min-0.4eq (—), rGO-VitC-30min-1eq (—), rGO-VitC-24hr-1eq (—), rGO-VitC-24hr-0.04eq (—) and GHG (—) and b) the weight loss (%) for each sample at 800°C

The reduced samples are showing steady degradation profiles from 250°C up till 800°C with different values of weight loss depending on the degree of reduction of the sample. When the C/O ratio is low, the weight loss is higher because the sample has more oxygen functionalities (labile or strongly bonded) to lose. The rGO-Hz is the reduced sample with the least weight loss while the other reduced samples are having higher weight losses, in line with their reduction extent, indicated by their C/O ratios. Increasing the reaction time from 30 minutes to 24 hours when using high amounts of L-AA lead to an increase in weight loss, indicative of having more oxygen content to lose. The L-AA degradation profile is showing an abrupt weight loss at 200°C

and a continuous steep weight loss till 800°C. Such behavior was not observed in any of the rGO-VitC samples, indicating the success of the Soxhlet technique in removing any remaining L-AA from the samples after the reduction.

The pieces of information gathered so far were plotted together in Figure (III.9), showing the C/O ratios from XPS and EA along with the weight remaining at 800°C from TGA. The weight remaining at 800°C was chosen for the plot instead of weight loss for more consistency and clarity in the plot. It is complementary to the weight loss at 800°C (their sum is equal to 100%), meaning a small weight loss for a reduced sample is equivalent to large weight remaining at 800°C. The trends in C/O ratio adequately match using different techniques. Most importantly, the puzzling decrease in C/O ratio going from rGO-VitC-30min-1eq to rGO-VitC-24hr-1eq was confirmed using various techniques (XPS, EA and TGA) as displayed by the highlighted box in Figure (III.9).

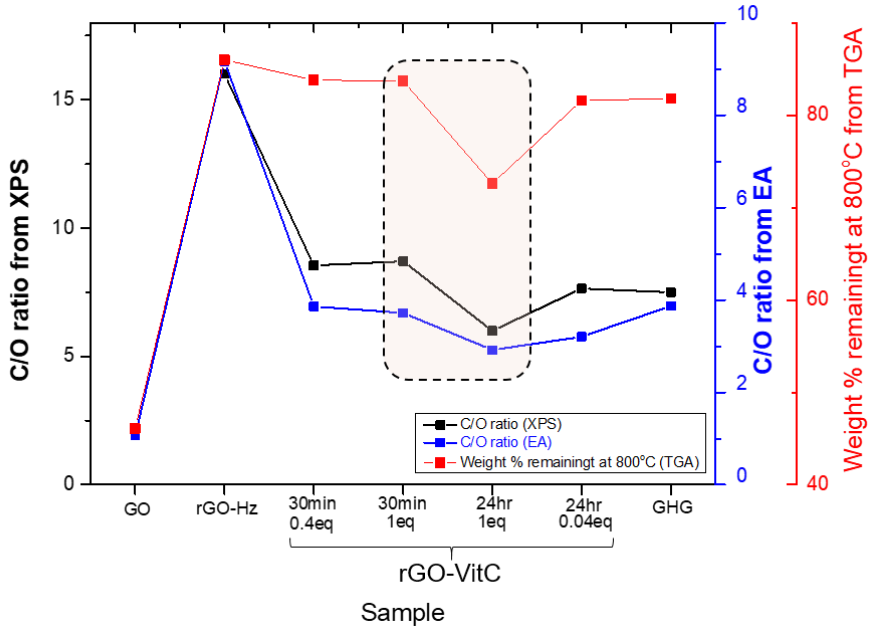

Figure III. 9 : The relation between C/O ratio from XPS and EA, and the weight % remaining at 800°C from TGA. The enclosed area shows the abnormal trendwhen increasing reduction time from 30 min to 24 h with 1eq of L-AA

Taking into consideration our new finding that longer reaction times with higher L-AA can lead to results opposite to those desired, it seems that shorter reaction times can be recommended for high amounts of L-AA while longer reaction times are recommended for low amounts of L-AA to get higher reduction. At such stage, the premise of L-ascorbic acid leading to the re-oxidation of rGO can be safely inferred from such a decrease in C/O ratio when leaving the reaction to continue for more time. In order to be able to postulate and claim the reasons of such an increase in the oxygen content, the type of this extra oxygen content must be deciphered.

Consequently, High Resolution C1s and O1s XPS spectra were recorded and analyzed. Herein, only the figures with the C1s and O1s HR-XPS peak fitting of GO, rGO-VitC-30min-1eq and rGO-VitC-24hr-1eq will be displayed. The peak fitting of the other samples will not be displayed because differences between these samples are quite hard to be inferred directly from the figures; however, the results of their peak fitting will be displayed in tables and discussed in text. The peak fitting of the C1s HR-XPS spectra of rGO-VitC-30min-1eq and rGO-VitC-24hr-1eq is shown in Figure (III.10). The fitted peaks of the HR-XPS C1s peak of GO (Figure III.10(a)) show the presence of C=C/C-C, C-O, C=O and COO at 284.3, 286.3, 287.4 and 288.5 eV, respectively.

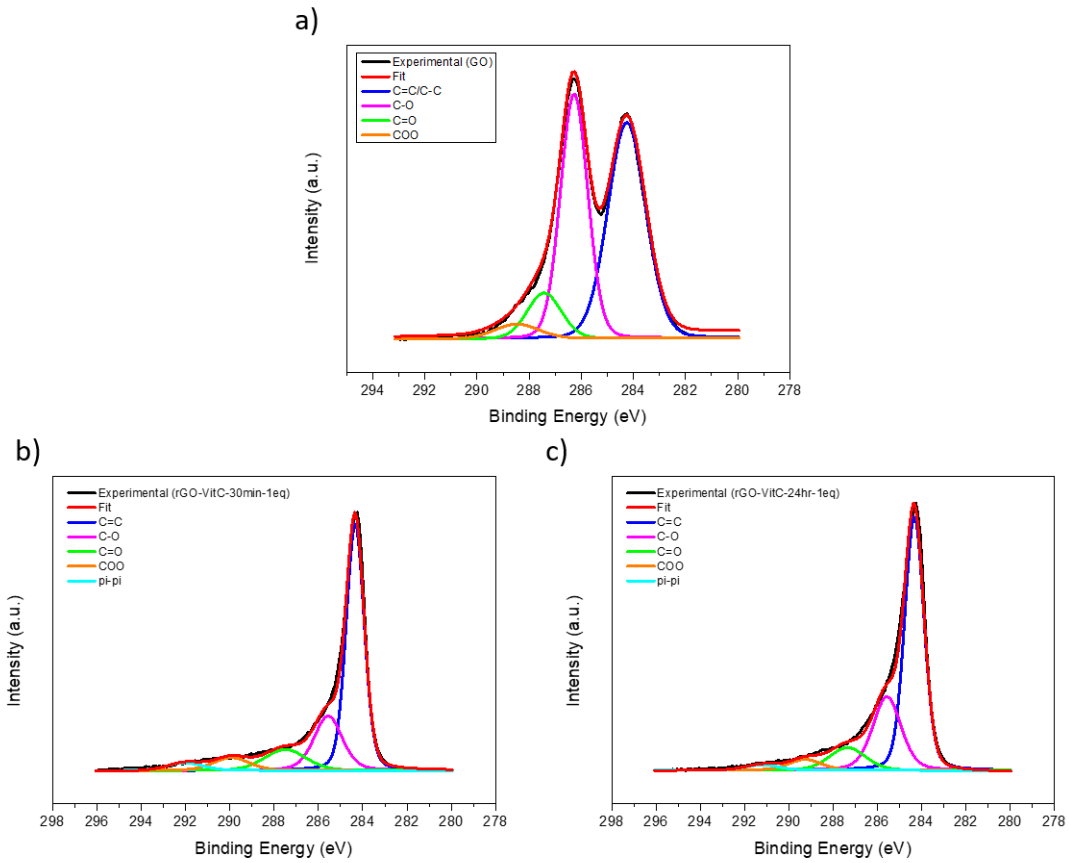

Figure III. 10 : Peak fitting of HR-XPS C1s spectra of a) GO, b) rGO-VitC-30min-1eq and c) rGO-VitC-24hr-1eq

Sample	sp^2/sp^3 (at. %)	C-O (at. %)	C=O (at. %)	COO (at. %)	π-π* (at. %)
GHG	59.58	21.07	10.51	5.49	3.35
rGO-VitC-24hr-0.04eq	58.18	20.37	11.67	6.4	3.38
rGO-VitC-24hr-1eq	58.07	25.74	9.63	4.35	2.21
rGO-VitC-30min-1eq	57.58	20.94	11.28	6.34	3.86
rGO-VitC-30min-0.4eq	55.95	21.98	10.17	5.4	6.5
rGO-Hz	59.65	20.4	9.81	6.08	4.05
GO	48.78	27.84	15.57	7.81	-

Table III. 3 : Atomic percentage of each of the components of the HR-XPS C1s spectra of GO, rGO-Hz, rGO-VitC-30min-0.4eq, rGO-VitC-30min-1eq, rGO-VitC-24hr-1eq, rGO-VitC-24hr-0.04eq and GHG

The reduced samples, regardless of the reduction method, show a decrease in the area under the peaks of the oxygen containing carbons as well as the narrowing of the carbon peak at ~284.3 eV (Figure III.10(b) & (c)). The former is indicative of the reduction of the samples as less oxygen containing carbons are present after reduction. The latter is indicative of the partial restoration of the sp^2 carbon network because pure sp^2 carbon XPS peaks have a narrower FWHM compared to the broader ones when sp^2 and sp^3 carbons co-exist so narrowing of the peaks means more sp^2 carbons compared to sp^3 carbons. The restoration of the sp^2 carbons can also be inferred from the appearance of the π-π^* satellite peak at ~292 eV in the reduced samples and not in GO, which can be assigned to the shake-up phenomenon in which the π electrons of aromatic rings are excited through exiting photoelectrons [11]. From the figures of rGO-VitC-30min-1eq (Figure III.10(b)) and rGO-VitC-24hr-1eq (Figure III.10(c)), it seems that the area under the C-O peak is larger in rGO-VitC-24hr-1eq compared to that in rGO-VitC-30min-1eq. To validate such qualitative observation, peak integration was carried out for all the peaks to get the quantitative values as those presented in Table (III.3). It can be quantitatively observed that the increased oxygen content in the rGO-VitC-24hr-1eq is originating from an increase in C-O groups (probably C-OH or C-O-C). From such an integration of the peaks for the rest of the samples, the high content of oxygen containing carbons in GO can be noted, showing the success of the oxidation by the modified Hummer's method. The reduced samples display a decrease in the oxygen containing carbons with an increase in the sp^2 carbon content as a result of the successful reduction leading to the partial removal of oxygen functionalities and thus the partial recovery of the sp^2 carbon network.

To verify the results obtained from the peak fitting of the C1s HR-XPS spectra, O1s HR-XPS spectra were recorded and their peak fitting was done (Figure III.11) to identify the type of oxygen bonding (C-O and C=O) available in the various samples. The fitted peaks were integrated to extract the relative percentages of the different types of carbon oxygen bonds (Table III.4).

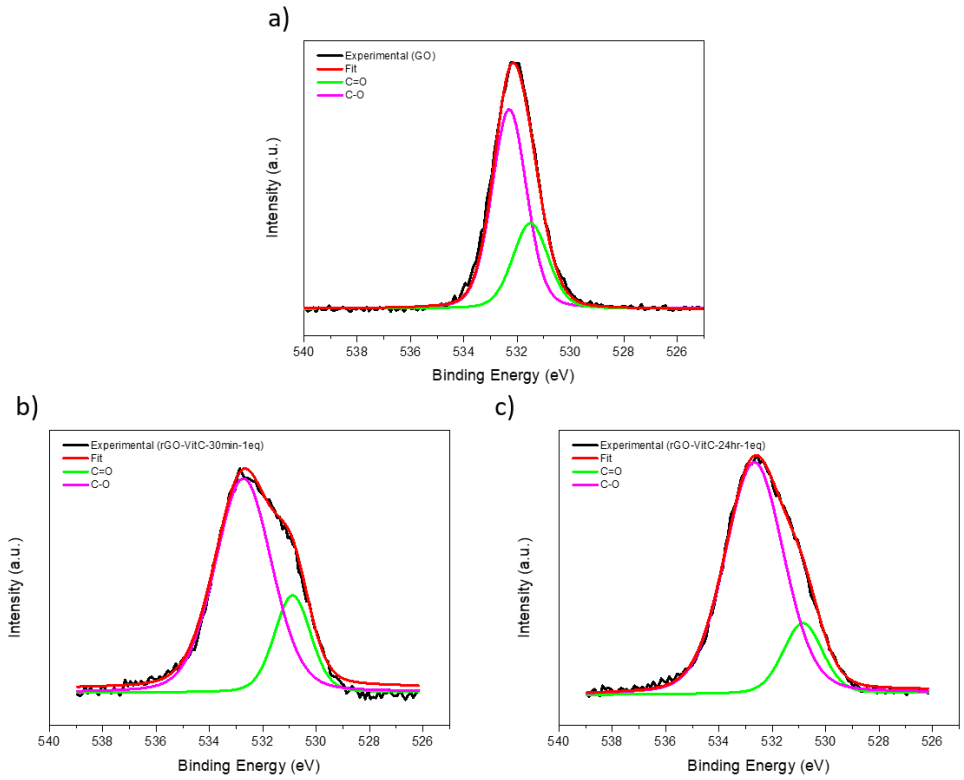

Figure III. 11 : Peak fitting of HR-XPS O1s spectra of a) GO, b) rGO-VitC-30min-1eq and c) rGO-VitC-24hr-1eq

Sample	C=O (at. %)	C-O (at. %)	Overall C=O * (at. %)	Overall C-O * (at. %)
GHG	33.41	66.59	3.91	7.78
rGO-VitC-24hr-0.04eq	24.59	75.41	2.81	8.60
rGO-VitC-24hr-1eq	16.95	83.05	2.4	11.77
rGO-VitC-30min-1eq	22.5	77.5	2.29	7.87
rGO-VitC-30min-0.4eq	19.65	80.35	2.04	8.33
rGO-Hz	32.51	67.49	2.1	4.35
GO	30.58	69.42	9.24	20.98

**Overall X = (X at. % from O1s * Total O at. %) /100 X= C-O or C=O*

Table III. 4 : Atomic percentage of each of the components of the HR-XPS O1s spectra of GO, rGO-Hz, rGO-VitC-30min-0.4eq, rGO-VitC-30min-1eq, rGO-VitC-24hr-1eq, rGO-VitC-24hr-0.04eq and GHG

The peak fitting of the HR O1s XPS spectra of all the samples showed the appearance of two peaks corresponding to C=O and C-O. Those peak appeared, respectively, at ~531.4 eV and ~532.3 eV in the GO sample. The reduced samples showed a decrease in the overall amount of both C=O and C-O with the latter being the most reduced. This is in line with the proposed reduction mechanisms for hydrothermal reduction, reduction with Hz and reduction with L-AA. A decrease in C=O was observed with the samples reduced with L-AA, while a reduction mechanism of the carbonyl groups using L-AA was not proposed before, although being reported to take place [4]. Increasing the reduction time from 30 minutes to 24 hours, using one molar equivalence of L-AA to GO, lead to an increase in the overall C-O percentage. This

confirms that such an increase in the oxygen with the reduction time using high amounts of L-AA can be attributed to the increase in C-O bonds as in hydroxyl or epoxy groups.

III.3.3 The Calm Before The Storm - A Recap

The chemical analysis presented in the above section emphasizes the chemical differences between GO and various reduced samples as well as the chemical differences among the reduced samples themselves. GO has a low C/O ratio due to the presence of various oxygen functionalities such as epoxy, hydroxyl, carbonyl and carboxylic groups resulting from the oxidation of graphite. All the reduced samples show a higher C/O ratio compared to that of GO due to the partial removal of the different oxygen functionalities and the partial restoration of the sp^2 carbon network upon reduction. rGO-Hz shows the highest C/O ratio as it is the most efficient reducing agent of GO. The hydrothermal reduction and reduction with L-AA proved their reducing capabilities as they demonstrated C/O ratios higher than that of GO. Different L-AA reduction conditions lead to differences in the reduction extent. Reduction of GO in 30 minutes using 0.4 or 1 molar equivalents of L-AA to GO yielded the 2nd and 3rd highest C/O ratios after that of rGO-Hz, demonstrating the potential of such reduction conditions in achieving a high reduction extent in the shortest period of time compared to the other techniques (24 hours for reduction using Hz and 17 hours for hydrothermal reduction). Increasing the reaction time from 30 minutes to 24 hours lead to an increase in oxygen content. The rGO-VitC-24hr-0.04eq sample yielded a C/O ratio comparable to that of GHG.

The increase in oxygen content when the reduction time is increased upon reducing the GO using L-AA was never observed when Hz was used to reduced GO or when GO was reduced hydrothermally. Such an increase in oxygen content is counterintuitive. In 30 minutes, the sample reached a certain C/O ratio due to the partial removal of various oxygen functionalities; however, when the sample was left more in the same reducing medium, it got re-oxidized. This was evidenced by the decrease in the C/O ratio and the increase in the oxygen content, particularly oxygens forming C-O bonds. Such an observation was never mentioned, to the best of my knowledge, in the literature concerning the reduction of GO using L-AA as presented in the introductory section (Chapter 1).

III.3.4 The Storm - Can L-Ascorbic Acid Oxidize Reduced Graphene Oxide?

The observed re-oxidation of the rGO-VitC might be a result of in-situ production of hydrogen peroxide (H_2O_2) due to the various possible reactions involving L-AA in its different forms. The oxidation of L-AA and the various pathways such oxidation follows have been studied, especially in biological media; however, they are still poorly understood [12]. A well-

documented oxidation reaction of L-AA is interrelated to the capability of its de-protonated form to reduce the Fe(III) and Cu(II) ions. Such reaction takes place in acidic media where the L-AA partially exists as mono-anion ascorbate (L-AA^{-}) (pK_{a1} = 4.2). The L-AA^{-}, being an electron donor, can reduce present Fe(III) and Cu(II) ions to Fe(II) and Cu(I) ions, respectively, while simultaneously being oxidized into ascorbyl radical anion (L-AA$^{-\bullet}$) (Eq. III.1) [13]. Such metallic ions can be oxidized while reducing molecular oxygen to generate superoxide anion radicals (Eq. III.2). These superoxide anion radicals ($O_2^{-\bullet}$) disproportionate (dismutate) to generate molecular oxygen and hydrogen peroxide (H_2O_2) (Eq. III.3) [14], [15], while the oxidized metal ions can be reduced once again to Fe(II) and Cu(I) using L-AA^{-} (Eq. III.1). Then, those recently reduced ions will reduce H_2O_2, producing OH^{-} and $OH^{\bullet}$ (Eq. III.4) [14], [16]. Such a reaction is similar to the Haber-Weiss reaction (the superoxide-driven Fenton reaction) in which L-AA^{-} reduces the Fe(III) and Cu(II) ions instead of being reduced by $O_2^{-\bullet}$ (Eq. III.1), thus, allowing the $O_2^{-\bullet}$ to disproportionate more into O_2 and H_2O_2 (Eq. III.3) which in turn will lead to the production of more hydroxyl radicals according to Eq. (III.4). Such hydroxyl radicals can oxidize the rGO-VitC sheets, thus affecting their degree of reduction.

$$L-AA^{-} + Fe(III)/Cu(II) \rightarrow L-AA^{-\bullet} + Fe(II)/Cu(I) \quad (III.1)$$

$$O_2 + Fe(II)/Cu(I) \rightarrow O_2^{-\bullet} + Fe(III)/Cu(II) \quad (III.2)$$

$$2O_2^{-\bullet} \xrightarrow{2H^+} O_2 + H_2O_2 \quad (III.3)$$

$$H_2O_2 + Fe(II)/Cu(I) \rightarrow OH^{\bullet} + OH^{-} + Fe(III)/Cu(II) \quad (III.4)$$

From the reaction sequence and description, Fe(III) or Cu(II) ions can be regarded as catalysts. Accordingly, this oxidation pathway of L-AA can be referred to as the metal-catalyzed oxidation of L-AA. The oxidation of L-AA in presence of these ions was validated in cell culture media where such ions are present [14]. It is believed that such a reaction can be catalyzed by just traces of these transition metal ions that can be present in the cell culture glassware, reagents, buffer solutions, plastic dishes, etc. Chelating agents were used to verify the effect of the presence of these ions. Accordingly, the oxidation was slowed down but wasn't stopped completely, indicating that there might be another contributors to the oxidation process. One of such possible metal-free oxidation pathways is the auto-oxidation of L-AA. In such an oxidation reaction, ascorbate species can reduce molecular oxygen into superoxide anion radical while being oxidized into L-AA$^{-\bullet}$. The ascorbate species that can donate electrons are mono-anion ascorbate (L-AA^{-}) and di-anion ascorbate (L-AA^{-2}). The later, being the stronger electron donor, is considered to be the ascorbate species that is significantly capable of true

auto-oxidation (Eq. III.5) [17]. The former can be involved in the auto-oxidation [18] but with a much slower rate of reaction (Eq. III.6) [17].

$$O_2 + L-AA^{-2} \rightarrow O_2^{-\bullet} + L-AA^{-\bullet} \qquad k = 10^2\ M^{-1}s^{-1}\ (III.5)$$

$$O_2 + L-AA^{-} \rightarrow O_2^{-\bullet} + L-AA^{-\bullet} \qquad k = 10^{-4}\ M^{-1}s^{-1}\ (III.6)$$

At physiological pH (7.4), the L-AA^{-} dominates over L-AA^{-2}, however, the amount of L-AA^{-2} becomes appreciable as the pH increases [14], [19] or the amount of added L-AA increases at a constant pH [14]. In addition, as L-AA^{-2} is consumed in the auto-oxidation reaction, more L-AA^{-2} are produced to re-establish the equilibrium [14]. The superoxide anion radicals produced from the metal independent auto-oxidation of L-AA disproportionate into O_2 and H_2O_2 (Eq. III.3). In the absence of transition metals ions such Fe(II) or Cu(I), H_2O_2 just accumulates in the medium without generating neither OH^{-} nor $OH^{\bullet}$. The accumulating H_2O_2 can then decompose, yielding oxygen radicals ($OH^{\bullet}$ and $OOH^{\bullet}$) [20] through heating [21]–[23] and/or catalytic decomposition over Mn ions [20], [24], [25]. The thermal degradation of H_2O_2 was never mentioned in the literature regarding the auto-oxidation of L-AA as these studies were done at lower temperatures (RT and physiological temperatures (37°C)). In the following sub-section, the referenced papers regarding the decomposition of H_2O_2 and the role played by the produced radicals in oxidizing graphene based materials will be detailed.

Schemes of the two oxidation routes of L-AA, namely the metal-catalyzed oxidation and the auto-oxidation, are presented below in Figure (III.12).

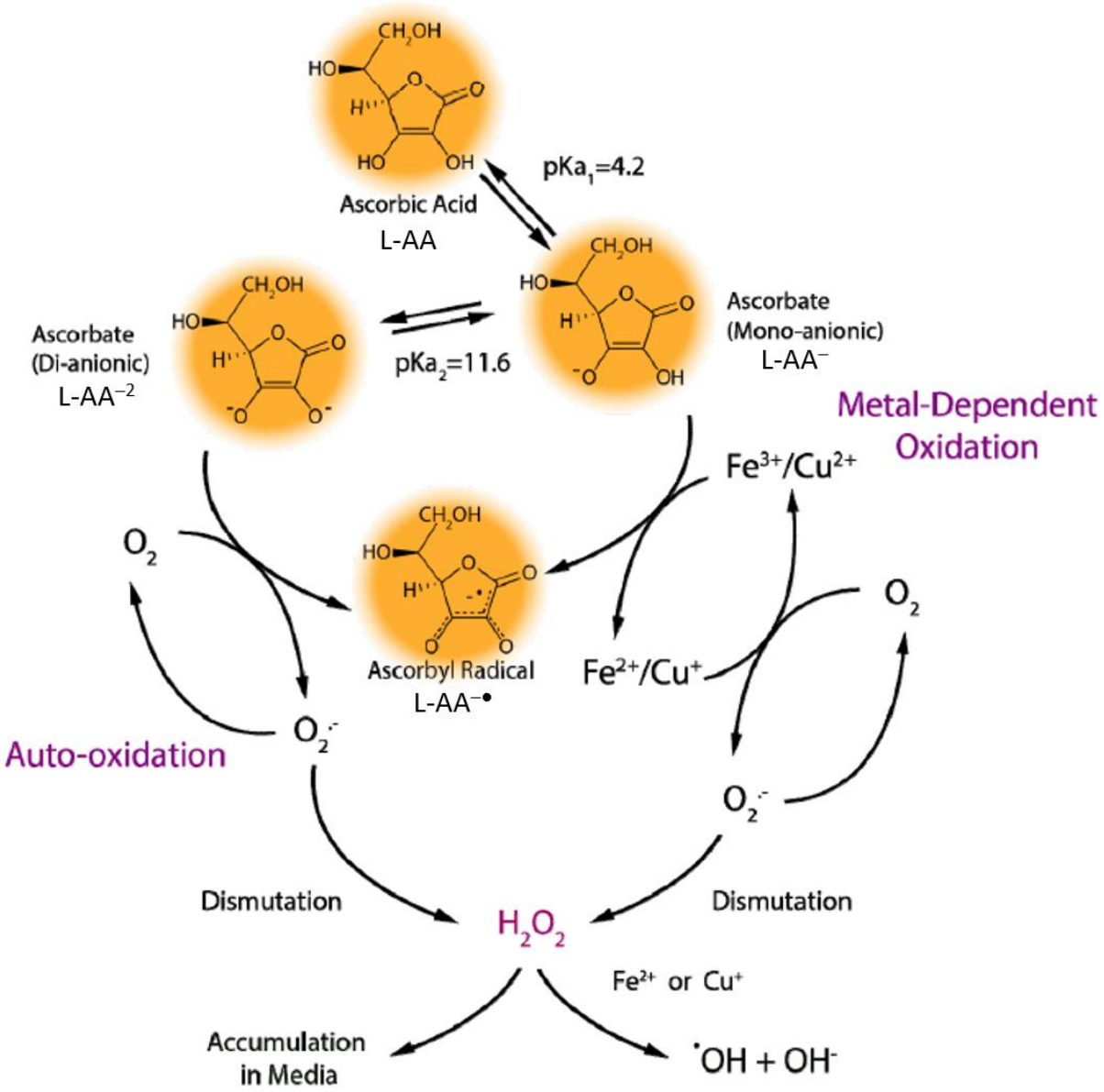

Figure III. 12 : Different proposed oxidation mechanisms of L-ascorbic acid: Auto-oxidation on the left hand side and Metal-Dependent on the right hand side

III.3.4.1 The Role of H_2O_2 in Oxidizing Graphene-Based Materials

A survey regarding the oxidation of various graphene-based materials via H_2O_2 is presented. Vittore, A. et al demonstrated the possibility of edge oxidizing High Surface Area Graphite (HSAG) by mixing it with H_2O_2 at 60°C [21]. A decrease in the C/O ratio was confirmed using XPS. This was attributed to an increase in oxygen functionalities, particularly carbonyl and carboxylic groups. In addition, FT-IR further confirmed the increase in oxygen content through the emerging of peaks corresponding to oxygen bearing carbon bonds. The presence of the oxygen groups at the edges of the sheets was inferred from the retention of the 002 peak position of the starting HSAG with even a narrower FWHM. Such narrowing down was attributed to loss of amorphous carbon due to long exposure to H_2O_2. The oxidation of rGO

(reduced in a furnace maintained at 1100°C under inert gas) was carried out using H_2O_2 at 60°C by Suhas, P. D. et al [22]. The oxidation was confirmed by elemental analysis. Ogunsona, E.O. et,al. edge oxidized biocarbons using H_2O_2 at 80°C [23]. An increase in the oxygen content was observed in XPS and was attributed to an increase in various oxygen functionalities at the edges: phenolic, carbonyl and carboxylic. Water-dispersible Thermally Reduced Graphene Oxide (TRGO) was achieved by You, X. et al through Mn^{2+} catalyzed oxidation of TRGO using H_2O_2 at RT [20]. The oxidation was confirmed by increase in oxygen content, notably carboxylic groups, from XPS measurements. The oxidized TRGO showed good and stable dispersibility in various commonly used low-boiling solvents (water, methanol, ethanol, acetone, ethyl acetate) even at high temperatures (a concentration of approximately 6% was lost during 120 h of standing at 80°C in water). The Mn^{2+} ions catalyzed the decomposition of H_2O_2 into $OOH^{\bullet}$ and $OH^{\bullet}$. The possibility of $OH^{\bullet}$ to oxidize sp^3 carbons (oxygen containing ones and C-H ones) as well as the edge sp^2 carbons was investigated through computational thermodynamic calculations. The calculations showed that the formation of carboxylic groups from alcohol, aldehyde and ketone groups through the reaction with $OH^{\bullet}$ is thermodynamically favorable. The reaction between $OH^{\bullet}$ and edge sp^2 carbons was deemed thermodynamically favorable, leading to the formation of edge phenolic groups. Those edge phenolic groups and the carboxylic groups can explain the enhancement in the dispersibility of the oxidized TRGO in various solvents. Those published results show the role H_2O_2 can play in oxidizing various graphene-based materials, including rGO. Those results also demonstrate that oxidation takes place mainly at the edges, as the reactivity of carbons atoms at the edges is higher than that of carbon atoms in the basal planes [26].

III.3.5 The Grand Finale – Postulation and Verification

Building on the metal and non-metal dependent oxidation of L-AA, coupled with the various decomposition routes of H_2O_2, a mechanism can be proposed for the observed re-oxidation of rGO when reduced with large quantities of L-AA for long reduction time as confirmed by XPS, EA and TGA. For instance, the auto-oxidation mechanism of L-AA (non-metal dependent oxidation of L-AA) can be postulated (Figure III.12). Such mechanism is dependent on the pH and the quantity of the added L-AA. Before the addition of L-AA to the reaction medium, the pH was adjusted to be between 9 and 10 to promote the colloidal stability of the GO dispersion through electrostatic repulsion. At such pH values, the $L\text{-}AA^{-2}$ is expected to be present in significant amounts for the auto-oxidation to happen at a higher rate [27]. However, on adding L-AA to the reaction medium, the pH drops due to the acidity of the L-AA. As the reduction proceeds, GO loses some of the acidic phenolic groups on its surface,

which might result in an increase in the pH. Such possible increase in pH could lead to higher concentration of the L-AA^{-2}, which is capable of true auto-oxidation, leading to the production of H_2O_2. Given the high temperature at which the reduction takes place (95°C), the rate of the auto-oxidation might be enhanced and the produced H_2O_2 can decompose generating $OH^{\bullet}$ and $OOH^{\bullet}$ which in turn can oxidize back the rGO sheets as observed from the decrease in the C/O ratio when large quantities of L-AA were used for long GO reduction time. The Fe/Cu catalyzed oxidation of L-AA and decomposition of H_2O_2 (Figure III.12) cannot be ruled out even though no such metals were added to the reaction media, as it is reported in literature that trace amounts can significantly enhance the oxidation of L-AA [14], [17]. Such trace amounts can come from the glassware or the reagents used (L-AA included). The catalyzed decomposition of the produced H_2O_2 in both cases can take place through trace amounts of Mn^{2+} ions as discussed previously as some Mn^{2+} ions might be present in GO as a result of the use of $KMnO_4$ during the oxidation process. Such catalysis would have a higher effect in case of auto-oxidation than in case of metal-catalyzed degradation of L-AA as Fe(II) and Cu(I) are already known catalysts for H_2O_2 decomposition as mentioned earlier. In addition, the production of L-$AA^{-\bullet}$ through the auto-oxidation (Eq. III.5 and Eq. III.6) and the metal-catalyzed oxidation of L-AA (Eq. III.1) can offer another pathway to the production of H_2O_2 that is through the scavenging of the $O_2^{-\bullet}$ [28] rather than the disproportionation of $O_2^{-\bullet}$ into O2, and H_2O_2.

Such decomposition of L-AA is expected to take place simultaneously with the reduction. However, during the first minutes for the rGO-VitC-24hr-1eq, the reduction dominates and an increase in the C/O ratio is observed. After that, the reduction reaction reaches its completion, allowing the oxidation reaction of L-AA to dominate, resulting in the re-oxidation of the rGO as deduced from the decrease in the C/O ratio when the reaction proceeds in time. To test the theory of auto-oxidation based on L-AA^{-2}, pH was monitored during the course of the reaction as shown in Figure (III.13). The pH of the starting GO dispersion (0.8 mg/ml) was measured to be 3.35. On addition of 2 drops of 28wt% NH_4OH, the pH drastically increased to 10.08. When L-AA was added, the pH dropped to 3.04. As the reaction proceeded, the pH slightly decreased in the first few hours (2.83 after 3 hours) and then dropped to 2.36 after 17 hours. Such results show that there was no increase in pH. On the contrary the pH decreased, ruling out the probability of L-AA^{-2} taking part in auto-oxidation of L-AA. However, from the visual inspection of the aliquots drawn for pH measurements, a yellow color of the solution was obvious after an hour and half (see Figure III.14). At an hour and a half, the reduction is expected to be completed as verified from C/O measurements in previous studies shown in Figure (III.6).

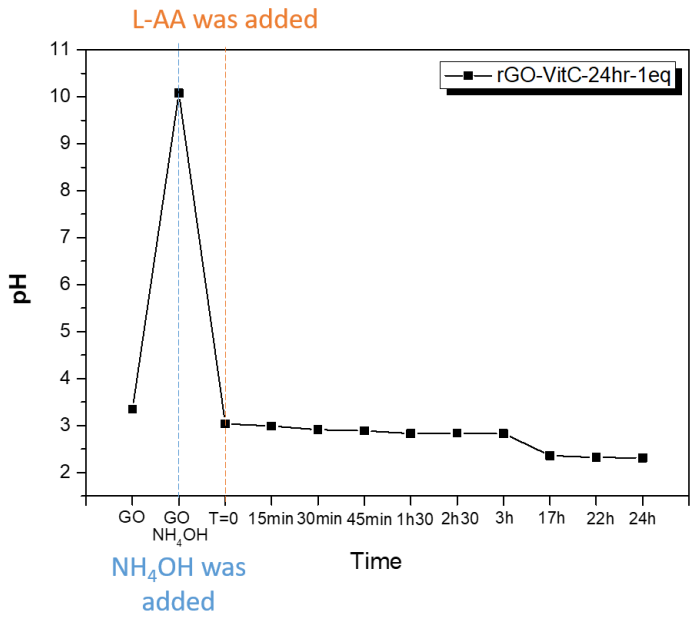

Figure III. 13 : pH values at different points in time during the reduction of rGO-VitC-24hr-1eq. The moments of addition of NH_4OH and L-AA are marked by vertical dashed lines

The color got more intense in the next aliquots and relatively stable dispersions of rGO-VitC were observed as shown below for the aliquots after 17, 22 and 24 hours that formed precipitation over the period of 60 hours. The appearance of the yellow color and its progression into orange color are indicative of the oxidation of L-AA and the formation of the DH-AA, which has a yellow to orange color in water depending on its concentration (Figure III.14). DH-AA is formed during the reduction of GO, however, no yellow color was observed during the reduction period (< 2 hours) and the color was only observed and got more intense after the reduction was completed. This shows that the oxidation of L-AA, thus, the production of DH-AA, continued even after the reduction was over. This hints at another process oxidizing the L-AA. Such process can be the metal-catalyzed oxidation of L-AA or the auto-oxidation of L-AA through $L\text{-}AA^-$ rather than $L\text{-}AA^{-2}$ as $L\text{-}AA^-$ is more abundant at such pH values shown in (Figure III.13).

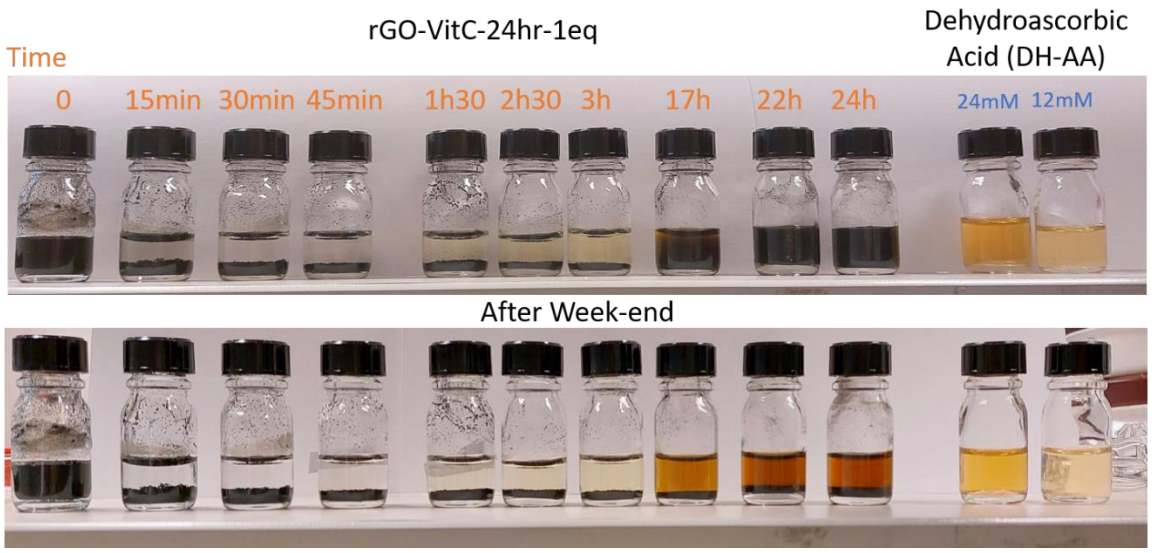

Figure III. 14 : Optical images of various aliquots withdrawn at different moments in time during the reduction of rGO-VitC-24hr-1eq along with 2 DH-AA solutions of different concentrations. The images below are the same as the ones on top but left to settle over a weekend

The participation of L-AA^{-} in auto-oxidation of L-AA is reported in literature to take place at a slower rate compared to L-AA^{-2} as shown from the rates in Eq. (III.5) and Eq. (III.6) [17]. However, such a slow rate can be compensated by higher amounts of L-AA, higher reaction temperatures and longer reaction times as it is the case with the reduction conditions of the rGO-VitC-24hr-1eq sample. This can lead to a higher rate of auto-oxidation of L-AA (formation of $O_2^{-\bullet}$ and L-AA$^{-\bullet}$). L-AA$^{-\bullet}$ is a stable radical, unreactive towards non-radical species, owing to its tri-carbonyl structure that stabilizes its radical through a highly delocalized π system [17]. It can only react with itself or other radicals such as $O_2^{-\bullet}$ [12]. If it reacts with another L-AA$^{-\bullet}$, they disproportionate into L-AA and DH-AA. On the other hand, if it reacts with $O_2^{-\bullet}$, it yields H_2O_2 and DH-AA. Both reactions are consistent with the appearance of the yellow color as they both yield DH-AA.

The observation of relatively stable rGO-VitC dispersion can be attributed to the further degradation of the DH-AA into oxalic acid which can form H-bonds with various H-bond accepting and donating oxygen groups at the edges of the rGO sheets, stabilizing their dispersion. Such an explanation is consistent with the decrease in the pH as oxalic acid is a stronger acid compared to L-AA and DH-AA as it has a lower pK_a values (Table III.5). It is also in line with literature regarding the proposed reasons behind the stability of rGO-VitC dispersions [5], [7].

Acid	pK_{a1}	pK_{a2}
L-AA	4.2	11.6
DH-AA	3.9	-
Oxalic Acid	1.23	4.19

Table III. 5 : pK_a values for L-AA, DH-AA and Oxalic acid

The stability of the ascorbyl radical ($L\text{-}AA^{-\bullet}$), mentioned above, allows its detection through Electron Paramagnetic Resonance (EPR) technique at room temperature [27]. Consequently, EPR experiments were done in a flat cell to detect the presence of ascorbyl radical in a 60mM vitC aqueous solution heated at 95°C and to monitor its concentration over time using 1µM TEMPOL solution as a reference. A drop of 28.wt% ammonia solution was added to adjust the pH to 10 to mimic the reduction conditions. GO was excluded from the media to avoid signals from GO and rGO. The doublet of the ascorbyl radical was detected with a hyperfine coupling constant (a_H) of 1.8 G (Figure III.15(a)), which is in agreement with the literature [27], [29]. The detection of the ascorbyl radical is a direct proof of the oxidation of L-AA on its own, in the absence of GO. The presence of such radical confirms the viability of the pathways proposed in Figure (III.12).

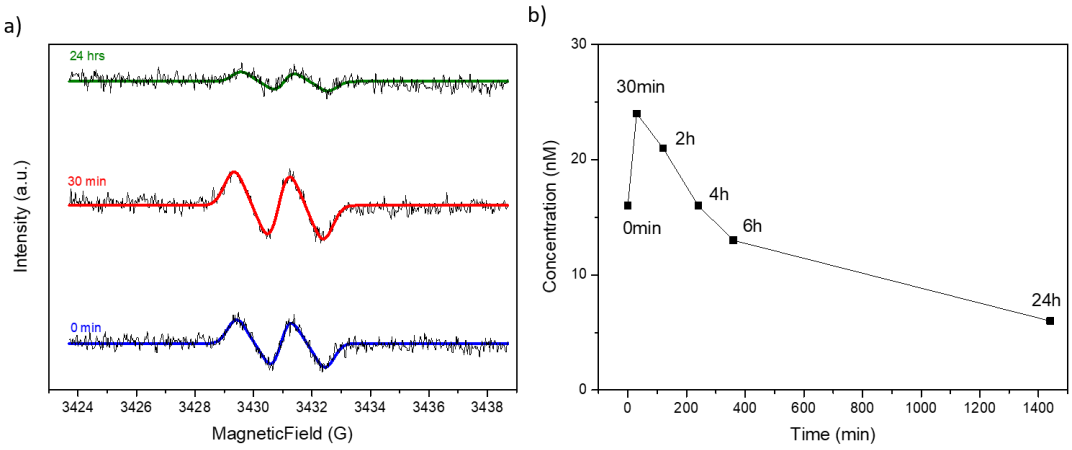

Figure III. 15 : a) EPR spectra of the ascorbyl radical in 60mM solution of L-AA at t=0, 30 min and 24 h along with their fitted simulated curves superimposed on them and b) Concentration of ascorbyl radical at different reduction time (referenced against 1µM TEMPOL)

The concentration of ascorbyl radical at different points in reaction time is shown in Figure (III.15(b)). An ascorbyl radical concentration of 16 nM was found in the first aliquot taken after the addition of L-AA to water heated at 95°C with a drop of NH_4OH, and then the concentration increased to 24 nM after 30 min of heating. After that, the concentration of ascorbyl radical started decreasing until it reached its lowest value (~6 nM) after 24hr. This shows that the ascorbyl radical production starts on the moment of addition of L-AA and continues to increase until it reaches a maximum (30 min) and then starts to decrease. The increase of ascorbyl radical content should be accompanied by an equal increase in superoxide radical anions, which can

then disproportionate to give H_2O_2. This means that probably around 30 min, a maximum concentration of superoxide radical anions and ascorbyl radical is attained. Accordingly, letting the reduction time exceed 30 min would allow time for the production of H_2O_2, resulting in possible side oxidation reactions. These EPR experiments were made possible thanks to **Dr. Vincent Maurel**

The decrease in concentration of the ascorbyl radical is in good agreement with color changes displayed in Figure (III.14). The ascorbyl concentration decreases because the ascorbyl radicals disproportionate, yielding L-AA and DH-AA that gives a yellow/orange color. Accordingly, when more ascorbyl radical are consumed, more DH-AA are produced and the color becomes darker orange.

III.4 Structural Analysis

After deciphering the anomalous behavior encountered during the chemical analysis, the structure of all the samples were studied collectively. Structural characterization is vital when monitoring the reduction of GO as the reduction procedure has a profound impact on the structure of the staring GO. As the reduction proceeds, the oxygen content decreases as different oxygen functionalities are removed and accordingly, the sp^2 carbon network is partially restored. Such restoration of the sp^2 carbon network has impacts on various structural parameters such as the inter-layer graphene spacing, the number of layer per crystallite, the degree of defects, the morphology, etc. These structural features along with the chemical ones, dictate the materials' properties such as the electrical conductivity. They can also be correlated to the electrochemical performance of these samples.

X-Ray Diffraction (XRD) was done to analyze the structure of the rGO upon reduction with L-AA and compare it to that of those reduced with Hz or hydrothermally. Such structural analysis includes the sheets stacking parameters like the inter-layer spacing, the size of the crystallite, the number of layers within a crystallite and the in-plane crystallite size. Figure (III.16) displays the diffractograms of all the samples. The graphite is showing its signature 002 peak at ~31°, corresponding to the expected inter-layer distance (d-spacing) of 0.34 nm. Upon its oxidation into GO, the graphitic peaks disappeared and a new 001 peak appeared around 14°, corresponding to an expanded inter-layer spacing of 0.73 nm. On reducing the GO, regardless of the method of reduction, the GO XRD peak disappeared while a new broad 002 peak between 26° and 28° appeared for the rGO samples. A small peak corresponding to the in-plane 100 periodicity can be seen for all the samples around 50°. The d-spacing values are summarized in Table (III.6).

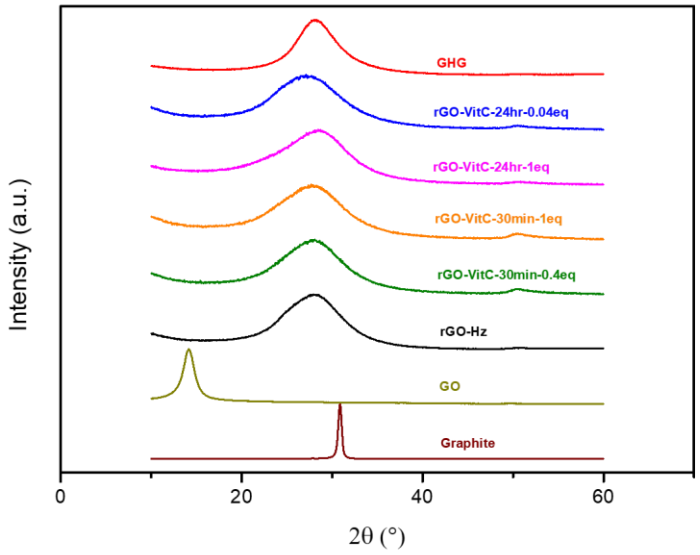

Figure III. 16 : The XRD profiles of Graphite (—), GO (—), rGO-Hz (—), rGO-VitC-30min-0.4eq (—), rGO-VitC-30min-1eq (—), rGO-VitC-24hr-1eq (—), rGO-VitC-24hr-0.04eq (—) and GHG (—)

The expanded inter-layer spacing of the GO is a direct consequence of the success of the oxidation method that adds various oxygen functionalities to the sheets of the graphene, breaking the sp^2 carbon network, thus, weakening the π-π interactions holding the sheets together at low d-spacing value as in graphite. When reducing the GO into rGO, the sp^2 carbon network is partially recovered, thus, partially restoring the π-π interactions, leading to smaller d-spacing values (between 0.36 and 0.38 nm) compared to that of GO (0.73 nm). This indicates the validity of the various reduction processes employed herein to efficiently reduce GO. The broadness of the rGO peaks compared to graphite can be attributed to microcrystalline broadening (broadening due to smaller crystallite sizes) and/or different d-spacing values, arising from less ordered re-stacking.

Sample	d-spacing (nm)	Crystallite Stack Height (nm)	Number of sheets in the crystallite	In-Plane Crystallite Size (nm)
GHG	0.37	1.77	5	6.87
rGO-VitC-24hr-0.04eq	0.38	1.23	3	7.99
rGO-VitC-24hr-1eq	0.36	1.28	4	7.62
rGO-VitC-30min-1eq	0.37	1.26	4	8.71
rGO-VitC-30min-0.4eq	0.37	1.33	4	8.87
rGO-Hz	0.37	1.38	4	8.37
GO	0.73	6.27	9	11.53
Graphite	0.34	21.74	65	48.61

Table III. 6 : Summary of the data extracted from the XRD profiles of the various samples analyzed

Scherrer's equations were applied to extract valuable structural information such as the crystallite stack heights, the number of sheets in the crystallites and the in-plane crystallite size. Looking at those parameters summarized in Table (III.6), a decrease in the number of layers in

the crystallite (from 65 to 9) and in the in-plane crystallite size (from ~49 to ~12 nm) can be observed when going from graphite to GO. This decrease can be assigned to the distortion of the sp^2 carbon network upon oxidation, leading to the disruption of the π-π interactions between the sheets. Accordingly, the sp^2 domains gets smaller and the long range stacking decreases. When reducing the GO into rGO, counter-intuitively, a decrease is observed in the number of layers per crystallite (from 9 to 3-5) and the in-plane crystallite size (from ~12 to 7-9 nm). The later can be explained by the creation of multiple small sp^2 carbon islands, leading to a smaller average size of the sp^2 domains. On the other hand, the former can be explained by the presence of the "structural water molecules", forming hydrogen bonds with the oxygen functionalities on the GO sheets, giving an extra form of interaction that is not present in the rGO samples as the oxygen functionalities are partially removed.

To further understand and validate the results obtained from XRD, Raman spectroscopy was carried out as it is a powerful technique to investigate the structure and the degree of disorder of the graphene-based materials. A very useful structure-indicating parameter is the I_D/I_G ratio that is the ratio between the intensity of the D-band over the intensity of the G-band. The G-band, the Graphitic band, is related to the vibrations of the sp^2 carbon network, while the D-band, the Disorder band, is related to disorder-induced vibration modes arising from various structural disorder or sp^3-like defects on the surface of the carbon [30], [31]. Accordingly, an increase in the I_D/I_G ratio implies and increase in the structural disorder. The $\frac{I_D}{I_G}$ ratio can be used to estimate the average crystallite size of the graphitic sp^2 domains according to the following equation [32]:

$$L_a(nm) = (2.4 * 10^{-10}) * \lambda^4 * \left(\frac{I_D}{I_G}\right)^{-1} \qquad (III.7)$$

Where L_a is the lateral dimension of sp^2 carbon clusters in nanographite (nm) and λ is the wavelenght of the excitation laser used (nm). The Raman spectra of graphite, GO and the various rGO samples are shown in Figure (III.17) and the I_D/I_G ratio and the average crystallite size of the graphitic sp^2 domains are summarized in Table (III.7).

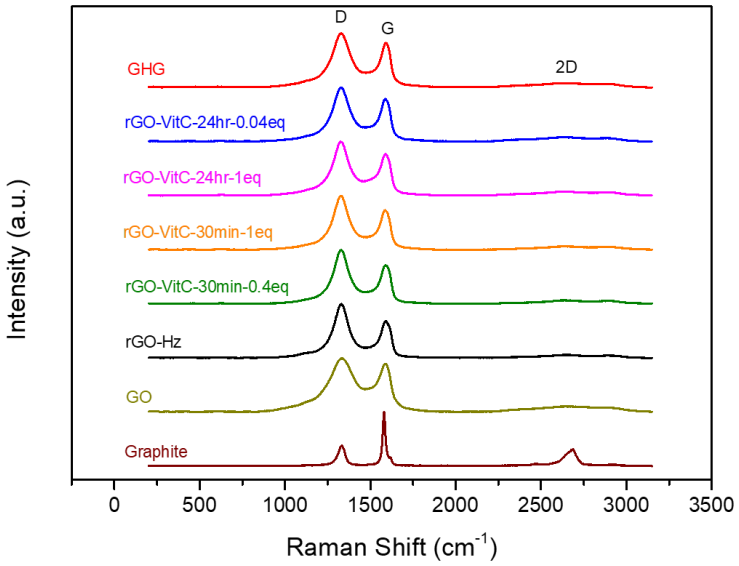

Figure III. 17 : Raman spectra of Graphite (—), GO (—), rGO-Hz (—), rGO-VitC-30min-0.4eq (—), rGO-VitC-30min-1eq (—), rGO-VitC-24hr-1eq (—), rGO-VitC-24hr-0.04eq (—) and GHG (—)

The graphite showed the expected G-band at 1580 cm^{-1} as reported in literature [30], however, this band is accompanied with a small D-band as expected for commercial graphite [33]. Such a D-band might be a consequence of the polycrystallinity of this commercial graphite and/or the fact that it is nano-graphite, meaning that it has many edges that can be thought of as sources of disorder compared to single crystal graphite with an infinite lattice where only the G-band appears. An intense 2D band was also observed, which is an indication of high degree of graphitization [34] expected from graphite. When the graphite was oxidized to GO, the D-band grew wider and more intense, indicating a higher degree of defects compared to that of graphite. This was confirmed via the increase in the I_D/I_G ratio from 0.4 for graphite to 1.13 for GO. The increase in the defect density can be attributed to the sp^3 carbons arising from the oxidation of the graphite, acting as defects in what used to be a continuous sp^2 carbon network in graphite prior to the oxidation. In addition, an up-shift to higher frequencies was observed for the G-band explained by the fact that isolated sp^2 bonds resonate at higher frequencies [34].

Sample	Raman Bands	Wavenumber (cm^{-1})	I_D/I_G	Average crystallite size of the graphitic sp^2 domains (L_a) (nm)
GHG	D-band G-band 2D-band	1330.5 1592.4 2652.9	1.21	31.8
rGO-VitC-24hr-0.04eq	D-band G-band 2D-band	1327.3 1587.1 2628.9	1.30	29.6
rGO-VitC-24hr-1eq	D-band G-band 2D-band	1324.1 1586.1 2645.8	1.30	29.6

rGO-VitC-30min-1eq	D-band G-band 2D-band	1326.2 1587.1 2630.7	1.37	28.1
rGO-VitC-30min-0.4eq	D-band G-band 2D-band	1330.5 1589.2 2638.7	1.39	27.7
rGO-Hz	D-band G-band 2D-band	1330.5 1591.3 2634.2	1.53	25.2
GO	D-band G-band 2D-band	1331.6 1591.3 2676.8	1.13	34.1
Graphite	D-band G-band 2D-band	1332.6 1579.9 2688.3	0.4	96.2

Table III. 7 : Summary of the Raman data (Raman bands, their wavenumbers, I_D/I_G ratio and L_a) for GO, rGO-Hz, rGO-VitC-30min-0.4eq, rGO-VitC-30min-1eq, rGO-VitC-24hr-1eq, rGO-VitC-24hr-0.04eq and GHG

Upon reduction, the intensity of the 2D-band was observed to be notably lower than that of graphite. This can be ascribed to a lesser degree of graphitization in those samples (compared to graphite) because despite the reduction of the sample and the partial removal of oxygen functionalities, the samples only partially recovered the sp^2 carbon network with some oxygen functionalities persisting after the reduction. The I_D/I_G ratio further increased compared to that of GO upon reduction, a counter intuitive observation, that can be explained by the formation of multiple small sp^2 carbon islands, leading to an average smaller sp^2 domain size. The boundaries between the small sp^2 islands and the sp^3 matrix can be thought of as defective boundaries where sp^2 and sp^3 carbons of different bonding angles are bonded together, thus, increasing disorder and leading to a higher I_D/I_G ratio. From another perspective, the presence of discontinues sp^2 carbons inside the sp^3 matrices can be treated as vacancy defects in the sp^3 lattice that was dominant in GO [35], leading to a higher I_D/I_G ratio. Another explanation for the increase in the I_D/I_G ratio is the presence of more exposed edges upon reduction [4]. Mathematically, the I_D/I_G ratio has an inversely proportional relation with the average crystallite size of the graphitic sp^2 domains according to Eq. (III.7), thus, as the average size of the sp^2 domains decrease, the I_D/I_G ratio increases.

The estimate of the average crystallite size of the sp^2 domains decrease from 96 to 34 nm upon oxidation of graphite into GO due to the partial disruption of the sp^2 carbon network as a result of the oxidation of the graphite. When reducing to rGO, regardless of the method utilized, the size of the sp^2 domains further decrease as multiple small sp^2 island start to appear owing to the partial removal of oxygen functionalities, leading to a smaller average size of such domains.

The morphology of the reduced samples were investigated through Scanning Electron Microscopy (SEM) (Figure III.18). The rGO-Hz sample displays a wrinkled and crumpled morphology (Figure III.18(a)) which can be attributed to the high degree of reduction, leading

to strong π-π interactions. On the other end of the reduction spectrum, GHG, the hydrothermally reduced sample, is showing a 3D macroporous inter-connected network of rGO sheets (Figure III.18(f)). Such a unique structure is a result of the hydrothermal reduction which, under no stirring, forms a monolith of inter-connected graphene sheets. The rGO-VitC samples are showing a variety of morphologies depending on their degree of reduction. The highly reduced samples such as rGO-VitC-30min-0.4eq (Figure III.18(b)) and rGO-VitC-30min-1eq (Figure III.18(c)) are showing morphologies closer to that of rGO-Hz with the wrinkling and crumpling being relatively lower than that of rGO-Hz as they are less reduced, leading to less π-π interactions between the sheets. On the other hand, the rGO-VitC sample with the lowest C/O ratio (rGO-VitC-24hr-1eq) shows a morphology similar to that of GHG (Figure III.18(d)), however denser with less porosity. The rGO-VitC-24hr-0.04eq (Figure III.18(e)) is displaying a morphology in-between that of rGO-Hz and GHG. It is wrinkled and crumpled as in rGO-Hz while being relatively fluffy and showing some porosity as in GHG.

Transmission Electron Microscopy (TEM) was carried out to assess the surface texture and local surface state of the rGO sheets. Figure (III.19) shows the TEM images for GO, rGO-Hz and rGO-VitC-24hr-0.04eq and GHG. The low magnification images (Figures (II.19(a), (c), (e) & (g)) show the overall morphology of the isolated particles. For GO, an extended single sheet was observed because GO can form stable good dispersions in various solvents owing to the various oxygen functional groups on its surface. On the other hand, the reduced samples displayed wrinkled multiple sheets per particle, which can be attributed to the π-π interactions between the sheets, resulting from the partial restoration of the sp^2 carbon network upon reduction.

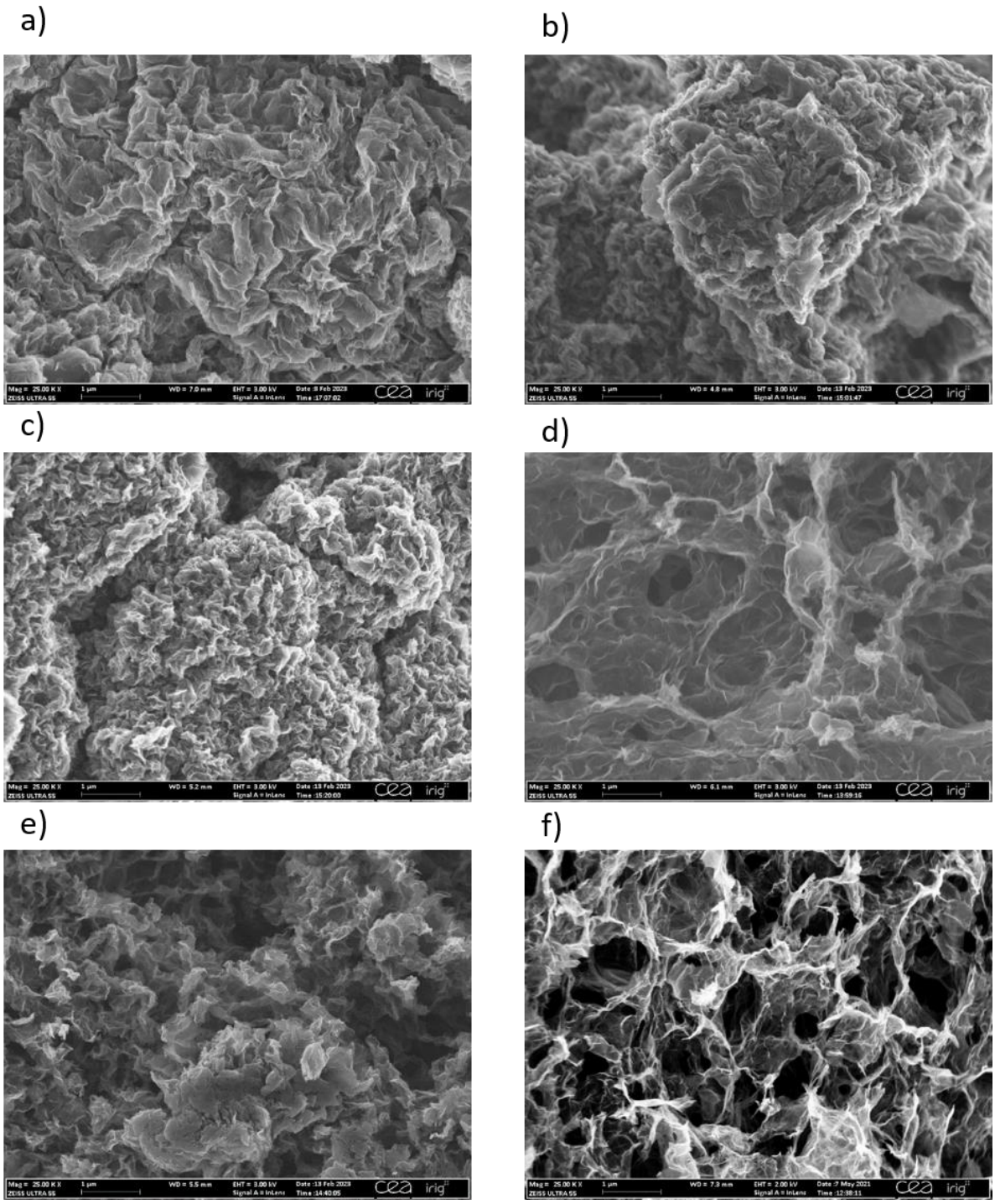

Figure III. 18 : SEM images at 25,000x of a) rGO-Hz, b) rGO-VitC-30min-0.4eq, c) rGO-VitC-30min-1eq, d) rGO-VitC-24hr-1eq, e) rGO-VitC-24hr-0.04eq and f) GHG

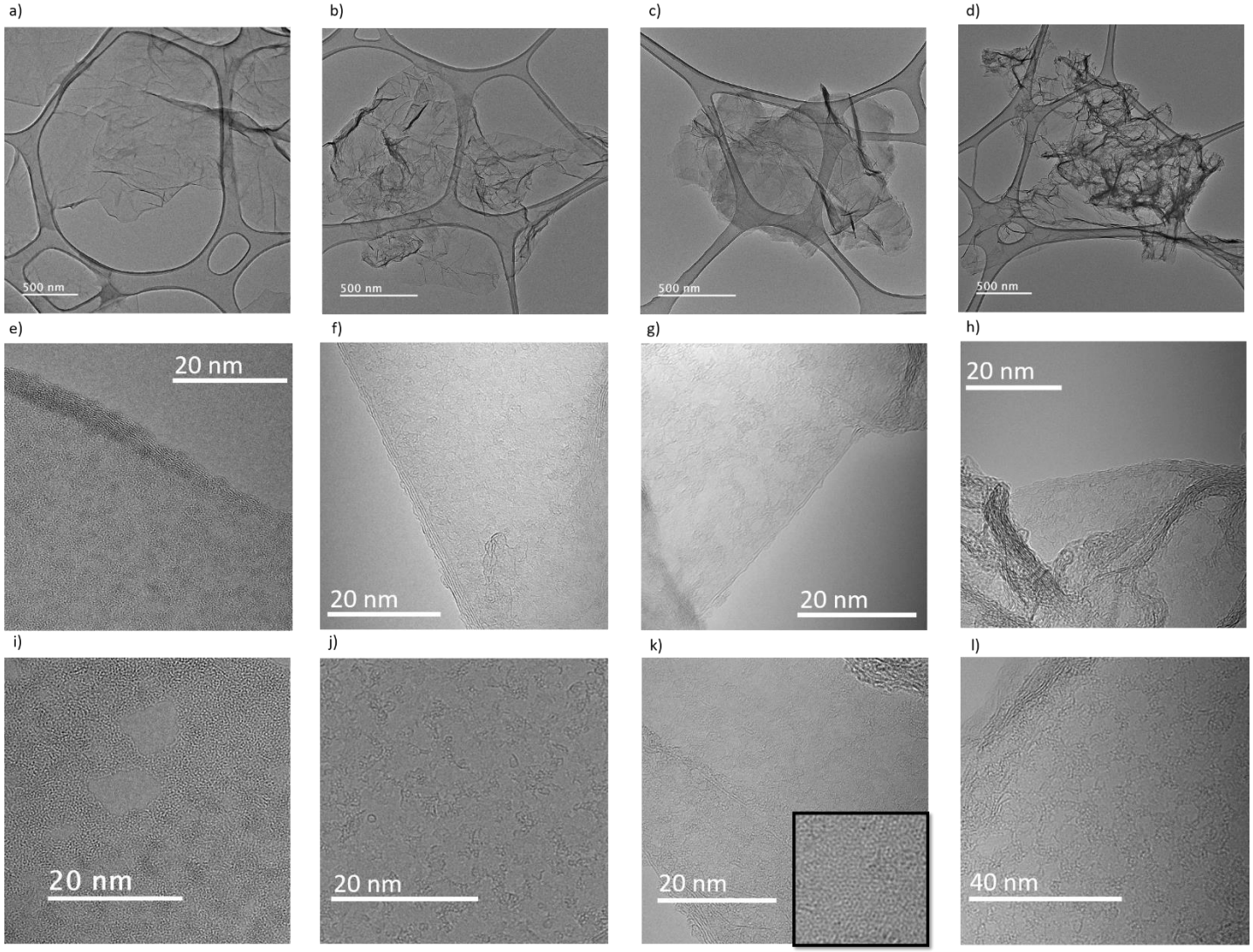

Figure III. 19 : Low magnification, high magnification and zoomed-in TEM images of (a, e and i) GO, (b, f and j) rGO-Hz, (c, g and k) rGO-VitC-24hr-0.04eq and (d, h and l) GHG

The number of sheets can be counted from the high magnification TEM images (Figures III.19 (e), (f), (g) & (h)) and the results were as follows: 9-12, 2-4, 2, 5-7 layers for GO, rGO-Hz, rGO-VitC-24hr-0.04eq and GHG.

The zoomed in TEM images (Figures III.19 (i), (j), (k) & (l)) show the surface texture and local chemistry of the samples. It can be seen that GO has a disorder matrix within which relatively big patches can be observed. Such patches can be attributed to sp^2 carbon islands. On the reduced samples, the number of patches increase and they become smaller in size compared to their size in GO. In the insert of Figure (III.19(k)), the hexagonal structure of the sp^2 carbon network can be observed. Such an observation is a direct optical indication on the partial restoration of the sp^2 carbon network.

The structural characterization presented so far gives indirect confirmation on the success of the oxidation of GO and the success of its reduction using various methods. The former was inferred from the disappearance of the 002 XRD peak of graphite and the appearance of the 001 XRD peak of GO and the increase in Raman's I_D/I_G ratio. The latter was deduced from the disappearance of the 001 XRD peak of GO and the appearance of the broad 002 XRD peak of rGO accompanied by a further increase in Raman's I_D/I_G ratio upon reduction. SEM and TEM showed differences in morphologies, surface texture and local chemistry in favor of the success of the reduction. The average size of the sp^2 carbon domains (L_a) was calculated from Raman's I_D/I_G ratio and from XRD using Scherrer's equations. Figure (III.20) compares the calculated values from both techniques, showing good agreement in the overall trend. The differences in the values or any slight differences in the trends can be a consequence of the method of calculation, knowing that Sherrer's equations require the assumption that microcrystalline broadening is the only source of peak broadening.

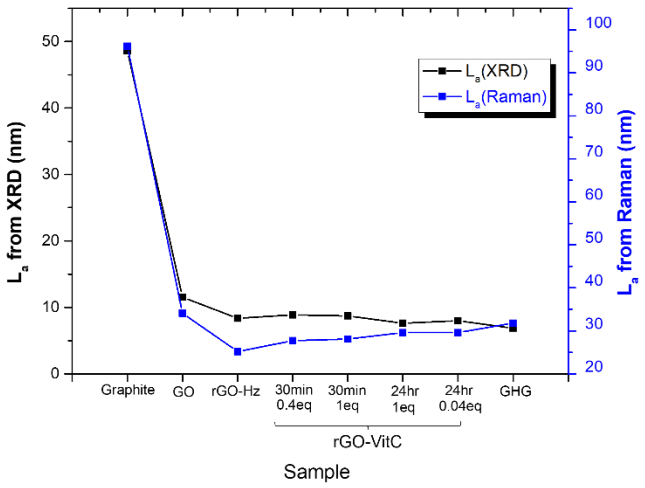

Figure III. 20 : Plot between the L_a values obtained from XRD and Raman for Graphite, GO, rGO-Hz, rGO-VitC-30min-0.4eq, rGO-VitC-30min-1eq, rGO-VitC-24hr-1eq, rGO-VitC-24hr-0.04eq and GHG

The number of rGO layers was calculated both from TEM and from XRD using Scherrer's equations and the values were in good agreement as shown in Table (III.8)

Sample	Number of rGO Layers (XRD)	Number of rGO Layers (TEM)
GHG	5	5-7
rGO-VitC-24hr-0.04eq	3	2-3
rGO-Hz	4	2-4
GO	9	9-12

Table III. 8 : Number of rGO layers calculated from XRD and counted from TEM images for GO, rGO-Hz, rGO-VitC-24hr-0.04eq and GHG

III.5 Electrical Conductivity Measurements

Electrical conductivity is an important property for materials used as electrodes for supercapacitor applications. An adequate electrical conductivity is the one that allows for fast electron transport and fast charge transfer at the electrode-electrolyte interface. For carbonaceous materials, it is a property that is sensitive to the reduction extent, the amount and the connectivity of the sp^2 carbon domains present in the samples. The electrical conductivity measurements were done on all the samples synthesized using a four-probe measurement. No electrical conductivity value was measured for GO, thus, confirming its electrical insulating character. The electrical conductivity values were found to be ~13350 , 2200 ±16, 1100 ±9, 980 ±9, 905 ±6, 370 ±8 and 500 ±8 S/m for rGO-Hz, rGO-VitC-30min-0.4eq, rGO-VitC-30min-1eq, rGO-VitC-24hr-1eq, rGO-VitC-24hr-0.04eq and GHG, respectively. The insulator behavior of GO can be explained by the disruption of the continuity of the sp^2 carbon network by the oxygen bearing sp^3 carbons due to the oxidation process. Upon reduction, the π-conjugated sp^2 carbon network is partially reinstituted, and thus, partially restoring the electrical conductivity.

III.6 Model Assembling

The characterization techniques done so far, chemical and structural, should not be treated in isolation from one another; however, they should go hand in hand to better understand the properties of the materials, such as the electrical conductivity, and to develop models for the various samples that can explain the results extracted from both the chemical and structural characterization. For instance, to further understand the trend in electrical conductivity values, those values were plotted against the C/O ratio (calculated from XPS) and the average crystallite size of the sp^2 carbon domains (calculated from Raman) of all the reduced samples (Figure III.21).

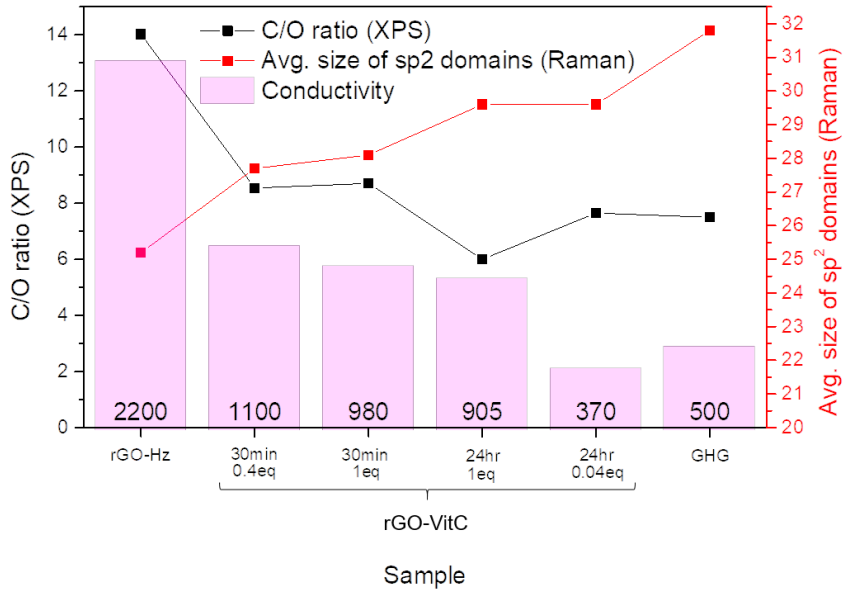

Figure III. 21 : The relation between C/O ratio from XPS, Avg. size of sp^2 domains calculated from Raman spectra and the electrical conductivity values

It can be seen that the highest electrical conductivity is possessed by the sample with the highest C/O ratio and the smallest average size of sp^2 domains (rGO-Hz). The high C/O ratio indicates a high degree of reduction, thus, a high degree of restoration of the conjugated sp^2 carbon network responsible for the electrical conductivity. The small avg. size of the sp^2 carbon network can be understood in light of the degree of reduction. When a sample is reduced, small sp^2 domains start growing numerously in various locations over the rGO sheets, thus bringing down the average size of the domains. When multiple formed sp^2 domains start to coalesce, larger domains are formed. The presence of those multiple small domains in close proximity allows the electrons to hop from a domain to another, thus, increasing the electrical conductivity of the material. Figure (III.21) shows an expected trend where the C/O ratios of rGO-VitC samples and GHG are lesser than that of rGO and their avg. sp^2 domain size is accordingly

higher, leading to a lower electrical conductivity as these domains are more spaced out. The rGO-VitC samples follow such trend except for the rGO-VitC-24hr-1eq sample (the sample that has a low C/O ratio as a result of its re-oxidation when left to reduce for 24hr in a 63mM solution of L-AA). Despite having a 31% lesser C/O ratio and 5% large avg. sp^2 domain sizes compared to the rGO-VitC-30min-1eq, the rGO-VitC-24hr-1eq sample is showing a comparable electrical conductivity. It is also showing an electrical conductivity 2.5 times that of rGO-VitC-24hr-0.04eq in spite of having a 20% lower C/O ratio. Such an electrical conductivity could be explained through examining the reduction process of such sample. First, just like rGO-VitC-30min-1eq sample, the rGO-VitC-24hr-1eq sample get reduced with a high C/O ratio during the first 30 minutes. Afterwards, the reduction starts to reach completion and due to the large quantity of L-AA, and high temperature, auto-oxidation of L-AA takes place and leads to the in-situ production of H_2O_2. Owing to the high temperature, H_2O_2 forms hydroxyl radicals that can attack the sp^2 carbons on the edges of the rGO sheets, adding phenolic groups on the edges. The addition of these hydroxyl groups was confirmed through XPS as an increase in the C-O quantity from both C1s and O1s HR spectra. The edge oxidation was confirmed by no increase in the d-spacing which is in line with literature [21]. Consequently, since the oxidation only takes place on the edges of the sheets or the edges of the holes, the sp^2 islands on the basal planes are conserved except for the ones extending till the edges, which explains the slightly lower electrical conductivity. In addition, the presence of the hydrogen bond donating and accepting phenolic groups on the edges of the rGO sheets, as a result of the re-oxidation, can play a role in bringing the rGO sheets together through the formation of H-bonds between those groups and other groups at the edges of the rGO sheets, such as carboxylic, carbonyls, or other similarly added phenolic groups due to the re-oxidation. Such H-bonds can compensate the decrease in sp^2 carbon domains through bringing the rGO sheets together, facilitating the hopping of electrons from one sheet to another. In short, the preserved integrity of the sp^2 carbons on the basal planes of the rGO sheets and the formation of H-bonds between the H-bond donating and accepting groups at the edges of the rGO sheets might be the reasons why such a sample has a high electrical conductivity although it has a low C/O ratio.

To conclude this characterization part, simplified models were proposed to simultaneously summarize and understand the different properties of the graphite, GO and all the different rGO samples (Figure III.22). These simplified models were constructed based on the data obtained from the various characterization techniques employed herein, in addition to what is reported in literature.

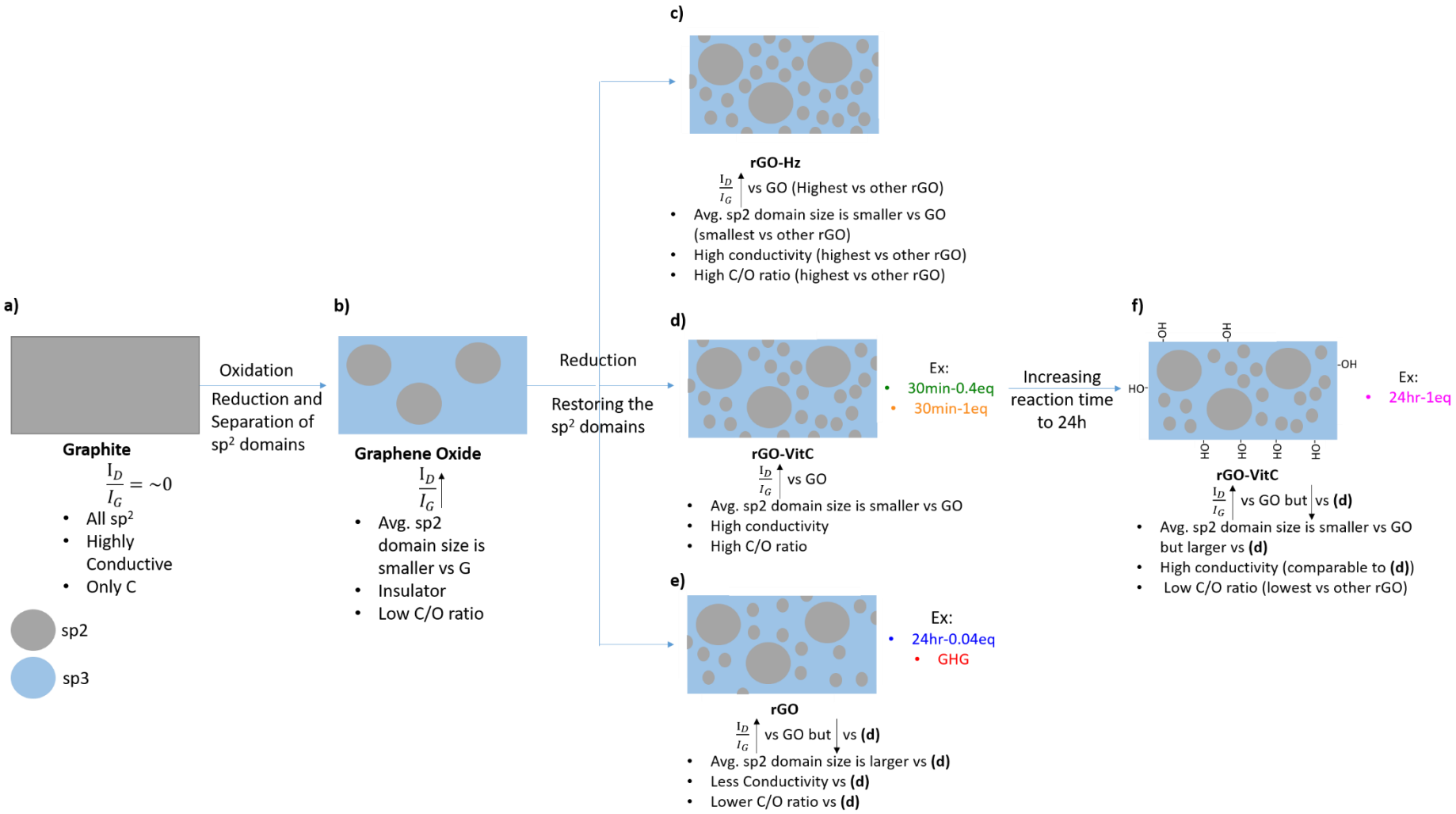

Figure III. 22 : Simplified Models proposed for various samples: a) Graphite, b) GO, c) rGO-Hz, d) rGO-VitC-30min-0.4eq and rGO-VitC-30min-1eq, e) rGO-VitC-24hr-0.04eq and GHG, and f) rGO-VitC-24hr-1eq

Graphite (Figure III.22(a)) has a multi-layered structure of sp^2 graphene sheets with only carbons, leading to high electrical conductivity. This leads to a Raman's I_D/I_G ratio equal to zero for single crystal graphite and near zero for polycrystalline graphite or nanographite with many edges or any other graphite with defects (substitutional atoms, etc.) [30]. When oxidized to GO (Figure III.22(b)), the sp^2 carbons are lesser in amounts and more separated as some of them are transformed into sp^3 carbons due to the addition of various oxygen functional groups as a result of the strong oxidation, leading to higher C/O ratio. This increase in disorder is manifested in an increase in the I_D/I_G ratio. The isolation of the remaining sp^2 carbons leads to the smaller avg. sp^2 carbon network as well as to the electrical insulation behavior of GO as the electron mobility is highly impeded. When reducing the GO into rGO, regardless of the reduction method, the C/O ratio decreases while the I_D/I_G ratio increases compared to that of GO. The rGO-Hz sample (Figure III.22(c)), being reduced with the most efficient GO reducing agent, is the rGO sample with the highest C/O ratio, highest I_D/I_G ratio, smallest avg. sp^2 carbon network, resulting from having numerous small sp^2 islands upon reduction, and thus the highest electrical conductivity. The rGO-VitC samples reduced with 0.4eq and 1eq of L-AA to GO in short reduction time (30 min) (Figure III.22(d)) are showing similar results to that of rGO-Hz but with lower C/O ratio, lower I_D/I_G ratio, larger avg. sp^2 domain size, as they are less numerous compared to the case of rGO-Hz, and accordingly, lower electrical conductivity. The rGO-VitC sample reduced with 0.04eq of L-AA to GO in 24 hours and the hydrothermally reduced sample (GHG) (Figure III.22(e)) are having lower C/O ratio, larger avg. sp^2 domain size, lower I_D/I_G ratio and lower electrical conductivity compared to rGO-VitC-30min-0.4eq and rGO-VitC-30min-1eq. For the sample that is left to reduce for 24 hours with 1eq of L-AA to GO (Figure III.22(f)), the C/O ratio is decreased due to the re-oxidation taking place because of the in-situ production of H_2O_2. Since the C/O ratio is higher than that of GO but lower than that of rGO-VitC-30min-1eq, the I_D/I_G ratio is expected to be higher than that of GO but lower than that of the more reduced rGO-VitC-30min-1eq. Consequently, according to Eq. (III.7), the avg. sp^2 carbon domain should be larger compared to rGO-VitC-30min-1eq because it has more oxygen. Similarly, since rGO-VitC-24hr-1eq has a lower C/O ratio compared to that of rGO-VitC-24hr-0.04eq (6 compared to 7.5), then the I_D/I_G ratio of rGO-VitC-24hr-1eq should be lower, however, this is not the case. This might be attributed to the fact that not all the oxygens contributing to the lower C/O ratio of rGO-VitC-24hr-1eq were at the expense of sp^2 islands; some might be a result of oxidizing an edge-sp^3 carbon, meaning that the C/O ratio will increase, but the size of the sp^2 carbon island will not. The oxygens, which reduce the number of the sp^2 islands are the ones that influence the I_D/I_G ratio.

To sum up, L-AA proved its efficiency as green alternative to Hz in reducing GO into rGO. The L-AA reduction method (0.4eq - 30 min) was superior to the hydrothermal reduction in producing rGO with higher C/O ratios (8.71 compared to 7.5 calculated from XPS and 3.87 compared to 3.21 calculated from EA) and more than double the electrical conductivity (1100 S/m compared to 500 S/m). This high degree of reduction was achieved at nearly half the hydrothermal reduction temperature (95°C vs 180°C) in a much shorter reaction time (30 min vs 17 h). Compared to reduction by Hz, the rGO-VitC samples show lower C/O ratio as well as lower electrical conductivity (around half the values). However, the environmental and safety concerns along with the price of the removal of the waste of the reducing agent should be taken into consideration when putting the rGO-Hz and the rGO-VitC samples in comparison. To evaluate the sufficiency of the obtained C/O ratio and electrical conductivity of the rGO-VitC samples for their use as electrode materials for supercapacitors as alternatives to rGO-Hz, electrochemical analysis must be carried out.

III.7 Electrochemical Analysis

Electrochemical Analysis were done to examine the viability of using the rGO-VitC sample as an electrode material for supercapacitor applications through comparing its performance in common aqueous electrolytes to that of rGO-Hz and GHG. If such materials show a comparable performance to that of rGO-Hz, then they can be used as greener, safer and cheaper alternatives for rGO-Hz. Accordingly, the L-AA can be used as a reducing agent for various rGO based materials, including the pillared graphene materials that are of interest herein.

To carry out such analysis, three different commonly used aqueous electrolytes were selected: i) acidic electrolyte (3M H_2SO_4), ii) basic (6M KOH) and iii) neutral (0.5M K_2SO_4). The electrochemical analysis was done in three-electrode Teflon Swagelok® cells. The WE consisted of 80% active material, 10% Acetylene black as conductive additive, 10% PVDF as binder and NMP as dispersing media, drop casted on a Stainless Steel (SS) disc. The CE was a free-standing YP50 electrode, ten times the mass of the WE so that it is not limiting. The RE was a pseudo-reference silver wire thinly coated with AgCl.

In the upcoming sub-sections, the results of the electrochemical testing of the reduced samples in various common aqueous electrolytes for supercapacitor applications will be presented. All the electrochemical plots are average plots of the electrochemical results produced from multiple electrodes with reproducible CVs. The error bars are always plotted

except when it affects the clarity of the plots. The rationale behind this data reporting methodology is presented in chapter 5 (see page 225).

III.7.1 Acidic Media (3M H_2SO_4)

Figure (III.23) shows the CVs and rate capability plots of the reduced samples cycled at 5 mV/s in 3M H_2SO_4. The prevailing CV shape is quasi-rectangular with additional redox peaks. The capacitance values were calculated to be 91 ±4, 109 ±14, 113 ±4, 107 ±2, 123 ±2 and 139 ±7 F/g for rGO-Hz, rGO-VitC-30min-0.4eq, rGO-VitC-30min-1eq, rGO-VitC-24hr-1eq, rGO-VitC-24hr-0.04eq and GHG, respectively. The rGO-VitC samples and GHG are showing higher capacitance than rGO-Hz (up to 35% for rGO-VitC-24hr-0.04eq and 53% for GHG at 5 mV/s). All the samples seem to possess a high rate capability as demonstrated by the near plateau shape of their rate capability plots. Only rGO-VitC-24hr-1eq displayed a fast decaying rate capability plot.

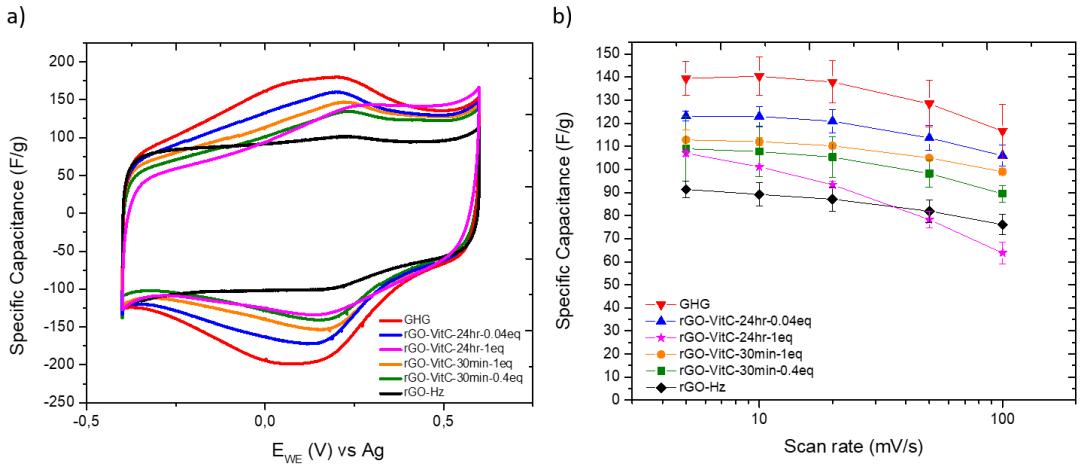

Figure III. 23 : a) Cyclic voltammograms at 5mV/s and b) rate capability of GO (—), rGO-Hz (—), rGO-VitC-30min-0.4eq (—), rGO-VitC-30min-1eq (—), rGO-VitC-24hr-1eq (—), rGO-VitC-24hr-0.04eq (—) and GHG (—) in 3M H_2SO_4 along with their associated error bars

The quasi-rectangular CV shape is indicative of (EDLC) as expected for carbonaceous materials. The presence of redox peaks indicates fast surface or near surface redox reactions, most probably involving the remaining oxygen functionalities. From the capacitance values, all the rGO-VitC samples are showing average capacitance values higher than that of rGO-Hz and less than that of GHG at all scan rates, except rGO-VitC-24hr-1eq (rGO-VitC-24hr-0.04eq is the best performing rGO-VitC sample in such electrolyte), although the rGO-Hz is the most conductive sample among the tested samples. This shows that the rGO-VitC samples possess sufficient electrical conductivity and that any further increase in such conductivity is no longer the decisive parameter to the performance. Such an observation also sheds the light on the importance of the surface chemistry in enhancing the performance of the reduced GO samples

as electrode materials for supercapacitors cycled in acidic electrolytes. To ascertain the role of the surface chemistry, the amount of C=O groups are plotted against the average specific capacitance. This representation shows the effect of the amount of basic oxygen functional groups on the average specific capacitance in an acidic electrolyte (Figure III.24). The choice of plotting the effect of basic groups, rather than all groups or acidic ones, was done based on the literature as well as on the confirmation of the literature's findings in chapter 2 that basic groups are electrochemically active in acidic media.

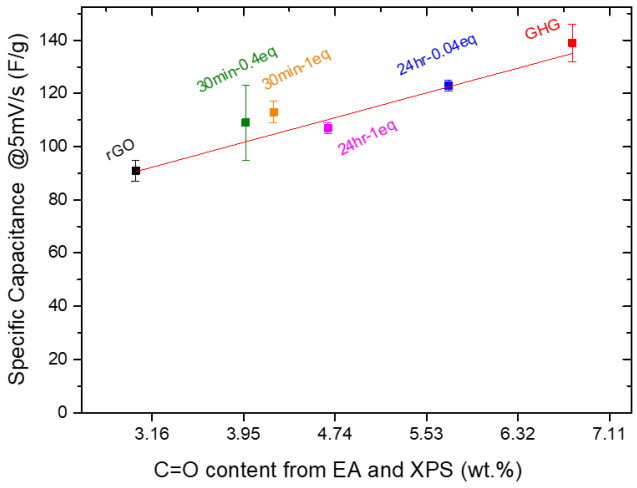

Figure III. 24 : Effect of C=O content on the average specific capacitance of rGO-Hz, rGO-VitC-30min-0.4eq, rGO-VitC-30min-1eq, rGO-VitC-24hr-1eq, rGO-VitC-24hr-0.04eq and GHG in 3M H_2SO_4 (red line is a linear fit to guide the eye)

It can be seen that as the content of carbonyl groups increases, the overall average capacitance increases. The increase in average capacitance can be attributed to an increase in the redox reactions involving the quinone/carbonyl groups remaining after the reduction. Consequently, the less reduced and less conductive samples (such as GHG and rGO-VitC-24hr-0.04eq) show higher average capacitance values in 3M H_2SO_4 because they have more quinone/carbonyl groups compared to the other samples.

The abnormal fast capacitance drop at scan rates ≥ 10 mV/s for rGO-VitC-24hr-1eq could be explained by the presence of extra hydroxyl groups at the edges of the sheets due to their re-oxidation by oxygen containing radicals produced during the (auto-) oxidation of ascorbic acid as highlighted earlier. These hydroxyl groups can form hydrogen bonds between the various rGO sheets, bringing them and particles closer to each other, thus, decreasing the accessibility of the inter-particles pores to the ions at higher scan rates. Such hypothesis can be backed up by the appearance of a percolating network (observed by SEM) that is denser than that of GHG (explaining why such behavior is not observed for GHG), compared to wrinkled and crumpled

sheets observed for the other rGO-VitC samples. This explanation is in line with the visual inspection of the electrode prior to electrochemical cycling. This particular sample yielded electrodes of sizes smaller than the size of the electrode support on which their NMP dispersion was drop casted (Figure III.25). A preferential organization of the rGO-sheets together instead of being uniformly divided on the surface of the SS discs was observed.

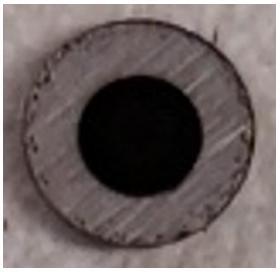

Figure III. 25 : Optical image of an rGO-VitC-24hr-1eq electrode

Electrochemical impedance spectroscopy analysis was done to extract information regarding the Equivalent Series Resistance (R_{ESR}) and the effective ionic transport resistance of the ions inside the pores of the various rGO-VitC samples. Comparing these values to those obtained for rGO-Hz and GHG, the effects of the reduction method on such parameters can be verified. The experiments were carried out at OCV in a frequency range from 10mHz to 100KHz. The average Nyquist plots of all the tested samples are shown in Figure (III.26).

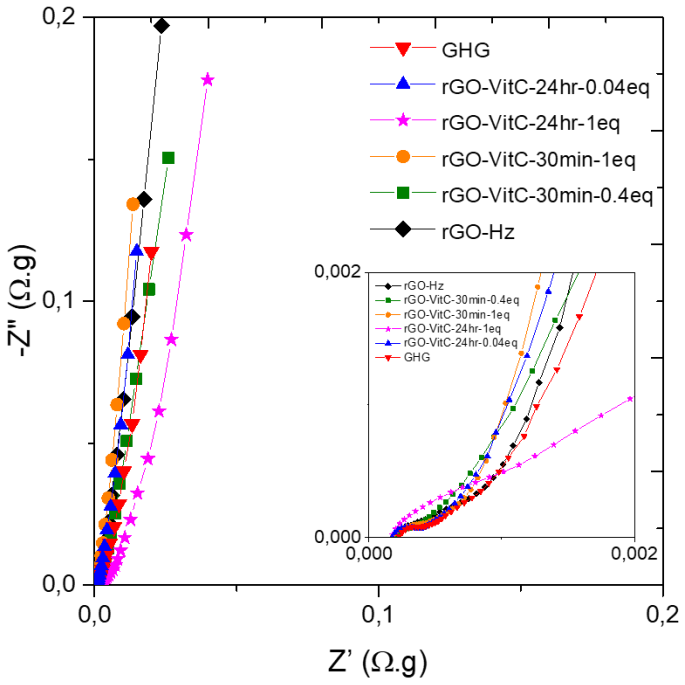

Figure III. 26 : Average Nyquist plots of rGO-Hz (—), rGO-VitC-30min-0.4eq (—), rGO-VitC-30min-1eq (—), rGO-VitC-24hr-1eq (—), rGO-VitC-24hr-0.04eq (—) and GHG (—) in 3M H_2SO_4. Insert: a zoom in for the high frequency region

The ESR values range from 0.17 to 0.22 mΩ.g, indicating that such a parameter is similar in all the samples. The rGO-vitC-30min-1eq, rGO-VitC-24hr-0.04eq and rGO-VitC-30min-0.4 seem to have slightly better ionic diffusion than rGO-Hz and GHG as they possess shorter intermediate frequency regions. The rGO-VitC-24hr-1eq clearly shows a lower ionic diffusion compared to the rest of the samples as evidenced by the long intermediate frequency region. This is in good agreement with the observed poor rate capability of this sample that was explained in the previous sub-section. At low frequencies, a near vertical line was observed as expected for porous carbonaceous materials.

The complex model was applied on the data in order to determine the real capacitance at low frequency and compare its trend to that obtained from the CVs, and to extract the effective ionic transport resistance inside the pores. The real capacitance is plotted against the frequency in Figure (III.27(a)) and the imaginary capacitance is plotted against the real impedance in Figure (III.27(b)).

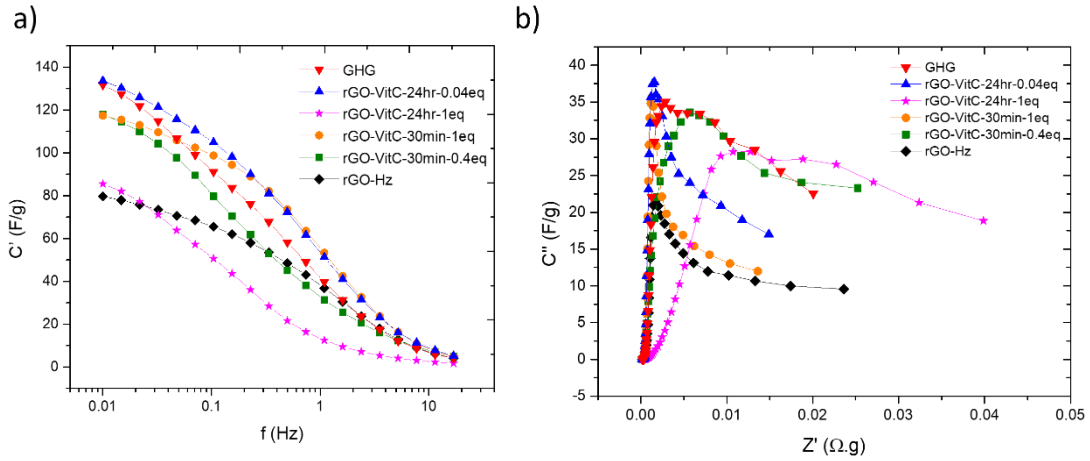

Figure III. 27 : a) Real Capacitance versus the frequency and b) Imaginary Capacitance versus the real impedance of rGO-Hz (—), rGO-VitC-30min-0.4eq (—), rGO-VitC-30min-1eq (—), rGO-VitC-24hr-1eq (—), rGO-VitC-24hr-0.04eq (—) and GHG (—) in 3M H_2SO_4

The real capacitance values at 10 mHz were 80 ±2, 118 ±8, 117 ±3, 85 ±7, 134 ±9, 132 ±3 F/g for rGO-Hz, rGO-VitC-30min-0.4eq, rGO-VitC-30min-1eq, rGO-VitC-24hr-1eq, rGO-VitC-24hr-0.04eq and GHG, which is in agreement with the trend in values obtained from the CVs. The rGO-VitC-24hr-1eq sample showed a fast deterioration of performance at higher frequencies, even worse than rGO-Hz, in agreement with the rate capability plot. The ionic transport resistance values range between 1 and 4.5 mΩ.g for all the samples except for rGO-VitC-24hr-1eq that gives 8 mΩ.g, consistent with its poor performance at high scan rates and frequencies. Although this rGO-VitC sample has more carbonyl content and higher capacitance at low scan rate compared to rGO-Hz, its performance decays at higher scan rates or higher

frequencies, and it possesses capacitance values lower than that of rGO-Hz. This hints on an accessibility issue that is not present when lower scan rates are used. This can strengthen the previously proposed explanation of tightened inter-particle spaces due to the formation of H-bond network between the particles, bringing them closer to each other.

The electrochemical results obtained so far showed the viability of using L-AA as a reducing agent for GO to form electrode materials for supercapacitor based on 3M H_2SO_4. The capacitance values are higher than that of rGO-Hz (up to 35% with rGO-VitC-24hr-0.04eq), while their R_{ESR} and ionic transport resistances are comparable. An exception is the rGO-VitC-24hr-1eq sample for the reasons discussed earlier. The GHG sample is the sample with best capacitance so far in such an acidic electrolyte.

III.7.2 Basic Media (6M KOH)

Another common performance aqueous electrolyte, the basic 6M KOH, was utilized to further validate the use of the greener rGO-VitC samples as electrode materials instead of rGO-Hz. The CVs and the rate capability of the samples cycled in 6M KOH are shown below in Figure (III.28). All the rGO-VitC samples were cycled in such electrolytes, however, only the best performing rGO-VitC sample (rGO-VitC-24hr-0.04eq) is presented below against rGO-Hz and GHG.

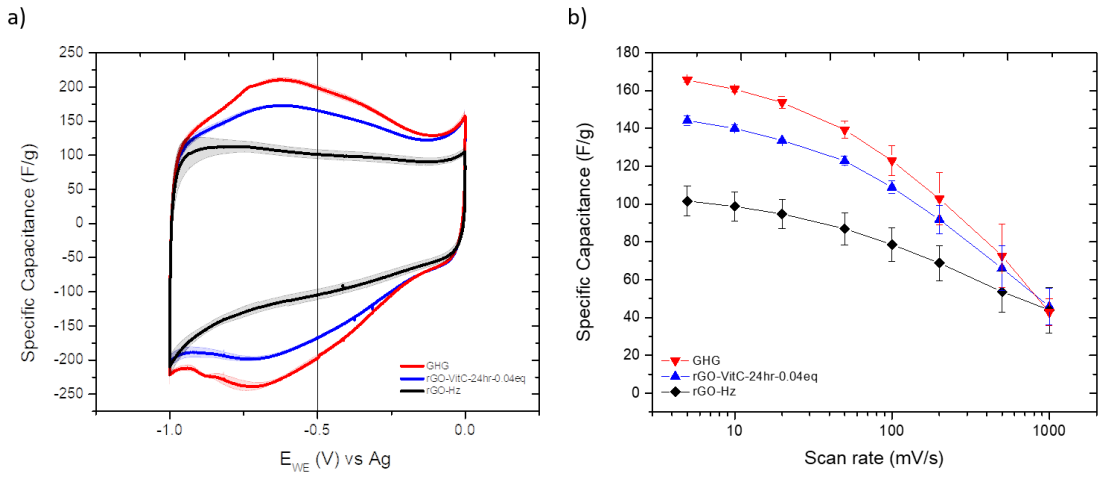

Figure III. 28 : a) Cyclic voltammograms at 5mV/s and b) rate capability of rGO-Hz (—), rGO-VitC-24hr-0.04eq (—) and GHG (—) in 6M KOH along with their associated error bars

The CV shape for rGO-Hz is a quasi-rectangle with slight asymmetry on the y-axis. The CV shapes of rGO-VitC-24hr-0.04eq and GHG are also quasi-rectangular but coupled with broad redox-peaks. The average specific capacitance was calculated to be 102 ±8, 144 ±3 and 166 ±1 F/g at a scan rate of 5mV/s for rGO-Hz, rGO-VitC-24hr-0.04eq and GHG. The rGO-VitC and GHG are showing higher capacitance than rGO-Hz by 41% and 63% respectively. The rate

capability of the three samples is similar in terms of decay over time, showing good rate capability of such materials up to 100 mV/s. However, GHG is displaying higher average capacitance values at all scan rates followed by rGO-VitC-24hr-0.04eq and then rGO-Hz.

The asymmetrical CV shape observed for rGO-Hz is showing a larger enclosed area at more negative potential (where K^+ ions are supposed to diffuse inside the pores under the effect of the negatively applied potential). Such an increase in the enclosed area under the CV might be assigned to specific adsorption of K^+ on remaining carbonyl or quinone groups via ion-dipole attraction. Such interaction can change the local electronic charge near such oxygen groups, leading to boost the EDLC at those negative potentials beyond the EDLC of the non-specific adsorption of K^+ on carbon [36]. These interactions can be also present in rGO-VitC-24hr-0.04eq and GHG samples but probably masked by broad peaks appearing across the potential window. These broad peaks can be attributed to fast surface or near surface redox reactions involving the acidic oxygen functional groups remaining in the samples such as the phenolic groups. The acidic groups are expected to be electrochemically active in basic electrolytes as shown in Eq. (III.8) for the oxidation of acidic phenolic groups.

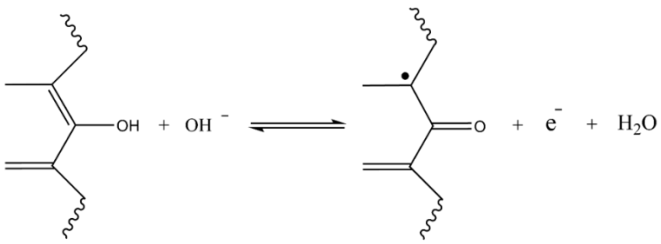

(III.8)

Plotting the C-O content from EA versus the average specific capacitance show the positive effect of oxygen functionalities on the average specific capacitance (Figure III.29).

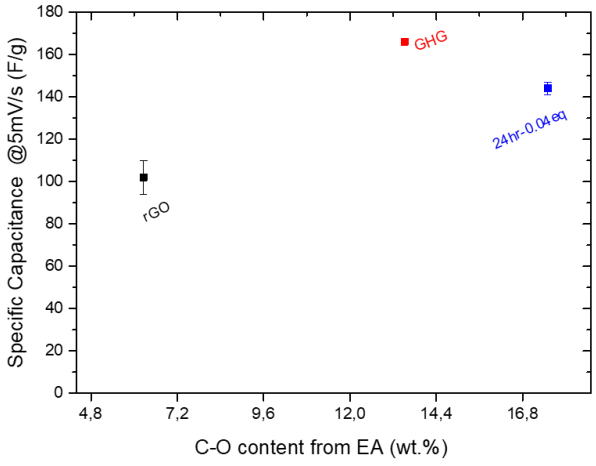

Figure III. 29 : Effect of C-O content on the average specific capacitance of rGO-Hz, rGO-VitC-24hr-0.04eq and GHG in 6M KOH

Herein, the sample with the highest C-O content is not the one with the highest capacitance in 6M KOH because not all C-O groups are electrochemically active in such basic media. Only acidic ones like phenolic groups are electrochemically active and quantifying such groups and differentiating them from the epoxy groups is challenging. Accordingly, we can conclude that GHG, despite not having the highest oxygen content, has the highest content of electrochemically active oxygen functionalities in 6M KOH, yielding the highest capacitance. rGO-Hz, the most reduced and most conductive sample, is the sample with the least average specific capacitance as it lacks sufficient oxygen functionalities to partake in redox reactions. On the contrary, GHG, the least reduced sample and with much lower electrical conductivity compared to rGO-Hz, is the sample with the highest average specific capacitance. This ascertains the impact of the chemistry of the samples on their performance as electrode materials for supercapacitor applications. It also shows once again that the electrical conductivity, being a vital parameter, is not the only parameter affecting the average specific capacitance. This shows that it is possible to compromise on electrical conductivity (moderate to low) if the chemistry is well adapted.

In turn, Electrochemical Impedance Spectroscopy (EIS) measurements were done at OCV in 6M KOH, in a frequency range from 10 mHz to 100 KHz as shown in the Nyquist plot in Figure (III.30).

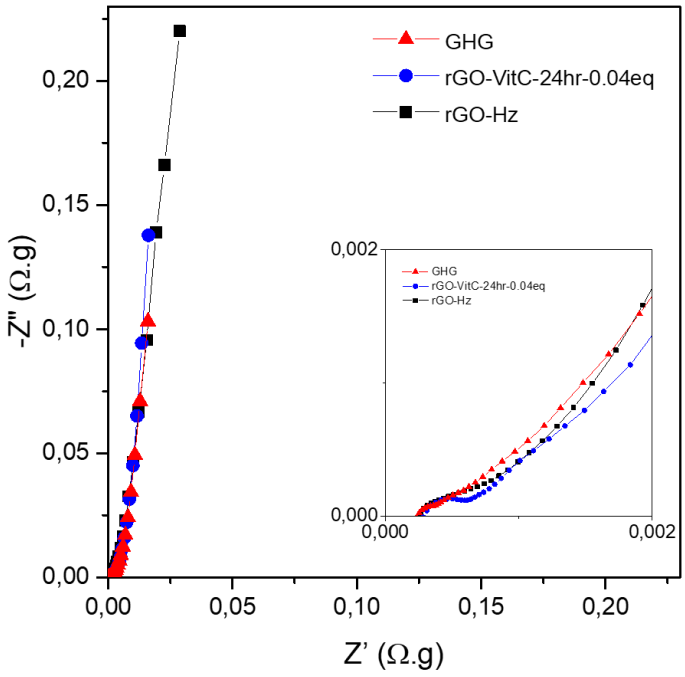

Figure III. 30 : Average Nyquist plots of rGO-Hz (—), rGO-VitC-24hr-0.04eq (—) and GHG (—) in 6M KOH. Insert: a zoom in for the high frequency region

The R_{ESR} was extracted from the X-axis intercept at high frequencies, and was found to be in the range of 0.24-0.29 mΩ.g, showing that the samples have very similar ESR in such an electrolyte in such a three-electrode assembly. The ionic diffusion of the three samples seem close as evident from their similar intermediate frequency regions.

At low frequencies, a steep rise in the imaginary component of the impedance, resulting in near vertical lines, was observed for all the samples indicative of the capacitive nature of such materials.

From the complex models, real and imaginary capacitances can be extracted and used to get insights on the capacitance values at low frequencies and on the effective ion transport resistance. The real capacitance is plotted against the frequency in Figure (III.31(a)) while the imaginary capacitance is plotted against the real impedance in Figure (III.31(b)).

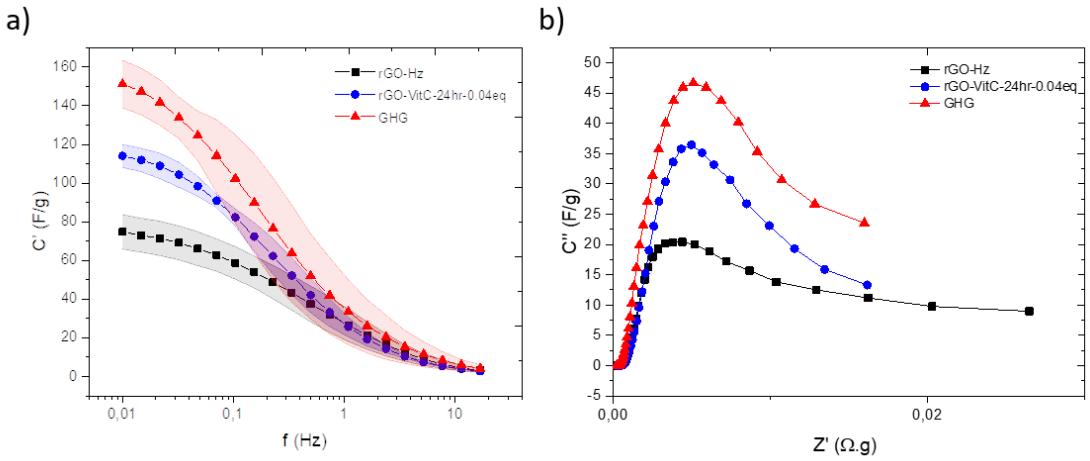

Figure III. 31 : a) Real Capacitance versus the frequency and b) Imaginary Capacitance versus the real impedance of Graphite rGO-Hz (—), rGO-VitC-24hr-0.04eq (—) and GHG (—) in 6M KOH

Figure (III.31(a)) clearly shows a trend in capacitance values at low frequencies similar to that shown by the CVs (GHG>rGO-VitC-24hr-0.04eq>rGO-Hz). At 10mHz, the capacitance was calculated to be 151 ±12, 114 ±6 and 75±9 F/g for GHG, rGO-VitC-24hr-0.04eq and rGO-Hz, respectively. At high frequencies, the capacitance values tend to zero as the electrodes behave as resistors at such frequencies. The effective ionic transport resistance of the electrolyte inside the porous structures of the samples can be deduced from Figure (III.31(b)). The values were in the 3.13-4.62 mΩ.g range, showing very close values for the three samples in KOH. These electrochemical analysis collectively indicate that GHG and rGO-VitC-24h-0.04eq are good alternatives to rGO-Hz in 6M KOH.

III.7.3 Neutral Electrolyte (0.5M K_2SO_4)

To further validate the use of rGO-VitC samples as alternative supercapacitor electrode materials to rGO-Hz, a neutral reference electrolyte was used, that is 0.5M K_2SO_4. The CVs are shown in Figure (III.32) only for rGO-Hz, GHG and rGO-VitC-24hr-0.04eq (the best performing rGO-VitC sample based on acidic and basic electrolytes). The CV shapes are quasi-rectangular with slight asymmetric areas enclosed by the CV curves. As mentioned for the study performed in KOH electrolyte, this asymmetry can be assigned to specific adsorption of K^+ on remaining carbonyl or quinone groups via ion-dipole attraction, which in turn can change the local electronic charge near such groups, leading to a boost in the EDLC [36].

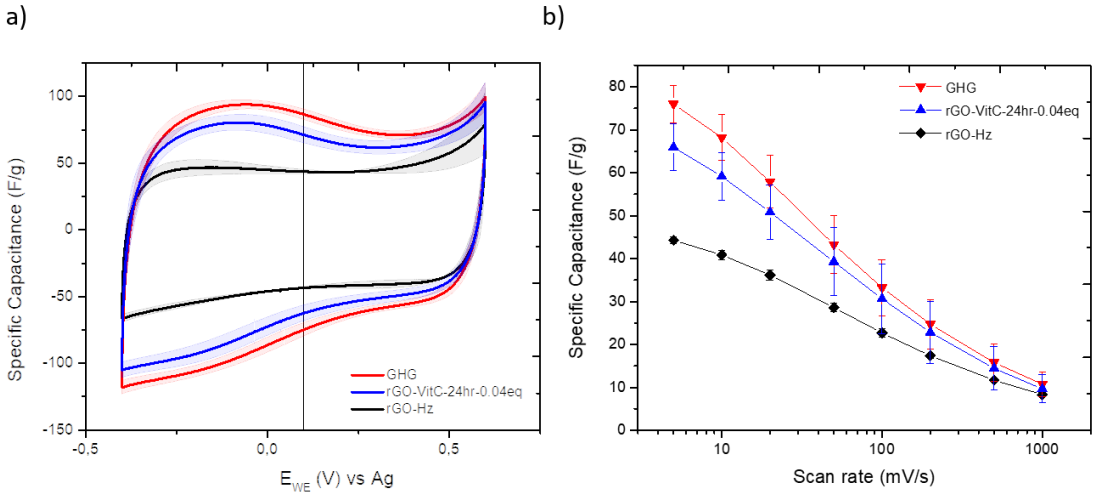

Figure III. 32 : a) Cyclic voltammograms at 5mV/s and b) rate capability of rGO-Hz (—), rGO-VitC-24hr-0.04eq (—) and GHG (—)in 0.5M K_2SO_4 along with their associated error bars

The capacitance values at a scan rate of 5 mV/s are 44 ±1, 66 ±5 and 76 ±4 F/g for rGO-Hz, rGO-VitC-24hr-0.04eq and GHG, respectively. The rGO-VitC and GHG are showing higher capacitance than rGO-Hz by 50% and 73% respectively. The rate capability shows superior performance of the rGO-VitC and GHG samples compared to rGO-Hz even at high scan rates (as was the case with 3M H_2SO_4 and 6M KOH), which can be attributed to the morphology of these samples. The rGO-VitC sample is less wrinkled and crumpled compared to rGO-Hz and GHG has a 3D macroporous network. These morphologies might allow better pore accessibility to the ions at higher scan rates and thus allowing more ions to adsorb and more oxygen functionalities to be accessed. The capacitance values obtained in 0.5M K_2SO_4 are lower than those obtained in 3M H_2SO_4 or 6M KOH. Such an observation can be explained with the lack of redox activities when using such an electrolyte compared to the rest.

The specific capacitance was plotted against the C=O content (Figure III.33) and an increasing trend was observed, confirming the importance of the chemistry of those reduced samples in

influencing their performance as electrode materials for supercapacitors applications even in neutral electrolyte.

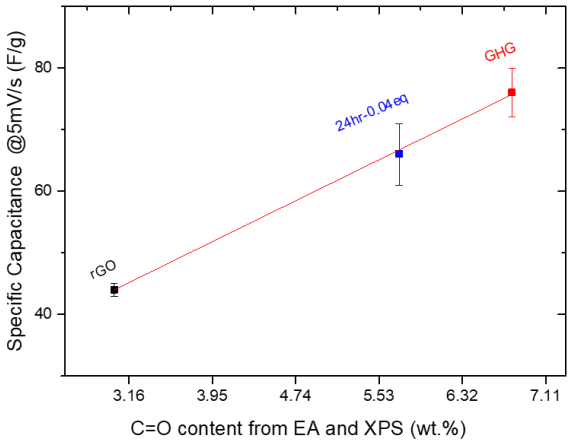

Figure III. 33 : Effect of C=O content on the average specific capacitance of rGO-Hz, rGO-VitC-24hr-0.04eq and GHG in 0.5M K_2SO_4 (red line is a linear fit to guide the eye)

The EIS data in 0.5M K_2SO_4 confirm the trends of capacitance and show similar R_{ESR}, ionic diffusion, and ionic transport resistance inside the pores as evidenced from Figure (III.34). The specific capacitance values at 10 mHz are 34 ±1, 56 ±5 and 57 ±5 for rGO-Hz, rGO-VitC-24hr-0.04eq and GHG, respectively.

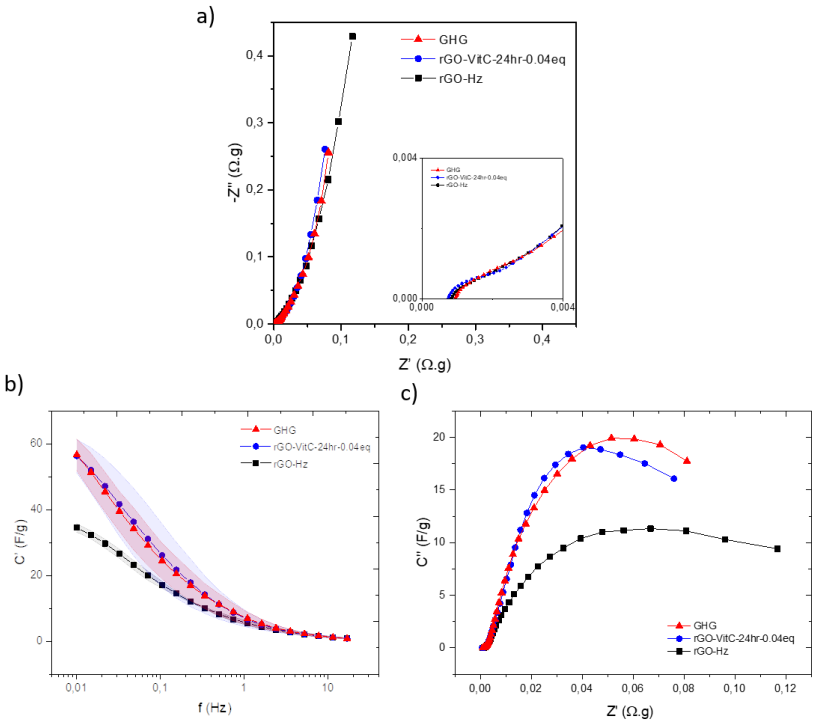

Figure III. 34 : a) Average Nyquist plots, b) Real Capacitance versus the frequency and c) Imaginary Capacitance versus the real impedance of rGO-Hz (—), rGO-VitC-24hr-0.04eq (—) and GHG (—) in 0.5M K_2SO_4 . Insert: a zoom in for the high frequency region

The electrochemical results presented so far in various electrolytes show the high potential of rGO-VitC and GHG as greener alternative electrode materials to rGO-Hz for supercapacitor applications. Despite being less conductive than rGO-Hz, these samples displayed a higher specific capacitance in all electrolytes tested compared to rGO-Hz while maintaining similar resistance values. The key to such better performance can be mainly attributed to higher oxygen content that can partake in various redox reactions depending on their type and the electrolyte used. Also, the less wrinkled and crumpled, more open structure of these samples might explain their better performance at high scan rates when the redox reactions are limited.

III.7.4 Stability Tests

Stability tests were carried out to verify the viability of using rGO-VitC samples as greener alternatives to rGO-Hz for supercapacitor applications. Such tests inspect the samples' performances under long cycling conditions. The tests were done on rGO-Hz and rGO-VitC-24hr-0.04eq in 3M H_2SO_4 at 200 mV/s for 15000 cycles (Figure III.35).

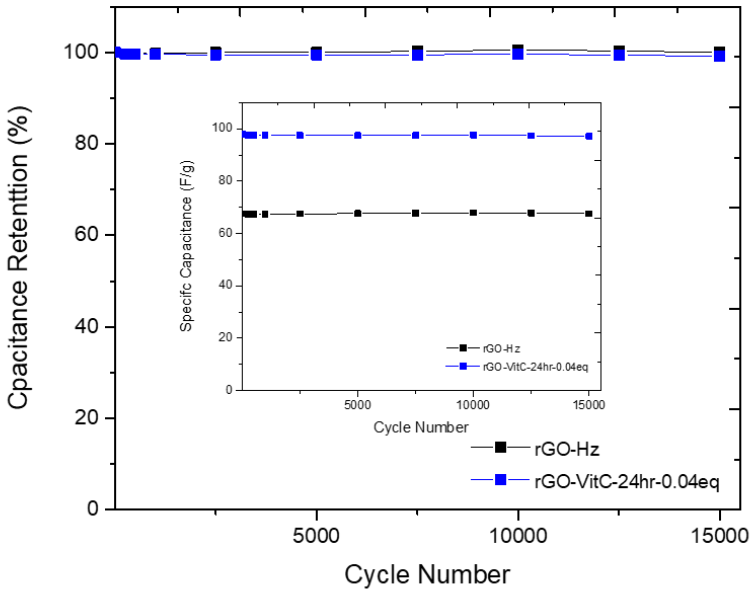

Figure III. 35 : Stability Test for rGO-Hz (–▪–) and rGO-VitC-24hr-0.04eq (–▪–) at 200 mV/s for 15000 cycles in 3M H_2SO_4

The two samples show exceptional stability as evidenced by their very high capacitance retention (~100%) after 15000 cycles. Simultaneously, rGO-VitC-24hr-0.04 maintained a capacitance that is 45% higher than that maintained by rGO-Hz as shown in the insert of Figure (III.35). Not only was the rGO-VitC sample as highly stable as rGO-Hz, but also it showed much better performance. This proves that such sample can indeed be a greener and better electrode material for supercapacitor electrodes in the tested electrolytes compared to rGO-Hz.

III.8 What are the Best Reduction Conditions?

After showing the performance of the different rGO-VitC as electrode materials for supercapacitors, specific reduction conditions can be recommended depending on the properties targeted for the application of interest. If the highest electrical conductivity is required, then the conditions of rGO-VitC-30min-0.4eq are recommended, while if the highest specific capacitance in aqueous electrolytes including 3M H_2SO_4, 6M KOH and 0.5M K_2SO_4 is needed, then the conditions used to obtain rGO-VitC-24hr-0.04eq are the best. GHG is electrochemically outperforming all the rGO-VitC samples in specific capacitance metrics, however, their performance is expected to drastically fall behind when expressed as volumetric capacitance due to their very low density. On another note, if high electrical conductivity is desired along with some oxygen functionalities, particularly hydroxyl groups, for post-functionalization, the use of the conditions leading to rGO-VitC-24hr-1eq are advised.

III.9 Conclusions

Herein, the viability of using L-ascorbic acid as a greener alternative reducing agent to hydrazine was tested. Various reduced graphene oxide samples were synthesized using different reduction methods: i) chemically using hydrazine, ii) chemically using L-ascorbic acid and iii) hydrothermally. Various reduction conditions were experimented for reduction using L-AA.

The chemical analysis proved the successful reduction of GO using L-AA under different reduction conditions as evidenced by an increase in the C/O ratio from XPS and EA. Such an analysis revealed an abnormal behavior when a high concentration of L-AA was used to reduce the sample in 24 h. The reduced sample had a higher C/O ratio compared to the one with the same amount of L-AA but reduced in 30 min. Such mystery was unraveled through various observations and measurements, suggesting the in-situ production of H_2O_2 via the oxidation of L-AA (whether metal catalyzed or not). The production of H_2O_2 is reported to generate oxygen containing radicals than can even oxidize graphite.

Structural properties extracted from XRD showed a d-spacing value for rGO-VitC in the same range of that of rGO-Hz and GHG. Raman spectroscopy allowed tracking the restoration of the sp^2 carbon network and calculating the avg. size of the sp^2 domains. SEM showed the differences in morphologies ranging from wrinkled and crumpled rGO-Hz to 3D macroporous interconnected GHG.

Electrical conductivity of the various samples were evaluated and related to different chemical and structural parameters. Models were built to gather all these inter-related pieces of information together to correlate the chemistry and structure to the various observed characteristics such as C/O ratios, I_D/I_G ratios, avg. size of sp^2 islands and electrical conductivity values.

Electrochemical Analysis were carried out to assess the samples' performances in various common aqueous electrolytes: i) 3M H_2SO_4, ii) 6M KOH and iii) 0.5M K_2SO_4. The results showed better performance of the GHG and the rGO-VitC samples compared to that of rGO-Hz in all electrolytes while maintaining similar internal and ionic transport resistances. This shows the feasibility of using the rGO-VitC samples with better capacitance as a greener alternative to lower capacitance rGO-Hz. The electrochemical results presented in this chapter affirmed the great importance of oxygen functionalities in determining the capacitance of different samples in aqueous electrolytes, due to their ability to partake in various oxidation reactions that contribute to the overall capacitance.

III.10 References

[1] K. K. H. De Silva, H.-H. Huang, R. K. Joshi, and M. Yoshimura, 'Chemical reduction of graphene oxide using green reductants', *Carbon*, vol. 119, pp. 190–199, Aug. 2017, doi: 10.1016/j.carbon.2017.04.025.

[2] Y. Zhou, Q. Bao, L. A. L. Tang, Y. Zhong, and K. P. Loh, 'Hydrothermal Dehydration for the "Green" Reduction of Exfoliated Graphene Oxide to Graphene and Demonstration of Tunable Optical Limiting Properties', *Chem. Mater.*, vol. 21, no. 13, pp. 2950–2956, Jul. 2009, doi: 10.1021/cm9006603.

[3] M. J. Fernández-Merino *et al.*, 'Vitamin C Is an Ideal Substitute for Hydrazine in the Reduction of Graphene Oxide Suspensions', *J. Phys. Chem. C*, vol. 114, no. 14, pp. 6426–6432, Apr. 2010, doi: 10.1021/jp100603h.

[4] K. K. H. De Silva, H.-H. Huang, and M. Yoshimura, 'Progress of reduction of graphene oxide by ascorbic acid', *Applied Surface Science*, vol. 447, pp. 338–346, Jul. 2018, doi: 10.1016/j.apsusc.2018.03.243.

[5] D. He, L. Shen, X. Zhang, Y. Wang, N. Bao, and H. H. Kung, 'An efficient and eco-friendly solution-chemical route for preparation of ultrastable reduced graphene oxide suspensions', *AIChE Journal*, vol. 60, no. 8, pp. 2757–2764, 2014, doi: 10.1002/aic.14499.

[6] C. Xu, X. Shi, A. Ji, L. Shi, C. Zhou, and Y. Cui, 'Fabrication and Characteristics of Reduced Graphene Oxide Produced with Different Green Reductants', *PLOS ONE*, vol. 10, no. 12, p. e0144842, Dec. 2015, doi: 10.1371/journal.pone.0144842.

[7] J. Zhang, H. Yang, G. Shen, P. Cheng, J. Zhang, and S. Guo, 'Reduction of graphene oxide viaL-ascorbic acid', *Chem. Commun.*, vol. 46, no. 7, pp. 1112–1114, Feb. 2010, doi: 10.1039/B917705A.

[8] X. Zhu, Q. Liu, X. Zhu, C. Li, M. Xu, and Y. Liang, 'Reduction of Graphene Oxide Via Ascorbic Acid and Its Application for Simultaneous Detection of Dopamine And Ascorbic Acid', *International Journal of Electrochemical Science*, vol. 7, no. 6, pp. 5172–5184, Jan. 2012, doi: 10.1016/S1452-3981(23)19612-X.

[9] S. Park *et al.*, 'Chemical structures of hydrazine-treated graphene oxide and generation of aromatic nitrogen doping', *Nat Commun*, vol. 3, no. 1, Art. no. 1, Jan. 2012, doi: 10.1038/ncomms1643.

[10] Y. Wang *et al.*, 'Magnetic graphene oxide nanocomposites: nanoparticles growth mechanism and property analysis', *J. Mater. Chem. C*, vol. 2, no. 44, pp. 9478–9488, Oct. 2014, doi: 10.1039/C4TC01351D.

[11] J. Onoe, A. Nakao, and K. Takeuchi, 'XPS study of a photopolymerized C 60 film', *Phys. Rev. B*, vol. 55, no. 15, pp. 10051–10056, Apr. 1997, doi: 10.1103/PhysRevB.55.10051.

[12] Y.-J. Tu, D. Njus, and H. B. Schlegel, 'A theoretical study of ascorbic acid oxidation and HOO˙/O2˙− radical scavenging', *Org. Biomol. Chem.*, vol. 15, no. 20, pp. 4417–4431, May 2017, doi: 10.1039/C7OB00791D.

[13] M. Lin and J. Z. Yu, 'Assessment of Interactions between Transition Metals and Atmospheric Organics: Ascorbic Acid Depletion and Hydroxyl Radical Formation in Organic-Metal Mixtures', *Environ. Sci. Technol.*, vol. 54, no. 3, pp. 1431–1442, Feb. 2020, doi: 10.1021/acs.est.9b07478.

[14] A. J. Michels and B. Frei, 'Myths, Artifacts, and Fatal Flaws: Identifying Limitations and Opportunities in Vitamin C Research', *Nutrients*, vol. 5, no. 12, p. 5161, Dec. 2013, doi: 10.3390/nu5125161.

[15] B. H. J. Bielski and A. O. Allen, 'Mechanism of the disproportionation of superoxide radicals', *J. Phys. Chem.*, vol. 81, no. 11, pp. 1048–1050, Jun. 1977, doi: 10.1021/j100526a005.

[16] N. Miyake, M. Kim, and T. Kurata, 'Stabilization of <small>L</small>-Ascorbic Acid by Superoxide Dismutase and Catalase', *Bioscience, Biotechnology, and Biochemistry*, vol. 63, no. 1, pp. 54–57, 1999, doi: 10.1271/bbb.63.54.

[17] G. R. Buettner and B. A. Jurkiewicz, 'Catalytic Metals, Ascorbate and Free Radicals: Combinations to Avoid', *Radiation Research*, vol. 145, no. 5, p. 532, May 1996, doi: 10.2307/3579271.

[18] N. Miyake, M. Kim, and T. Kurata, 'Formation Mechanism of Monodehydro-L-ascorbic Acid and Superoxide Anion in the Autoxidation of L-Ascorbic Acid', *Bioscience, Biotechnology, and Biochemistry*, vol. 61, no. 10, pp. 1693–1695, 1997, doi: 10.1271/bbb.61.1693.
[19] R. W. Peterson and J. H. Walton, 'The Autoxidation of Ascorbic Acid [1]', *J. Am. Chem. Soc.*, vol. 65, no. 6, pp. 1212–1217, Jun. 1943, doi: 10.1021/ja01246a053.
[20] X. You *et al.*, 'Green and Mild Oxidation: An Efficient Strategy toward Water-Dispersible Graphene', *ACS Appl. Mater. Interfaces*, vol. 9, no. 3, pp. 2856–2866, Jan. 2017, doi: 10.1021/acsami.6b13703.
[21] A. Vittore, M. R. Acocella, and G. Guerra, 'Edge-Oxidation of Graphites by Hydrogen Peroxide', *Langmuir*, vol. 35, no. 6, pp. 2244–2250, Feb. 2019, doi: 10.1021/acs.langmuir.8b03489.
[22] D. P. Suhas, T. M. Aminabhavi, H. M. Jeong, and A. V. Raghu, 'Hydrogen peroxide treated graphene as an effective nanosheet filler for separation application', *RSC Adv.*, vol. 5, no. 122, pp. 100984–100995, Nov. 2015, doi: 10.1039/C5RA19918B.
[23] E. O. Ogunsona, T. Grovu, and T. H. Mekonnen, 'Fabrication of nano-structured graphene oxide-like few-layer sheets from biocarbon via a green process', *Sustainable Materials and Technologies*, vol. 26, p. e00208, Dec. 2020, doi: 10.1016/j.susmat.2020.e00208.
[24] S. Tian *et al.*, 'Controllable Edge Oxidation and Bubbling Exfoliation Enable the Fabrication of High Quality Water Dispersible Graphene', *Sci Rep*, vol. 6, no. 1, Art. no. 1, Sep. 2016, doi: 10.1038/srep34127.
[25] M. B. Yim, B. S. Berlett, P. B. Chock, and E. R. Stadtman, 'Manganese(II)-bicarbonate-mediated catalytic activity for hydrogen peroxide dismutation and amino acid oxidation: detection of free radical intermediates.', *Proceedings of the National Academy of Sciences*, vol. 87, no. 1, pp. 394–398, Jan. 1990, doi: 10.1073/pnas.87.1.394.
[26] K. Kinoshita, *Carbon: Electrochemical and Physicochemical Properties*. 1988.
[27] G. R. Buettner and B. A. Jurkiewicz, 'Ascorbate free radical as a marker of oxidative stress: An EPR study', *Free Radical Biology and Medicine*, vol. 14, no. 1, pp. 49–55, Jan. 1993, doi: 10.1016/0891-5849(93)90508-R.
[28] M. Scarpa, R. Stevanato, P. Viglino, and A. Rigo, 'Superoxide ion as active intermediate in the autoxidation of ascorbate by molecular oxygen. Effect of superoxide dismutase.', *Journal of Biological Chemistry*, vol. 258, no. 11, pp. 6695–6697, Jun. 1983, doi: 10.1016/S0021-9258(18)32271-3.
[29] O. Augusto, D. R. Truzzi, and E. Linares, 'Electron paramagnetic resonance (EPR) for investigating relevant players of redox reactions: Radicals, metalloproteins and transition metal ions', *Redox Biochemistry and Chemistry*, vol. 5–6, p. 100009, Dec. 2023, doi: 10.1016/j.rbc.2023.100009.
[30] A. Ferrari, J. Robertson, S. Reich, and C. Thomsen, 'Raman spectroscopy of graphite', *Philosophical Transactions of the Royal Society of London. Series A: Mathematical, Physical and Engineering Sciences*, vol. 362, no. 1824, pp. 2271–2288, Sep. 2004, doi: 10.1098/rsta.2004.1454.
[31] S. M. Tan, A. Ambrosi, C. K. Chua, and M. Pumera, 'Electron transfer properties of chemically reduced graphene materials with different oxygen contents', *J. Mater. Chem. A*, vol. 2, no. 27, pp. 10668–10675, Jun. 2014, doi: 10.1039/C4TA01034E.
[32] L. G. Cançado *et al.*, 'General equation for the determination of the crystallite size La of nanographite by Raman spectroscopy', *Applied Physics Letters*, vol. 88, no. 16, p. 163106, Apr. 2006, doi: 10.1063/1.2196057.
[33] F. Tuinstra and J. L. Koenig, 'Raman Spectrum of Graphite', *Journal of Chemical Physics*, vol. 53, pp. 1126–1130, Aug. 1970, doi: 10.1063/1.1674108.
[34] I. K. Moon, J. Lee, R. S. Ruoff, and H. Lee, 'Reduced graphene oxide by chemical graphitization', *Nat Commun*, vol. 1, no. 1, Art. no. 1, Sep. 2010, doi: 10.1038/ncomms1067.
[35] S. Wang *et al.*, 'The role of sp2/sp3 hybrid carbon regulation in the nonlinear optical properties of graphene oxide materials', *RSC Adv.*, vol. 7, no. 84, pp. 53643–53652, Nov. 2017, doi: 10.1039/C7RA10505C.
[36] C.-T. Hsieh, S.-M. Hsu, J.-Y. Lin, and H. Teng, 'Electrochemical Capacitors Based on Graphene Oxide Sheets Using Different Aqueous Electrolytes', *J. Phys. Chem. C*, vol. 115, no. 25, pp. 12367–12374, Jun. 2011, doi: 10.1021/jp2032687.

Conclusions & Perspectives

Chapter 4: Conclusions and Perspectives

IV.1 Conclusions

In chapter 1, Pillared graphene materials were introduced as one of the proposed solutions to mitigate the restacking problem of rGO sheets when the up-scalable chemical oxidation-exfoliation method is used to produce single rGO sheets. Their synthesis methods were surveyed and various publications were detailed, demonstrating the potential of such field for SuperCapacitor (SC) applications. The lack of sufficient fundamental studies on such class of materials was also highlighted and the need for such studies was stressed upon. The health, safety and environmental impacts of the use of hydrazine hydrate during the reduction process were discussed, and the use of greener alternative was detailed. It was pinpointed that literature lacked a study aiming at rationalizing experimental conditions and understanding reduction mechanism with such green reducing agent. At end of this introductory chapter, the aim of the thesis was presented based on the shortcomings identified in literature. The thesis, herein, goes from materials development to thorough studies to provide valuable understanding on electrochemical storage behavior and reduction processes.

Experiments, presented in Chapter 2, were designed to synthesize and study different pillared graphene materials. These materials are a good platform for fundamental studies as they exhibit a range of different structural and chemical properties, as proven by various chemical and structural characterization techniques. Electrochemical analyses were done in electrolytes of varying cation and anion sizes to test the performances of the synthesized pillared materials and relate them to their physico-chemical and structural properties. The pillaring strategy allowed the creation of microporous galleries, which in turn opened up new sites for adsorption and rendered the surface oxygen functionalities more accessible for redox reactions, if any were to occur. This was evidenced by higher specific capacitance observed for pillared samples compared to rGO. For instance, 7RP-NCH3 showed a 68% increase in average specific capacitance compared to rGO (69 ±2 F/g versus 41±4 F/g). The PGM local structure, revealed by the d-spacing (CL peak), was shown to be an important parameter, particularly, in its relation to the size of the ions. In neutral electrolytes, ions with hydrated sizes smaller than the d-spacing could access the pores while those with bigger hydrated sizes could not. An example is the accessibility of the pores of 7RP-NCH3 (0.84 nm) to the ions as these pores are of sizes larger than those of the hydrated ions, as evidenced by its near constant performance in all the neutral electrolytes (0.5M Li_2SO_4, 0.5M K_2SO_4 and 1M KNO_3). Contrary, such a constant performance was not observed for 6RP and 8RP-OO (0.75 nm) whose performances were enhanced on using cations and anions of sizes smaller than their d-spacing values such as 1M KNO_3. Ion-exchange

and co-ion desorption were proposed as charging mechanisms for the negative applied potentials in neutral electrolytes. The chemistry of the samples was not of less importance, the amount of carbonyl and quinone groups were found to be the more decisive parameter for the specific capacitance of these materials in 3M H_2SO_4. This was emphasized by the better capacitance values of samples with higher C=O content. In addition, specific capacitance increase seemed to be correlated to the increase of nitrogen and oxygen groups when neutral electrolytes where used. It is expected that such groups might form specific adsorption sites triggered by ion-dipole interactions between the groups and the cations, leading to local charge changes that could finally enhance the capacitance.

The reduction of graphene oxide using a green reducing agent such as L-ascorbic acid (commonly known as vitamin C) was the focus point of Chapter 3. Various reaction conditions were experimented and the resulting materials were chemically and structurally compared to hydrazine-reduced graphene oxide. The oxidation of L-ascorbic acid (catalyzed or not) was proven, for the first time, to play a role in determining the extent of reduction of the reduced graphene oxide. Such a role is related to the probable in-situ production of H_2O_2 as a final product of the oxidation of L-ascorbic acid either by molecular oxygen (auto-oxidation) or catalyzed by trace amounts of transition metals such as Fe^{3+} and Cu^{2+}. The production of H_2O_2 can generate different oxygen containing radicals, which in turn can oxidize the edges of the rGO sheets. The rGO-VitC samples yielded a C/O ratio in the 6-9 range, and electrical conductivity values in the 370-1000 S/m range depending on the starting conditions, compared to 14 and 2000 S/m for rGO-Hz. The rGO-VitC samples showed superior electrochemical performance compared to hydrazine-reduced graphene oxide in all tested electrolytes (3M H_2SO_4, 6M KOH and 0.5 M K_2SO_4). For instance, rGO-vitC-24hr-0.04eq showed a 40% increase in capacitance compared to rGO-Hz in 6M KOH (144 ±3 F/g versus 102 ±8 F/g). The effect of oxygen functionalities was illustrated in various electrolytes. The L-ascorbic acid was found to be an efficient reducing agent that can be a good substitute to hydrazine; particularly for supercapacitor applications, with its environmental friendliness, absence of safety concerns and superior electrochemical performance compensating the lower C/O ratios and electrical conductivity values compared to those of rGO-Hz.

IV.2 Perspectives

Building on what was established in the previous chapters, various openings could be identified. The next step we envision in such a field of research is to try new pillars with pseudocapacitive groups, aiming at adding a pseudocapacitive contribution, in addition to the double layer one, which may result in an increase in the capacitance and energy density. Trying

new chemistries for chemically bonding the molecular pillars onto graphene is an important topic as well to be considered. Maybe catalysts can be introduced to make the reactions faster, more specific, with higher yield, and ensure the chemical bonding of the pillars, rather than their physical adsorption on the graphene sheets. In parallel to such efforts, research has to be done on making the reduction of those pillared materials greener and safer. Another important study is an in-depth surface area analysis using various gases to unlock the porosity of these samples. In the upcoming sections, two research topics are suggested and preliminary results are displayed and discussed. These two topics were identified based on the results and needs encountered in the studies discussed in chapters 2 and 3.

IV.2.1 Promoting Cross-Linking (CL) and Adding Pseudocapacitance

In Chapter 2, the importance of increasing the density of adsorption sites by opening up new microporous galleries was shown to help in enhancing specific capacitance. In addition, the role played by various pseudocapacitive redox reactions involving different oxygen functionalities in enhancing the capacitive performance was stressed upon. However, the PGM presented in Chapter 2, are bi-phasic materials: they consist of two different phases, a graphitic one and a pillared one. In order to increase the accessible adsorption sites, the pillared part, with adequate d-spacing value for the size of the ions used, must be increased. Regarding the pseudocapacitance, the presence of oxygen functionalities in the pillared samples is a direct consequence of the efficiency of the reducing agent and the control on the type of persisting oxygen functionalities is difficult. In addition, too many oxygen functionalities drastically deteriorates the electrical conductivity (graphene oxide has 30wt% oxygen and is an electric insulator). Consequently, a new pillar was synthesized to allow for a larger pillared content and for additional pseudocapacitive trait without compromising the system's electrical conductivity. The pillar consisted of a ferrocene complex chemically modified with two (-CH_2NH_2) groups, one per each cyclopentadiene (Figure IV.1). This product was synthesized and obtained in high yield thanks to the great organic chemistry work of **Mr. Yves Chenavier** and the help of **Dr. Amélie Kochem**. This pillar was designed to bridge graphene sheets together through the reactions between its amines and the various oxygen functional groups on the surface of the sheets. Also, π-π interactions between the sp^2 carbons of the graphene sheets and the cyclopentadiene of the ferrocene complex might allow for favorable interactions between the two entities. These two forecasted types of interaction are expected to lead to more robust pillars and/or to a higher density of pillars, which might result in more efficient inhibition of the restacking of the rGO sheets.

Pillaring was done following the previously described procedure: first, functionalization took place and then the samples were reduced, according to Figure (IV.1). The pillar is called Ferrocenedimethylamine and was abbreviated as (FDA), thus, the pillared material is called RP-FDA.

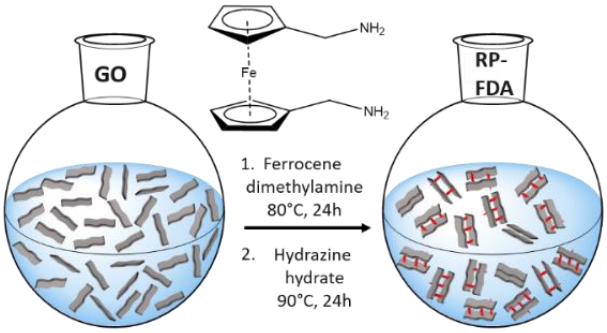

Figure IV. 1 : Synthesis procedure of RP-FDA

The detection of Fe in its oxidized form (Fe^{2+}), as shown from the Fe2p3/2 HR-XPS spectrum (Figure IV.2), confirms the presence of the ferrocene moiety.

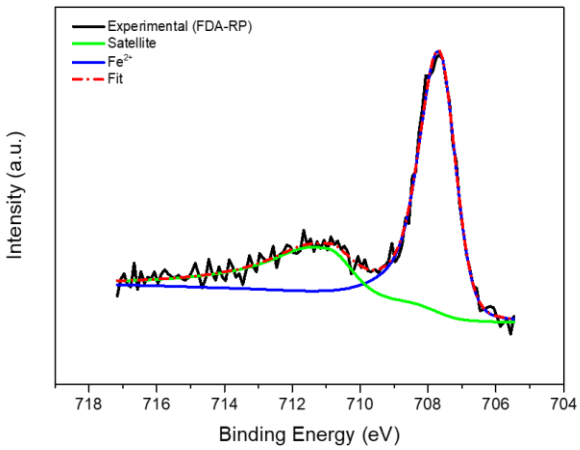

Figure IV. 2 : Peak fitting of HR-XPS Fe2p3/2 spectrum of RP-FDA

XRD was carried out on such sample and was compared to that of non-pillared rGO (Figure IV.3). It can be clearly seen that the RP-FDA sample does not show a strong rGO peak as the one appearing in rGO corresponding to a d-spacing of 0.37 nm. Instead, it is showing a main peak corresponding to a d-spacing of 0.57 nm, a small broad peak corresponding to a d-spacing of 0.44 and a tiny graphitic peak, corresponding to a d-spacing of 0.34 nm as evidenced from the peak fitting done on HighScore Plus software.

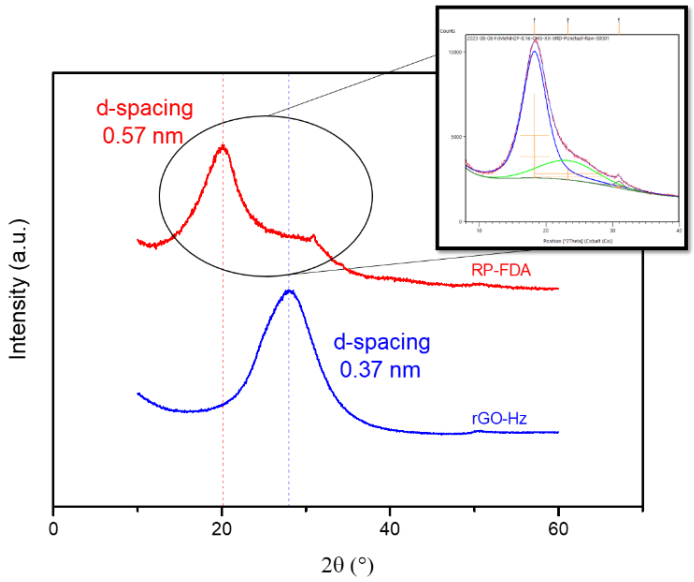

Figure IV. 3 : : The XRD profiles of rGO (—) and RP-FDA (—). Insert: Fitting of the XRD peak of RP-FDA using HighScore Plus software

Such an XRD profile of the pillared sample shows the success of the pillaring strategy in inhibiting the formation of rGO particles, leading to a nearly monophasic material with a d-spacing of 0.57 nm. The XRD peak fitting through HighScore Plus shows the presence of 2 different d-spacing values, which might be a consequence of 2 different orientations of the pillar inside the sample. It is more probable that the more abundant orientation is the one in which the ferrocene complexes are sitting between the rGO sheets through π-π interactions.

Electrochemical testing of these materials was done in 3M H_2SO_4 and preliminary results were obtained. The CVs at 5 mV/s are displayed in Figure (IV.4). The redox peaks of ferrocene are quite visible, further proving its presence inside the structure. Those peaks are attributed to the reversible oxidation of Fe^{2+} into Fe^{3+} as depicted in Figure (IV.4).

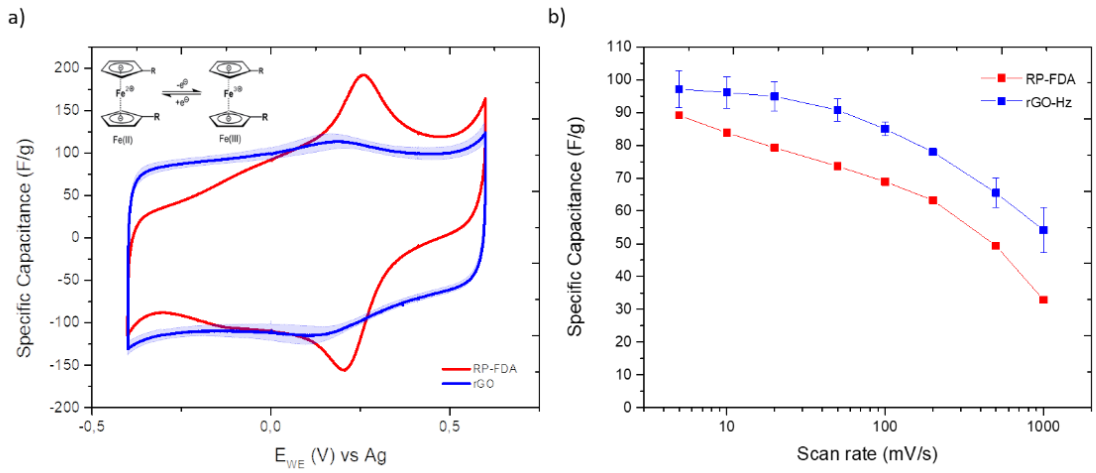

Figure IV. 4 : a) Cyclic voltammograms at 5mV/s and b) rate capability of rGO (—) and RP-FDA (—) in 3M H_2SO_4

The electrochemical performance of RP-FDA was not up to par with that of rGO-Hz as evidenced from its poor performance at all scan rates as seen from the rate capability plot (Figure IV.4(b)). Such a poor performance can be assigned to high loading of FDA (roughly estimated to be 40 wt%) that could have led to clogging the pores of the sample or could have adsorbed on the surface, screening the carbon below from the electrolytic ions, thus, decreasing the double layer capacitance. In literature, loadings of anthraquinone molecules that are more than 7 wt.% lead to a significant drop in the double layer capacitance for the reasons mentioned above [1], [2]. Accordingly, the experiments have to be repeated with lower loading of FDA as to find the sweet spot between maintaining the double layer capacitance of rGO and successfully prohibiting the π-π stacking. Nevertheless, the incorporation of ferrocene in the structure was proved and the complete inhibition of the XRD rGO peak was successfully demonstrated.

IV.2.2 Transferring the L-AA reduction Knowledge to Pillared Graphene Assemblies

The reduction of GO using L-AA was proven to be a green efficient alternative to that done using Hz. Transferring the knowledge obtained on this matter to reducing pillared graphene samples is of great importance to the work presented in this manuscript. Accordingly, preliminary experiments were done in that direction.

Based on the findings presented in Chapter 3, L-AA was selected to reduce pillared samples and the conditions of reduction were selected based on the sample giving the best electrochemical performance. Thus, a reduction using 0.04eq of L-AA for 24 hours was applied to the pillared graphene oxide sample. The synthesis of 6RP and 7RP-NCH3 were attempted according to the scheme shown in Figure (IV.5). The functionalization of graphene oxide is done in the 1st step, followed by the reduction during the 2nd one (either with Hz or L-AA).

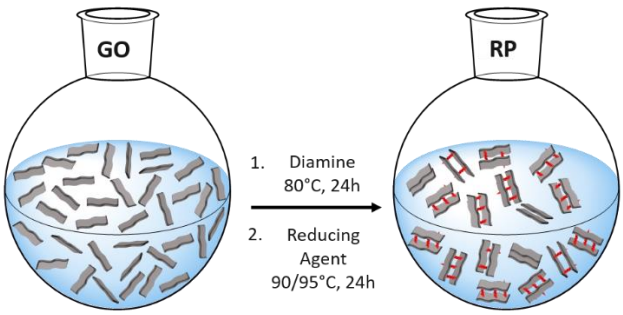

Figure IV. 5 : General scheme of the synthesis procedure of the pillared samples

Following the synthesis, XPS analysis was done to compare the chemical composition of the samples synthesized (6RP-Hz, 6RP-VitC, 7RP-NCH3-Hz and 7RP-NCH3-VitC). The at.%

values were transformed into wt.% in order to account for the N content coming from the insertion of N functionalities in the graphitic sheets when Hz is used for reduction. The results are summarized in the Table (IV.1).

Sample	C (wt. %)	N (wt. %)	O (wt. %)	C/O
7RP-NCH3-VitC	78.71	7.38	13.9	5.7
7RP-NCH3-Hz	82.78	6.69	10.53	7.9
6RP-VitC	78.84	5.53	15.63	5
6RP-Hz	81.9	4.86	13.2	6.2

Table IV. 1 : C, N and O content, in weight %, of 6RP-Hz, 6RP-VitC, 7RP-NCH3-Hz and 7RP-NCH3-VitC along with their associated C/O ratio

From Table (IV.1), the C/O ratios confirm the different reducing capabilities of the samples. It seems that the pillared samples reduced with L-AA have more oxygen than those reduced with Hz, which is consistent with the results showed earlier. The C/O ratios were calculated, assuming similar pillaring degree as seen from close N content values.

XRD was done to check for the success of the pillaring and calculate the inter-layer distance (Figure IV.6).

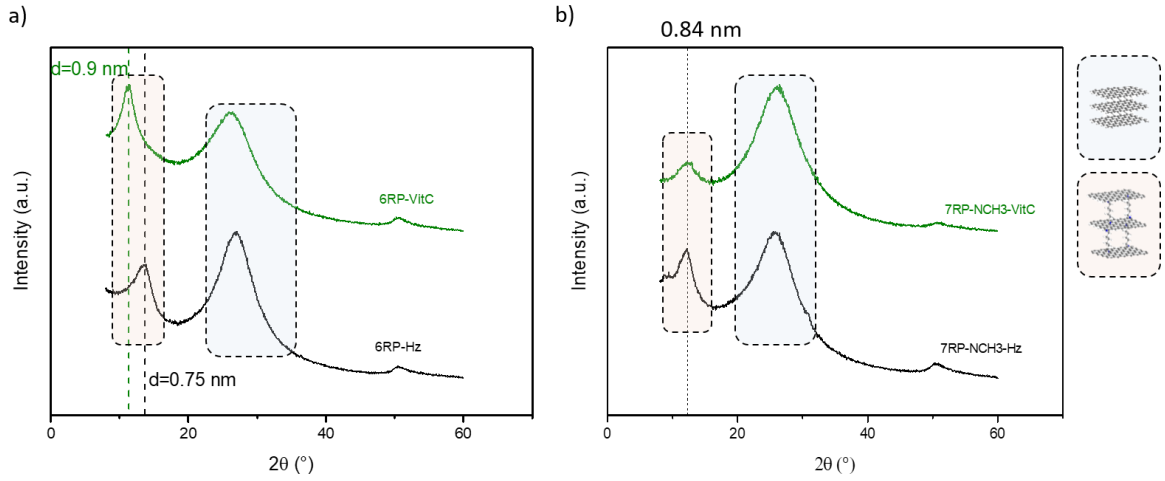

Figure IV. 6 : a) XRD profiles of 6RP-Hz (—) and 6RP-VitC (—), and b) XRD profiles of 7RP-NCH3-Hz (—) and 7RP-NCH3-VitC (—)

The XRD profiles of both 6RP samples show differences in the peak position of both the graphitic peak (highlighted in light blue) and the CL peak (highlighted in light orange). The 6RP-VitC sample is showing larger d-spacing values for the graphitic and the pillared domains. This might be attributed to the higher oxygen content in the sample, leading to larger d-spacing due to repulsive forces before surface oxygen groups. On the other hand, the 7RP-NCH3 samples show great similarities in their XRD profiles. Both the G and CL peaks are appearing at the same 2θ values, indicating same d-spacing values. Such difference in behavior between 6RP and 7RP-NCH3 can be explained by the lower amount of oxygen groups in the 7RP-NCH3

samples compared to 6RP samples as well as the longer d-spacing offered by the pillars of 7RP-NCH3. The lower amount of oxygen means less repulsive forces and the longer spacing can mitigate those repulsive forces between the surface oxygen groups at different rGO sheets.

Electrochemical testing was done on the 6RP samples in 3M H_2SO_4 and on 7RP-NCH3 samples in 1M KNO_3. The CVs at 5 mV/s and rate capabilities of the samples are shown in Figure (IV.7). In both electrolytes, it is clear that the shape of the CVs of the L-AA reduced pillared samples are similar to those of the Hz reduced pillared samples. This indicates similar charge storage mechanism in both electrolytes and similar redox reactions taking place in 3M H_2SO_4. However, the rate capability of the L-AA reduced pillared samples is poorer than that of Hz reduced pillared samples.

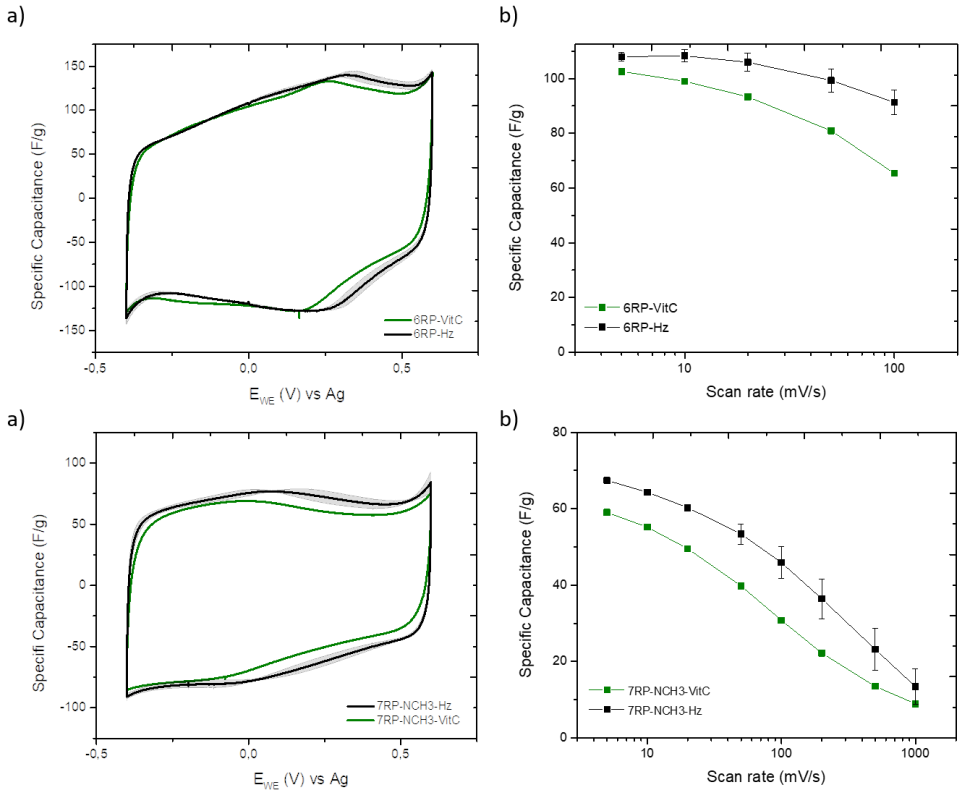

Figure IV. 7 : Cyclic voltammograms at 5mV/s and rate capability of (a,b) 6RP-Hz and 6RP-VitC, and (c,d) 7RP-NCH3-Hz and 7RP-NCH3-VitC

Such a discrepancy in the capacitance values at different scan rates needs extra experiments for reproducibility validation and further characterizations to be able to relate these differences to certain properties, which in turn can allow fine-tuning the reduction conditions. For instance, if the electrical conductivity of such L-AA reduced pillared samples is the impeding parameter, other reduction conditions can be used, leading to higher electrical conductivity values.

The loss in performance must be weighed against the health and environmental conditions associated with the use of Hz. Regardless, this is a proof of concept concerning the viability of

reducing pillared graphene samples using L-AA and the use of these electrodes as greener alternatives to their Hz reduced counterparts.

IV.3 Closing Remarks

Since materials' properties have a profound impact on their performances as electrode materials for supercapacitors and because of the complex nature of pillared graphene materials, researchers have to correlate PGM properties to their electrochemical performances in order to optimize the final materials and reach enhanced storage performances. To achieve that, advanced characterization techniques are to be employed and their results are to be analyzed hand-in-hand with those from the frequently used ones. For example, TEM images and XRD diffractometer could be advantageously combined to investigate the d-spacing through obtaining data from the real and reciprocal spaces, respectively. When inter-graphene sheets distance is too large that the cross-linked peak is observed at too low 2θ values, other characterization methods have to be used to confirm cross-linking such as Wide Angle X-Ray Scattering (WAXS). Investigation of the multi-scale porosity could be established using combined Small and Wide Angle X-Ray and Neutron Scattering (SAXS-WAXS & SANS-WANS) analyses [3], [4]. Fleischmann, S. et al. explained that the next step would be to study in-situ the diffusion of electrolytic species in these confined 2D porosity at the very local scale using Quasi-Elastic Neutron scattering (QENS) analysis, alongside solid-state NMR [5]. Regarding composition and structural modifications upon cycling, in-situ and operando analysis such as in-situ NMR, operando X-ray diffraction, X-ray absorption and scattering experiments would help relate these electrochemical performances to cyclability and sample evolution [6]. Revolutionary techniques like EQCM [7] and SECM [8] analysis would enable identifying the species involved in the charge storage mechanism and relating macro-scale performances to local dynamics. In-situ/operando Atomic Force Microscopy (AFM) and dilatometry can also be combined to investigate the relation between the electrochemistry and the mechanics of such samples. In-situ and operando AFM can also be used to investigate local electrochemical processes [9]. Raman spectroscopy can be utilized to probe the electrode electrolyte interface under dynamic conditions [10].

Apart from characterization techniques that help in relating the property to the performance, pillared graphene material development efforts have to be fostered. The advancements on the material side can include the use of new pillars and more efficient synthetic procedures, particularly and importantly greener, safer, and cheaper ones. The experimental efforts also need to work in tandem with equally motivated theoretical ones, such as DFT calculations and ab initio molecular dynamics, to validate and explain the experimental results in order to

elucidate the charge storage mechanism, electronic structure of materials and ion dynamics inside different pores. Also, the booming fields of Artificial Intelligence (AI), machine learning and big data have to be capitalized on. For instance, Deebansok, S. et al. are using supervised machine learning to differentiate between capacitive and battery materials (pre-print [11]). AI and machine learning can be used to propose new pillars and new grafting methods or conditions, thus, saving lot of time and effort usually lost in trial and error experiments. All of this would remain ink on paper without the motivation, determination and creativity of today's researchers and their honest unselfish willingness to collaborate to push forward science and technological advancements.

IV.4 References

[1] G. Pognon, T. Brousse, and D. Bélanger, 'Effect of molecular grafting on the pore size distribution and the double layer capacitance of activated carbon for electrochemical double layer capacitors', *Carbon*, vol. 49, no. 4, pp. 1340–1348, Apr. 2011, doi: 10.1016/j.carbon.2010.11.055.

[2] M. Deschanels, F. Favier, O. Fontaine, and S. L. Vot, 'Electrochemical evidence of the modification of carbon materials with anthraquinone moiety by a Diels Alder process', *Electrochimica Acta*, vol. 361, p. 137027, Nov. 2020, doi: 10.1016/j.electacta.2020.137027.

[3] D. Saurel *et al.*, 'A SAXS outlook on disordered carbonaceous materials for electrochemical energy storage', *Energy Storage Materials*, vol. 21, pp. 162–173, Sep. 2019, doi: 10.1016/j.ensm.2019.05.007.

[4] S. Boukhalfa *et al.*, '*In Situ* Small Angle Neutron Scattering Revealing Ion Sorption in Microporous Carbon Electrical Double Layer Capacitors', *ACS Nano*, vol. 8, no. 3, pp. 2495–2503, Mar. 2014, doi: 10.1021/nn406077n.

[5] S. Fleischmann, M. A. Spencer, and V. Augustyn, 'Electrochemical Reactivity under Confinement Enabled by Molecularly Pillared 2D and Layered Materials', *Chem. Mater.*, vol. 32, no. 8, pp. 3325–3334, Apr. 2020, doi: 10.1021/acs.chemmater.0c00648.

[6] S. Fleischmann *et al.*, 'Continuous transition from double-layer to Faradaic charge storage in confined electrolytes', *Nat Energy*, vol. 7, no. 3, Art. no. 3, Mar. 2022, doi: 10.1038/s41560-022-00993-z.

[7] W.-Y. Tsai, P.-L. Taberna, and P. Simon, 'Electrochemical Quartz Crystal Microbalance (EQCM) Study of Ion Dynamics in Nanoporous Carbons', *J. Am. Chem. Soc.*, vol. 136, no. 24, pp. 8722–8728, Jun. 2014, doi: 10.1021/ja503449w.

[8] A. Sumboja, U. M. Tefashe, G. Wittstock, and P. S. Lee, 'Investigation of Charge Transfer Kinetics of Polyaniline Supercapacitor Electrodes by Scanning Electrochemical Microscopy', *Advanced Materials Interfaces*, vol. 2, no. 1, p. 1400154, 2015, doi: 10.1002/admi.201400154.

[9] Q. Gao, W.-Y. Tsai, and N. Balke, 'In situ and operando force-based atomic force microscopy for probing local functionality in energy storage materials', *Electrochemical Science Advances*, vol. 2, no. 1, p. e2100038, 2022, doi: 10.1002/elsa.202100038.

[10] R. Vicentini *et al.*, 'Raman probing carbon & aqueous electrolytes interfaces and molecular dynamics simulations towards understanding electrochemical properties under polarization conditions in supercapacitors', *Journal of Energy Chemistry*, vol. 60, pp. 279–292, Sep. 2021, doi: 10.1016/j.jechem.2021.01.003.

[11] S. Deebansok *et al.*, 'A Novel Approach for Classifying Battery and Pseudocapacitor Materials Using Capacitive Tendency and Supervised Machine Learning', 2023, doi: 10.21203/rs.3.rs-2930525/v1.

Materials and Methods

Chapter 5: Materials and Methods

Herein, the synthesis of the various materials are detailed along with the various characterization and electrochemical techniques employed in the studies presented in chapters 2 and 3. The synthesis procedures of the following samples are detailed:

- Graphene Oxide (GO)
- Reduced Graphene Oxide via Hydrazine (rGO-Hz)
- Pillared Graphene Materials (PGM)
    - PGM, pillared with 1,6-diaminohexane (6RP)
    - PGM, pillared with 3,3′-Diamino-N-methyldipropylamine (7RP-NCH3)
    - PGM, pillared with 2,2’-(ethylenedioxy)bis(ethylamine) (8RP-OO)
- Hydrothermally reduced Graphene Oxide (GHG)
- Reduced Graphene Oxide via L-ascorbic acid (rGO-VitC)

The characterization techniques are detailed in terms of the specifications of the instruments used and the conditions of the measurements. The techniques include:

- Solid state NMR (ssNMR)
- X-ray Phototelectron Spectroscopy (XPS)
- Elemental Analysis (EA)
- Thermal Gravimetric Analysis (TGA)
- Fourier-Transform Infrared spectroscopy (FT-IR)
- X-ray Diffraction (XRD)
- Raman Spectroscopy
- Electron Paramagnetic Resonance (EPR)
- Scanning Electron Microscopy (SEM)
- Transmission Electron Microscopy (TEM)
- Water Contact Angle measurement (WCA)
- Electrical Conductivity measurement

Electrochemical analysis are detailed after, including the specificities of the 3-electrode Swageloks® cells utilized, the electrode preparation method, the electrolytes used, the electrochemical sequence adopted and the data treatment.

V.1 Materials Synthesis

V.1.1 GO synthesis

Graphite nanopowder (CAS #7782-42-5 - 400 nm APS, 99.9% purity) was bought from Nanostructured & Amorphous Materials Inc. and washed with hexane and ethyl acetate prior to using to removing any possible contaminants adsorbed on the surface of the graphite sheets. Concentrated sulfuric acid (CAS #7664-93-9 - 95-97%) and Hydrochloric acid (CAS #7647-01-0 - 37% solution) were bought from Sigma Aldrich, Sodium Nitrate (CAS #7631-99-4 - 99.7%) and Hydrogen Peroxide (CAS #7722-84-1 - 30% solution) were bought from VWR Chemical and potassium permanganate (CAS #7722-64-7 - 99%) was bought from OSI France and used as received without further purification.

3.0 g of graphite was added to a 1L beaker in an ice bath, followed by 90 ml of concentrated sulfuric acid. The mixture was kept under stirring till the temperature dropped around 4°C. At such temperature, 1.5 g of sodium nitrate was added and the mixture was left to stir for 2 h, while ensuring the temperature did not exceed 5°C. Then, 9.1 g of potassium permanganate was very slowly and carefully added not to increase the temperature above 4-5°C, and the mixture was left to stir for 90 min while maintaining the temperature between 0 and 3°C. The beaker was then removed from the ice bath and left to reach room temperature. Afterwards, 100 ml of milliQ water (18MΩ) was added slowly using a Pasteur pipette controlling that the temperature would not exceed 95°C. Then the temperature was set to 95°C and the mixture was left to stir for 2 h. The color changed from purple to brown during the course of the addition of the 100 ml of milliQ water. Another 300 ml of milliQ water was added to the mixture and the mixture was left to stir for 90 more minutes at 95°C. The heating was stopped and the mixture was allowed to cool down to room temperature. Then, 30 ml of 30% hydrogen peroxide solution was added and the mixture was left to stir for 30 min before adding 450 ml of milliQ water and leaving the mixture overnight under stirring.

Then, the brown mixture was filtered under vacuum on cellulose filter paper using fritted funnels. The precipitate was collected and re-dispersed in a 1L beaker using 900 ml of milliQ water. This suspension was then sonicated for 1 h in a water sonication bath. Afterwards, 100 ml of 37% hydrochloric acid was added and the mixture was left to stir overnight.

The upcoming steps are summarized in Figure (V.1) and detailed below. These steps were carried out to remove any acid molecules remaining, except for the last step which was meant for size selection. The size selection is carried out to remove the un-oxidized graphite as well as the less oxidized large graphene oxide sheets.

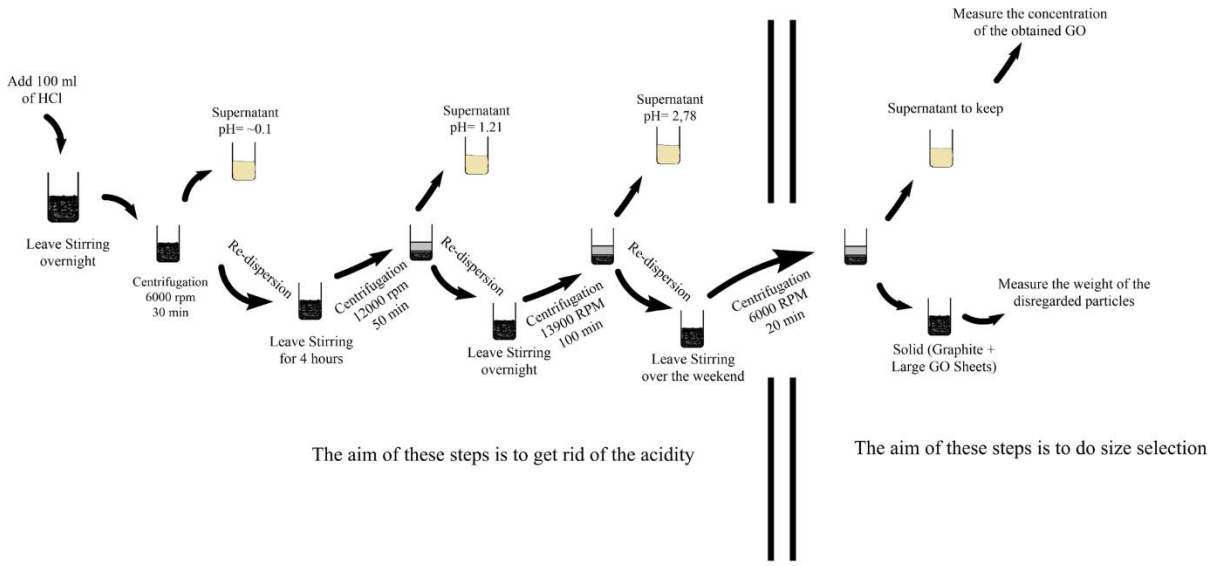

Figure V. 1 : Steps for acidity removal and size selection

Subsequently, the mixture was centrifuged at 6000 rpm for 30 min and the precipitate was re-dispersed using a volume of milliQ water between 800 and 1400 ml before being left to stir for 3 h and 20 min. The pH of the supernatant of the 1st centrifugation was measured to be 0.32 before being discarded. Another centrifugation was done, at 12000 rpm for 50 min. The pH of the supernatant was found to be 1.46, the precipitate was re-dispersed in a volume of milliQ water between 800 and 1400 ml and then left to stir overnight.

Then further centrifugation was done at 13900 rpm for 100 min followed by measuring the pH of the supernatant (2.7) and re-dispersing the precipitate with a volume of milliQ water between 800 and 1000 ml. The mixture was then left to stir over the week-end.

Finally, the mixture was centrifuged at 6000 rpm for 20 min. Afterwards, the supernatant was kept while the precipitate was discarded. A 25 ml aliquot was drawn from the supernatant for freeze drying. The freeze dried sample was weighed and the concentration was calculated. The concentration is to be adjusted to 5 mg/ml by adding water or evaporating water using a rotary evaporator in case the concentration was higher or lower than 5 mg/ml, respectively. The GO in water dispersion was stored in a bottle in a dark place away from light to avoid self-reduction of epoxides.

V.1.2 rGO-Hz synthesis

Hydrazine hydrate (CAS #10217-52-4 - 50-60%) was bought from Sigma Aldrich and used as received with no further purifications.

12.5 ml of hydrazine hydrate was added to 75 ml of 5 mg/ml GO in water dispersion and the mixture was left to stir at 90°C for 24 h under reflux. Then, the mixture was filtered

under vacuum on an ash-less cellulose filter paper (ash content < 0.01 %) using a P4 fritted glass funnel. The produced powder was then washed with copious amounts of milliQ water to remove any traces of hydrazine, then washed with ethanol followed by a last wash with absolute ethanol. The sample was then left overnight to dry at 80°C in an oven under the fume hood. The product was weighed and found to be 175 mg. The sample was stored in a desiccator with silica beads.

V.1.3 Pillared Graphene Materials (PGM)

1,6-diaminohexane (CAS #124-09-4 - 98%) and Hydrazine hydrate (CAS #10217-52-4 - 50-60%) were bought from Sigma Aldrich and 3,3′-Diamino-N-methyldipropylamine (CAS #105-83-9 - >98%) and 2,2'-(ethylenedioxy)bis(ethylamine) (CAS #929-59-9 - >98%) were bought from TCI Chemicals. The 3,3′-Diamino-N-methyldipropylamine and 2,2'-(ethylenedioxy)bis(ethylamine) were stored into multiple glass sealed ampoules under argon gas as they are air sensitive liquids. No further purifications were carried out prior to the use of these chemicals.

V.1.3.1 6RP Synthesis

The synthesis was done in two steps: chemical functionalization followed by chemical reduction. For the functionalization, 0.99 g (8.49 mmol) of 1,6-diaminohexane was dissolved in 105 ml of absolute ethanol in a 250 ml round bottom flask. Then, 105 ml of 5 mg/ml GO in water dispersion was added and the mixture was stirred at 80°C for 24 h under reflux. Then, the mixture was filtered under vacuum on an ash-less cellulose filter paper (ash content < 0.01 %) using a P4 fritted glass funnel. The solid sample was then washed with ethanol, milliQ water and finally absolute ethanol before being left to dry for 1 h at 80°C in an oven.

The functionalized sample was then transferred to a round bottom flask. 28 ml of hydrazine hydrate was added to the sample and the mixture was left to stir at 90°C for 24 h under reflux. Afterwards, the mixture was filtered under vacuum on an ash-less cellulose filter paper (ash content < 0.01 %) using a P4 fritted glass funnel. The sample was then washed with copious amounts of milliQ water to remove any traces of hydrazine, then washed with ethanol followed by a final wash with absolute ethanol. The sample was then left overnight to dry at 80°C in an oven under the fume hood. The product was weighed and found to be ~330 mg. The sample was stored in a desiccator with silica beads.

V.1.3.2 7RP-NCH3 Synthesis

The synthesis was done in two steps: chemical functionalization followed by chemical reduction. For the functionalization, 1456 µL (9.03 mmol) of 3,3′-Diamino-N-methyldipropylamine was added to 30 ml of 5 mg/ml GO in water dispersion in a 100 ml round

bottom flask. Then, the mixture was stirred at 80°C for 24 h under reflux. Then, the mixture was filtered under vacuum on an ash-less cellulose filter paper (ash content < 0.01 %) using a P4 fritted glass funnel. The solid sample was then washed with ethanol, milliQ water and finally absolute ethanol before being left to dry for 1 h at 80°C in an oven.

The functionalized sample was then transferred to a round bottom flask. 10 ml of hydrazine hydrate was added to the sample and the mixture was left to stir at 90°C for 24 h under reflux. Subsequently, the mixture was filtered under vacuum on an ash-less cellulose filter paper (ash content < 0.01 %) using a P4 fritted glass funnel. The sample was then washed with copious amounts of milliQ water to remove any traces of hydrazine then washed with ethanol followed by a final wash with absolute ethanol. The sample was then left overnight to dry at 80°C in an oven under the fume hood. The product was weighed and found to be ~80 mg. The sample was stored in a desiccator with silica beads.

V.1.3.3 8RP-OO Synthesis

The synthesis was done in two steps: chemical functionalization followed by chemical reduction. For the functionalization, a 330 µL (2.26 mmol) of 2,2'-(ethylenedioxy)bis(ethylamine) was added directly to a 30 ml of 5 mg/ml GO in water dispersion in a 100 ml round bottom flask. Then, the mixture was stirred at 80°C for 24 h under reflux. Then, the mixture was filtered under vacuum on an ash-less cellulose filter paper (ash content < 0.01 %) using a P4 fritted glass funnel. The solid sample was then washed with ethanol, milliQ water and finally absolute ethanol before being left to dry for 1 h at 80°C in an oven.

The functionalized sample was then transferred to a round bottom flask. 10 ml of hydrazine hydrate was added to the sample and the mixture was left to stir at 90°C for 24 h under reflux. Subsequently, the mixture was filtered under vacuum on an ash-less cellulose filter paper (ash content < 0.01 %) using a P4 fritted glass funnel. The sample was then washed with copious amounts of milliQ water to remove any traces of hydrazine then washed with ethanol followed by a final wash with absolute ethanol. The sample was then left overnight to dry at 80°C in an oven under the fume hood. The product was weighed and found to be 92 mg.

V.1.4 GHG Synthesis

30 ml of 5 mg/ml GO in water dispersion was added to the Teflon inner container of an autoclave. The Teflon container was then put in a water sonication bath for 15 minutes before being put inside the hydrothermal autoclave reactor. The reactor was heated at 180°C for 17 h. The product was then washed for 30 min on a P3 fritted glass funnel with no filter paper and

no vacuum, while maintaining the product always covered with water. The product was then frozen using liquid nitrogen for 10 minutes followed by its freeze-drying in a lyophilizer for 2 days. The self-standing monolith was found to be weighing 77 mg. The sample was stored in a desiccator with silica beads.

V.1.5 rGO-VitC Synthesis

L-Ascorbic Acid (CAS #50-81-7 - 99%) was bought from Sigma Aldrich and Ammonia solution (CAS #1336-21-6 - 28% solution) was bought from BASF and both were used as received with no further purifications prior to use.

40 ml of 5 mg/ml GO in water dispersion was placed in a 250 ml round bottom flask followed by 200 ml of milliQ water (concentration of GO: 0.83 mg/ml). Two drops of 28wt.% ammonia solution was added to bring the pH between 9 and 10 (measured pH: 9.7). Then, 1.08, 2.72, 2.72 or 0.11 g of L-ascorbic acid was added to the mixture to make rGO-VitC-30min-0.4eq, rGO-VitC-30min-1eq, rGO-VitC-24hr-1eq or rGO-VitC-24hr-0.04eq, respectively. The mixture was left to stir at 95°C under reflux for 30 min for rGO-VitC-30min-0.4eq and rGO-VitC-30min-1eq and for 24 h for rGO-VitC-24hr-1eq and rGO-VitC-24hr-0.04eq. The mixture was then filtered under vacuum on an ash-less cellulose filter paper (ash content < 0.01 %) using a P4 fritted glass funnel. The produced powder was then washed with copious amounts of milliQ water and with ethanol. The sample was then transferred to a cellulose thimble to be inserted in a Soxhlet set-up to further remove any traces of L-ascorbic acid. The Soxhlet purification was done with milliQ water for 24 h. The samples were then dried in an oven at 80°C overnight. The samples were weighed and yielded 120, 115, 160 and 118 mg for rGO-VitC-30min-0.4eq, rGO-VitC-30min-1eq, rGO-VitC-24hr-1eq or rGO-VitC-24hr-0.04eq, respectively. The samples were stored in a desiccator with silica beads.

V.2 Characterization Techniques

V.2.1 Solid State NMR (ssNMR)

ssNMR experiments were done on a Bruker AVIII 400 MHz spectrometer equipped with 3.2 mm $^{1}H/^{13}C/^{79}Br/^{15}N$ triple channel Magic Angle sample Spinning (MAS) probe. $\{^{1}H-\}^{13}C$ Cross-Polarization (CP)MAS experiments were recorded using 100 kHz nutation for ^{1}H $\pi/2$ pulses with the MAS set to 12 kHz. A ramped (50-100%) power was utilized to match a Hartmann-Hahn CP condition when using 50 kHz for ^{13}C nutation during 2 ms CP spin-locking. A SWf-TPPM heteronuclear decoupling was employed during the free-induction decay (FID) acquisition. An acquisition of 6114 transients was recorded for the $\{^{1}H-\}^{13}C$ CPMAS experiments, using a recycle delay of 1.2 s between transients. The chemical shifts of the ^{13}C

spectra were calibrated using Adamantane. Topspin software was used for data acquisition and Origin software was used for plotting the ssNMR spectra.

V.2.2 X-Ray Photoelectron Spectroscopy (XPS)

The XPS analysis was done using a PHI Versa Probe II spectrometer with a monochromatized Al K_α X-ray source (1486.6 eV) with a beam size of 200 µm. The samples were loaded on a conductive Cu double-faced tape surrounded by Stainless Steel (SS) rings to facilitate replenishing the surface charge state. For insulating samples like GO, double charge compensation, involving the use of an electronic charge neutralizer and an electron gun, was applied. The samples were analyzed on areas of average 200 μm^2 under ultra-high vacuum. The survey spectra were acquired with a pass energy of 117.4 eV with a range from 0 to 1100 eV. The High Resolution (HR) spectra were acquired with a pass energy of 23.5 eV with ranges from 276 to 298 eV, 523 to 545 eV and 389 to 411 eV for C1s, O1s and N1s, respectively. X-ray induced secondary electron images (SXI) were recorded for each sample. The C1s sp^2/sp^3 peak at 284.3 eV was used as binding energy reference. The peak fitting was done using Multipak software. Origin software was used for plotting the survey and HR spectra along with their fitted peaks.

V.2.3 Elemental Analysis (EA)

EA experiments were performed on a UNICUBE® organic elemental analyzer (C, H, N and S) by Elementar. The samples were loaded in Sn boats and their masses were kept between 1.5 and 2 mg. Three sample-loaded Sn boats were prepared for each sample for statistical analysis. The samples were then introduced in the oven under He gas, then burnt at 1150°C in the presence of O_2, and the resulting gases were treated in a reduction tube at 850°C. The resulting gases then passed through an adsorption column where thermal programmed desorption took place at the following temperatures: 40°C for N_2, 60°C for CO_2, 150°C for H_2O and 210°C for SO_2. A thermoconductivity detector quantified the amounts of each element from the difference between the thermal conductivity of pure He gas and a mixture of He gas and the gas carrying the element of interest (ex. CO_2 for detection of C). Oxygen amount was then assumed to occupy the remaining weight percentage, after confirming the existence of only C, N and O from XPS. Origin software was used for plotting histograms of the C, H, N and O content of each sample.

V.2.4 Thermal Gravimetric Analysis (TGA)

TGA experiments were carried out using a Setaram TGA 92 equipment. The experiments were done under Ar gas from 30°C to 800°C with a heating ramp of 5 °C/min. Stabilization was done at 30°C for 30 minutes prior to heating to reach a stable mass before

carrying out the analysis. The number of moles of pillars per gram of sample was calculated from the weight loss recorded between the changes in slopes in the degradation profile before and after the degradation step of the pillars, as shown for 6RP in Figure (V.2). This weight loss is then corrected through subtracting the weight loss of rGO-Hz, in the same temperature region, from it to account for any oxygen losses taking place in such temperature range. Origin software was used for plotting the degradation profiles.

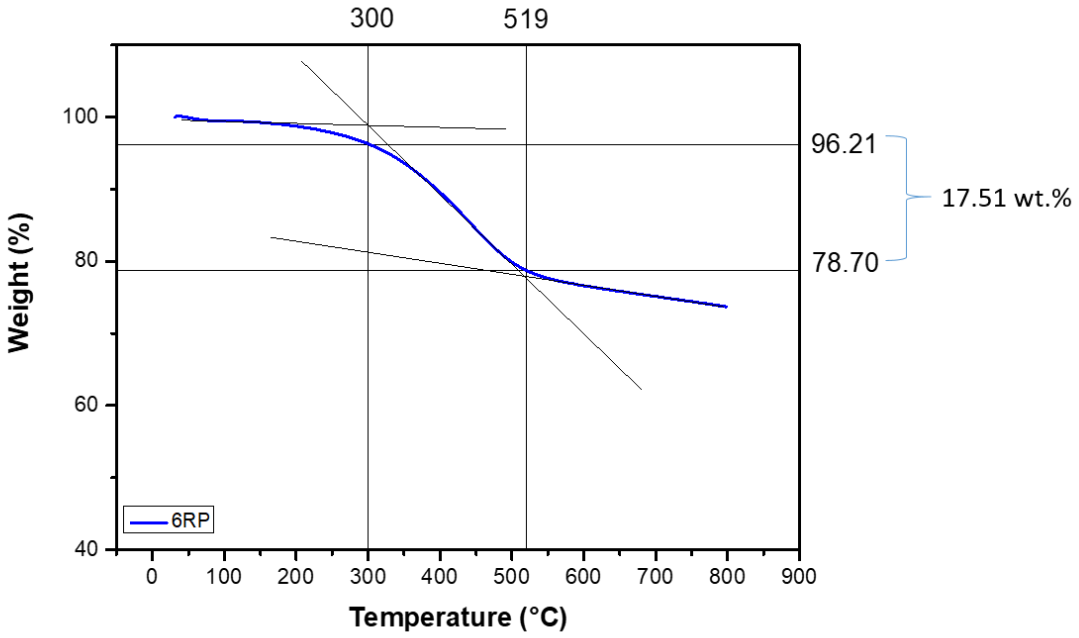

Figure V. 2 : TGA profile of the 6RP sample with the difference in weight % calculated from the changes in the slopes of the degradation profile before and after the degradation step

V.2.5 Fourier-Transform Infrared spectroscopy (FT-IR)

FT-IR experiments were done using a Thermofischer IS50 spectrometer in the Attenuated Total Reflectance (ATR) mode in the wavenumber range 400-4000 cm^{-1}. The background spectrum was recorded prior to measuring and the samples measurements were done through accumulating 32 scans. OMNIC software was used for data acquisition. Origin software was used for baseline correction and plotting the FT-IR spectra.

V.2.6 X-ray Diffraction (XRD)

XRD experiments were performed on a Panalytical X'pert PRO X-ray diffractometer using a Co Kα radiation source (λ=1.798 Å). The measurements were done in a θ-θ goniometer configuration in reflection mode. The samples analyzed were in the form of pellets of a diameter of 6 mm, weighing around 10-12 mg. The pellets were done through pressing the samples in a mold under 2 Tons of pressure for 15 min. The alignment prior to measurements were done using a 1/32 fixed slit, a 4 mm fixed mask, a 5 mm fixed mask and a programmable beam

attenuator Fe 0.1 m with an attenuation factor of 84.96 on the incident beam side and a 0.27 receiving slit on the detector side. A ponctuel 0-D detector was used. Alignments are done for 2θ (angle between incident and reflected beams), Ω (angle between incident beam and sample's surface) and z (the height of the sample holder stage). During measurements, the 1/32 fixed slit is replaced by 1/8 fixed slit, the attenuator is stopped and the 0.27 slit was removed. The measurement was done from 3° to 60° with a step size of 0.05°. The diffractograms of the various samples were fitted using HighScore to extract the d-spacing, peak position and FWHM of the peaks (Figure V.3). Origin software was used for plotting the diffractograms.

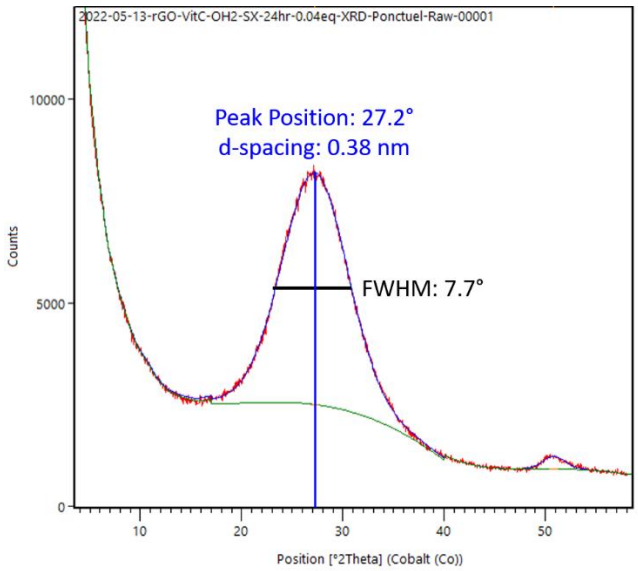

Figure V. 3 : An example of the 002 XRD peak fitting of rGO-VitC-24hr-0.04eq

V.2.7 Raman Spectroscopy

Raman spectroscopy experiments were carried out on a LabRam HR confocal Raman spectroscopy instrument by Horiba Scientific. The laser used was a red laser with a wavelength of 632.81 nm. The laser was warmed up for 30 minutes before each measuring session. The analysis was done in the range 200-3150 cm^{-1}. A silicon wafer was used for calibration prior to measurements. The analysis was done using a 100× long working distance optical objective with the sample mounted on a Märzhäuser scanning stage. A 600 grating was selected and an ND filter of 25% was selected to avoid local burning of the sample. The acquisition time was 100 s per scan and 4 scan were accumulated per sample (total 7:02 min). Each sample was investigated on 2 different zones. LabSpec 6 software was used for data acquisition. Origin software was used for background subtraction, peak fitting and plotting the Raman spectra.

V.2.8 Electron Paramagnetic Resonance (EPR)

EPR experiments were done on a Bruker EMX spectrometer equipped with Bruker ER4104OR EPR resonator. The analyzed aqueous solutions were transferred into a WG-

Wilmad 812-Q flat cell. The measurements were done with a microwave frequency of 9.65 GHz, a microwave Power of 20 mW, a modulation amplitude of 1.5 G and a time constant of 10 s for a total acquisition time of 18 min per sample. 1μM TEMPOL solution was used as a concentration reference. EasySpin MATLAB toolbox was used for simulating and fitting the EPR signals.

V.2.9 Scanning Electron Microscopy (SEM)

SEM Images were obtained using a Zeiss Ultra 55 electron microscope with an accelerating voltage of 3 kV. The samples were stuck on the sample holder using a two-faced conductive copper tape. No sputtering of a conductive layer was done. The Working Distance (WD) was adjusted per sample. An in-lens detector was used to detect Secondary Electrons (SE). SmartSEM software was used to control the instrument and for data acquisition.

V.2.10 Transmission Electron Microscopy (TEM)

TEM images were obtained via monochromated TEM imaging using a Titan Ultimate (Thermo Fisher) operating at 80 keV with an aberration corrector. The samples were dispersed in 1-propanol using an ultra-water bath sonication system. A Ti wire is folded to form a loop, which is dipped in the solution to extract a small drop. The loop is then put in contact with a Lacey carbon coated Cu grid, leading to the drop transfer onto the grid which is then left to dry in air for a while, before being transferred to the microscope equipment.

V.2.11 Water Contact Angle measurement (WCA)

WCA measurements were done using the Drop Shape Analyzer DSA25E by KRUSS inside a clean room with a measured ambient temperature of ~22°C. The samples analyzed were in the form of pellets of a diameter of 6 mm, weighing around ~15 mg. The pellets were done through pressing the samples in a mold under 2 Tons of pressure for 30 minutes. The drops were deposited manually using a syringe and the exact volume deposited was controlled through the ADVANCE software. At least 2 drops were deposited per sample and the contact angles were calculated over time using a circular model. The angles were then averaged and standard deviation was calculated.

V.2.12 Electrical Conductivity measurement

Electrical conductivity measurements were done using the four-point probe method. A low intensity current flows between the outer two probes, and the voltage is measured across the two inner probes. The samples analyzed were in the form of pellets of a diameter of 6 mm, weighing around 10-12 mg. The pellets were done through pressing the samples in a mold under

2 Tons of pressure for 15 minutes. The electrical conductivity was calculated according to the following equations:

$$R_s = \frac{V}{I} * CF \qquad (V.1)$$

$$\rho = R_s W \qquad (V.2)$$

$$\sigma = \frac{1}{\rho} \qquad (V.3)$$

Where R_s is the sheet resistance ($\Omega/square$), V is the measured voltage (V), I is the applied current (A), CF is a shape-related correction factor, ρ is the resistivity ($\Omega.m$), W is the thickness of the sample (m) and σ is the electrical conductivity (S/m). The shape-related correction factor is based on the ratio between different shape and probe related dimensions as shown in Figure (V.4). Such a correction factor was found to be 3.2 for our pellets.

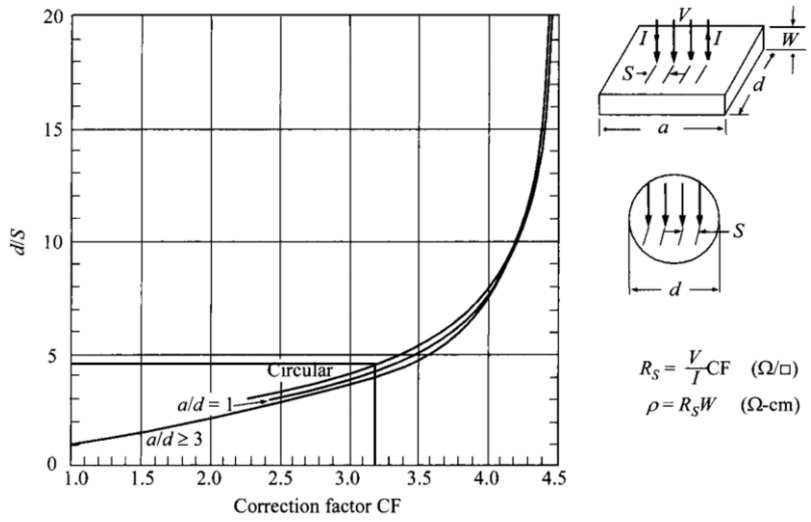

Figure V. 4 : The shape related correction factor for the electrical conductivity measurement using a four-point probe along with the CF of 3.2 corresponding to the diameter of the pellets used (Adapted from [1])

V.3 Electrochemistry

V.3.1 Electrode Preparation

The working electrode was prepared as follows: 80 wt% active material, 10 wt% PVDF as binder and 10 wt% acetylene black as conductive additive. An ultra-high precision balance (d = 0.01 mg) was used for weighing the different components. The mixture was ground in a mortar using a pestle for 15 min and then dispersed in NMP (150 µL per 10 mg of mixture) and homogenized with sonication in an ultra-sonication water bath for 15 min. The dispersion was then drop casted on Stainless Steel discs of 6.2 mm diameter (30 µL per SS disc), leading to loadings ~2 mg per electrode (corresponding to a loading density ~6.6 mg/cm^2). Such a method yielded homogenous electrodes with high reproducibility. Such a method was compared to the

slurry method in which the same constituents are wet ground together in a mortar with few drops of NMP and then transferred to the SS electrodes using a spatula before left to dry in the oven for an hour. The yielded electrodes are shown in Figure (V.5). The drop casting method shows full uniform coverage of the surface of the SS discs, in addition to being a consistent methodology that requires very small amount of NMP.

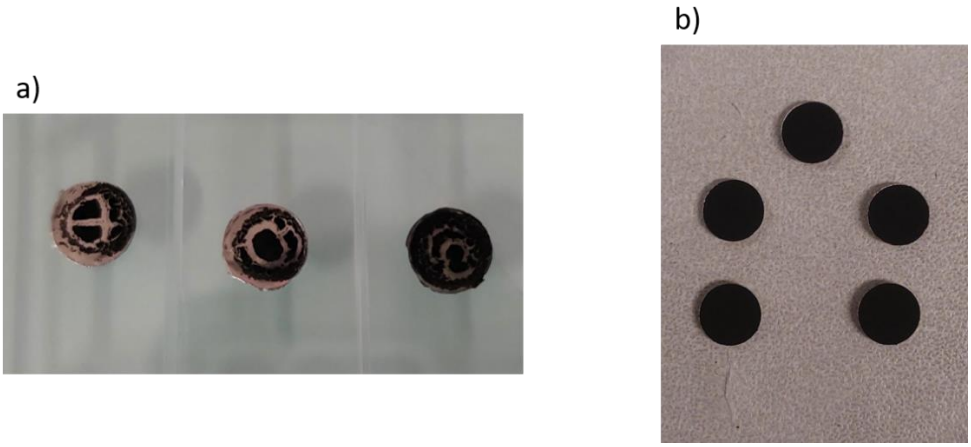

Figure V. 5 : Electrodes prepared through a) Slurry method and b) drop casting method

The Counter Electrode (CE) was prepared by mixing 80 wt% YP50, 15 wt% acetylene black as conductive additive and 5 wt% PTFE as binder. The mixture was then dispersed in a minimum amount of EtOH and left to stir till a dense dispersion is formed. Such a dispersion was then moved to a flat glass surface and was worked out with spatulas until a paste was formed. The paste was then spread on an aluminum foil and left to dry overnight in oven at 80°C. When necessary, the CE was cut into circles of 8 mm diameter.

V.3.2 Electrochemical Setup

Three-electrode Swagelok® Teflon cells (Figure V.6) were used. The WE was 80% active graphene-based material, 10% acetylene black and 10% PVDF drop casted on a SS disc as detailed in the previous section. The CE was YP50, ten times the mass of the WE so that it is not limiting. The RE was a pseudo-reference silver wire thinly coated with AgCl through dipping in 0.1M HCl for 5 s prior to use followed by its washing with milliQ water. Glass microfiber filter papers were used as separators. They were cut into 10 mm diameter circles and 2 separators were used per cell. The cells were assembled in the following order: i) the current collector is inserted in the Swagelok® Teflon cell, ii) the working electrode is inserted on the current collector, iii) two separators are added on top of the working electrodes, iv) drops of the electrolyte are added to the separators, v) the CE is positioned on top of the wet separators, followed by the second current collector, vi) the WE and CE sides are tightly sealed, vii) the cell is filled with electrolyte from the RE side and viii) the RE is tightly screwed into the cell.

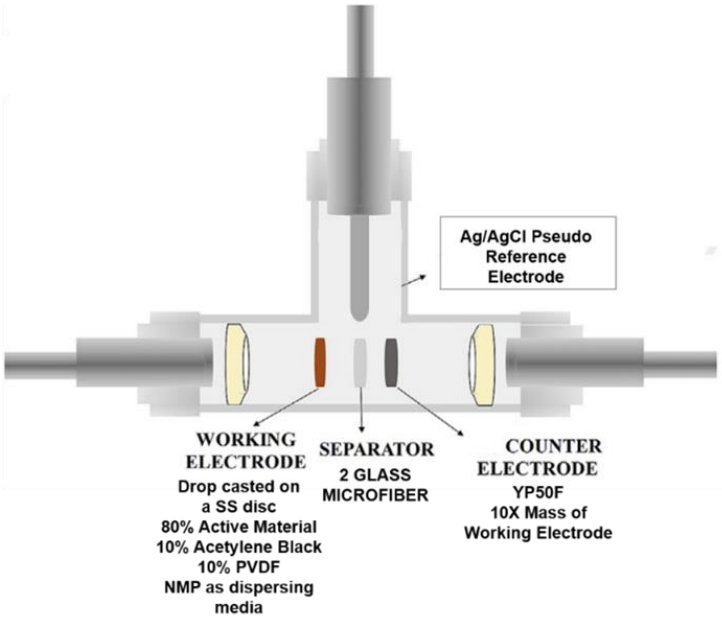

Figure V. 6 : A three-electrode Swagelok® cell configuration

V.3.3 Electrolytes

The aqueous electrolytes used for electrochemical testing were 3M H_2SO_4, 0.5M Li_2SO_4, 0.5M K_2SO_4, 1M KNO3 and 6M KOH. Concentrated sulfuric acid was added to milliQ water to reach the desired concentration while the salts of the other electrolytes were weighed and dissolved in milliQ water. The properties of these electrolytes can be summarized in the following table:

Electrolyte	Cation and its hydrated diameter size (nm)	Anion and its hydrated diameter size (nm)	Ionic Conductivity (mS/cm)	pH
3M H_2SO_4	H^+ 0.560*	SO_4^{2-} 0.758*/0.764**	721.7	−0.48+
0.5M Li_2SO_4	Li^+ 0.764*	SO_4^{2-} 0.758*/0.764**	42.2	6.77
0.5M K_2SO_4	K^+ 0.662*	SO_4^{2-} 0.758*/0.764**	71	6.44
1M KNO_3	K^+ 0.662*	NO_3^- Mean: 0.632** Axial: 0.53** Equatorial: 0.69**	80***	6.47
6M KOH	K^+ 0.662*	OH^- 0.600*	691****	14.8+

* from [2], ** from [3], *** from [4] and **** from [5]

+calculated

Table V. 1 : A summary of the properties of the aqueous electrolytes employed for electrochemical testing

V.3.4 Electrochemical Sequence

The Open Circuit Voltage (OCV) of the sample was measured before any cycling was done on the electrode. The electrode was then cycled through Cyclic Voltammetry (CV) at 50 mV/s for 300 cycles for stabilization as electro-wetting behavior has been evidenced. Figure

(V.7) displays the evolution of the CVs and capacitance during the stabilization of 7RP-NCH3 in 0.5M K_2SO_4, indicating ~17% increase in capacitance after 150 stabilization cycles at 50 mV/s, after which, the capacitance is stable. Afterwards, a chronoamperometry at the OCV was conducted for 1 min to set the potential to the OCV before carrying out the Electrochemical Impedance Spectroscopy (EIS). The EIS experiments were carried out at OCV in a frequency range from 10 mHz to 100 KHz with an AC perturbation of 10 mV. Following the EIS measurements, the samples were cycled through CV at 5, 10, 20, 50, 100, 200, 500 and 1000 mV/s for 10 cycles at each scan rate. Then galvanostatic charge and discharge was carried out at constant currents of 5, 10, 15, 20 and 50 mA. For the analysis of diffusion limited and non-diffusion limited contributions (Conway's method and Dunn's method), CVs were recorded at lower scan rates, such as 1, 2, 3 and 4 mV/s. The potential window for 3M H_2SO_4, 0.5M Li_2SO_4 and 0.5M K_2SO_4 was from -0.4 V to 0.6 V while that for 6M KOH was from -1 V to 0 V.

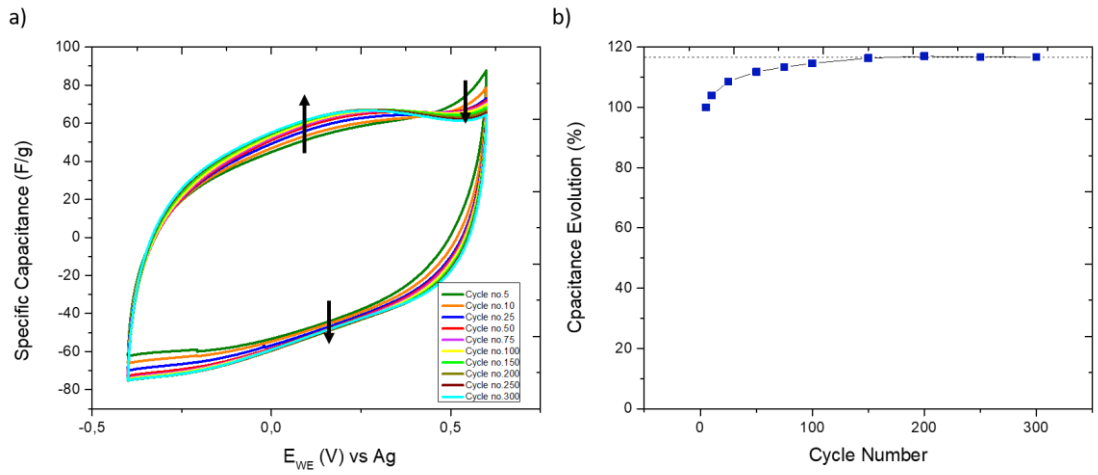

Figure V. 7 : a) The evolution of the CVs and b) The evolution of the capacitance during the 300 stabilization cycles of 7RP-NCH3 in 0.5M K_2SO_4 at 50 mV/s. The arrows indicate the direction of evolution with cycles

V.3.5 Electrochemical Data Treatment

The specific capacitance in F/g was calculated from the CVs according to the following equation:

$$C_s = \frac{\int_{V_1}^{V_2} I\, dV}{2 * \Delta V * s * m} \qquad (V.4)$$

Where C_s is the specific capacitance (F/g), V_1 and V_2 are the limits of the potential window (V), I is the current response (A), ΔV is the potential window (V), s is the scan rate (V/s) and m is the mass of the electrode (g). The nominator of Eq. (V.4) means integrating the whole area enclosed by the CV curve. Accordingly, a factor of 2 is added to the denominator. Such a calculation is done through a Matlab code written particularly for calculating i) the capacitance

and plotting the current density versus working electrode potential, ii) the specific capacitance versus working electrode potential and iii) the rate capability plot from an excel sheet containing the current and potential value of the cycles to be analyzed at different scan rates.

The specific capacitance was calculated from the GCD discharge curves according to the following equation:

$$C_s = \frac{I}{\frac{\Delta V}{\Delta t} * m} \qquad (V.5)$$

Where C_s is the specific capacitance (F/g), I is the constant applied current (A), $\frac{\Delta V}{\Delta t}$ is the rate of change of potential with respect to time (the slope of the discharge curve in a time versus potential plot) and m is the mass of the electrode (g). The slope is calculated through linear fitting the discharge curve, excluding the ohmic voltage drop region. The fitting was done manually through Origin software. An R^2 coefficient >0.99 was obtained for all the fittings.

Real and Imaginary capacitances were calculated based on Eq. (V.6) and Eq. (V.7) according to the complex model reported by Taberna, P.L. et al. [6].

$$C' = \frac{-Z''(\omega)}{\omega|Z(\omega)|^2} \qquad (V.6)$$

$$C'' = \frac{Z'(\omega)}{\omega|Z(\omega)|^2} \qquad (V.7)$$

Where C' and C'' are the real and imaginary parts of the capacitance, respectively; $Z'(\omega)$ and $Z''(\omega)$ are the real and imaginary parts of the impedance, respectively and ω is the angular frequency ($\omega = 2\pi f$ where f is the frequency). The real component of the capacitance (C') represents the capacitance of the electrode as a function of the frequency, thus, at low frequency, a capacitance value can be extracted, corresponding to that extracted from charge/discharge curves and CVs. The imaginary component of the capacitance (C'') corresponds to energy dissipation due to irreversible processes.

V.3.6 Conway and Dunn

Conway devised an empirical method where the current response at a certain potential (usually at peak potential, if any exists) follows the below power-law relationship with the scan rate.

$$i(v) = av^b \qquad (V.8)$$

Where $i(v)$ is the current response at a certain potential, a and b are adjustable constants and v is the scan rate. The values of a and b were extracted from plotting $\log(i)$ versus $\log(v)$ with b being the slope of such curve and $\log(a)$ is the y-intercept based on the following equation (obtained by taking the logarithm of both sides of Eq. (V.8)):

$$\log(i) = b\log(v) + \log(a) \qquad (V.9)$$

The extracted b values were used to give a quick indication of the electrode's kinetics. If b is equal to 0.5 ($i \propto v^{\frac{1}{2}}$), then the electrochemical reaction is dominated by diffusion processes and if b is equal to 1 ($i \propto v$), the capacitive non-diffusion limited process (surface-driven behavior) predominates. A b value between 0.5 and 1 represents the transition between battery-like kinetics to capacitor-like kinetics, respectively. A b value of 0.75 can indicate a spherical diffusion process while a value between 0.85 to 1 means that the non-diffusion limited contribution prevails over the diffusion-controlled one. [7], [8]

Dunn generalized Conway's method and proposed the uncoupling of the total current response at any potential value into two current responses as follows:

$$i = k_1 v^{\frac{1}{2}} + k_2 v \qquad (V.10)$$

Where $k_1 v^{\frac{1}{2}}$ is the diffusion limited contribution of the current response and $k_2 v$ is the non-diffusion limited contribution of the current response, with i being the current response, v being the scan rate and $k_1$and k_2 being constants. To get these contributions, the constants k_1 and k_2 were extracted through plotting $\frac{i}{v^{\frac{1}{2}}}$ versus $v^{\frac{1}{2}}$ to get k_1 as the y-intercept and k_2 as the slope according to Eq. (V.11).

$$\frac{i}{v^{\frac{1}{2}}} = k_1 + k_2 v^{\frac{1}{2}} \qquad (V.11)$$

This method was carried out at all potential values, giving insights on the different processes taking place at different potentials. CVs were recorded at slow scan rates (1, 2, 3, 4 and 5 mV/s) and were used for such calculations to avoid errors arising from ohmic drops occurring at high scan rates [9]. The plotting and fitting of Eq. (V.11) at all the potential values was done through a Matlab code, that takes the corresponding current values at 1, 2, 3, 4 and 5 mV/s at each potential point from an excel sheet of these values, plots $\frac{i}{v^{\frac{1}{2}}}$ versus $v^{\frac{1}{2}}$, does linear fitting to extract k_1 and k_2 and finally exports k_1 and $k_2 v^{\frac{1}{2}}$ values for all the 5 scan rates in an excel sheet.

V.3.7 Error Analysis

Error is a crucial parameter in data reporting and analysis in all fields of science and engineering. There are three different types of error in experimental fields: i) systematic error, ii) random error and iii) human error. Systematic error means that the error is consistent and happens in a certain direction, making it identifiable and thus can be corrected. An example is when a balance is reading 2 g in its tared mode, leading to all the measurements done by the balance to be off by extra 2 g. Such a problem can be identified and corrected through calibrating the balance. Random errors are errors that are hard to identify and takes place in all directions in a random non consistent fashion. For instance, when weighing a beaker multiple times successively, the balance gives different readings, whether higher or lower. Due to the random nature of such errors, it is hard to correct for them. Human errors are errors related to the human factor such as mis-reporting or mis-reading the values of a measurement. Scientists and researchers always aim at reducing the factors of errors through periodic instrument maintenance and calibration, establishing proper working conditions, and raising awareness of various sources of errors that they can encounter. Regardless of such vital and crucial efforts that help in error reduction, an error free environment is far from reality. However, further error mitigation can be done through reproducibility tests and reporting the average values when possible. More rigorous analysis and tracking the uncertainty of every single used instrument or measuring device are also possible and lead to more precise analysis; however, such a very rigorous analysis is time consuming and might not be necessary if such error values are negligible compared to the reported values. Looking at today's published scientific articles on supercapacitors, error is not given much attention when reporting the values of different energy storage metrics such as capacitance, energy density and power density. In literature, the highest values, I believe, are usually reported for these metrics. It is understandable that researchers would want to show the potential of their research and the impact their work might have on enhancing different energy storage parameters. However, the highest values are not necessarily representative of a sample's performance as they might be just outliers arising from different types of errors as mentioned above.

I believe that reproducing the experiments multiple times and reporting the average values along with their respective standard deviation instead of picking the highest values promotes scientific rigor and prevents misinterpretations. Such a way of reporting values leads to more trust in the reported values and allows the researchers to make proper interpretations and comparisons. The more the experiments are reproduced, the more realistic and precise the results are. However, it will take long time and will consume large amounts of materials to

reach such very high precision. This might impede the process of science development and generate much waste. Nevertheless, this does not justify the absence of reproducibility tests and/or the reporting of the average values. A compromise can be done through carrying out a reasonable number of trials to get more precise average values without consuming so much time and materials.

Therefore, herein, I decided to report the average value and standard deviation of the various electrochemical metrics extracted from cyclic voltammograms, galvanostatic charge and discharge and electrochemical impedance spectroscopy. The process starts with carrying out the electrochemical analysis on different electrodes of the same material. Then, the CVs of the various electrodes are selected based on their reproducibility so that we end up with at least three similar CV signatures. This means that irreproducible CVs are rejected even though they might correspond to higher capacitance values. Figure (V.8) shows the reproducible CVs of 6RP in 0.5M Li_2SO_4 and 7RP-NCH3 in 3M H_2SO_4. Consequently, the capacitance values for at least three samples with similar reproducible CVs are averaged and the standard deviation is calculated.

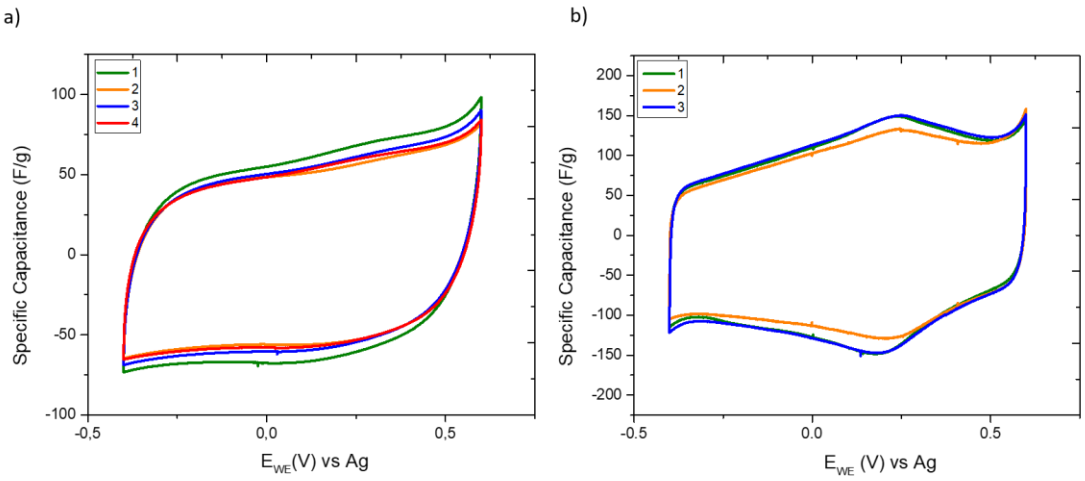

Figure V. 8 : Reproducibility of CVs of a) 6RP and b) 7RP-NCH3 in 0.5M Li_2SO_4

For plotting the CVs, the CVs are averaged and are plotted with their error bars illustrated with shaded areas, indicating the standard deviation, so that the visual presentation of the CVs is matching the reported values. Figure (V.9) shows the averaging process of CVs of 6RP in 0.5M Li_2SO_4 and 7RP-NCH3 in 3M H_2SO_4.

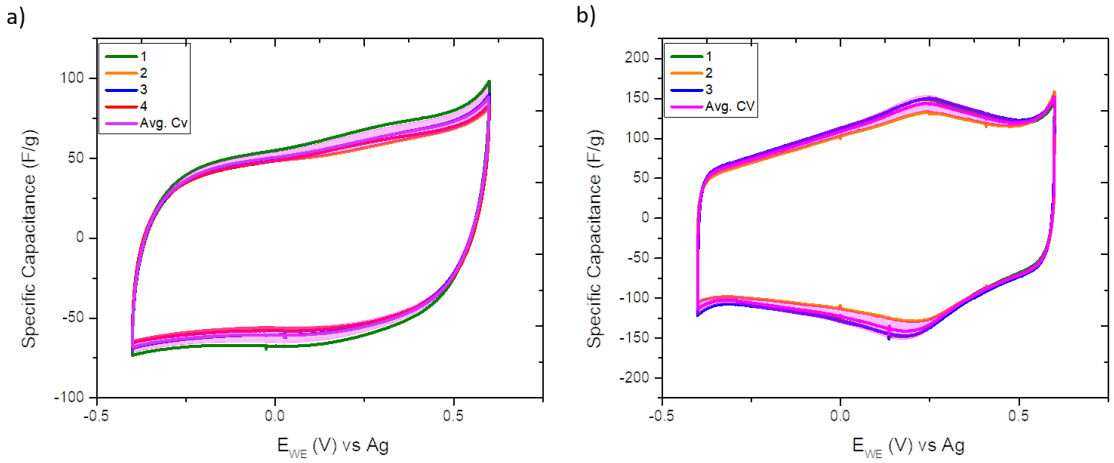

Figure V. 9 : Examples of CVs of different electrodes along with their average CV: a) 6RP in 0.5M Li_2SO_4 and b) 7RP-NCH3 in 3M H_2SO_4 along with the error bars displayed as shaded areas, representing standard deviation

For EIS, after selecting the electrodes based on their CV's reproducibility, their impedance data are treated to generate various plots such as Nyquist plots, C' versus frequency and C'' versus Z'. The values extracted from these plots such as the specific capacitance at low frequency are averaged and their standard deviation is calculated. However, for plotting these plots, an average of the plots must be used as the features of these plots might change from one plot to another of the same sample; as shown in Figure (V.10) for 8RP-OO in 1M KNO_3. The average plots would be accompanied by the error bars illustrated with a shaded area, representing the standard deviation as shown below where the original plots are plotted along with their average plot and standard deviation. However, in the main chapters, such error areas were omitted in Nyquist plots and C'' versus Z' for the sake of the clarity of the plots because plots of various samples are displayed on the same graph.

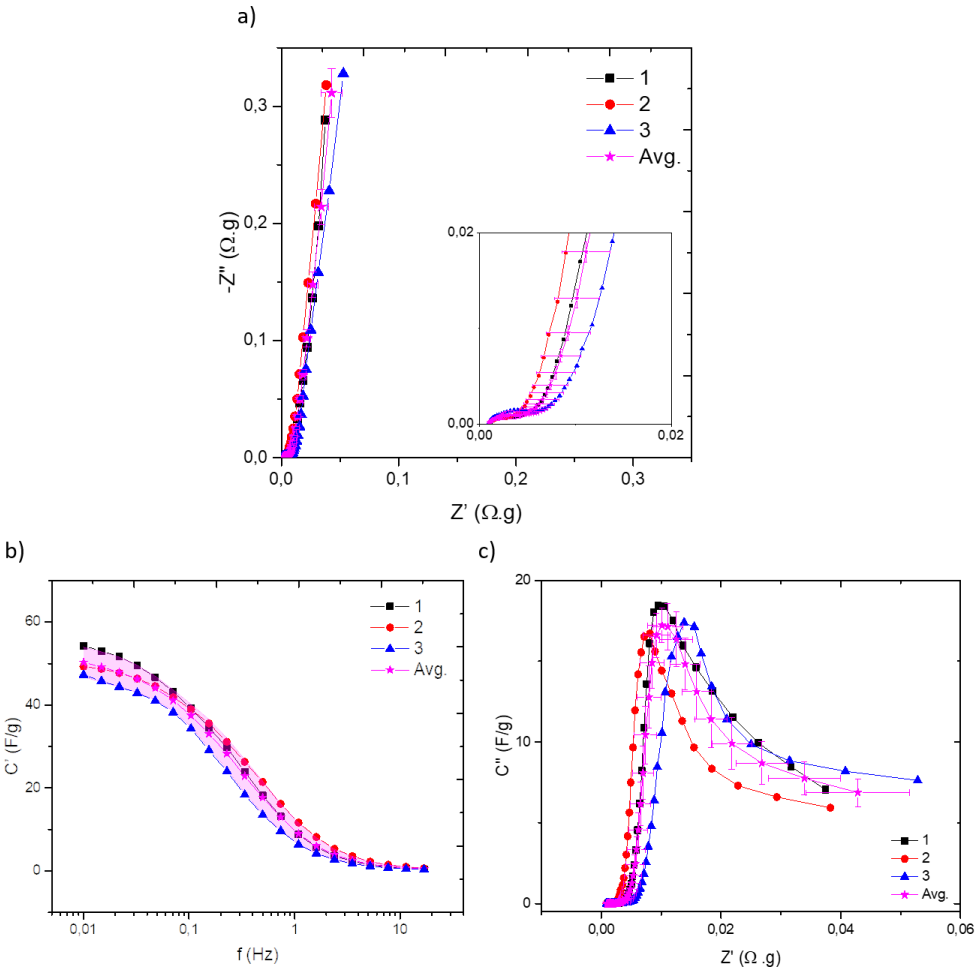

Figure V. 10 : Example of a) Nyquist plots, b) C' versus frequency and c) C'' versus Z' of 3 different 8RP-OO electrodes in 1M KNO_3 along with their average and its associated error bars, representing standard deviation

Similar treatment is done for the galvanostatic charge and discharge curves as the slope might differ from one electrode to another. Accordingly, the average plots are presented along with the standard deviation areas as shown in Figure (V.11) for rGO, 6RP, 7RP-NCH3 and 8RP-OO in 3M H_2SO_4.

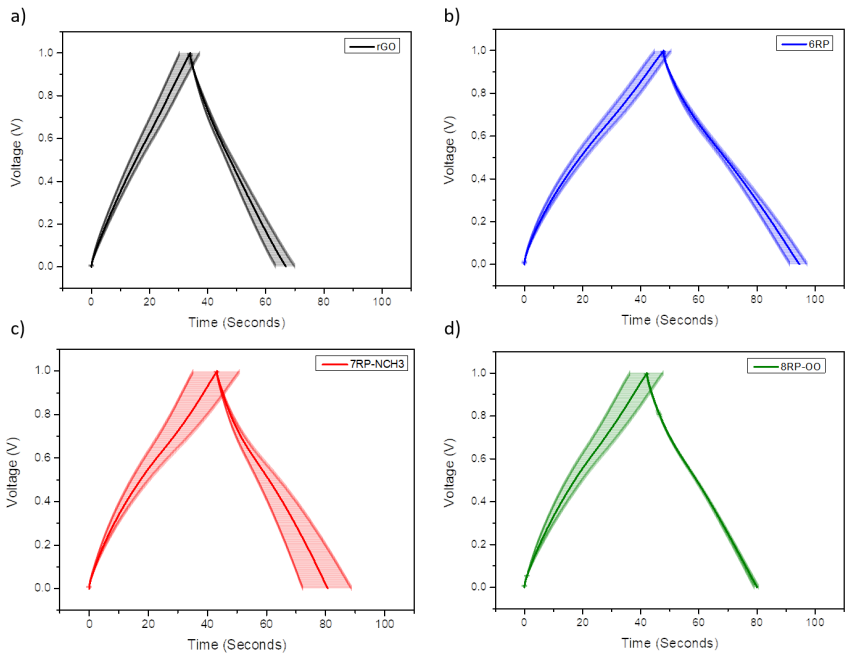

Figure V. 11 : Average galvanostatic charge and discharge curves at a constant current of 5mA for a) rGO, b) 6RP, c) 7RP-NCH3 and d) 8RP-OO along with their error bars illustrate with shaded areas, representing standard deviation

V.4 References

[1] S. M. Sze and K. K. Ng, “Physics of Semiconductor Devices | Wiley Online Books.” Accessed: Mar. 16, 2024. [Online]. Available: /10.1002/0470068329

[2] C. Zhong, Y. Deng, W. Hu, J. Qiao, L. Zhang, and J. Zhang, ‘A review of electrolyte materials and compositions for electrochemical supercapacitors’, *Chem. Soc. Rev.*, vol. 44, no. 21, pp. 7484–7539, Oct. 2015, doi: 10.1039/C5CS00303B.

[3] C. Kikuchi, H. Kurane, T. Watanabe, M. Demura, T. Kikukawa, and T. Tsukamoto, ‘Preference of Proteomonas sulcata anion channelrhodopsin for NO3− revealed using a pH electrode method’, *Sci Rep*, vol. 11, no. 1, Art. no. 1, Apr. 2021, doi: 10.1038/s41598-021-86812-z.

[4] Y.-Z. Chen, P. Li, X. Zhao, J.-Q. Zhang, and H.-M. Luo, ‘One-step synthesis of nitrogen-doped porous carbon for supercapacitors utilizing KNO3 as an electrolyte’, *J Solid State Electrochem*, vol. 21, no. 1, pp. 171–181, Jan. 2017, doi: 10.1007/s10008-016-3350-0.

[5] M. Chiku, S. Tomita, E. Higuchi, and H. Inoue, ‘Preparation and Characterization of Organic-Inorganic Hybrid Hydrogel Electrolyte Using Alkaline Solution’, *Polymers*, vol. 3, no. 4, Art. no. 4, Dec. 2011, doi: 10.3390/polym3041600.

[6] P. L. Taberna, P. Simon, and J. F. Fauvarque, ‘Electrochemical Characteristics and Impedance Spectroscopy Studies of Carbon-Carbon Supercapacitors’, *J. Electrochem. Soc.*, vol. 150, no. 3, p. A292, Jan. 2003, doi: 10.1149/1.1543948.

[7] B. E. Conway and D. C. W. Kannangara, ‘Zinc Oxidation and Redeposition Processes in Aqueous Alkali and Carbonate Solutions: II . Distinction Between Dissolution and Oxide Film Formation Processes’, *J. Electrochem. Soc.*, vol. 134, no. 4, p. 906, Apr. 1987, doi: 10.1149/1.2100594.

[8] T.-C. Liu, W. G. Pell, B. E. Conway, and S. L. Roberson, ‘Behavior of Molybdenum Nitrides as Materials for Electrochemical Capacitors: Comparison with Ruthenium Oxide’, *J. Electrochem. Soc.*, vol. 145, no. 6, p. 1882, Jun. 1998, doi: 10.1149/1.1838571.

[9] J. Wang, J. Polleux, J. Lim, and B. Dunn, ‘Pseudocapacitive Contributions to Electrochemical Energy Storage in TiO2 (Anatase) Nanoparticles’, *J. Phys. Chem. C*, vol. 111, no. 40, pp. 14925–14931, Oct. 2007, doi: 10.1021/jp074464w.

Résumé

Les supercondensateurs sont des dispositifs de stockage d'énergie de plus en plus recherchés car ils servent dans de nombreuses applications, telles que les moyens de transport, les équipements de chantier impliquant le port de charges lourdes, les éoliennes, etc. Ils doivent leur popularité à leur densité de puissance élevée, leur cyclabilité élevée, leur longue durée de vie, leur indépendance vis-à-vis des matériaux toxiques et nobles et leur large plage de températures de fonctionnement. Cependant, les supercondensateurs présentent une limitation importante qui empêche d'étendre leurs usages: leur faible densité d'énergie. De nombreux groupes essaient de lever ce verrou i) en développant de nouveaux matériaux d'électrode pour améliorer leur capacité, et ii) en élargissant la fenêtre de potentiel de l'électrolyte utilisé. Aujourd'hui, le carbone activé est le matériau d'électrode le plus couramment utilisé pour les supercondensateurs en raison de sa surface spécifique élevée, de son prix bon marché et de sa facilité de production. Néanmoins, sa capacité est limitée à 150 F/g dans les électrolytes organiques, ce qui contraint ses domaines d'application. L'un des matériaux prometteurs comme alternative est le graphène. Depuis sa découverte en 2004 [1], il est considéré comme un matériau à fort potentiel en raison de ses propriétés attractives. L'une d'entre elles est sa surface développée élevée, qui devrait théoriquement lui permettre d'atteindre une capacité électrochimique à double couche de 550 F/g [2]. Or la méthode de synthèse employée pour produire du graphène en suffisamment grande quantité pour répondre aux besoin de cette application est l'exfoliation chimique du graphite ; et malheureusement, cette méthode produit de l'oxyde de graphène réduit (rGO) dont les feuillets sont réempilés, ce qui limite l'exploitation de toute la surface développée du graphène pour l'électro-adsorption.

Le greffage de molécules organiques, aussi appelées « piliers » car intercalées entre les feuillets de graphène, s'est avérée être une technique efficace pour limiter les interactions π-π et empêcher partiellement le réempilement des feuillets de rGO [3]. En effet, on retrouve dans la littérature des exemples de graphène ponté pour lesquelles des valeurs de capacité augmentées par rapport à celles obtenues avec le rGO ont pu être obtenues. L'objectif de cette thèse est de mieux comprendre cette nouvelle classe de matériaux et leur emploi comme matériau d'électrode pour supercondensateurs. Les travaux effectués au cours de cette thèse ont donc eu pour but d'analyser i) l'effet de la chimie de surface, de la polarité des piliers et de la distance inter-feuillets de graphène de ces matériaux sur leurs performances électrochimiques, ainsi que ii) les mécanismes d'adsorption de charges associés. Ces corrélations permettront dans le futur d'optimiser le matériau pour atteindre des performances de stockage plus élevées.

Au cours de ces travaux de thèse, trois molécules de nature chimique et de longueurs différentes ont été utilisées comme agents pontant afin d'obtenir des assemblages de feuillets de graphène pontés ayant des propriétés structurelles et chimiques différentes (différentes valeurs d'espacement inter-feuillets (d-spacing) et différentes compositions chimiques des piliers). Pour évaluer le succès de la technique de pontage, pour déterminer la composition chimique et pour analyser la structure des échantillons, diverses techniques de caractérisation ont été utilisées, telles que la DRX, l'ATG, l'XPS, l'AE, l'IR-FT, la spectroscopie Raman, ainsi que les observations MEB et TEM, et les mesures d'angle de contact et de conductivité. Le coeur du travail de compréhension a consisté à essayer de corréler ces propriétés physico-chimiques aux performances de stockage de ces matériaux comme matériaux d'électrodes pour supercondensateurs. En conséquence, ces assemblages ont été cyclés électrochimiquement, et leurs capacitances ont été comparées à celles du rGO comme échantillon de référence en milieu H_2SO_4. Cette étude a permis de mettre en évidence que les échantillons pontés présentent tous une capacitance supérieure à celle du rGO dans ce milieu. Ces structures à distance inter-feuillets de graphène contrôlée permettent d'étudier les phénomènes d'appariement entre la taille des micropores créées (d-spacing) et le diamètre des ions électrolytiques. Cette étude a été réalisée en milieu aqueux dans différents électrolytes neutres pour essayer d'observer le rôle de la taille de l'ion solvaté (différentes tailles de cations Li^+, K^+ et d'anions SO_4^{2-}, NO_3^-). Les assemblages de graphène ponté ont également démontré des performances capacitives améliorées par rapport au rGO dans tous ces électrolytes neutres. Une corrélation entre ces performances améliorées et les différentes caractéristiques physico-chimiques a été établie, mettant en évidence le rôle important joué par la nature chimique du pilier et de l'espacement inter-feuillet (d). Le rôle prépondérant joués par les fonctions C=O, dans les réactions redox ou dans la formation de sites d'adsorption spécifiques, a pu être mis en évidence. Par ailleurs, l'espacement inter-feuillet est très important car l'ion ne perd pas (totalement) sa sphère de solvatation, et il est nécessaire que la taille de l'ion solvaté soit inférieure à la distance inter-feuillet de gaphène pour que ces ions accèdent à la microporosité crée par ces pontages moléculaires. Ainsi, l'échantillon qui a permis d'obtenir la capacité la plus élevée est celui dont l'espacement inter-feuillet est très proche ou supérieur aux tailles des cations et anions solvatés employés: la microporosité formée est bien accessible aux ions. Pour les échantillons et conditions de cyclage pour lesquelles les espèces électrolytiques peuvent accéder à cette microporosité, la densité de C=O devient alors le paramètre qui semble gouverner la valeur de la capacité. Les comparaisons croisées des résultats d'électrochimie, incluant aussi ceux de spectroscopie d'impédance électrochimique, ont également permis d'obtenir des informations indiquant que les anions sont impliqués dans le mécanisme d'adsorption des cations. Ces travaux ont confirmé l'intérêt du

pontage pour ouvrir de nouveaux sites d'électro-adsorption. Ils ont également permis d'acquérir de nouvelles connaissances sur ces assemblages, et de proposer de nouvelles pistes d'optimisation (décrites en conclusion), telles que l'utilisation de piliers redox actif ou l'obtention d'échantillons uniformément pontés.

Malgré l'efficacité démontrée des PGM, la plupart de leurs méthodes de préparation ne sont généralement pas éco-responsable car elles impliquent l'utilisation d'hydrate d'hydrazine (Hz) comme agent réducteur. L'hydrazine étant un produit chimique très toxique, des travaux ont été menés pour trouver des alternatives à son utilisation. De nombreux agents réducteurs ont été testés, et l'acide L-ascorbique (L-AA), communément appelé vitamine C, s'est révélé être un agent réducteur efficace, et offrant un processus de réduction « vert » [4]. Dans la littérature, de nombreux protocoles de réduction impliquant le L-AA ont été décrits. En conséquence, les travaux réalisés dans une seconde partie de cette thèse ont visé à rationaliser les paramètres de réaction importants permettant d'obtenir un rGO-VitC le plus réduit possible.

Ainsi, une étude des protocoles de réduction de l'oxyde de graphène à l'aide de L-AA a été réalisée, en faisant variant deux paramètres expérimentaux : la quantité de L-AA et la durée de la réaction. Les matériaux correspondant ont été analysés par XPS, AE, DRX, ATG, MEB, TEM, spectroscopie Raman, et des mesures de conductivité ont été effectuées. Le L-AA a démontré une efficacité de réduction importante. Les relations entre les conditions expérimentales et les propriétés physico-chimiques, structurelles et morphologiques intrinsèques des différents rGO-VitC ont été mises en évidence. De façon inattendue, on observe des conditions de réduction optimum pour des conditions de synthèse intermédiaires : augmenter la quantité de L-AA et la durée de réaction ne conduit pas à l'échantillon le plus réduit. En effet, le degré de réduction le plus élevé est obtenu pour l'échantillon ayant été réduit avec une quantité de L-AA élevée mais au cours d'une réaction courte. Ces observations ont conduit à la réalisation d'expériences de contrôles conçues pour essayer de comprendre quels intermédiaires réactionnels étaient formés, et conduisaient à cette ré-oxydation lors des réactions longues. Les mesures RPE ont notamment permis de mettre en évidence la présence du radical ascorbyle. Ensuite, les performances de stockage électrochimique des échantillons de rGO-VitC et rGO-Hz ont été évaluées dans divers électrolytes (acides, basiques et neutres) puis comparées. Le rGO-VitC a montré des performances supérieures à celles du rGO-Hz, tout en présentant des valeurs de résistance (ionique et ESR) similaires, dans tous les électrolytes. Les résultats obtenus ouvrent la voie à l'utilisation du L-AA comme méthode de réduction éco-responsable, non seulement pour obtenir du rGO, mais également pour préparer des matériaux tels que les graphènes pontés.

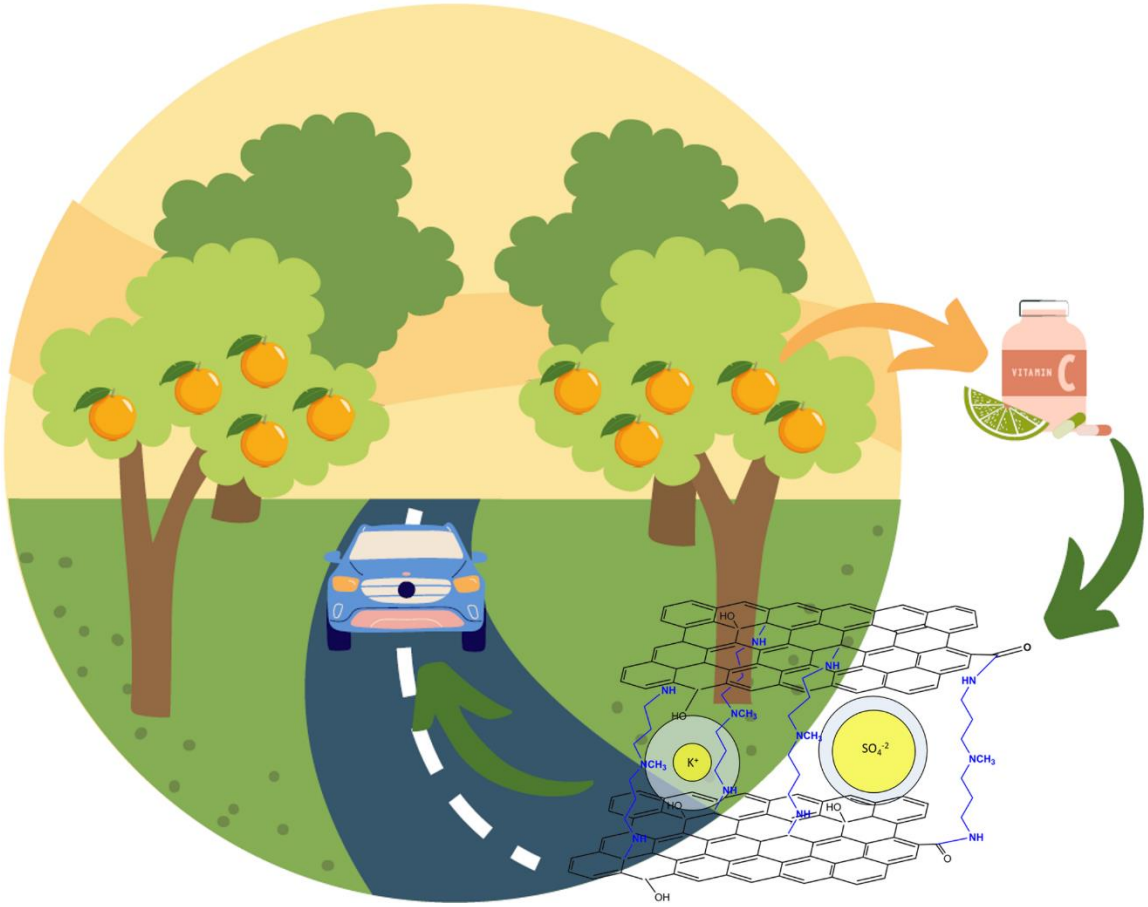

References:

[1] K. S. Novoselov *et al.*, 'Electric Field Effect in Atomically Thin Carbon Films', *Science*, vol. 306, no. 5696, pp. 666–669, Oct. 2004, doi: 10.1126/science.1102896.

[2] J. Zhu, D. Yang, Z. Yin, Q. Yan, and H. Zhang, 'Graphene and Graphene-Based Materials for Energy Storage Applications', *Small*, vol. 10, no. 17, pp. 3480–3498, 2014, doi: 10.1002/smll.201303202.

[3] H. Banda *et al.*, 'Sparsely Pillared Graphene Materials for High-Performance Supercapacitors: Improving Ion Transport and Storage Capacity', *ACS Nano*, vol. 13, no. 2, pp. 1443–1453, Feb. 2019, doi: 10.1021/acsnano.8b07102.

[4] K. K. H. De Silva, H.-H. Huang, R. K. Joshi, and M. Yoshimura, 'Chemical reduction of graphene oxide using green reductants', *Carbon*, vol. 119, pp. 190–199, Aug. 2017, doi: 10.1016/j.carbon.2017.04.025.